



University
of Glasgow

Kelly, Mary E. (2010) *Predicting the high-frequency airloads and acoustics associated with blade-vortex interaction*. PhD thesis.

<http://theses.gla.ac.uk/1513/>

Copyright and moral rights for this thesis are retained by the author

A copy can be downloaded for personal non-commercial research or study, without prior permission or charge

This thesis cannot be reproduced or quoted extensively from without first obtaining permission in writing from the Author

The content must not be changed in any way or sold commercially in any format or medium without the formal permission of the Author

When referring to this work, full bibliographic details including the author, title, awarding institution and date of the thesis must be given.

Predicting the High-frequency Airloads and Acoustics Associated with Blade-Vortex Interaction

Mary E. Kelly

Submitted in fulfilment of the requirements
for the degree of
Doctor of Philosophy

Department of Aerospace Engineering
Faculty of Engineering
University of Glasgow

March 2010

© 2010 M. E. Kelly

Abstract

As a rotorcraft descends or manoeuvres, the interactions which occur between the rotor blades and vortical structures within the rotor wake produce highly impulsive loads on the blades and with these a highly intrusive external noise. Brown's Vorticity Transport Model has been used to investigate the influence of the fidelity of the local blade aerodynamic model on the quality of the prediction of the high-frequency airloads associated with blade-vortex interactions and thus on the accuracy with which the acoustic signature of the aircraft can be predicted. Aerodynamic, wake structure and acoustic predictions using the Vorticity Transport Model are compared against the HART II wind tunnel data for an experimental rotor based on the characteristics of the Bo105 rotor. The model can resolve very accurately the structure of the wake, and allows significant flexibility in the way that the blade loading can be represented. The predictions of two models for the local blade aerodynamics are compared for all three of the HART II flight cases. The first model is a simple lifting-line model and the second is a somewhat more sophisticated lifting-chord model based on unsteady thin aerofoil theory. The predicted positions of the vortex cores agree with measured data to within a fraction of the blade chord, and the strength of the vortices is preserved to well downstream of the rotor, essentially independently of the resolution of the calculation or the blade model used. A marked improvement in accuracy of the predicted high-frequency airloads and acoustic signature of the HART II rotor is obtained when the lifting-chord model for the blade aerodynamics is used instead of the lifting-line type approach. Errors in the amplitude and phase of the loading peaks are reduced and the quality of the prediction is affected to a lesser extent by the computational resolution of the wake. Predictions of the acoustic signature of the rotor are

similarly affected, with the lifting-chord model at the highest resolution producing the best representation of the distribution of sound pressure on the ground plane below the rotor.

Acknowledgements

I would like to thank my supervisor, Prof. Richard Brown, for his patience, encouragement and guidance throughout the course of my PhD. His wealth of knowledge and enthusiasm for his subject have been greatly appreciated.

I would also like to extend my appreciation to the members of the HART team for providing the data that was used in this study. In particular, I would like to thank Dr. Berend van der Wall and Dr. Joon Lim for their encouragement and comments during the course of the research leading to this dissertation.

I would like to thank, past and present members of the Rotorcraft Aeromechanics Laboratory for their support and advice and their individual help over the past years. In particular, Dr. Adam Kenyon for his help in setting up simulations which included a fuselage, Dr. Karthikeyan Duraisamy for provision of the acoustic post-processor used in this work and Dr. Hyo won Kim for his endless help with latex and tecplot.

Finally I would like to express my appreciation to my friends and family, particularly my parents, who have supported me through, not only my PhD, but my academic career to date. A special mention goes to Constantinos Regas, Ali Downes and Joanne and Keith Irwin, who have helped immensely in the proof reading of this dissertation.

To my parents

Table of contents

Abstract	2
Acknowledgements	4
Dedication	5
Table of Contents	6
List of Figures	9
List of Tables	22
Nomenclature	24
1 Introduction	31
1.1 Sources of helicopter noise	32
1.2 Predicting BVI noise	34
1.2.1 Previous work	35
1.2.2 HART initiative	39
1.2.3 Wake modelling	40

1.3	Present research objectives	43
1.4	Synopsis	44
1.5	Publications	45
2	Computational model	48
2.1	Introduction	48
2.2	Vorticity Transport Model	50
2.3	Numerical implementation	52
2.3.1	Grid structure	53
2.3.2	Weighted average flux method	56
2.3.3	Calculation of the velocity field	58
2.4	Calculation of the vorticity source	64
2.5	HART II rotor	67
2.6	Structural dynamics	67
2.6.1	Prescription of the blade dynamics	68
2.7	Control algorithm	70
2.8	Acoustic analysis	71
2.9	Fuselage model	73
2.10	Summary	75
3	Aerodynamic modelling of the rotor blades	77
3.1	Model implementation	81
3.1.1	Lifting-line model	82

3.1.2	Lifting-chord model	83
3.1.3	Compressibility effects and stall	85
3.2	Model verification	86
3.2.1	Wagner’s problem	88
3.2.2	Küssner’s problem	89
3.2.3	Interaction with an isolated vortex	90
3.3	Summary	92
4	Airload prediction	94
4.1	Verification of structural dynamics	95
4.2	Predictions of the HART II blade airload	100
4.2.1	Low-frequency component of airload	102
4.2.2	High-frequency component of airload	107
4.2.3	Effect of including a representation of the drive enclosure	114
4.3	Summary	114
5	Wake geometry	117
5.1	Wake visualisation	118
5.1.1	Wake sensitivity to blade aerodynamic model	120
5.2	Trajectory of tip vortices	122
5.2.1	Influence of blade aerodynamic model	125
5.2.2	Effect of grid resolution	126
5.2.3	Effect of including a representation of the drive enclosure	127

5.2.4	Minimum noise and minimum vibration cases	129
5.3	Roll-up of the tip vortex	134
5.4	Summary	144
6	Acoustic prediction	146
6.1	Sound Pressure Levels	147
6.2	Acoustic sources	154
6.2.1	Baseline HART II flight case	155
6.2.2	Minimum noise HART II flight case	164
6.2.3	Minimum vibration HART II flight case	172
6.3	Summary	180
7	Conclusions	182
	References	187
	Appendix	198
A	Interpolation coefficients for blade deformations	198
A.1	Elastic torsion motion (θ_{el}) coefficients	198
A.2	Elastic flap motion (Z_{el}) coefficients	199
A.3	Elastic lag motion (Y_{el}) coefficients	200

List of Figures

2.1	Nested grid structure where the resolution decreases with increasing distance from the rotor hub, showing overlapped region at grid level boundaries.	55
2.2	Stencil for the calculation of the inter-cell fluxes of vorticity.	57
2.3	Interaction between target and source clusters using the multipole method to calculate the velocity field.	60
2.4	Evaluation of the velocity field on cluster i and the categorisation of the velocity-inducing clusters into the near-field (light grey), the intermediate-field (dark grey) and the far-field (white) velocity components.	63
2.5	Representation of the ‘near-wake’.	65
2.6	Flapping, lead-lag and feathering motion of the rotor blade.	68
3.1	A schematic of the Weissinger-L lifting-line model, showing a part of the rotor blade.	82
3.2	A schematic of the lifting-chord model, showing a part of the rotor blade.	84
3.3	Wagner’s problem for the aerodynamic response of an aerofoil to a step change in angle of attack. (The step change in angle of attack is applied at time $t = 0$).	87
3.4	Analytical and numerical solutions to Küssner’s problem compared. (The leading edge of the aerofoil encounters the gust at time $t = 0$).	90

3.5	Predicted aerodynamic response of an aerofoil to interaction with an isolated vortex. (The vortex passes $0.25c$ below the quarter-chord of the aerofoil at time $t = 0$).	91
3.6	Predicted aerodynamic response of an aerofoil to interaction with isolated vortices with varying core sizes but constant circulation, core size decreases from left to right. (The vortex passes below the quarter chord of the aerofoil at time $t = 0$).	92
4.1	Comparison of the interpolated and experimentally measured deflections for the reference blade of the HART II model rotor over a single rotor revolution.	96
4.2	Comparison of the interpolated and experimentally measured deflection at 87% span for the reference blade of the HART II model rotor.	97
4.3	Comparison of the interpolated and experimentally measured deflection at the blade tip for the reference blade of the HART II model rotor.	97
4.4	Prediction of the blade loading ($C_N M^2$) at 87% span (BL case, with six coefficients in the radial direction and varying numbers of coefficients in the azimuthal direction).	98
4.5	Prediction of the blade loading ($C_N M^2$) at 87% span (BL case, with six coefficients in the radial direction and varying numbers of coefficients in the azimuthal direction, signal filtered to include only higher harmonic components, greater than 10/rev.	98
4.6	Prediction of the blade loading ($C_N M^2$) at 87% span (BL case, comparison of predictions using van der Wall's synthesised blade deflections (Ref. 1) and variable-separable interpolation on the HART II experimental data).	99
4.7	Prediction of the blade loading ($C_N M^2$) at 87% span (BL case, comparison of predictions using van der Wall's synthesised blade deflections (Ref. 1) and variable-separable interpolation on the HART II experimental data, signal filtered to include only higher harmonic components, greater than 10/rev).	99

4.8	Contours of non-dimensional lift ($C_N M^2$) as predicted by the VTM at various computational resolutions using the lifting-line and the lifting-chord representations of the blade aerodynamics, for the HART II BL case. (A representation of the drive enclosure has not been included in the calculations).	102
4.9	Contours of non-dimensional lift ($C_N M^2$) as predicted by the VTM at the medium computational resolution using the lifting-line and the lifting-chord representations of the blade aerodynamics, for all three HART II flight cases. (A representation of the drive enclosure has not been included in the calculations).	103
4.10	Comparison of blade loading ($C_N M^2$) at 87% span, as predicted using lifting-line and lifting-chord representations of the blade aerodynamics, against experimental data for all three HART II flight cases. (A representation of the drive enclosure has not been included in the calculations).	104
4.11	Comparison of blade loading ($C_N M^2$) at 87% span, as predicted using lifting-line and lifting-chord representations of the blade aerodynamics, against experimental data for all three HART II flight cases. (A representation of the drive enclosure has not been included in the calculations).	105
4.12	Comparison of blade loading ($C_N M^2$) at 87% span, as predicted using lifting-line representation of the blade aerodynamics, with and without a representation of the blade area between the hub and the root cut-out. (A representation of the drive enclosure has not been included in the calculations).	106

- 4.13 Comparison of blade loading ($C_N M^2$) at 87% span, as predicted using lifting-line representation of the blade aerodynamics, with and without a representation of the blade area between the hub and the root cut-out. The signal has been filtered to include only higher harmonic components, greater than 10/rev. (A representation of the drive enclosure has not been included in the calculations). 107
- 4.14 Contours of non-dimensional lift ($C_N M^2$) as predicted by the VTM at the medium computational resolution using the lifting-line and the lifting-chord representations of the blade aerodynamics. The signal has been filtered to include only the higher harmonic components, greater than 10/rev. (A representation of the drive enclosure has not been included in the calculations). 108
- 4.15 Comparison of blade loading ($C_N M^2$) at 87% span, as predicted using lifting-line and lifting-chord representations of the blade aerodynamics, against experimental data for the HART II BL case. The signal has been filtered to include only higher harmonic components, greater than 10/rev. (A representation of the drive enclosure has not been included in the calculations). 110
- 4.16 Comparison of blade loading ($C_N M^2$) at 87% span, as predicted using lifting-line and lifting-chord representations of the blade aerodynamics, against experimental data for the HART II MN case. The signal has been filtered to include only higher harmonic components, greater than 10/rev. (A representation of the drive enclosure has not been included in the calculations). 111
- 4.17 Comparison of blade loading ($C_N M^2$) at 87% span, as predicted using lifting-line and lifting-chord representations of the blade aerodynamics, against experimental data for the HART II MV case. The signal has been filtered to include only higher harmonic components, greater than 10/rev. (A representation of the drive enclosure has not been included in the calculations). 112

4.18	Comparison of blade loading ($C_N M^2$) at 87% span, as predicted using the lifting-line representation of the blade aerodynamics, against experimental data for all three HART II flight cases, with and without a representation of the drive enclosure (fuselage) included in the calculations.	113
4.19	Comparison of blade loading ($C_N M^2$) at 87% span, as predicted using the lifting-line representation of the blade aerodynamics, against experimental data for all three HART II flight cases, with and without a representation of the drive enclosure (fuselage) included in the calculations. The signal has been filtered to include only higher harmonic components, greater than 10/rev.	114
5.1	Locations of PIV measurement planes superimposed on the wake structure predicted by the VTM for the HART II BL case.	119
5.2	Visualisation of the VTM-predicted wake geometry from simulations of the HART II rotor at the medium computational resolution (a representation of the drive enclosure has been included in the calculations).	120
5.3	Geometry of the rotor wake, with the reference blade at 70° azimuth, as predicted using lifting-line and lifting-chord representations of the blade aerodynamics, for the HART II MN flight case. (A representation of the drive enclosure has not been included in the calculations).	121
5.4	Computed wake structure (contours of vorticity magnitude) and vortex core positions (symbols) estimated from the experimental data compared on a longitudinal slice through the wake at 40% of the rotor radius. (HART II BL flight case).	122
5.5	Computed wake structure (contours of vorticity magnitude) and vortex core positions (symbols) estimated from the experimental data compared on a longitudinal slice through the wake at 55% of the rotor radius. (HART II BL flight case).	123

5.6	Computed wake structure (contours of vorticity magnitude) and vortex core positions (symbols) estimated from the experimental data compared on a longitudinal slice through the wake at 70% of the rotor radius. (HART II BL flight case).	123
5.7	Computed wake structure (contours of vorticity magnitude) and vortex core positions (symbols) estimated from the experimental data compared on a longitudinal slice through the wake at 85% of the rotor radius. (HART II BL flight case).	124
5.8	Computed wake structure (contours of vorticity magnitude) and vortex core positions (symbols) estimated from the experimental data compared on a longitudinal slice through the wake at 97% of the rotor radius. (HART II BL flight case).	124
5.9	Computed structure of wake vorticity (contours) and measured vortex core positions (symbols) compared on longitudinal slices through the wake at 40% of the rotor radius, at both the medium and fine computational resolutions. (HART II BL flight case).	126
5.10	Computed structure of wake vorticity (contours) and measured vortex core positions (symbols) compared on longitudinal slices through the wake at 70% of the rotor radius, at both the medium and fine computational resolutions. (HART II BL flight case).	127
5.11	Computed structure of wake vorticity (contours) and measured vortex core positions (symbols) compared on longitudinal slices through the wake at 70% of the rotor radius, with and without a representation of the drive enclosure. (HART II BL flight case).	128
5.12	Computed wake structure (contours of vorticity magnitude) and vortex core positions (symbols) estimated from the experimental data compared on a longitudinal slice through the wake at 40% of the rotor radius. (HART II MN flight case).	128

5.13	Computed wake structure (contours of vorticity magnitude) and vortex core positions (symbols) estimated from the experimental data compared on a longitudinal slice through the wake at 55% of the rotor radius. (HART II MN flight case).	129
5.14	Computed wake structure (contours of vorticity magnitude) and vortex core positions (symbols) estimated from the experimental data compared on a longitudinal slice through the wake at 70% of the rotor radius. (HART II MN flight case).	129
5.15	Computed wake structure (contours of vorticity magnitude) and vortex core positions (symbols) estimated from the experimental data compared on a longitudinal slice through the wake at 85% of the rotor radius. (HART II MN flight case).	130
5.16	Computed wake structure (contours of vorticity magnitude) and vortex core positions (symbols) estimated from the experimental data compared on a longitudinal slice through the wake at 97% of the rotor radius. (HART II MN flight case).	130
5.17	Computed wake structure (contours of vorticity magnitude) and vortex core positions (symbols) estimated from the experimental data compared on a longitudinal slice through the wake at 40% of the rotor radius. (HART II MV flight case).	131
5.18	Computed wake structure (contours of vorticity magnitude) and vortex core positions (symbols) estimated from the experimental data compared on a longitudinal slice through the wake at 55% of the rotor radius. (HART II MV flight case).	131
5.19	Computed wake structure (contours of vorticity magnitude) and vortex core positions (symbols) estimated from the experimental data compared on a longitudinal slice through the wake at 70% of the rotor radius. (HART II MV flight case).	132

5.20	Computed wake structure (contours of vorticity magnitude) and vortex core positions (symbols) estimated from the experimental data compared on a longitudinal slice through the wake at 85% of the rotor radius. (HART II MV flight case).	132
5.21	Computed wake structure (contours of vorticity magnitude) and vortex core positions (symbols) estimated from the experimental data compared on a longitudinal slice through the wake at 97% of the rotor radius. (HART II MV flight case).	133
5.22	Experimental vorticity distribution at the resolution of the PIV experimental data compared to experimental data where the resolution has been reduced to be comparable to that of the fine computation. (Position 17a, i.e. vortex age 5.3°).	135
5.23	Comparison of vorticity field on the advancing side of the rotor, at a wake age of 5.3° (BL case, position 17a), using lifting-line representation of the blade aerodynamics and at various computational resolutions.	136
5.24	Comparison of vorticity field on the advancing side of the rotor, at a wake age of 25.3° (BL case, position 17), using lifting-line and lifting chord representations of the blade aerodynamics and at the medium computational resolution.	137
5.25	Comparison of vorticity field on the advancing side of the rotor, at a wake age of 205.3° (BL case, position 19), using lifting-line and lifting chord representations of the blade aerodynamics and at the medium computational resolution.	138
5.26	Comparison of vorticity field on the advancing side of the rotor, at a wake age of 425.3° (BL case, position 22), using lifting-line and lifting chord representations of the blade aerodynamics and at the medium computational resolution.	139

5.27	Comparison of vorticity field on the advancing side of the rotor, at a wake age of 5.3° (BL case, position 17a) behind each blade of the HART II rotor, showing the blade-to-blade variability of the wake structure, using a lifting-line representation of the blade aerodynamics and at the fine computational resolution.	141
5.28	Variation of tip vortex circulation with wake age (Advancing side of the rotor disc, baseline HART II case).	142
5.29	Variation of the tip vortex circulation with wake age for various computational resolutions (Advancing side of the rotor disc, baseline HART II case).	142
5.30	Variation of the vortex core radius with wake age (Advancing side of the rotor disc, baseline HART II case).	142
5.31	Position of the vortex core as a function of wake age on the advancing side of the rotor disc. Bars attached to data represent the size of the vortex core. (Baseline HART II case, position 17).	143
6.1	Predicted and measured SPL noise contours for the HART BL flight case. (The rotor position is marked by a dashed circle and small circles mark the positions of the microphones located at the SPL maxima in the measured data).	148
6.2	Difference between the predicted and measured SPL noise contours for the HART BL flight case. (The rotor position is marked by a dashed circle and small circles mark the positions of the microphones located at the SPL maxima in the measured data).	149
6.3	Predicted and measured SPL noise contours for the HART MN flight case. (The rotor position is marked by a dashed circle and small circles mark the positions of the microphones located at the SPL maxima in the measured data).	150

6.4	Difference between the predicted and measured SPL noise contours for the HART MN flight case. (The rotor position is marked by a dashed circle and small circles mark the positions of the microphones located at the SPL maxima in the measured data).	151
6.5	Predicted and measured SPL noise contours for the HART MV flight case. (The rotor position is marked by a dashed circle and small circles mark the positions of the microphones located at the SPL maxima in the measured data).	152
6.6	Difference between the predicted and measured SPL noise contours for the HART MV flight case. (The rotor position is marked by a dashed circle and small circles mark the positions of the microphones located at the SPL maxima in the measured data).	153
6.7	Time history of acoustic pressure for one blade passage and the corresponding BVI-induced airloads and source density distribution on the rotor for an observer (marked by small circle) located at the experimentally-measured SPL maximum on the retreating side of the rotor (HART II BL case). Numerical results are for the <i>coarse</i> computational resolution.	157
6.8	Time history of acoustic pressure for one blade passage and the corresponding BVI-induced airloads and source density distribution on the rotor for an observer (marked by small circle) located at the experimentally-measured SPL maximum on the retreating side of the rotor (HART II BL case). Numerical results are for the <i>medium</i> computational resolution.	158
6.9	Time history of acoustic pressure for one blade passage and the corresponding BVI-induced airloads and source density distribution on the rotor for an observer (marked by small circle) located at the experimentally-measured SPL maximum on the retreating side of the rotor (HART II BL case). Numerical results are for the <i>fine</i> computational resolution.	159

6.10	Time history of acoustic pressure for one blade passage and the corresponding BVI-induced airloads and source density distribution on the rotor for an observer (marked by small circle) located at the experimentally-measured SPL maximum on the advancing side of the rotor (HART II BL case). Numerical results are for the <i>coarse</i> computational resolution.	160
6.11	Time history of acoustic pressure for one blade passage and the corresponding BVI-induced airloads and source density distribution on the rotor for an observer (marked by small circle) located at the experimentally-measured SPL maximum on the advancing side of the rotor (HART II BL case). Numerical results are for the <i>medium</i> computational resolution.	161
6.12	Time history of acoustic pressure for one blade passage and the corresponding BVI-induced airloads and source density distribution on the rotor for an observer (marked by small circle) located at the experimentally-measured SPL maximum on the advancing side of the rotor (HART II BL case). Numerical results are for the <i>fine</i> computational resolution.	162
6.13	Geometry of the root and tip vortices as generated by each blade, when the reference blade lies at an azimuth of 40°	163
6.14	Time history of acoustic pressure for one blade passage and the corresponding BVI-induced airloads and source density distribution on the rotor for an observer (marked by small circle) located at the experimentally-measured SPL maximum on the retreating side of the rotor (HART II MN case). Numerical results are for the <i>coarse</i> computational resolution.	166
6.15	Time history of acoustic pressure for one blade passage and the corresponding BVI-induced airloads and source density distribution on the rotor for an observer (marked by small circle) located at the experimentally-measured SPL maximum on the retreating side of the rotor (HART II MN case). Numerical results are for the <i>medium</i> computational resolution.	167

6.16	Time history of acoustic pressure for one blade passage and the corresponding BVI-induced airloads and source density distribution on the rotor for an observer (marked by small circle) located at the experimentally-measured SPL maximum on the retreating side of the rotor (HART II MN case). Numerical results are for the <i>fine</i> computational resolution.	168
6.17	Time history of acoustic pressure for one blade passage and the corresponding BVI-induced airloads and source density distribution on the rotor for an observer (marked by small circle) located at the experimentally-measured SPL maximum on the advancing side of the rotor (HART II MN case). Numerical results are for the <i>coarse</i> computational resolution.	169
6.18	Time history of acoustic pressure for one blade passage and the corresponding BVI-induced airloads and source density distribution on the rotor for an observer (marked by small circle) located at the experimentally-measured SPL maximum on the advancing side of the rotor (HART II MN case). Numerical results are for the <i>medium</i> computational resolution.	170
6.19	Time history of acoustic pressure for one blade passage and the corresponding BVI-induced airloads and source density distribution on the rotor for an observer (marked by small circle) located at the experimentally-measured SPL maximum on the advancing side of the rotor (HART II MN case). Numerical results are for the <i>fine</i> computational resolution.	171
6.20	Time history of acoustic pressure for one blade passage and the corresponding BVI-induced airloads and source density distribution on the rotor for an observer (marked by small circle) located at the experimentally-measured SPL maximum on the retreating side of the rotor (HART II MV case). Numerical results are for the <i>coarse</i> computational resolution.	174

6.21	Time history of acoustic pressure for one blade passage and the corresponding BVI-induced airloads and source density distribution on the rotor for an observer (marked by small circle) located at the experimentally-measured SPL maximum on the retreating side of the rotor (HART II MV case). Numerical results are for the <i>medium</i> computational resolution.	175
6.22	Time history of acoustic pressure for one blade passage and the corresponding BVI-induced airloads and source density distribution on the rotor for an observer (marked by small circle) located at the experimentally-measured SPL maximum on the retreating side of the rotor (HART II MV case). Numerical results are for the <i>fine</i> computational resolution.	176
6.23	Time history of acoustic pressure for one blade passage and the corresponding BVI-induced airloads and source density distribution on the rotor for an observer (marked by small circle) located at the experimentally-measured SPL maximum on the advancing side of the rotor (HART II MV case). Numerical results are for the <i>coarse</i> computational resolution.	177
6.24	Time history of acoustic pressure for one blade passage and the corresponding BVI-induced airloads and source density distribution on the rotor for an observer (marked by small circle) located at the experimentally-measured SPL maximum on the advancing side of the rotor (HART II MV case). Numerical results are for the <i>medium</i> computational resolution.	178
6.25	Time history of acoustic pressure for one blade passage and the corresponding BVI-induced airloads and source density distribution on the rotor for an observer (marked by small circle) located at the experimentally-measured SPL maximum on the advancing side of the rotor (HART II MV case). Numerical results are for the <i>fine</i> computational resolution.	179

List of Tables

2.1	Rotor operational parameters	67
4.1	Computational resolution	101
A.1	Interpolation coefficients to recreate the elastic torsion motion of Blade 1. (HART II BL case, degrees, R in metres).	198
A.2	Interpolation coefficients to recreate the elastic torsion motion of Blade 2. (HART II BL case, degrees, R in metres).	198
A.3	Interpolation coefficients to recreate the elastic torsion motion of Blade 3. (HART II BL case, degrees, R in metres).	199
A.4	Interpolation coefficients to recreate the elastic torsion motion of Blade 4 (HART II BL case, degrees, R in metres).	199
A.5	Interpolation coefficients to recreate the elastic flap motion of Blade 1. (HART II BL case, mm, R in metres).	199
A.6	Interpolation coefficients to recreate the elastic flap motion of Blade 2. (HART II BL case, mm, R in metres).	199
A.7	Interpolation coefficients to recreate the elastic flap motion of Blade 3. (HART II BL case, mm, R in metres).	200
A.8	Interpolation coefficients to recreate the elastic flap motion of Blade 4. (HART II BL case, mm, R in metres).	200

A.9 Interpolation coefficients to recreate the elastic lag motion of Blade 1. (HART II BL case, mm, R in metres).	200
A.10 Interpolation coefficients to recreate the elastic lag motion of Blade 2. (HART II BL case, mm, R in metres).	200
A.11 Interpolation coefficients to recreate the elastic lag motion of Blade 3. (HART II BL case, mm, R in metres).	201
A.12 Interpolation coefficients to recreate the elastic lag motion of Blade 4. (HART II BL case, mm, R in metres).	201

Nomenclature

Rotor System

b	: blade semi-chord
c	: blade chord
C_D	: drag, scaled by $\frac{1}{2}\rho(\Omega R)^2 c$
C_L	: lift, scaled by $\frac{1}{2}\rho(\Omega R)^2 c$
C_M	: moment, scaled by $\frac{1}{2}\rho(\Omega R)^2 c^2$
C_T	: rotor thrust, scaled by $\rho A(\Omega R)^2$
\dot{h}	: aerofoil plunge velocity
N_b	: number of blades on rotor
r	: radial position, scaled by R
q	: aerofoil pitch rate
R	: rotor radius
α	: aerofoil incidence
α_0	: aerofoil incidence due to camber
λ	: rotor inflow scaled by ΩR
θ	: control angle $\theta = \theta_0 + \theta_{1c} \cos \psi + \theta_{1s} \sin \psi$
θ_0	: collective
θ_{1c}	: lateral cyclic
θ_{1s}	: longitudinal cyclic
μ	: rotor forward speed scaled by ΩR

σ : rotor solidity
 Ω : rotor rotational speed
 ψ : azimuthal location

Fluid Dynamic Model

F : intercell vorticity flux
 i : cell index
 M : Mach number
 M : the number of substeps in the time-stepping scheme
 N : number of grid cells
 p : pressure in the flow
 Q : solution domain
 q : any flow variable
 S : vorticity source
 t : time
 \mathbf{u} : flow velocity
 \mathbf{u}_b : flow velocity relative to blade
 V : cell volume
 W : weighting function
 Δ_0 : cell edge-length of the underlying Cartesian stencil
 Δt : timestep
 Δx : cell edge-length
 ν : kinematic viscosity of the flow
 ν : cell Courant number
 τ : unit vector parallel to the trailing edge of the blade
 λ : wave-amplifier function
 ρ : flow density
 ω : vorticity

ω_b : bound vorticity

Fast Multipole Method

a_k : k^{th} Taylor coefficient of K_δ

b_k : k^{th} Taylor coefficient of ϕ_δ

K : Biot-Savart kernel

K_δ : regularised Biot-Savart Kernel

m_k : k^{th} moment of vorticity

δ : kernel smoothing parameter

ε : error

ϕ_δ : regularised Newtonian potential

Structural Dynamics

a_{ij} : interpolation coefficients

D : deflection

N_r : number of radial interpolation functions

N_a : number of azimuthal interpolation functions

$P_j(\psi)$: azimuthal interpolation functions

$R_i(r)$: radial interpolation functions

z_{el} : elastic flap deflection

y_{el} : elastic lag deflection

θ_{el} : elastic blade torsion

Control Algorithm

F	: vector of overall force and moment coefficients
F^*	: vector of target force and moment coefficients
\bar{F}	: time average of force and moment coefficients
N_a	: number of azimuthal interpolation functions
K	: trim coupling matrix
ζ	: array of control inputs

Acoustics

a_0	: speed of sound
F	: force vector
p'	: acoustic pressure
r	: observer distance from source
t	: observer time
v_n	: velocity of blade surface
τ	: acoustic source time

Fuselage Model

A_{ij}	: matrix of influence coefficients
\mathbf{n}	: unit vector normal to the panel
N_{fus}	: number of fuselage panels
U_∞	: freestream velocity
w	: wake induced velocity
ϕ	: velocity potential

Γ_j : martrix of vortex loop strengths

Blade Aerodynamic Model

C_l : sectional lift coefficient

C_d : sectional drag coefficient

C_m : sectional moment coefficient

f : reverse flow parameter

w_n : normal blade velocity relative to the flow

φ : Glauert's variable

λ_n : normal velocity due to vorticity in the flow

Γ_b : bound vorticity on blade section

Abbreviations

AFDD : US Army Aeroflightdynamics Directorate

AHS : American Helicopter Society

BL : Baseline

BVI : Blade Vortex Interaction

CFD : Computational Fluid Dynamics

CSD : Computational Structural Dynamics

DNW : Duits-Nederlandse Wind-tunnel

FMM : Fast Multipole Method

HART : Higher Harmonic Control Aeroacoustics Rotor Test

HHC : Higher Harmonic Control

HSI : High Speed Impulsive

LDV : Laser Doppler Velocimetry

LLF : Large Low-speed Facility
MN : Minimum Noise
MV : Minimum Vibration
NASA : National Aeronautics and Space Administration
PIV : Particle Image Velocimetry
SPL : Sound Pressure Level
TV : Total Variation
TVD : Total Variation Diminishing
UTRC : United Technologies Research Center
VTM : Vorticity Transport Model
VTOL : Vertical Take-off and Landing
WAF : Weighted Average Flux

Chapter 1

Introduction

The main advantages of rotary-wing aircraft when compared to conventional fixed-wing aircraft are their ability to land and take-off vertically and to hover in the air. Such manoeuvring capabilities, whilst adding significantly to the value of a helicopter, have brought with them unique acoustic problems. Despite being considered the quietest of all VTOL aircraft, the helicopter still produces noise which is loud enough to compromise its utility. As legislated restrictions on aircraft noise have become more rigorous over the years, noise reduction has, correspondingly, become an issue of particular importance to the designers of modern rotorcraft.

The noise sources which are associated with a helicopter in flight are mainly due to the complex aerodynamic environment which it creates. The aerodynamic environment in which a rotorcraft operates is dominated by the strong vortical structures that are generated by the rotating blade system. The interactions between these vortices and the various structural components of the aircraft account for many of the design problems which rotorcraft encounter. In particular, the localised aerodynamic interactions between the rotor blades and the vortices in the wake induce impulsive fluctuations of pressure along the blade span, that are a significant source of noise and vibration.

The intensity and directivity of the noise generated by a helicopter is of considerable importance for both civilian and military applications as strict certification and community

noise constraints often apply. For civilian applications, the public acceptance of helicopters is highly dependent on the levels of external noise, especially where helicopters come in to land close to or within highly populated areas. Noise reduces the stealth capabilities of military rotorcraft, which can reduce their military effectiveness and compromise their tactical advantage. Such requirements have led industry to investigate the sources of noise associated with helicopters in flight with the aim of significantly reducing current noise levels.

Since the rotors also provide the thrust, lift and directional control of the helicopter, there is an inevitable trade-off between the need to reduce the noise that is produced and the resulting impact on the overall rotor performance. Moreover, the various components of the rotorcraft are aerodynamically more tightly coupled than in the case of a fixed-wing aircraft, where the noise reduction can be made on a component by component basis without significantly affecting the overall performance of the aircraft. These issues make it difficult to decouple the noise reduction problem from the efficiency or performance of the helicopter as a whole. Despite this, the helicopter community's understanding of the mechanisms which generate the noise that is associated with helicopter flight has advanced substantially in recent years due to improvements in both computational methods and experiments.

1.1 Sources of helicopter noise

Noise is essentially produced by the propagation of a pressure fluctuation through a fluid medium. In the context of a helicopter, the major sources of noise can be characterised as 'mechanical' or 'aero-acoustic'. Mechanical noise is generated by the engine and gear-box and by vibrations of the airframe. Noise from mechanical sources tends not to propagate very far and thus affects most strongly regions which are in close proximity to the source of the sound. As a result, mechanical sources are strong contributors to the internal noise of the helicopter. The pressure changes that result through the production of lift and drag and the unsteady aerodynamics within the flow-field contribute to the aero-acoustic noise. The pressure waves generated by aero-acoustic sources can radiate into the far-field

and are therefore significant contributors to the external noise of the helicopter. Aero-acoustic noise comes from a variety of different sources. Depending on its source, the noise produced has a distinct range of frequencies and a specific direction in which it will propagate. Aero-acoustic sources can be broken down into three main categories: ‘rotational/harmonic’, ‘broadband’ and ‘impulsive’.

The term ‘broadband noise’ is used to characterise the high-frequency noise that is produced by the random fluctuations in loading (e.g. due to turbulence) which occur across the rotor disc. This noise extends over a wide range of frequencies (typically 150-1000Hz in the helicopter context). The random fluctuations in force which cause this noise source are mainly due to the unsteady aerodynamics within the flow-field. The unsteady aerodynamics can be caused by a turbulent wake, vorticity shedding from the trailing edge of the blade, and boundary layer turbulence and separation. A comprehensive account of the current state of broadband noise prediction is given by Brooks and Burley in Ref. 2.

Main rotor harmonic or loading noise results from the time-varying airloads on the rotor disc in forward flight. The radiated noise is generally in the low-frequency range (typically 0-100Hz). Where the noise is due to the production of lift, the sound waves radiate below the plane of the rotor and towards the ground, whereas noise due to drag tends to radiate in the plane of rotor. Tail rotor harmonic noise is caused by the changing loads on the tail rotor. This noise is similar in nature to that of the main rotor but, as the rotational speed of the tail rotor is higher than that of the main rotor, the harmonic noise produced by the tail rotor occurs at a higher frequency (typically 60-200Hz).

Impulsive noise is caused by the very steep gradients of pressure which occur at localised points on the rotor disc. Impulsive noise has received, and probably will continue to receive, most research attention as it is responsible for much of the noise radiated from helicopters today. There are two main sources of impulsive noise. Main rotor high speed impulsive (HSI) noise is caused by transonic effects which may occur close to the blade tip, particularly when the helicopter is travelling at high speed. In this case, the tip Mach number can become high enough to cause a shock wave to form near the tip of the advancing blade. The shock wave can ‘delocalise’ so that it extends past the rotor tip

and propagates into the far-field, causing an impulsive source of noise. Flight tests and experiments have been used to characterise and understand this source of noise with the result that the numerical prediction of HSI noise has reached a reasonable level of accuracy (Ref. 3). Radiation of HSI noise occurs mostly in the plane of the rotor. This noise can often be mitigated by flying at lower forward speeds to reduce the tip Mach numbers, particularly on the advancing side of the disc, or by using innovative designs for the blade tip.

The second source of impulsive noise is the localised interaction between the blades of the rotor and individual vortices in the wake. These interactions, known as blade-vortex interactions (BVIs), produce highly impulsive changes in the airload along the blade span which in turn results in a significant source of noise and vibration. BVI noise is responsible for the distinctive ‘slapping’ noise which is characteristic of a helicopter in descent or manoeuvring flight. This source of noise is known to be highly directional and to propagate forward and towards the advancing side of the rotor disc and aft and to the retreating side of the rotor disc. The frequency of the propagated noise is concentrated in the low to medium range (approximately 75-500Hz). BVI noise can increase significantly the overall sound pressure level that is experienced on the ground. The higher frequency component within this BVI noise range, and the impulsive nature of the sound, make it particularly annoying to the human ear. The prediction and subsequent reduction of BVI noise is a topic of ongoing and intensive research (Refs. 4,5).

1.2 Predicting BVI noise

Blade vortex interaction noise is dominant in low speed descending flight and during some manoeuvres, where conditions occur that are conducive to the blades passing close to vortices that have been shed into the wake at some earlier time. An interacting vortex induces steep velocity gradients near the blades which, in turn, produce sharp changes in the effective angle of attack that is experienced by the interacting blade. The change in angle of attack leads to an impulsive change in pressure on the surface of the blade. This induces a pressure fluctuation which radiates out from the blade producing a highly

impulsive noise.

The radiation of BVI noise to the far-field depends upon the geometry and strength of the interactions at the source of the noise and also on how the noise is propagated through the surrounding flow. The impulsiveness of the pressures that are induced on the surface of the blade by the interacting vortex, and hence the strength of the radiated noise, depends strongly on the vertical ‘miss-distance’ between the blade and the vortex, and also on the strength and core radius of the vortex. The miss-distance is strongly influenced by the trajectory of the tip vortices and the elastic deformation of the blades. The strength of the tip vortex and its trajectory are dependent upon various operational parameters including the rotor tip Mach number and advance ratio. The intensity of the interaction is also affected by the location of the interaction on the rotor disc, and therefore the velocity of the tip vortex relative to the blade and the orientation of the tip vortex with respect to the blade. In certain instances where the vortex and blade lie parallel to each other, the resulting interactions are particularly strong. Near-parallel interactions often occur on the retreating side, towards the rear of the rotor disc. Understanding the local dynamic and aerodynamic state of the rotor during BVI is essential to predicting BVI-induced noise.

1.2.1 Previous work

As BVI related noise is the greatest barrier to the community’s acceptance of rotorcraft, particularly where they operate close to highly populated areas, significant effort has been focused on its understanding, prediction, and ultimately its reduction. Lowson (Ref. 4) and more recently Yu (Refs. 5,6) have both presented reviews on BVI noise. In addition, Brentner and Farrassat (Refs. 7,8) have presented a historical review and an assessment of the current status of acoustic prediction methods relating to helicopter flight. In this Section, the key contributions to BVI noise modelling and prediction will be reviewed.

Since the sixties, much research has been carried out on measuring and predicting the noise generated by the helicopter main rotor. Piston engines that were used on helicopters were generally the dominant noise source, but, due to the advent of quieter turboshaft engines in the beginning of the 1960’s, noise sources that originated on the rotor became

an increasingly important issue. Through the early experimental studies by Leverton and Taylor (Ref. 9), it became apparent that the occurrence of impulsive noise often coincided with the presence of vortex-induced fluctuations in the blade airload. Their experiments simulated both parallel and perpendicular vortex interactions using a series of jets which were directed at a rotating blade. Time histories of the acoustic pressure were recorded, and, by comparing these with the acoustic signal gathered from a helicopter in flight, this fundamental work helped to establish the link between impulsive noise at low speed and the high-frequency airloads that are induced by blade-vortex interactions.

Initially, the early acoustic theories that were developed for propellers (for example by Gutin in Ref. 10) were used to predict the noise produced by a hovering helicopter. As these theories neglected the effects of the unsteady loading on the blade, they were found to be inadequate for helicopter applications. Despite this, studies in the propeller field helped to increase knowledge of the different mechanisms that contribute to the total noise that is generated by the rotor blade, and in particular the effects of blade loading and blade thickness. In the late sixties, several new theories were developed (e.g. those by Wright (Ref. 11) and Widnall (Ref. 12)) to predict specifically the noise that is radiated from a main rotor of a helicopter as a result of the fluctuating forces along the rotor blades. Lawson developed a solution for the noise radiated from a moving point source (Ref. 13) and along with his colleague Ollerhead (Ref. 14), used this theory to develop the first computational analysis, applicable in both the time and frequency domains, for the noise radiated by a helicopter rotor. Their work, however, was limited by the lack of computational resources at the time.

Lighthill (Ref. 15) was among the first to model aerodynamic sources of noise mathematically, by reformulating the Navier-Stokes equations as a wave equation to describe the propagation of pressure through a fluid. His approach was derived for jet noise and so could not be applied directly to rotorcraft noise. Ffowcs Williams and Hawkings (Ref. 16) developed a more general formulation of Lighthill's approach using generalised function theory. In this form, the noise source distribution in the flow-field surrounding the body is described by a quadrupole term, and monopole and dipole terms represent the sources

of noise that originate on the surface of the body. The ‘Ffowcs Williams-Hawkings Equation’ can be applied to any body in arbitrary motion through a fluid. This approach was initially applied to helicopters by Hawkings and Lawson (Ref. 17) and Farassat (Ref. 18) in the late seventies and has since been used extensively to predict rotor related noise. The Ffowcs Williams-Hawkings equation has been recast into more useful forms, perhaps the most notable being the ‘1’ and ‘1A’ formulations developed by Farassat (Refs. 19, 20) which are used in many rotorcraft acoustic codes today.

Lack of computational resources throughout the seventies limited the computational development of these theories, and led to some of the approximations that are still prevalent in acoustic codes that are still in use. In addition, the aerodynamic theories that were available at the time were not sophisticated enough to predict accurately the high-frequency airloads which are required as inputs to most acoustic codes. Despite this, model-scale experiments, flight tests and an emphasis on theoretical development led to a fairly complete understanding and classification of the physical sources of helicopter rotor noise, by the 1980s (Ref. 3).

In the late seventies, an in-flight measurement approach was developed by Schmitz and Boxwell (Refs. 21, 22) at the NASA Ames Research Centre, in which a fixed wing aircraft was used to gather acoustic measurements from a number of different helicopters in flight. Using their approach, periodic noise data could be gathered allowing the characteristics present in the acoustic pressure data to be related to discrete aerodynamic events on the rotor disc. Moreover, the noise directivity could be obtained by flying the fixed wing aircraft at different azimuthal and elevation angles with respect to the helicopter. The first tests used a Mohawk (OV-1C) fixed wing aircraft to characterise the full-scale impulsive noise of a UH-1H helicopter (Ref. 21). In subsequent flight tests, the quieter Y0-3A fixed-wing aircraft was used to measure the noise characteristics of the AH-1S and the UH-1H helicopters at different advance ratios and at moderate descent rates (Ref. 22).

Schmitz *et al.* (Ref. 23) compared the BVI acoustic data for an AH-1 series helicopter that were gathered during flight test to that radiated from a 1/7-scale model of the main-rotor of a AH-1 under similar operating conditions. They showed that, provided the advance

ratio (μ), the thrust coefficient (C_T), rotor tip-path plane angle (a_{TTP}), and hover tip Mach number (M_T) of the model and full-scale rotors were matched, the acoustic data from model-scale rotor would compare favourably to that gathered during the flight test. The main differences lay in the width of acoustic pulses which were generally smaller for the full-scale rotor than for the model-scale data. It was suggested that this was most likely due to differences in the vortex core sizes of the vortices trailed from the blade tips in each case. Changing the miss-distance and strength of the interacting vortices by modifications to the thrust coefficient or tip path plane angle affected the pressure fluctuations on the rotor disc. Both the hover tip Mach number and the advance ratio affected the basic vortex characteristics as well the trajectory of the tip vortices, changing the interaction geometry. The directivity of the radiated noise was documented, confirming that BVI noise is highly directional and is radiated at an angle of between 30° to 45° relative to the rotor plane in a direction forward and below the rotor.

In the early eighties, increased emphasis on noise certification and regulation of aircraft forced the US helicopter industry, for the first time, to consider noise reduction at the vehicle design stage. Work conducted under the NASA/AHS Rotorcraft Noise Reduction Program (Ref. 24), along with the steady improvement in super-computing technology, significantly aided the development of acoustic prediction codes in the late eighties.

At the same time several wind tunnel tests were conducted in the anechoic test section of the Duits-Nederlandse Wind-tunnel (DNW) (for example Refs. 25–27). Burley and Martin (Ref. 28) presented detailed BVI noise data associated with a model Bo105 helicopter. The researchers examined extensively the effect of tip path plane angle and advance ratio on the BVI noise that is radiated by the rotor. They concluded that the strongest BVI noise that is radiated by the helicopter occurs over a narrow range of tip-path plane angles and that this range reduces at lower advance ratios. In the mid-nineties, European helicopter manufacturers, universities, and research institutes carried out several initiatives, such as the EU-funded HELINOISE (Ref. 29) and HELISHAPE (Ref. 30) programmes, to improve aerodynamic and aero-acoustic prediction capabilities for advanced blade designs and to investigate the effect of blade planform shape on noise produced.

Acoustic codes have reached a maturity where it is possible to achieve good comparisons between predicted and measured noise levels if blade pressures are known accurately. In recent years, research directed at the prediction of BVI noise has therefore been focussed on modelling the pressure fluctuations that are induced by the BVI events on the surface of the blade. The principal challenges in predicting the loading perturbations on the blade are to determine accurately the position and strength of the vortical structures in the wake and also the correct position and deformation of the rotor blades as they interact with these structures. The complexity of the rotor wake, and the strong mutual dependence of the aerodynamics and structural dynamics, renders accurate prediction of the BVI-related blade airloads a particularly challenging task. All of these elements must be addressed in order to obtain an accurate acoustic prediction.

1.2.2 HART initiative

Collaborative efforts where experimental tests and acoustic predictions have been performed alongside each other have greatly aided the rotorcraft community's understanding of the mechanisms involved in BVI noise and, by implication, have greatly improved the ability of current computational methods to predict BVI noise. The Higher Harmonic Control Aeroacoustics Rotor Test (HART) research programme was initiated in 1990 as a major international co-operation between researchers from the German DLR, the French ONERA, the DNW, NASA Langley, and the US Army Aeroflightdynamics Directorate (AFDD). Two comprehensive wind tunnel tests (HART I and HART II) were performed with the aim of increasing basic understanding of noise generation by rotor blade-vortex interactions and to improve the analytical modelling of this phenomenon (Ref. 31–34). The wind-tunnel tests were conducted in the Large Low-Speed Facility (LLF) of the DNW in its anechoic flow facility. The 6.0 by 8.0m test section was used in the open jet configuration.

After completion of the HART I test programme, it was noted that a more refined measurement of the rotor wake would be required to gain a better understanding of the BVI phenomenon, especially in descending flight (Ref. 35). As a result, the focus of the second test programme, HART II (Refs. 31–34), was to investigate the effect of higher-harmonic

pitch control on the structure of the wake for a rotor flown in a shallow descent. In particular, the experiment aimed to determine the influence of subtle changes in the structure of the rotor wake, introduced by the additional control inputs, on the levels of noise and vibration produced by the rotorcraft. At the time of HART II, flow measurement methods had significantly matured, compared to the three-component Laser Doppler Velocimetry (LDV) technique that was used in the earlier HART programme, with more sophisticated Particle Image Velocimetry (PIV) techniques being routinely used. Three different flight cases were studied – a baseline (BL) case with conventional control inputs, and two cases with different higher harmonic control (HHC) inputs applied to the rotor at a frequency of three cycles per rotor revolution, the so-called minimum-vibration (MV) and minimum-noise (MN) cases.

The release into the public domain in 2005 of part of the HART II experimental database has provided the developers of rotorcraft CFD tools with a well-defined set of measurements against which the predictions of their models can be verified. In addition, biannual workshops held since 2005 have provided a platform for increased understanding of BVI noise and collaboration between members outside the initial research team.

1.2.3 Wake modelling

Deficiencies in modelling the dynamics of the rotor wake, and the flow that is induced through the rotor, is known to be a key factor in limiting the quality of aero-acoustic predictions. Unlike in the case fixed-wing aircraft, where the vortices that are produced at the tips of the wings are quickly convected downstream, the vortices that are produced by a helicopter stay close to the rotating system of blades. In any computational representation of their dynamics, these vortices need to be preserved for numerous rotor revolutions. As the equations of motion of a fluid are described fully by the Navier-Stokes equations, by far the most rigorous method of modelling the flow-field that surrounds a helicopter in flight is the direct solution of these equations on a computational domain surrounding the helicopter.

Datta *et al.* (Ref. 36) presented a detailed review of the development of CFD-based

approaches in the last decade, and argued that CFD calculations of the flow around the entire rotorcraft, or even just the rotor, are extremely challenging. This is because simultaneous accurate representation of flow features on the scale of the rotor (for instance the overall geometry of the wake) and on the scale of the vortex cores (for instance the details of the roll-up process behind the blades that leads to the formation of the tip vortices) requires a method that can resolve the relevant physics over at least two spatial orders of magnitude. The typical CFD approach to wake computation is a straightforward direct solution of the Navier-Stokes or Euler equations, wherein reliance is placed on some order of grid resolution to capture the essential physics. However, it is clear that resolving length scales within the flow of the order of the vortex core diameter and, simultaneously, length scales of the order of a rotor diameter, imposes an enormous burden on such a solution. Moreover, conventional CFD schemes that solve the Navier-Stokes equations in velocity-pressure form are at a distinct disadvantage as their numerical diffusion of vorticity generally leads to the premature dissipation of vortical structures within the rotor wake. The accuracy of the solution is thus inevitably a trade-off between the need for high fidelity resolution of the wake and the computational cost that is incurred in achieving this fidelity. At present this compromise invariably results in solutions that are grid dependent since rotor calculations on grids that are sufficiently fine to resolve the detailed structure of the wake are usually prohibitive in terms of computational cost.

Recent advances in coupling Rotorcraft Computational Structural Dynamics (CSD) analyses to Rotorcraft CFD have demonstrated significant progress in accurately predicting the rotor blade motion and in capturing the associated blade airloads. Boyd (Ref. 37) and Lim and Strawn (Ref. 38) show encouraging results in comparison to the HART II experimental data for prediction of BVI-airloads and acoustics. However, their investigations show, that high grid densities (with cell numbers of up to 113 million) are required to reduce the numerical dissipation of standard CFD techniques to a level where the high frequency character of the BVI-generated airloads can be captured. The use of unstructured grids allows for more targeted refinement of the computational grid as it is easier to create or destroy cells in localised regions using this approach when compared to a method which is solved on a structured grid (e.g. Ref. 39). Targeted grid refinement can

reduce the total number of computational cells that are required. However, the areas of interest, for example where vorticity is present in the flow-field, are generally not known before the calculation begins. As a result, the computational grids must be re-adapted as the calculation progresses to increase refinement where it is required, again incurring an additional computational cost.

Higher order discretisation schemes can also be used to reduce the spatial smearing of the vortical structures in the flow when a conventional CFD approach is adopted. A comparison by Lim (Ref. 40) between the predictions obtained using a higher-order spatial difference scheme, WENOM, and a central difference scheme, showed that a slight improvement was achieved with the WENOM scheme in some cases but that a 73% increase in computational time was incurred when compared to the lower order method.

Vortex wake methods (Refs. 41–45) model the the tip vortices as a series of discrete line filaments which are trailed behind the rotating blades. A Lagrangian approach is then used to convect the discrete filaments through the computational domain and thus to represent the evolution of the rotor wake. The US Army Aeroflightdynamics Directorate (AFDD) and the German DLR have investigated free-wake models in which multiple filaments are trailed from the blades to represent the vortical structures in the wake (Ref. 42). van der Wall and Yin (Ref. 44) use a prescribed-wake approach based on the classical Beddoes wake model (Ref. 46) to represent the wake of the HART II rotor. Vortex wake methods, whether based on prescribed- or free-wake approaches, can preserve the integrity of the vortices in the wake over as many rotor revolutions as are required to capture adequately the high-frequency airloads on the rotor disc. They do, however, rely on a significant degree of empiricism to model the core structure, roll-up, and diffusion of the vorticity distribution in the wake and hence cannot be considered as a first-principles approach to representing the physics of the rotor wake.

The Vorticity Transport Model (VTM), proposed by Brown (Ref. 47), is based on the solution of the Navier-Stokes equations in vorticity-velocity form. Vorticity is explicitly conserved throughout the flow domain, thus the VTM is capable of preserving the vortical structures in the wake of a rotor for the very long times required to capture all the BVI

events which occur on the rotor disc. The model is therefore well suited to modelling the interactions between the vortices generated by the blades of a helicopter and the blades themselves. Unlike vortex wake methods, no additional empirical models or prior assumptions are required to model the position, core growth or roll-up of the vortices that are present in the flow-field.

1.3 Present research objectives

Given the current industrial focus on reduction of noise, a tool that can predict accurately the high frequency components of the blade loading, the rotor wake structure and the radiated noise for flight associated with blade-vortex interactions, would be of significant benefit to the designers of modern rotorcraft. Indeed, particularly in the context of rotor design, there is a need to develop methods which can produce high fidelity predictions of the rotor aero-acoustic noise but at a much reduced computational cost when compared to CFD calculations of full helicopter configurations.

The research described in this dissertation aims to refine understanding of how the predictions of acoustic signature of the rotor are affected by both the fidelity of the model that is used to predict its aerodynamic loading and the quality of the representation of the geometry of the rotor wake. Brown's Vorticity Transport Model (Refs. 47,48) has been used to investigate the influence of the fidelity of the local blade aerodynamic model on the quality of the prediction of the high-frequency airloads associated with blade-vortex interactions and thus on the accuracy with which the acoustic signature of the rotorcraft can be predicted. To assess this, predictions using the Vorticity transport model and incorporating two different models for the local blade aerodynamics are compared to experimental data for all three of the HART II flight cases.

1.4 Synopsis

This dissertation is arranged as follows: in Chapter 2 the Vorticity Transport Model, which is used to represent the helicopter and flow-field surrounding it, is described. This Chapter includes a description of the form of the governing equations that are used in the Vorticity Transport Model and describes how these equations are solved numerically. The computational grid, how the vorticity field is evolved through time, and the coupling which exists between the velocity field and the vorticity distribution are each discussed. Descriptions of how the outer wake model is coupled to the inner model for the local blade aerodynamics and how the structural dynamics of the blades are modelled are given in the subsequent Sections. The method used to provide control and to trim the helicopter is also discussed. Details are also provided in this Chapter of how solid bodies such as a fuselage are represented by the computational method. Finally, the method is described by which the acoustic field radiated by the helicopter is determined.

The inner model used to represent the local aerodynamics of the rotor blades is discussed in Chapter 3. In this Chapter the essential aspects which are required of a blade aerodynamic model are described and the two different models that are used to represent the rotor blades throughout the rest of the dissertation are introduced. The details of an investigation of the response of each of the models to two well known two-dimensional problems from linearised, unsteady aerofoil aerodynamics and to an interaction with an isolated vortex is given.

The effect of the fidelity of the blade aerodynamic model on the prediction of the airloads that are associated with blade vortex interactions is assessed in Chapter 4. Predictions of blade airloads obtained using the VTM in conjunction with each of the blade aerodynamic models, described in Chapter 3, are compared against data gathered during the HART II experimental programme. The effects on both the low-frequency and high-frequency components the blade airload of including a model of the drive enclosure of the HART II test, and of changing the spatial and temporal resolution of the computational domain, are also investigated, and the discussion is included in this Chapter.

In Chapter 5, the ability of the computational model to represent the geometry of the wake created by the HART II rotor is examined. The computed trajectories of the individual tip vortices, as they are convected back and through the rotor disc, are compared to experimental estimates of the vortex core positions derived from detailed Particle Image Velocimetry (PIV) measurements of the flow-field. In addition, the evolution of the vorticity distribution behind the advancing blade that is predicted by the the VTM is compared to experimental data in order to assess the ability of the VTM to capture both quantitatively and qualitatively the roll-up of the vortex sheet behind the blades on the advancing side of the HART II rotor.

The predicted and experimentally-measured sound pressure levels (SPL) for the HART II test configuration for all three flight cases are compared in Chapter 6. The radiated noise is calculated from the airloads predicted by the VTM using a Farassat-1A formulation of the Ffowcs Williams-Hawkings Equations. Three computational resolutions were used to expose the effect of grid resolution on the quality of predictions. Furthermore, the noise that is radiated by the rotor is then related back to the individual BVI events at its source.

Finally, in Chapter 7, this dissertation concludes with a summary and discussion of the work presented in the previous Chapters and a discussion of possible future work.

1.5 Publications

Some elements of the research presented in this dissertation have been published previously in several papers.

In January 2008, a paper including predictions of the airloads, the resultant wake system and the acoustics of the HART II rotor using the Vorticity Transport Model was presented at the 9th American Helicopter Society Aeromechanics Specialists' Meeting, in San Francisco, USA (Ref. 49). This paper confirmed that the Vorticity Transport Model, using a lifting-line approach to model the local aerodynamics of the rotor blades, was well suited to capturing the geometry of the wake to the accuracy and detail that is required for the high-frequency components of the blade airload that are associated with BVI to be

resolved correctly. The experimental airloads, in particular the higher harmonic loading associated with blade vortex interactions, was matched well by the computations. The computed vorticity distribution in the wake also showed good correlation with the vortex positions that were estimated using the HART II experimental data. This work also showed how including a representation of the fuselage within the computation yielded a marked improvement in the prediction of the vortex positions when compared to similar calculations for an isolated rotor. An acoustic analysis, based on a Ffowcs Williams-Hawkings approach, was shown to predict accurately the locations of the sound pressure maxima and the upstream attenuation of the sound that was radiated by the rotor. These investigations form parts of Chapters 4 to 6.

In September 2008, a paper focussing on predicting the wake structure of the HART II rotor using the Vorticity Transport Model and a lifting-line representation of the aerodynamics of the rotor blades was presented at the 34th European Rotorcraft Forum in Liverpool, England (Ref. 50). In this paper the possible origins of the deficiencies in the airloads and acoustics on the advancing side of the disc were examined by comparing the predicted vortex geometry and vortex core characteristics to those recorded during the HART II rotor test. A detailed assessment of the ability of the model to resolve the geometry of the wake was given. In particular, an investigation was carried out of the dynamics of the complex roll-up process that occurs in the wake on the advancing side of the rotor and the ability of the method to accurately predict the circulation of the resultant tip vortex. PIV images of the wake structure were compared against numerical predictions of the detailed geometry of the rotor wake using three different computational resolutions of the flow. This investigation forms the basis of Chapter 5.

A paper, detailing the effect of the fidelity of the local aerodynamic model of the rotor blades on the prediction of high-frequency airloads on the rotor and also on the resultant wake structure of the HART II rotor, was presented at the 65th American Helicopter Society Annual Forum, Grapevine, Texas, USA (Ref. 51) in May 2009. In this study, Brown's Vorticity Transport Model was coupled with two different models for the local blade aerodynamics – the first, a simple lifting-line model, and the second, a somewhat

more sophisticated lifting-chord model based on unsteady thin aerofoil theory. A marked improvement in the accuracy of the predicted high-frequency airloads of the HART II rotor was obtained when the lifting-chord model for the blade aerodynamics was used instead of the lifting-line approach. These results form parts of Chapters 4 and 5.

In September 2009, the analysis of the May 2009 paper (Ref. 51) was extended to determine the effect of the local model for the aerodynamics of the blades on the predicted acoustic signature of the HART II rotor. This work was presented at the 35th European Rotorcraft Forum, Hamburg, Germany (Ref. 52). The predictions obtained using each of the two models for the local blade aerodynamics were compared for all three of the HART II flight cases. The various features in the acoustic signal produced by the rotor were related to specific features within the blade loading to determine how the predictions of acoustic signature of the rotor are affected by the fidelity of the model that is used to predict its aerodynamic loading. This investigation forms the basis of Chapter 6.

Chapter 2

Computational model

2.1 Introduction

The flow around a helicopter is unsteady and highly non-uniform due to the strong vortical structures which dominate its wake. These persist in the surrounding flow-field for significant periods of time and their interactions with the various structural components of the helicopter, particularly the blades, produce the highly dynamic and complex aerodynamic environment in which the helicopter operates. Prediction techniques can be used to increase understanding of the mechanisms which underly these interactions, in the drive to reduce the rather objectionable characteristics that these interactions produce. In particular to predict accurately the noise and airloads that are associated with blade-vortex interactions is essential to capture accurately the position and strength of the vortical structures within the wake. Moreover, the integrity of the vortices must be maintained for numerous rotor revolutions if all the BVI events present on the rotor are to be captured correctly by the numerical method.

Computational Fluid Dynamics (CFD) offers a rigorous approach to modelling the flow-field which surrounds any aircraft, since the equations which govern the underlying dynamics of the fluid motion are solved directly. CFD models for rotorcraft applications have traditionally been derived from those used in fixed wing research and thus are for-

mulated in terms of pressure, velocity and density. As vorticity is not explicitly conserved in this approach, such schemes are susceptible to considerable numerical dissipation of the vorticity distribution in the flow-field, as the calculation is progressed through time. This effect can be reduced by increasing the cell density and thus reducing the truncation error in the calculation or resorting to higher-order numerical schemes. However this, in turn, increases significantly the computational expense of the simulation.

It seems more appropriate in the context of vortex-dominated flows, such as those which surround a rotorcraft, that the governing equations be re-formulated to conserve explicitly the vorticity present in the flow-field. Even where this is the case, however, grid-based methods still have the tendency to diffuse the vortices within the flow with the result that they lose their spatial compactness over time. This spatial-smearing effect can be reduced by choosing an appropriate method to convect the vorticity field through time.

The Vorticity Transport Model (VTM) is a comprehensive rotorcraft simulation tool in which the analysis of the flow in the computational domain is decomposed into an outer wake evolution problem, and an inner problem involving the generation of the aerodynamic forces on the blade. This Chapter describes the outer wake evolution problem and the numerical implementation of the VTM in detail. The governing equations, which are cast in terms of vorticity and velocity, are defined in Section 2.2, and the numerical implementation of these equations in order to evolve the vorticity field through time is described in Section 2.3. Section 2.4 details how the outer wake evolution is coupled to the inner model for the aerodynamic environment of the blades by means of a local vorticity source. A discussion of the specific details of the blade aerodynamic model are deferred to Chapter 3, however. The blade structural model and rotor trim algorithm are described in Sections 2.6 and 2.7 respectively. Solid bodies, such as a fuselage, where present in the flow field, are represented using a vortex panel method, and the acoustic radiation of the rotorcraft is calculated using the Ffowcs Williams-Hawkings equation – as described in Sections 2.9 and 2.8 respectively.

2.2 Vorticity Transport Model

The Vorticity Transport Model (VTM) developed by Brown (Ref. 47) and extended by Brown and Line (Ref. 48) is a comprehensive rotorcraft model, solved computationally on a structured grid system. The evolution of the wake is based on a time-dependent vorticity-velocity formulation of the Navier-Stokes equations. This yields an accurate representation of the wake geometry since the method explicitly conserves the vorticity within the flow-field.

Since compressibility effects are only significant close to the tips of the rotating blades, it is reasonably well-justified to assume that the flow-field which surrounds the rotor system is incompressible. The manner in which compressibility is accounted for in the blade aerodynamic characteristics is described in Chapter 3. The incompressible Navier-Stokes equations which describe the motion of the fluid surrounding the rotorcraft can be written in velocity-pressure form as

$$\frac{\partial}{\partial t} \mathbf{u} + \mathbf{u} \cdot \nabla \mathbf{u} = -\frac{1}{\rho} \nabla p + \nu \nabla^2 \mathbf{u} \quad (2.1)$$

$$\nabla \cdot \mathbf{u} = 0. \quad (2.2)$$

Since the flow surrounding the helicopter is dominated by the vortical structures in the rotor wake, it is more convenient to reformulate the Navier-Stokes equations so that vorticity is the fundamentally conserved parameter within the flow. The unsteady vorticity transport equation,

$$\frac{\partial}{\partial t} \omega + \mathbf{u} \cdot \nabla \omega - \omega \cdot \nabla \mathbf{u} = \nu \nabla^2 \omega, \quad (2.3)$$

can be derived directly by taking the curl of Eq. (2.1), and is used within the VTM to evolve the vorticity distribution $\omega = \nabla \times \mathbf{u}$ through the computational domain, where ν is the viscosity of the fluid.

If $\omega = \nabla \times \mathbf{u}$ then $-\nabla \times \omega = -\nabla \times \nabla \times \mathbf{u}$ and hence for an incompressible flow where $\nabla \cdot \mathbf{u} = 0$, the velocity at any point in the flow can be obtained from the vorticity distribution by

inverting the differential form of the Biot-Savart equation

$$\nabla^2 \mathbf{u} = -\nabla \times \boldsymbol{\omega}. \quad (2.4)$$

The Reynolds numbers of the flows which are of interest in this dissertation are very high, and so the flow-field which surrounds the rotor can be assumed to be inviscid, with the exception of within the thin boundary layers on the surfaces of any bodies which are immersed in the flow. This assumption means that the viscous term $\nu \nabla^2 \boldsymbol{\omega}$ in Eq. (2.3) becomes non-zero only on those surfaces, and can therefore be replaced by a local vorticity source S , so that Eq. (2.3) can be rewritten as,

$$\frac{\partial}{\partial t} \boldsymbol{\omega} + \mathbf{u} \cdot \nabla \boldsymbol{\omega} - \boldsymbol{\omega} \cdot \nabla \mathbf{u} = S. \quad (2.5)$$

The VTM allows significant flexibility in the way that the local source of vorticity into the wake can be generated. For instance, a simple lifting-line model for the blade aerodynamics can be used, or a full, velocity-pressure CFD calculation that resolves the flow in the immediate vicinity of the blades can be embedded into the calculation (Ref. 53). This flexibility makes the VTM ideal for studying the effect of the fidelity of the model of the aerodynamics of the blades on the prediction of the high-frequency, BVI-induced blade loads experienced by the rotor, as discussed further in Chapters 3 and 4.

A number of previous studies have used the VTM to investigate the interactional aerodynamics, performance and flight dynamics of rotorcraft. Such studies have demonstrated that the VTM is capable of reproducing accurately the geometry of the wake as well as the dynamics and power consumption of both single and coaxial rotors (Refs. 54, 55), as well as more complex configurations (Ref. 56). The ability of the VTM to preserve the vortical structures within the rotor wake for significant lengths of time has also enabled the operational characteristics of rotors to be investigated. For instance, the model has been used to examine the behaviour of a rotorcraft as it interacts with the wake of an airliner (Ref. 57), for the study of helicopter main rotor - fuselage interaction (Ref. 58) and main rotor - tail rotor interaction (Ref. 59), as it operates close to the ground (Ref. 60), in

'brown-out' conditions (Refs. 61,62) and in undesirable flight regimes such as the vortex ring state (Ref. 63).

2.3 Numerical implementation

Within the VTM, the governing equations, Eq. (2.5), are solved within a solution domain Q surrounding the rotor. The solution domain is discretised into a finite set of control volumes or cells. Each computational cell contains a vorticity distribution which is uniform over its volume. The vorticity field is evolved through time in discretised time intervals Δt so that the time at the n^{th} timestep is $t = n\Delta t$ where $n \in \mathbb{N}$.

The spatial and temporal integration over a single computational cell, i , with volume Q_i and during a timestep Δt , for any flow variable $q(x, t)$ can be defined as

$$[q]^n = \int_{Q_i} q(x, n\Delta t) dQ \quad (2.6)$$

and

$$[q]_{\Delta t}^n = \int_{(n)\Delta t}^{(n+1)\Delta t} [q]^n dt. \quad (2.7)$$

Using these integrals, a discretised form of the vorticity transport equation, Eq. (2.5) can be written as

$$[\omega]^{n+1} - [\omega]^n = [\omega \cdot \nabla \mathbf{u}]_{\Delta t}^n - [\mathbf{u} \cdot \nabla \omega]_{\Delta t}^n + [S]_{\Delta t}^n. \quad (2.8)$$

At the beginning of the n^{th} time step, at $t = n\Delta t$, the velocity field $\mathbf{u}^n = \mathbf{u}([\omega]^n)$ is calculated from the vorticity distribution using the Biot-Savart relationship, Eq. (2.4). An operator-splitting approach is then used to evaluate each integration operator in Eq. (2.8) sequentially in order to construct the vorticity field at time $t = (n + 1) \Delta t$:

$$\begin{aligned} [\omega]^* &= [\omega]^n + [S]_{\Delta t}^n \\ [\omega]** &= [\omega]^* + [\omega \cdot \nabla \mathbf{u}]_{\Delta t}^n \\ [\omega]^{n+1} &= [\omega]** - [\mathbf{u} \cdot \nabla \omega]_{\Delta t}^n. \end{aligned} \quad (2.9)$$

The vorticity transported into cell i as a result of advection, $[u \cdot \nabla \omega]_{\Delta t}^n$, is approximated using Toro's weighted average flux (WAF) method (Ref. 64). The wave-amplifiers that are used within the WAF act to control the spatial smearing of the vortical structures within the wake whilst ensuring that the total vorticity in the domain is conserved. The vorticity that is produced by vortex stretching over a single timestep Δt , $[\omega \cdot \nabla u]_{\Delta t}^n$, is evaluated using Runge-Kutta integration. The vorticity sourced into cell i between timesteps n and $n + 1$ as a result of lifting surfaces immersed in the flow is $[S]_{\Delta t}^n$. This local source of vorticity is calculated by a separate model which, in physical terms, represents the aerodynamic environment of the rotor blades.

Provided that the numerical approximation used for each operator is at least second order accurate in time, the overall operator splitting approach results in a solution for the vorticity at the following timestep, $[\omega]^{n+1}$, that is also second order accurate (Ref. 65). Most importantly, this procedure is stable if each of the operators is allowed to advance within its own particular stability limit (Ref. 65).

A mismatch in the timesteps that are required to ensure the stability and accuracy of the blade aerodynamic calculation and the evolution of the vorticity transport equation can cause a stiffness within the computational method. This stiffness is introduced because, in general, the model for the unsteady aerodynamics and associated high-frequency structural dynamics requires a much smaller integration step than that at which the vorticity can be evolved through the grid in the absence of sources of vorticity into the flow-field. Within the VTM, a smaller timestep, Δt_{inner} , is used to calculate the aerodynamic loads on the blades and a larger timestep, Δt , (typically four to eight times larger) is used to manage the evolution of vorticity in the wake. These different timesteps are reconciled using a sub-stepping approach as described in Section 2.4.

2.3.1 Grid structure

An adaptive Cartesian grid, which is fixed in the rotor hub frame of reference, provides the discretisation of the domain on which the vorticity transport equation, Eq. (2.5) is solved. The grid does not need to remain fixed in size, but as the calculation progresses it

is essential that the grid encapsulates all the vorticity that is present in the evolving flow-field. As described in Section 2.3.3, the Cartesian fast multipole method which is used in the present version of the VTM to calculate the velocity field from the vorticity distribution does not require direct application of boundary conditions. This is because it assumes that no vorticity exists outside the computational domain. As a result, only regions of the flow that actually contain vorticity need to be contained within the computational domain. The number of computational cells and hence, the memory required by the calculation, is minimised by using a grid that contains a variable number of cells that are adaptively generated and destroyed to follow the vorticity-containing regions of the flow.

This computational grid is formed within an underlying virtual Cartesian stencil which tessellates the computational domain into cubes, each with side of length Δ_0 . As vorticity is sourced into the grid, cells are created at appropriate locations on the stencil. The cells which immediately neighbour these vorticity-containing cells are also created to allow the vorticity to be advected through the grid in the subsequent timestep. As the vorticity moves to a new location, new cells are created around all vorticity-containing cells and any cells that no longer contain vorticity, providing that they are not neighbours of vorticity-containing cells, are destroyed.

The computational grid is free to follow the evolution of the wake surrounding the helicopter and can expand in space effectively to infinity. Thus it is necessary to control the number of cells contained within the computational domain to prevent the available computational resources from being exhausted as the calculation proceeds. A nested grid system allows for fine resolution close to the rotor and then a systematic decrease in resolution with distance from the rotor hub (Fig. 2.1). At the lowest grid level the computational cells have sides of length equal to that of the underlying stencil length, Δ_0 . At each subsequent grid level the resolution of the grid is reduced so that the computational cells have sides of double the length of those on the preceding level. This scheme allows the total number of cells to remain within manageable limits while ensuring that the vorticity will not encounter the boundary of the computational grid during the course of a calculation.

An octree data structure is used to manage efficiently the grid structure and to provide a

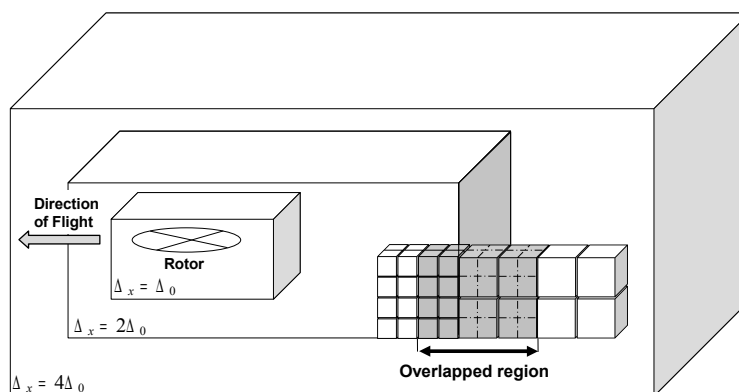


Figure 2.1: *Nested grid structure where the resolution decreases with increasing distance from the rotor hub, showing overlapped region at grid level boundaries.*

convenient means to implement the required changes in grid resolution. Moreover, it provides the essential infrastructure that is required by the fast multipole method, described in Section 2.3.3, that is used to calculate the velocity field within the computational domain. The advection of vorticity between grid levels is achieved by overlapping the cells at the interface between adjacent levels as shown in Fig. 2.1. The vorticity flux across the interface of the cells in the overlap region is first calculated on the finer grid and is then extrapolated onto the coarser grid.

The nested grid structure also allows the timestep to be increased when moving from a grid level with fine resolution to a coarser, higher grid level, whilst still maintaining the stability of the solution. The maximum stable time step is set by the Courant-Friedrichs-Lewy (CFL) condition in explicit time-stepping schemes such as the Weighted Average Flux (WAF) method (see Section 2.3.2), and depends upon the local velocity and the local resolution of the grid. On moving from one nested grid level to the next where the length of the side of a cell doubles, the flow can be evolved at a timestep close to twice that used to convect the flow on the finer grid level. Computational effort is thus focused, both spatially and temporally, where it is most required, that is, on the flow in the most highly resolved regions of the computational domain closest to the rotor.

2.3.2 Weighted average flux method

Essential to the accurate prediction of the high-frequency airloads that are associated with blade vortex interaction is the accurate portrayal and preservation of the vortical structures in the wake of the helicopter. Furthermore, to ensure that all the BVI events which occur on the rotor disc are captured, the compactness of the vortical structures in the wake must be maintained over a large number of rotor revolutions. The numerical diffusion that is present in all CFD methods, even when the vorticity is explicitly conserved as in the case of the VTM, can often lead to smearing of the vorticity field. Toro's Weighted Average Flux (WAF) method (Ref. 64) is used within the VTM to convect the solution through time. Highly compressive wave-amplifiers within the particular implementation of the WAF method that is used, control the local rate of numerical diffusion, and thus minimise the smearing of the vorticity distribution in the computational domain.

The WAF method is based on a second order accurate Riemann solver for hyperbolic conservation laws and has been shown to be able to capture effectively discontinuous solutions where high density gradients are present – such as near shock waves in compressible gas dynamic calculations. This quality makes the method ideally suited to resolving the steep vorticity gradients that can occur within rotor wakes.

Advection of the vorticity through the computational domain is modelled in the VTM by evaluating the advection operator,

$$[\omega]^{n+1} = [\omega]^n + [\mathbf{u} \cdot \nabla \omega]_{\Delta t}^n . \quad (2.10)$$

A space-operator splitting technique, proposed by Strang (Ref. 66), is used to decompose the three-dimensional advection operator into three one-dimensional operators. Integration of each of the resulting one-dimensional equations over each cell i , yields a solution for the vorticity in the cells at time $n + 1$ given by

$$[\omega_i]^{n+1} = [\omega_i]^n - \frac{\Delta t}{\Delta x} \left(F_{i+\frac{1}{2}} - F_{i-\frac{1}{2}} \right) \quad (2.11)$$

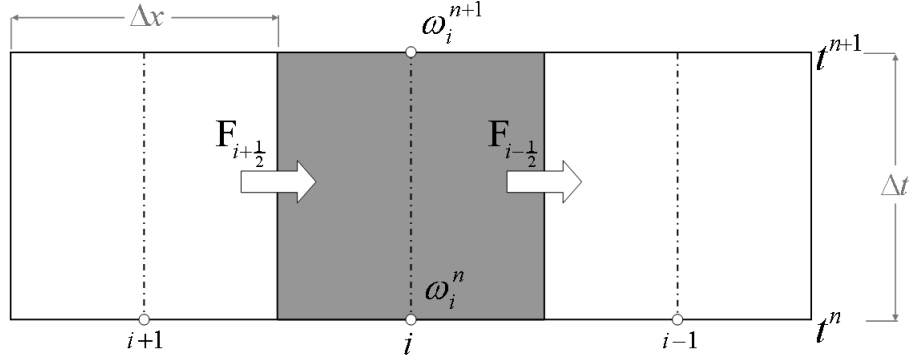


Figure 2.2: Stencil for the calculation of the inter-cell fluxes of vorticity.

where $F_{i+\frac{1}{2}}$ is the flux of vorticity on the interface between cells i and $i+1$. The value of $[\omega_i]^n$ is constant across each cell and varies discontinuously across each cell interface. The inter-cell flux may thus be evaluated using the solution to a piecewise constant Riemann problem. In the treatment of the Riemann problem by the WAF scheme, the inter-cell flux, at the interface between cells i and $i+1$, is viewed as a wave of vorticity that emanates from the face of the cell at $x_{i+\frac{1}{2}}$ and travels at the speed of the flow, $\mathbf{u}_{i+\frac{1}{2}}$, at the cell interface. The weighted-average flux of vorticity across the interface $i + \frac{1}{2}$ is defined as

$$F_{i+\frac{1}{2}} = W_1 F_{i+\frac{1}{2}}^{(1)} + W_2 F_{i+\frac{1}{2}}^{(2)} \quad (2.12)$$

where the partial fluxes on the left and right side of the wave front, namely $F_{i+\frac{1}{2}}^{(1)}$ and $F_{i+\frac{1}{2}}^{(2)}$ respectively, are given by

$$F_{i+\frac{1}{2}}^{(1)} = \mathbf{u}_{i+\frac{1}{2}}^n [\omega_i]^n \quad (2.13)$$

$$F_{i+\frac{1}{2}}^{(2)} = \mathbf{u}_{i+\frac{1}{2}}^n [\omega_{i+1}]^n . \quad (2.14)$$

This is shown pictorially in Fig. 2.2. The weighting functions, W_1 and W_2 , which represent the geometric extent of the partial fluxes on either side of the wave front, are defined in

terms of the local Courant Number ν and a wave-amplifier function λ , as

$$W_1 = \frac{1}{2} \left(1 + \lambda_{i+\frac{1}{2}} \nu_{i+\frac{1}{2}} \right) \quad (2.15)$$

$$W_2 = \frac{1}{2} \left(1 - \lambda_{i+\frac{1}{2}} \nu_{i+\frac{1}{2}} \right). \quad (2.16)$$

The local cell Courant number is defined as

$$\nu_{i+\frac{1}{2}} = \frac{\mathbf{u}_{i+\frac{1}{2}} \Delta t}{\Delta x} \quad (2.17)$$

and the wave-amplifier function depends upon the local Courant number and the vorticity distribution ratio,

$$r_{i+\frac{1}{2}}^n = \frac{\omega_i^n - \omega_{i-1}^n}{\omega_{i+1}^n - \omega_i^n}. \quad (2.18)$$

The wave-amplifiers are selected to maintain the monotonicity of the solution by ensuring that the solution is Total Variation Diminishing (TVD). The Total Variation is defined at timestep n for a discrete representation of the vorticity field as

$$TV^n(\omega) = \sum_i |[\omega_{i+1}]^n - [\omega_i]^n| \quad (2.19)$$

and for the scheme to be fully TVD the wave-amplifier functions must force the solution to satisfy

$$TV^{n+1}(\omega) \leq TV^n. \quad (2.20)$$

A number of wave-amplifier functions that ensure the scheme is fully TVD have been derived by Toro (Ref. 64), including the SUPERA type flux limiter which similar to the limiter is used in the VTM.

2.3.3 Calculation of the velocity field

At the beginning of each timestep, the velocity on the cell interfaces must be calculated before the WAF algorithm can be used to advance the vorticity transport equation, Eq. (2.5), through time. The Biot-Savart relationship couples the velocity \mathbf{u} at any point \mathbf{x} near the

rotor to the vorticity distribution within the computational domain. For a domain Q , in which all the vorticity within the flow-field is contained, the Biot-Savart equation can be written in integral form as

$$\mathbf{u}(\mathbf{x}) = \int_Q K(\mathbf{x}, \mathbf{y}) \times \omega(\mathbf{y}) d\mathbf{y} \quad (2.21)$$

where the Biot-Savart kernel K is given by

$$K(\mathbf{x}, \mathbf{y}) = -\frac{1}{4\pi} \frac{(\mathbf{x} - \mathbf{y})}{|\mathbf{x} - \mathbf{y}|^3}. \quad (2.22)$$

Since this kernel is singular when $\mathbf{x} = \mathbf{y}$, an approximation is used within the VTM in which the Biot-Savart kernel is substituted with the regularised Rosenhead-Moore kernel

$$K_\delta(\mathbf{x}, \mathbf{y}) = -\frac{1}{4\pi} \left(\frac{(\mathbf{x} - \mathbf{y})}{(|\mathbf{x} - \mathbf{y}|^2 + \delta^2)^{3/2}} \right) \quad (2.23)$$

where δ is an artificial smoothing parameter. The resulting approximation to the induced velocity field is given by

$$\mathbf{u}(\mathbf{x}) \approx \int_Q K_\delta(\mathbf{x}, \mathbf{y}) \times \omega(\mathbf{y}) d\mathbf{y}. \quad (2.24)$$

Using the Rosenhead-Moore kernel, the un-physical velocities which are associated with the singularity in the Biot-Savart kernel are avoided. The value of δ is set to ensure that the maximum in the velocity profile that is induced by the vorticity distribution within a cell of width Δx will occur on the faces of the cell. This approach ensures that the resolution of the velocity field remains linked to the size of the computational cells as this is varied.

The approximation of the velocity field given by Eq. (2.24) requires an integration over all the vorticity-containing cells in the computational domain. The velocity induced at \mathbf{x} by the vorticity ω_i , which is contained in cell i and lies at \mathbf{y}_c can be evaluated by

approximating Eq. (2.24) using Euler integration as

$$\mathbf{u}(\mathbf{x}) = \sum_{i=1}^N \mathbf{K}_\delta(\mathbf{x}, \mathbf{y}_c) \times \omega_i. \quad (2.25)$$

N^2 Biot-Savart interactions exist between the N vorticity-containing cells which are contained within the computational domain. This results in a computational cost of $\mathcal{O}(N^2)$ when a direct summation approach is used to evaluate Eq. (2.25). The computational cost of such a calculation can quickly become prohibitive as the number of cells within the domain is increased. The fast multipole method (FMM), introduced by Greengard and Rokhlin (Ref. 67), is employed within the VTM to greatly reduce the computational costs involved in the velocity calculation. Moreover, it eliminates the requirement for explicit boundary conditions at the edge of the computational domain. The specific implementation of the fast multipole method used within the VTM exploits the underlying rectangular topology of the grid so that an algebraic series can be used, as described below, to expand the integral in Eq. (2.24). This thus avoids the use of the complex trigonometric expansions of the more general formulations of the algorithm (Ref. 67).

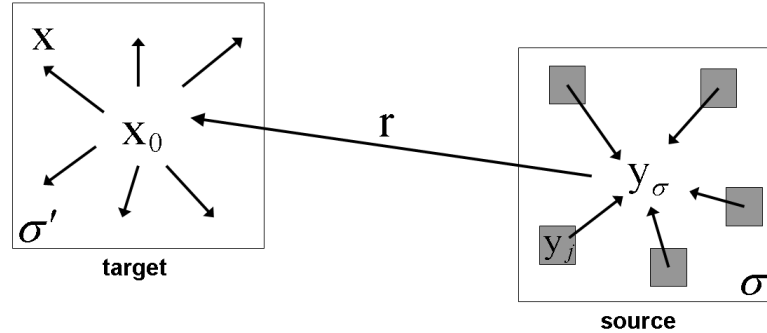


Figure 2.3: Interaction between target and source clusters using the multipole method to calculate the velocity field.

Assuming that a total of N vorticity-containing cells exist within the computational domain, then a cluster σ which encloses N_σ vorticity-containing cells may be defined as shown in Fig. 2.3. The vorticity-weighted centre (centroid) of the cluster lies at \mathbf{y}_σ , and the centre of each vorticity-containing cell, j , lies at \mathbf{y}_j . The vorticity within the cluster

σ , induces a velocity

$$\mathbf{u}(\mathbf{x}_0) = \sum_{j \in \sigma} \mathbf{K}_\delta(\mathbf{x}_0, \mathbf{y}_j) \times \omega_j \quad (2.26)$$

at the centroid \mathbf{x}_0 of a second cluster σ' . Provided that the second cluster is far removed from the first, the cost of the calculation of the induced velocity \mathbf{u} is reduced to $\mathcal{O}(N \log N)$. This is achieved by expressing the multiple, long-range interactions that occur between the individual cells of the source cluster and the cells of the target cluster as a single, converging algebraic series. The algebraic series is then used to compute the influence of the source cluster on all the other clusters which are located at large distances from it. This approach is particularly effective in the present calculation since the magnitude of the Biot-Savart interaction decreases rapidly with distance. Eq. (2.24) is expanded as a Taylor series about the centre of the source cluster σ , and the series is then truncated after the p th term, so that

$$\mathbf{u}(\mathbf{x}_0) = \sum_{j \in \sigma} \mathbf{K}_\delta(\mathbf{x}_0, \mathbf{y}_\sigma + (\mathbf{y}_j - \mathbf{y}_\sigma)) \times \omega_j \quad (2.27)$$

$$= \sum_{j \in \sigma} \sum_{\mathbf{k}} \frac{1}{\mathbf{k}!} D_{\mathbf{y}}^{\mathbf{k}} \mathbf{K}_\delta(\mathbf{x}_0, \mathbf{y}_\sigma) (\mathbf{y}_j - \mathbf{y}_\sigma)^{\mathbf{k}} \times \omega_j \quad (2.28)$$

$$\approx \sum_{\mathbf{k}=0}^{\mathbf{p}} \mathbf{a}_{\mathbf{k}}(\mathbf{x}_0, \mathbf{y}_\sigma) \times \mathbf{m}_{\mathbf{k}}(\sigma) \quad (2.29)$$

where \mathbf{k} is the order of the expansion. The Taylor expansion is three-dimensional and therefore the index of each term is a vector $\mathbf{k} = (k_1, k_2, k_3)$. It follows therefore that $D_{\mathbf{y}}^{\mathbf{k}} = \frac{\partial}{\partial y_1^{k_1}}, \frac{\partial}{\partial y_2^{k_2}}, \frac{\partial}{\partial y_3^{k_3}}$, $\mathbf{k}! = k_1! k_2! k_3!$, and $\mathbf{x}^{\mathbf{k}} = x_1^{k_1}, x_2^{k_2}, x_3^{k_3}$ for $k_i \geq 0$, where the subscripts 1, 2 and 3 denote the three Cartesian directions x , y and z . Truncating this series yields an approximate method, the accuracy of which can be tailored by controlling the degree of truncation.

The tensors \mathbf{a} , given by

$$\mathbf{a}_{\mathbf{k}}(\mathbf{x}_0, \mathbf{y}_\sigma) = \frac{1}{\mathbf{k}!} D_{\mathbf{y}}^{\mathbf{k}} \mathbf{K}_\delta(\mathbf{x}_0, \mathbf{y}_\sigma), \quad (2.30)$$

are simply weighted derivatives of the Rosenhead-Moore kernel and depend upon the

distance between the point of interest and the interacting cluster. The moments of vorticity

$$\mathbf{m}_{\mathbf{k}}(\sigma) = \sum_{j \in \sigma} (\mathbf{y}_j, \mathbf{y}_\sigma)^{\mathbf{k}} [\omega_j] \quad (2.31)$$

describe the local distribution of vorticity throughout the cluster.

The cost of the calculation can be reduced further, from $\mathcal{O}(N \log N)$ to $\mathcal{O}(N)$, by representing the discrete velocities in the target cluster σ' , which are induced by the vorticity in the source cluster, using a truncated Taylor expansion of the velocity about the centroid of the target cluster. This expansion requires the spatial derivatives of \mathbf{u} to be evaluated at the centroid of that cluster, \mathbf{x}_0 . These derivatives are given by

$$D_{\mathbf{x}}^{\mathbf{n}} \mathbf{u}(\mathbf{x}_0) = (-1)^{\mathbf{n}} \sum_{\mathbf{k}=\mathbf{n}}^{\mathbf{p}} \frac{\mathbf{k}!}{(\mathbf{k}-\mathbf{n})!} \mathbf{a}_{\mathbf{k}}(\mathbf{y}_{\sigma'}, \mathbf{y}_\sigma) \times \mathbf{m}_{\mathbf{k}-\mathbf{n}}(\sigma) . \quad (2.32)$$

The velocity at a nearby position, \mathbf{x} can then be approximated using a Taylor series expansion about \mathbf{x}_0 so that

$$\mathbf{u}(\mathbf{x}) \approx \mathbf{u}(\mathbf{x}_0) (-1)^{\mathbf{n}} \sum_{\mathbf{k}=\mathbf{n}}^{\mathbf{p}} \frac{1}{\mathbf{k}!} D_{\mathbf{x}}^{\mathbf{k}} \mathbf{u}(\mathbf{x}_0) (\mathbf{x} - \mathbf{y}_{\sigma'})^{\mathbf{k}} . \quad (2.33)$$

The derivatives of the velocity field can also be projected to \mathbf{x} in a similar fashion.

A hierarchical octree data structure is implemented within the VTM to exploit the FMM. This is the same structure that is used to manage efficiently the adaptive grid system within the VTM as described in Section 2.3.1. At the lowest level of the octree lie the cells themselves. The next level of the octree is formed by collecting together the cells from eight neighbouring locations (the ‘children’) to form a ‘parent’ cluster. The process of clustering is repeated on each level of the octree until a level is reached on which there exists only one single cluster that effectively contains the entire computational domain.

At the start of the velocity calculation, the FMM moves up through the octree structure and calculates the moments as defined in Eq. (2.31). The moments of each parent cluster σ can be written as the sum of the moments of its children $\bar{\sigma}$. At the next step the FMM calculates the velocity field whilst it moves back down through the octree. The velocity

at any point in the domain is made up of far-, intermediate- and near-field components. All the clusters which are immediate neighbours of a cluster i are defined as its near-field. The children clusters of parents which neighbour i and which do not form part of the near-field are considered as part of the intermediate-field of i . The far-field of cluster i is thus defined as all the other clusters which are not contained in either the near- or intermediate-fields. This arrangement is shown schematically in Fig. 2.4.

The far-field component of the velocity at cluster i on level n is inherited from the parent cluster of i located on level $n + 1$ of the octree. The velocity that is induced by the intermediate-field is obtained from the calculation of the cluster-cluster interactions on level n . The contribution to the velocity field from the far- and the intermediate-field components are then summed at the centroid of cluster i . This combined velocity is transferred to the children of i using Eq. (2.33) and forms the far-field velocity component for the children clusters on level $n - 1$. This process of evaluation and subsequent translation of the far- and intermediate-fields is conducted on all clusters on level n , after which the downward sweep through the octree moves to level $n - 1$, where this process is repeated. Once the lowest level of the octree has been reached, the far-field component of the velocity field is known for every cell. The intermediate- and near-field components of the velocity are then evaluated directly from the Biot-Savart equation. Once the calculation of the near- and intermediate-field components of the velocity is completed for every cell,

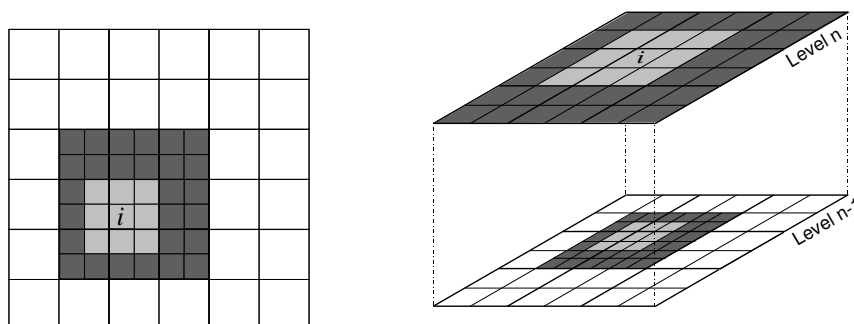


Figure 2.4: Evaluation of the velocity field on cluster i and the categorisation of the velocity-inducing clusters into the near-field (light grey), the intermediate-field (dark grey) and the far-field (white) velocity components.

the advection operator of Eq. (2.10) may be evaluated.

2.4 Calculation of the vorticity source

Since the flow surrounding the rotorcraft is assumed inviscid, the viscous term $\nu \nabla^2 \omega$ in Eq. (2.5) becomes non-zero only on the surfaces of bodies which are immersed in the flow and can therefore be replaced by a local vorticity source S . The aerodynamics of the rotor blades and the helicopter fuselage are thus accounted for by the source term operator $[S]_{\Delta t}^n$. Under the assumption that the computation of the flow surrounding the rotorcraft can be decomposed into an outer (wake evolution) and an inner (blade aerodynamic problem) the source term effectively couples the two calculations and acts as a feed-back loop between the loading along the blades and the strength and geometry of the vortical structures in the flow-field.

As alluded to previously, the timestep that is required to maintain the accuracy and stability of the blade aerodynamic calculation is generally very much smaller than the timestep that can be used to advance the vorticity transport equation through time in the absence of vorticity sources. This mismatch in timesteps can cause a stiffness in the algorithm which is addressed in the VTM by using a sub-stepping approach. A smaller, inner timestep Δt_{inner} , is used to calculate the aerodynamic loads on the blades and a larger, outer timestep Δt , is used to manage the evolution of vorticity in the wake, where

$$\Delta t_{inner} = \Delta t / M \quad (2.34)$$

and where M is the number of substeps. The number of substeps is user-predefined before the calculation proceeds and is set large enough to maintain the accuracy of the vorticity source and the stability of the algorithm used to calculate blade aerodynamics and yet small enough to prevent smearing of the relevant spatial features in the wake. The vorticity source generated over a single outer timestep Δt then becomes the sum of that from each

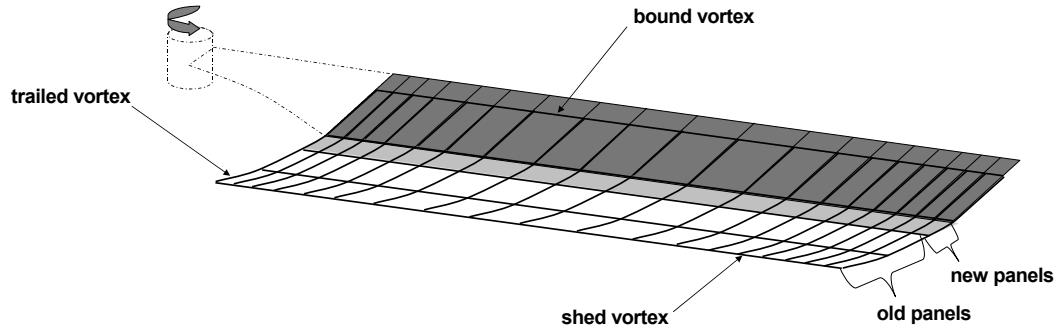


Figure 2.5: Representation of the ‘near-wake’.

inner timestep Δt_{inner} , so that

$$S = \sum_{i=0}^{M-1} [S]_{\Delta t_i}^{n+i/M} . \quad (2.35)$$

Although a similar approach to the construction of the source operator could be used if a more comprehensive theory of loads generation (for instance one incorporating fully three-dimensional, viscous, or compressible aerodynamic effects) were adopted within the VTM, here the inner model is constructed by assuming that the aerodynamic forces result from a distribution of bound vorticity which is confined to the neighbourhood of the blades.

The blade is discretised into a series of panels that each represent a segment of the blade (Fig 2.5). A discrete vortex is bound to a line which passes through the quarter chord of each panel and represents the circulation due to lift on that panel. The methods by which the strength of the bound vortex is determined, and thus how the airloads on the blade are calculated, are explained in detail in Chapter 3 of this dissertation.

As vorticity is conserved within an inviscid fluid, any changes in the bound vorticity must be accompanied by an equal and opposite distribution of vorticity being shed into the wake. At each inner timestep Δt_{inner} , a vortex panel containing trailed and shed vorticity is formed at the separation line which is fixed at the trailing edge of the blade. This

vortex panel is then added to a lattice of vortex panels which then define the ‘near-wake’ immediately downstream of the blade. The lattice structure is then convected freely by the local flow velocity. The near wake make up of shed and trailed vorticity consistent with the temporal and spatial gradients of bound vorticity on the blades, in other words

$$S = -\frac{d}{dt}\omega_b + \mathbf{u}_b \nabla \cdot \omega_b, \quad (2.36)$$

where ω_b is the bound vorticity and \mathbf{u}_b is the velocity of the trailing edge relative to the air. Assuming a single bound vortex, of strength Γ , lying along the span of the blade, Eq. (2.36) can be written as

$$S = -\tau \frac{\partial \Gamma}{\partial t} + \mathbf{u}_b \frac{\partial \Gamma}{\partial r}, \quad (2.37)$$

where τ is the unit vector parallel to the trailing edge of the blade. The local flow velocity \mathbf{u}_b has contributions from the freestream velocity, the wake induced velocity and the velocity due to blade motion. Most importantly in the present context, the shed vorticity distribution behind the blade is fully resolved using this approach. Its influence on the unsteady aerodynamic response of the system is thus captured directly in the simulations without the need to resort to empirical modelling of the response of the blade, as is done in some comprehensive codes in order to compensate for their under-resolution (or even omission in some cases) of the sheet of vorticity that is shed into the flow immediately behind the blades.

The vorticity at the back of the lattice structure is interpolated onto the computational grid once the panels reach a pre-specified age, measured in terms of inner timesteps. The azimuthal distance over which the vortex lattice exists is a matter of user choice, but must be sufficient to ensure that the roll-up of the individual trailed vortices into a concentrated tip vortex is modelled accurately.

2.5 HART II rotor

The rotor, studied during the HART II test programme, was based on the characteristics of the Bo105 main rotor. The HART II rotor had four blades and was scaled both geometrically and aeroelastically to 40% of the full Bo105 rotor size, giving a radius of 2m and a chord of 0.121m. The rotor blades had a NACA23012 aerofoil with the trailing edge modified to form a 4.46% chord tab. The blades were rectangular with a square tip and incorporated -8° of linear twist and a pre-cone angle of 2.5° .

The rotor was flown in descending flight at an advance ratio of 0.15 and an actual rotor shaft angle of 5.3° . This test point was selected as being analogous to the full-scale flight condition that yields maximum BVI noise radiation. A correction factor of $0.8-1.1^\circ$ to give an effective shaft angle of 4.5° was suggested to account for wind tunnel effects. This has not been included in the simulations presented in this dissertation, as it has been shown to have a minimal influence on the predictions of the high-frequency airloads. Further operational parameters for the test are summarised in Table 2.1. A detailed description of the rotor model and the measurement procedures used in the HART II test are given in Refs. 31–34.

Table 2.1: *Rotor operational parameters*

Forward velocity	33 m/s
Rotational speed	1041 rpm
Blade passage frequency	69.4 Hz
Shaft tilt	5.3°
Thrust coefficient	0.00457
Advance ratio	0.151

2.6 Structural dynamics

A simplified description of the rotor system is implemented within the VTM in order to limit the complexity of the structural dynamic model and ultimately to reduce the computational cost that is incurred. Typically the rotor hub is replaced by a series of

springs, dampers and hinges that are attached to rigid blades which are free to respond to the forces that are generated within the system. This arrangement can be used to mimic various types of rotor hub by sensible selection of stiffness and damping parameters. In this dissertation, however, as the focus is to investigate the modelling of the aerodynamic environment of the rotor blades, the dynamics of the blades have been prescribed to follow the experimentally-measured structural deformations of the HART II rotor system described in Section 2.5. This approach allows any effects on the quality of the simulation that are due to misrepresentation the blade dynamics to be separated from those that are induced by the aerodynamics of the system. Although the VTM is capable of capturing the dynamic coupling between the rotor and fuselage, in all the results presented within this dissertation, the rotor hub is assumed, for simplicity, to remain fixed relative to the prescribed trajectory of the helicopter. Fig. 2.6 shows a simplified representation the blade and hub and a definition of the blade motions.

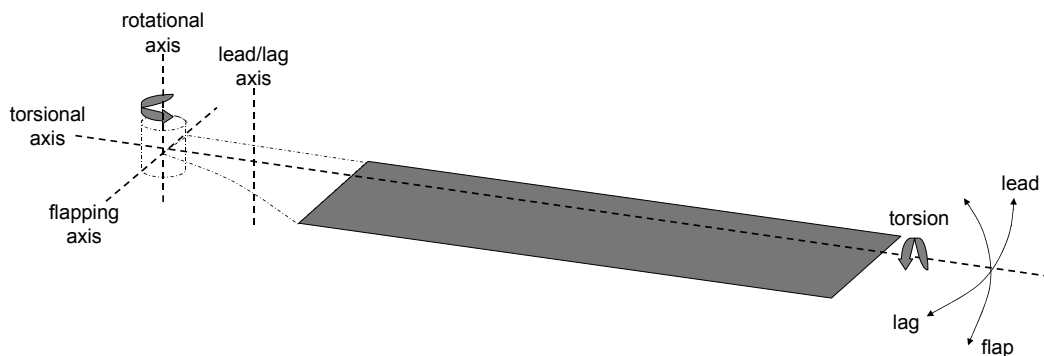


Figure 2.6: *Flapping, lead-lag and feathering motion of the rotor blade.*

2.6.1 Prescription of the blade dynamics

In the HART II tests, the blade deformation was measured using a non-intrusive optical method, called Stereo Pattern Recognition, as described in Refs. 68–70. Reflective markers were attached to both the leading and trailing edges of all four blades at eighteen regular radial stations from 23% span to the blade tip. The positions of the markers were then recorded at 15° intervals of the blade azimuth. The measurements of blade deflection were thus relatively sparse and are available only as a set of values defined at discrete

azimuthal and radial positions. There are missing data where the markers could not be viewed because they lay within the shadow of the drive enclosure and the mounting support, or because the markers had peeled off the blades. The data are provided as elastic deflections at each discrete location in three components – *flap*, which is defined relative to the precone angle and acts in a direction normal to the plane of rotation; *lag*, defined relative to the quarter-chord of the blade and acting in the plane of rotation; *torsion*, which is the rotational displacement about the quarter-chord of the blade and relative to the pre-twist and control angles. The elastic deformations for each blade on the model rotor vary due to differences in the internal structure of each blade and also differences in the instrumentation that has been applied to each blade. For all three HART II flight cases, data are available for each of the four blades individually.

To allow the computation of the displacement of the blade at any radial or azimuthal location, to interpolate over the gaps in the data, and to smooth the noise that is present in the measurements, an analytical description of the blade deflections was generated. Each component D of the deformation is reconstructed by fitting a separate interpolation surface, using the variable-separable form

$$D(r, \psi) = \sum_{i=1}^{N_r} \sum_{j=1}^{N_a} a_{ij} R_i(r) P_j(\psi), \quad (2.38)$$

to the discrete data for the deformations of each of the blades. N_r and N_a are respectively the number of radial and azimuthal interpolation functions $R_i(r)$ and $P_j(\psi)$ used to describe the blade deflection.

The radial interpolation functions were assumed to be polynomials and the azimuthal interpolation functions were assumed to be the components of a Fourier series so that

$$R_i(r) = r^{(i-1)} \quad (2.39)$$

and

$$P_j(\psi) = \begin{cases} \cos \frac{j-1}{2} \psi & \text{if } j \in \{1, 3, 5, \dots\} \\ \sin \frac{j}{2} \psi & \text{if } j \in \{2, 4, 6, \dots\}. \end{cases} \quad (2.40)$$

The coefficients a_{ij} of the interpolation function were calculated by enforcing a simple least squares fit to the measured data for the blade deformations. The sets of coefficients required to give an approximation to the elastic flap, lag and torsional deformations z_{el} , y_{el} and θ_{el} of the blades for the BL, MN and MV test cases are given in Appendix A.

A prescription of the blade dynamics can also be generated using a modal identification method. For example that described by van der Wall in Ref. 1, where reconstruction of the blade dynamics is based on a best fit to the lowest pre-computed mode shapes for the structural deformation of the blades. In his method it is possible to separate the contribution to the total deflection given by each individual mode. Using pre-defined mode shapes the physical boundary conditions (of zero displacement at the blade root and zero curvature at the blade tip) are explicitly applied. A comparison of the airloads produced using both the variable-separable interpolation detailed here and the modal identification method described by van der Wall (Ref.1) is given in Section 4.1.

Data obtained by the US Army Aeroflightdynamics Directorate (AFDD) using a CFD/CSD loose coupling methodology (Ref.71) was also released by the HART II team in the form of a motion file to be used to prescribe the structural dynamics of the HART II rotor. This motion file contained the translational and angular deformations of the quarter-chord of the blade and so included the elastic deflections, trimmed control motions and the precone but not the static twist. Without additional trimming of the rotor the thrust produced was found by the participants of the HART II workshop to be much less than that recorded during the experiment, when using this description of the blade dynamics. As a result this method is likely to give errors in the lower harmonic content of the blade airload, particularly where no additional trim algorithm is used, and hence is no longer used.

2.7 Control algorithm

Control inputs are used to alter the forces and moments that are generated by the rotor system in order to maintain a specified force coefficient or a particular rotorcraft attitude. The trim algorithm that is implemented within the VTM modifies the rotor controls $\zeta =$

$[\theta_0, \theta_{1s}, \theta_{1c}]$ so that their instantaneous rate of change is proportional to the error between the current values of an array of force and moments, $F = [C_{Fx}, C_{Fy}, C_{Fz}, C_{Mx}, C_{My}, C_{Mz}]$, which represents the overall loads on the vehicle, and the array F^* which contains prescribed target values for each force and moment. The resulting scheme is thus a simple first-order dynamical system,

$$\frac{d\zeta}{dt} = K (F^* - F(t)) \quad (2.41)$$

where K is a coupling matrix that governs the rate at which each of the controls should respond to any discrepancy between F^* and F . The values of K are selected to represent the control characteristics of the rotor system under study. Denoting the long term average of $F(t)$ by \bar{F} , the system is considered to be in a state of trim when

$$\bar{F} = F^* \quad (2.42)$$

The trim algorithm constantly adjusts the controls throughout the simulation in an attempt to reach the prescribed target loads on the vehicle and works much like a simplistic pilot model. This same algorithm can be used to define the trim condition of the vehicle in any given unsteady flight condition, where in such cases the target forces and moments F^* are chosen to obtain the required acceleration of the aircraft.

2.8 Acoustic analysis

The acoustic field that is radiated by the rotor is computed using a post-processor for the blade aerodynamic loads that implements the Farassat-1A formulation (Ref. 19) of the Ffowcs Williams-Hawkings (FW-H) equation (Ref. 16). This formulation is widely used in rotor acoustic calculations because of the efficiency and accuracy that results from its analytic representation of the observer time derivatives. The acoustic pressure, p' at a

point \mathbf{x} at time t can be written as

$$\begin{aligned}
 p'(\mathbf{x}, t) = & \frac{1}{4\pi} \frac{\partial}{\partial t} \iint_S \left[\frac{\rho v_n}{r(1 - M_r)} \right]_{\tau} dS + \frac{1}{4\pi a_0} \frac{\partial}{\partial t} \iint_S \left[\frac{F_r}{r(1 - M_r)} \right]_{\tau} dS \\
 & + \frac{1}{4\pi} \frac{\partial}{\partial t} \iint_S \left[\frac{F_r}{r^2(1 - M_r)} \right]_{\tau} dS
 \end{aligned} \tag{2.43}$$

where a_0 is the speed of sound and \mathbf{r} is the distance between the point x and the acoustic source. F_r is the component of local force which is exerted by the body on the fluid, and which acts in the direction of the observer ($F_r = \mathbf{F} \cdot \mathbf{r}$). M_r is the Mach number at which the source is moving relative to the observer ($M_r = \mathbf{M} \cdot \mathbf{r}$). The source time τ , also known as the ‘retarded time’, is the time at which the sound wave is emitted from the source relative to the observer time t . This accounts for the finite length of time that is required for the acoustic waves to reach the observer point from the location where they have been emitted.

The total noise includes contributions from loading, thickness and quadrupole sources. Thickness noise is caused when a moving rotor blade of finite thickness displaces fluid particles and as a result produces a pressure change and an associated noise contribution. This is represented by the first term in Eq. (2.43) where v_n is the local normal velocity of the blade surface. The second and third terms correspond to the far-field and near-field contributions by the loading noise. The loading noise is caused by the force exerted on the fluid by the moving blade surface. The contribution by the loading noise to the far-field is dependent on the rate of change of the pressure on the blade and if a compact source is assumed, can be directly related to the time rate of change of force on the blade. It is thus clear that the highly impulsive change in lift generated by the blade encountering a vortex will have a significant impact on the acoustic signature of the rotor.

Considerable simplification is introduced into the analysis by assuming that the sources of sound are acoustically compact in the chordwise direction. An acoustic source is said to be compact if its size is small relative to the wavelength of the sound waves that it generates. In this dissertation, the compactness of the chordwise loading distribution is justified because the aspect ratio of the blades is high and therefore the phase difference

between sounds which are radiated from sources in the chordwise direction can be assumed to be minimal. The chordwise distribution of noise sources which are due to loading can then be approximated as a point source.

The blade surface in the aerodynamic model is represented by a series of panels as described in Section 2.4 and in Chapter 3. The aerodynamic force contributed by each blade panel is used to construct a point acoustic source at the centre of each panel. The loading noise at any given observer location is then obtained by summation of these acoustic sources. The aerodynamic model assumes an infinitesimally thin blade; the thickness noise has thus to be modelled independently. This is done by attaching a source-sink pair to each blade panel. The quadrupole source term accounts for non-linear effects (e.g., non-linear wave propagation and steepening, variations in the local sound speed induced by compressibility and noise generated by shocks, vorticity and turbulence in the flow-field). Although this term does play an important role in BVI noise generation, particularly at higher tip Mach numbers, it is neglected in the present work as the associated flow Mach numbers are assumed to be sub-critical and non-linear effects are therefore minimal. No account is made for absorption and scattering due to the presence of bodies that are immersed in the flow-field, such as the experimental drive enclosure in the HART II test, even when it was included in the aerodynamic calculation.

2.9 Fuselage model

Fuselages or other solid bodies which are immersed within the flow-field are represented using an unsteady vortex panel method, as described in more detail in Ref. 58. The surface of the body is discretised into a system of N_{fus} quadrilateral panels. Each panel edge is represented as a vortex filament with constant strength Γ_j . The filaments on each panel thus form a closed loop of vorticity. The velocity at the centroid of any panel is calculated as the sum of the velocity induced by all the other vorticity within the flow w , the component of the freestream velocity U_∞ and the influences from all vortex filaments on the body. To determine the strengths of the vortex filaments on the body, a boundary

condition of zero through-flow is enforced simultaneously at the centroids of all panels,

$$(U_\infty + w)_i \cdot n_i \sum_{j=1}^{N_{fus}} A_{ij} \Gamma_j = 0 \quad (2.44)$$

and solved at each timestep. In Eq. (2.44), n_i is defined as the unit vector normal to the panel i .

The influence matrix, A , accounts for the velocity induced on each panel by every other panel and is of dimension N_{fus} by N_{fus} . The solid body should form a closed entity and this implies that the sum of the panel strengths must be zero. The influence matrix is thus singular. The inverse of the influence matrix is required to evaluate the vortex loop strengths, Γ_j , and is approximated using Singular Value Decomposition. Since the body is assumed rigid, the coefficients of the influence matrix do not change with time. The inversion of the influence matrix can be performed prior to the simulation, yielding a significant saving in computational time.

Once the boundary condition of zero through-flow has been satisfied on each panel, the vortex loop strengths are known and the velocities on the surface of the body can be calculated. The pressure on the surface of the body is then related to the velocity by the unsteady Bernoulli equation

$$\frac{p - p_\infty}{\frac{1}{2}\rho} = U_\infty - |\mathbf{u}|^2 - 2\frac{\partial\phi}{\partial t} \quad (2.45)$$

Since this equation is only valid in regions which are simply connected to the far-field, care should be taken when calculating the surface pressure in areas where discontinuities to the velocity potential are known to occur, such as across a wake sheet. The surface velocity \mathbf{u} includes a contribution from all the vorticity in the computational domain and also a correction term which models the self-influence of the vorticity on the panel as a equivalent vortex sheet. Both the change in panel strengths due to time-varying boundary conditions and the unsteady disturbances to the velocity potential which result when a vortex is convected through a fluid are accounted for in the evaluation of the unsteady potential term $\frac{\partial\phi}{\partial t}$.

Lift generation by the solid bodies, within the flow other than the rotor blades themselves, can be modelled in the VTM by satisfying the Kutta condition along a pre-specified separation line on the surface of the body. Vorticity is sourced into the computational grid to ensure that the net circulation around the separation line is zero. The strength of the vorticity source is thus equal to the difference in strength between the panels on either side of the separation line. This vorticity feeds back into the loading produced on the system and thus represents fully the circulatory contribution to the unsteady aerodynamic characteristics of any lifting surface in the flow. The viscous wakes that are created by any bodies immersed within the flow are not accounted for at present.

2.10 Summary

The present formulation of the VTM has been tailored for the aeromechanical analysis of rotorcraft systems and couples a model for the aerodynamics of the blade to an Eulerian representation of the dynamics of the vorticity in the flow field. The VTM is based on a time-dependent vorticity-velocity formulation of the Navier-Stokes equations, solved computationally on a structured Cartesian grid system surrounding the rotor. The method has been designed specifically to reduce numerical dissipation of the vorticity in the flow, thus maintaining the integrity, over many rotor revolutions, of the vortical structures that are present in the rotor wake. The VTM is therefore well suited to modelling the geometry of the wake to the accuracy and detail that is required for the high-frequency components of the blade airload that are associated with BVI to be captured correctly.

An adaptive grid is used to track the evolving vorticity in such a way that cells only exist in regions of the computational domain where the vorticity is non-zero. Thus, the grid structure is free to follow the evolution of the wake, eliminating the requirement for explicit numerical boundary conditions at the edge of the computational domain and increasing the computational efficiency of the method. Moreover, a nested grid system allows for fine resolution close to the rotor and then a systematic decrease in resolution with distance from the rotor hub. At each time step, the velocity at the cell faces is obtained from the vorticity distribution using a fast multipole method which further increases the

computational efficiency of the technique.

In the particular version of the model that was used in this work, the motion of the blades is prescribed, based on a variable-separable interpolation of the blade deformations that were measured at discrete azimuthal and radial locations on each blade during the HART II experiment. Fuselages or other solid bodies are modelled using an unsteady vortex panel method. The acoustic field that is radiated by the rotor is computed using a post-processor for the blade aerodynamic loads that implements the Farassat-1A formulation of the Ffowcs Williams-Hawkings equation. The thickness noise is modelled independently by attaching a source-sink pair to each blade panel. Noise due to quadrupole terms is neglected in the present work. The absorption and scattering due to the presence of any other bodies in the flow-field are also not modelled.

Chapter 3

Aerodynamic modelling of the rotor blades

The aerodynamic environment that is encountered by the rotor blades of a helicopter under typical operating conditions is highly unsteady. Although the main contributions to the blade angle of attack come from the control inputs and the elastic deformations, additional and not insignificant effects are introduced by the wake that is produced by the rotor in flight. In particular, the concentrated vortices that are trailed from the tips of the blades induce rapid changes in angle of attack over very short time scales when they encounter a blade. In order to capture the effects of these interactions on the loading, the blade aerodynamic model must be able to capture the aerodynamic response of the blade when subjected to these very transitory perturbations to its aerodynamic environment. In the context of predicting rotor airloads, the mathematical modelling of unsteady aerofoil behaviour is considerably more complex than if only the quasi-static behaviour of the aerofoil was of interest. As yet, a complete understanding of aerofoil behaviour, even in the absence of significant flow separation, has not been obtained (Ref. 72). The aerofoil behaviour is further complicated in situations where dynamic stall plays a major role, for instance, on the retreating side of the rotor near the blade root.

In a full CFD analysis of the rotor and its surrounding environment, the airloads and the

wake are part of the same numerical solution and the analysis is able to provide a full representation of the pressure distribution over the blade chord. Despite their future potential, CFD solutions are subject to outstanding technical problems, for example, in their modelling of transition and separation. These technical problems must be adequately resolved before CFD methods can be relied upon to predict accurately the unsteady aerodynamic response of the blade.

There is thus much interest, especially in the context of rotor design, in developing methods which offer high fidelity solutions but at a much reduced computational cost when compared to CFD calculations of both the blade aerodynamics and the resulting wake. One approach is via the so-called comprehensive code which uses a lifting-line or lifting surface type aerodynamic model to provide blade airload information and often a prescribed- or free-wake approach to portray the dynamics of the wake system. Lifting-line or lifting surface aerodynamic models are generally inviscid in nature and so the wake produced by the blades is modelled separately in terms of the trailed and shed vorticity from the blades. In many cases it is only the trailed vortices that are modelled and the shed vorticity is accounted for separately by an additional unsteady aerodynamic model which is then forced to rely upon a certain degree of empiricism. Unsteady models, such as the Leishman-Beddoes semi-empirical model (Ref. 73), often account for viscous effects, compressibility effects, flow separation and dynamic stall. Where the shed wake *is* modelled, for instance as part of a vortex lattice, additional considerations are still required to account for compressibility effects and stall.

Lifting-line or lifting surface models are relatively simple and easy to implement, but the physical accuracy of their portrayal of the dynamics of the wake, especially if based on a prescribed- or free-wake approach, can be called into question especially in terms of resolving the detail of the close blade-wake encounters associated with BVI. It is not clear it is the discrepancies in the wake model, or instead in the blade aerodynamic model, that are responsible for the deficiencies in prediction of the BVI-induced loads that appear to be characteristic of this type of approach.

The aerodynamic model within any comprehensive analysis must perform two tasks.

Firstly, it is required to generate the airloads (i.e. lift, drag and pitching moment) on the rotor blades which are caused by the relative motion of the blade section with respect to the surrounding flow-field. This requires accurate knowledge of the blade deformation, the freestream velocity and the velocities which are induced at each blade section by the vorticity in both the near and far wake. The blade deformations include contributions from both the structural dynamic response of the blades and the control angles that are required to ensure a trimmed flight condition. The resulting airloads depend upon the accurate calculation of the unsteady response of the aerofoil to these external excitations. The unsteady response of the aerofoil is influenced by the aerofoil shape, compressibility, boundary layer separation and stall, shock-boundary layer interactions and the local shed and trailed vorticity behind the trailing edge of the blade. Secondly, the aerodynamic model is also responsible, in an inviscid calculation, for the generation of the local source of vorticity into the wake.

Lifting-line theory, introduced by Lanchester and Prandtl (Ref. 74), is the simplest and perhaps the best known theory that describes the aerodynamic behaviour of three-dimensional wings in inviscid and incompressible flow. The theory is used widely, particularly in the fixed-wing community, generally because of its low computational cost and ease of implementation. Classical lifting-line theory assumes a large aspect ratio wing of finite span on which the circulation that is generated due to lift can be concentrated onto a line vortex which is bound to the quarter-chord of the wing. The airloads are then obtained by considering a two-dimensional problem at several locations along the wing. The influence of the wake is included as an induced angle of attack or downwash velocity which acts at each spanwise section. The variation in the distribution of vorticity along the chord of each section is ignored and the computed induced angle of attack is only calculated at a single point along the chord of any particular blade section. The later extensions of lifting-line theory by Weissinger (Ref. 75) reproduced the correct lift curve slopes for wings with a much smaller aspect ratio than can be accurately represented using the classical approach (Ref. 76). The Weissinger-L formulation allows the spanwise variation in circulation and lift, essential for rotorcraft applications, to be captured. Moreover, it provides an improved prediction of the blade loading, compared to conventional lifting-line theory, for

blades with arbitrary planforms (Ref. 75). The deficiencies of the Weissinger-L lifting-line approximation are primarily in its representation of the unsteady aerodynamic response of the wing, as discussed in detail by van Holten (Ref. 77) but the approach is still widely used in the helicopter community today.

The single-point boundary condition that is applied in the lifting-line model is based on the assumption that the velocity profile is relatively constant in the chordwise direction. While this may be true for most fixed wing situations, in the helicopter case this is often not justified, especially when BVIs are an issue. When the blade interacts with a concentrated tip vortex, the core size of the vortex is often small compared to the chord of the blade. As a result, steep gradients in velocity are induced within the chord's extent. The only way to account fully for the rapidly changing velocities is to apply boundary conditions along the chord rather than at one single point. Using classical, unsteady, thin-aerofoil theory at each blade section, where the aerofoil is represented as a thin surface in two dimensions, a zero through-flow boundary condition is enforced along the entire chord of the aerofoil. This theory can be used in the airload calculation at each blade section, to account more accurately than the simple lifting-line theory, for the rapid changes in velocity along the blade chord which occur during blade-vortex interaction.

The original unsteady, thin-aerofoil theory has been extended to include the effects of a time-varying freestream, subsonic compressibility, and trailing-edge flap deflections on the aerodynamic loads generated by an aerofoil. The particular implementation that was used in the present study is a simplified version of a state-space formulation of the theory that was developed for flexible aerofoils by Peters *et al.* (Ref. 78). Peters's theory has been reformulated to apply to an aerofoil that is performing large motions with respect to the air. The theory can be coupled with any unsteady wake model, including three-dimensional wake models, and thus can be adapted fairly straightforwardly to model the spanwise variation of loading along helicopter rotor blades. In addition, the theory can be linked conveniently to the dynamic model for the blades as it is formulated in terms of generalised deflections and generalised forces.

In the simulations presented in the later Chapters of this dissertation, the aerodynamics of

the rotor blades are modelled using either a lifting-line approach based upon Weissinger's L-method, or a 'lifting-chord' approach based upon Peters's formulation of unsteady thin aerofoil theory. The model for the blade aerodynamics is incorporated into the Vorticity Transport Model, as described in Chapter 2. In this form, the Vorticity Transport Model can be thought of as a comprehensive rotorcraft analysis tool where the flow surrounding the rotorcraft can be decomposed into coupled outer and inner aerodynamic problems. Since the flow-field is assumed to be inviscid, vorticity is generated only on lifting surfaces which are immersed in the fluid. The aerodynamic model is thus responsible for generating the source of vorticity into the grid and effectively couples the inner and outer calculations. This arrangement allows the loading on the blades to feed directly into the geometry and strength of the rotor wake, and hence, via Eqs. (2.5) and (2.4), back into the loading on the blades. The generation of the local source of vorticity into the grid is described in more detail in Section 2.4. The lifting-line model is described in Section 3.1.1 and the lifting-chord model is described in Section 3.1.2. To test if unsteady, thin-aerofoil theory is indeed capable of more accurately representing the aerodynamic response of the blade when compared to the lifting-line approach, the predictions of the two models for the aerodynamic of the blades are compared in Section 3.2. Firstly, their predicted responses to a step change in angle of attack and to a sharp-edged vertical gust are compared in Sections 3.2.1 and 3.2.2, respectively. The unsteady aerodynamic response to an interaction with a single, isolated vortex, as predicted by each model, is then compared in Section 3.2.3 to assess the ability of each of the blade models to predict accurately the impulsive airloads that are associated with blade-vortex interactions.

3.1 Model implementation

For both blade aerodynamic models, the blade is discretised into a series of individual panels that each represent a spanwise segment of the blade. A discrete vortex is bound to a line which passes through the quarter chord of each panel. This vortex represents the circulation due to lift on that panel. The distribution of panels, as a matter of experience, is usually specified by the user to vary as a cosine function along the blade so that a

concentration of panels is formed near the root and the tip. This allows a finer resolution of the steep gradients in the spanwise circulation that are usually encountered in these regions of the blade. The strength of the bound vortex can then be determined by enforcing a condition of zero through-flow normal to the blade surface. The method of enforcing the zero through-flow boundary condition differs for the two blade aerodynamic models, as described in the following Sections of this Chapter.

3.1.1 Lifting-line model

The first model for the blade aerodynamics is relatively simple and is based on an extension of the Weissinger-L formulation of lifting-line theory (Ref. 75). In the implementation of this approach, a discrete vortex, of strength Γ_b , is bound to a line which passes through the quarter-chord of each panel (see Fig. 3.1). A boundary condition of zero through-flow is then imposed at a sequence of control points that are located on the three-quarter chord line of each panel.

The zero through-flow condition implies that the normal component of velocity which is incident on the blade section at the three-quarter chord location must be identically equal

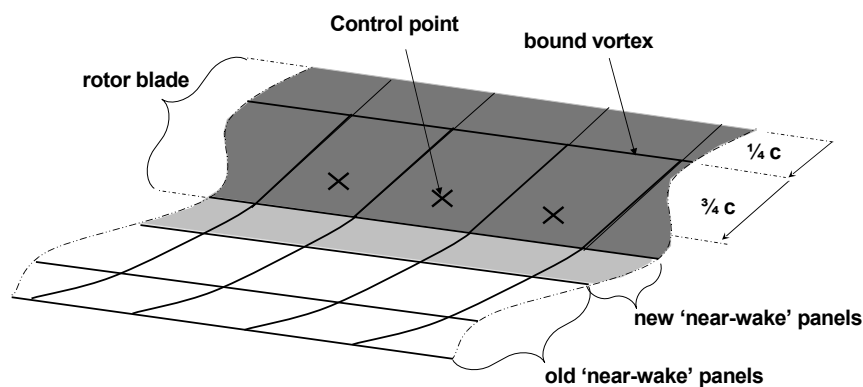


Figure 3.1: A schematic of the Weissinger-L lifting-line model, showing a part of the rotor blade.

to zero to prevent flow through the blades. In other words,

$$U_\infty \sin(\alpha - \alpha_0) = \frac{\Gamma}{2\pi b} \quad (3.1)$$

where α is the angle of attack of the blade and α_0 can be related to the camber of the blade. The incident velocity at any panel along the blade is composed of the local freestream velocity, and the induced velocities from the bound circulation itself, the near wake and all other vorticity in the flow-field. Once the circulation distribution which satisfies this criterion is known, then the blade loads can be calculated.

3.1.2 Lifting-chord model

The second model for the blade aerodynamics that has been investigated in this dissertation is based on an extension of classical unsteady thin aerofoil theory and uses a particular formulation for the airloads which is based on that developed in state-space form for flexible aerofoils by Peters *et al.* (Ref. 78).

Again, a zero through-flow boundary condition is applied to determine the strength of a vortex which is bound to a line located at the quarter-chord of each blade panel. In this case, the boundary condition is implicitly enforced at several points along the chord of the aerofoil rather than only at the three-quarter chord point as in the Weissinger-L theory (see Fig. 3.2).

The zero through-flow boundary condition allows the total bound circulation at each blade section to be written as

$$\Gamma = 2\pi b \left[f(w_0 - \lambda_0) + \frac{1}{2}(w_1 - \lambda_1) \right], \quad (3.2)$$

where f is a reverse flow parameter designed to enforce the Kutta condition at the downwind edge of the aerofoil (for forward motion $f = +1$ while for reverse flow $f = -1$). The

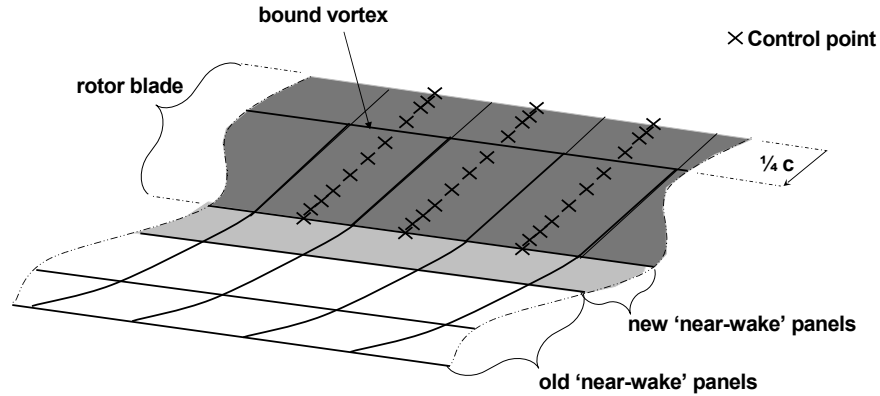


Figure 3.2: A schematic of the lifting-chord model, showing a part of the rotor blade.

circulation is defined in terms of the weighted integrals

$$\begin{aligned}\lambda_n &= \frac{1}{K_n} \int_0^\pi \lambda \cos^n \varphi \, d\varphi \\ &= \frac{1}{\pi} \int_{-b}^{+b} \frac{\lambda}{\sqrt{b^2 - x^2}} dx\end{aligned}\quad (3.3)$$

and

$$\begin{aligned}w_n &= \frac{1}{K_n} \int_0^\pi w \cos^n \varphi \, d\varphi \\ &= \frac{2}{\pi} \int_{-b}^{+b} \frac{\lambda}{b\sqrt{b^2 - x^2}} x dx\end{aligned}\quad (3.4)$$

where w is the component, normal to the blade camber-line, of the blade velocity relative to the uniform background flow and λ is the component, again normal to the blade camber-line, of the velocity due to all vorticity in the computational domain except that which is bound to the panel under consideration. These expressions make use of Glauert's variable φ , defined such that

$$x = b \cos \varphi \quad (3.5)$$

$$-b \leq x \leq +b, \quad 0 \leq \varphi \leq \pi$$

and the integral

$$K_n = \int_0^\pi \cos^n \varphi \, d\varphi . \quad (3.6)$$

These integrals are evaluated numerically after evaluating the integrands at several discrete points along the chord of each blade panel (see Fig. 3.2). In all simulations described in the later Chapters of this dissertation these points were cosine-distributed along the chord to give enhanced resolution of the steep loading gradient near the leading edge of the blade.

The sectional lift (per unit span) is then given by (Ref. 78)

$$\begin{aligned} L_0 &= 2\pi\rho b f U_\infty (w_0 - \lambda_0) + \pi\rho b U_\infty w_1 + \pi\rho b^2 (\dot{w}_0) \\ &= \rho U_\infty \left(\Gamma + \frac{1}{2} \lambda_1 \right) + \pi\rho b^2 (\dot{w}_0) . \end{aligned} \quad (3.7)$$

3.1.3 Compressibility effects and stall

Under quasi-steady conditions both models for the aerodynamics of the rotor blade reproduce the two-dimensional theoretical thin-aerofoil result,

$$C_{l_{(theory)}} = 2\pi (\alpha - \alpha_0) . \quad (3.8)$$

irrespective of the value of α . This is insufficient for helicopter applications, however, where compressibility near the blade tips and large post-stall angles of attack, especially near the root of the retreating blade, are encountered. These effects are accounted for by defining a modified distribution of circulation,

$$\Gamma^* = k\Gamma, \quad (3.9)$$

from which the blade loading and vorticity source into the wake are calculated. The constant k , is the ratio of the static lift coefficient for the ‘real’ aerofoil section, usually generated from experimentally-measured data, to the two-dimensional theoretical thin-

aerofoil result for the same angle of attack. In other words,

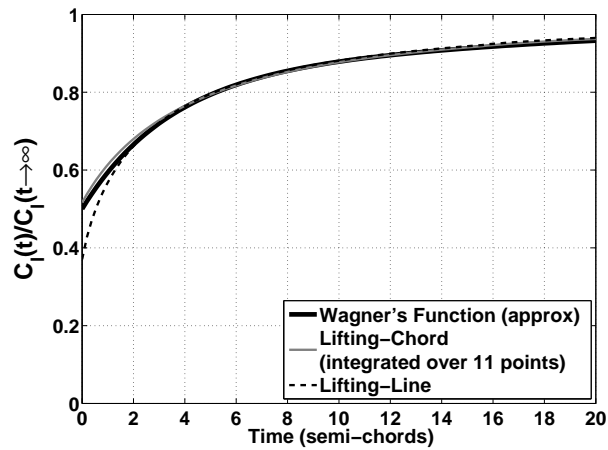
$$k = \frac{C_{l_{(expt)}}}{C_{l_{(theory)}}} \quad (3.10)$$

The experimentally measured two-dimensional characteristics of the rotor blade sections are provided as look-up tables, constructed for a specific Reynolds number. Values of $C_{l_{(expt)}}$, $C_{d_{(expt)}}$ and $C_{m_{(expt)}}$ are tabulated for a range of Mach numbers and angles of attack. As this approach is still essentially inviscid, the profile drag of the blade is calculated as a separate function of local angle of attack and is then added to the local aerodynamic force that is calculated from the blade aerodynamic model.

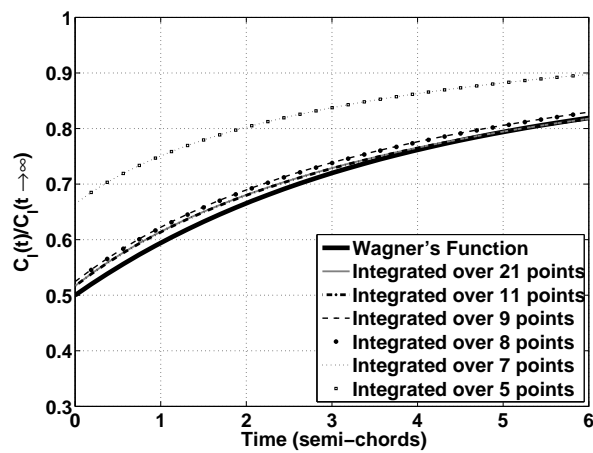
3.2 Model verification

Rotorcraft operate in an extremely complex aerodynamic environment and, as a result, the rotor is subjected to a velocity field which is highly non-uniform. Rapid transients in both the angle of attack of each blade section and the rate of change of angle of attack are caused by the pitching motions of the blade. In addition, the flapping motion of the blade results in a plunging motion at each blade section, and changes in the freestream flow cause each blade section to experience a non-uniform gust field. The unsteady aerodynamic response of the blade sections to each of these stimuli is different and thus the combined response can be extremely complex (Ref. 72). It is important that the model that is used to represent the aerodynamics of the blade is able to distinguish between the effects on the blade airload which arise from each of the stimuli mentioned above. In particular, the model that is used must be able to represent correctly both the unsteady response of the blade due to changes in angle of attack and the response which is due to a vertical gust velocity normal to the blade. The ability of both of the blade aerodynamic models to distinguish between these two phenomena can be ascertained by comparing their predicted response to the analytical solutions to Wagner's and Küssner's classical problems from the field of linearised, unsteady aerofoil aerodynamics. This comparison is made in the following two sections of the dissertation. As a prerequisite to an acceptable prediction of BVI noise,

it is also important to verify the ability of each of the blade models to predict accurately the aerodynamic response of an aerofoil to an encounter with an isolated vortex. The characteristics of the two blade models in this respect are investigated in Section 3.2.3.



(a) Analytical and numerical solutions compared



(b) Convergence of the lifting-chord model to the exact solution as the number of points is increased over which the lifting-chord integrals are evaluated

Figure 3.3: Wagner's problem for the aerodynamic response of an aerofoil to a step change in angle of attack. (The step change in angle of attack is applied at time $t = 0$).

3.2.1 Wagner's problem

Wagner's problem (Ref. 79) considers the transient lift response of a thin aerofoil, of chord $2b$, to a step change in angle of attack (from zero to α at time $t = 0$). Wagner showed that the lift response due to circulation was of the form

$$\frac{C_l(t)}{C_l(t \rightarrow \infty)} = \phi(s) \quad (3.11)$$

assuming that α is small, where $\phi(s)$ is known as Wagner's function and $s = U_\infty t/b$, i.e. the number of semi-chords travelled by the aerofoil in time t . Wagner's function has an initial value of one half and asymptotes to unity as time goes to infinity.

The lift response of an aerofoil,¹ as predicted using the lifting-line model and the lifting-chord model, to a step change in angle of attack is compared to Wagner's analytical result² in Fig. 3.3(a).

At the instant at which the blade is brought into motion, i.e. at $t = 0$, the lifting-line approach places vortices of equal strength, but opposite sense along the quarter-chord line and along the trailing edge of the blade. The zero through-flow condition that is imposed at the control point located at the three-quarter chord position may therefore be written as

$$U_\infty \sin \alpha = \frac{\Gamma}{2\pi c} + \frac{\Gamma}{2\pi c/2} \quad (3.12)$$

which results in a lift coefficient at time $t = 0$ of

$$C_{l(t=0)} = \frac{1}{3} 2\pi \sin \alpha \quad (3.13)$$

which is one third of the steady-state lift that is predicted by Wagner's analytical model (which reduces to classical, thin aerofoil theory in the quasi-steady limit). This discrepancy between the lifting-line theory and the classical result is clearly visible in Fig. 3.3(a). Although Wagner's theory allows for the distribution of vorticity along the chord of the aerofoil, at time $t = 0$ all the vorticity is concentrated at the *leading edge* and trailing

¹A two-dimensional aerofoil is modelled in the VTM as rotor blade with a very large aspect ratio.

²Actually, to Jones's indicial approximation (Ref. 80) to Wagner's exact solution.

edge of the aerofoil rather than at the quarter-chord and trailing edge as in the case of the lifting-line model. This results in an initial lift value of one half of the steady-state lift value. The weighted integrals in the lifting-chord model also weight the vorticity distribution along the chord towards the leading and trailed edges of the blade, and thus this model more accurately reproduces Wagner's exact solution.

Increasing the number of chordwise points over which the weighted integrals are evaluated increases the accuracy of the initial lift response of the lifting-chord model. Indeed, Figure 3.3(b) shows the lifting-chord solution to effectively converge onto the analytical solution once the integrals are evaluated at eleven or more points along the aerofoil chord.

3.2.2 Küssner's problem

In contrast to Wagner's problem, Küssner's problem (Ref. 81) considers the response of an aerofoil to a transient change in effective angle of attack as the aerofoil enters and progresses through a sharp-edged, vertical gust. The transient lift response can be written as

$$\frac{C_l(t)}{C_l(t \rightarrow \infty)} = \psi(s) \quad (3.14)$$

where $\psi(s)$ is known as Küssner's function. Küssner's function has an initial value of zero and asymptotes to unity as time goes to infinity.

The aerodynamic response of an aerofoil to penetration of a sharp-edged gust, as predicted using the lifting-line model and the lifting-chord model, is compared to Küssner's analytical solution in Fig. 3.4. The lifting-chord approach captures Küssner's analytical result correctly in that the response to the gust starts as soon as the leading edge of the aerofoil penetrates the gust. In contrast, in the lifting-line case, the blade does not respond until the forward edge of the gust reaches the three-quarter chord of the aerofoil, in other words the point at which the zero through-flow boundary condition is evaluated.

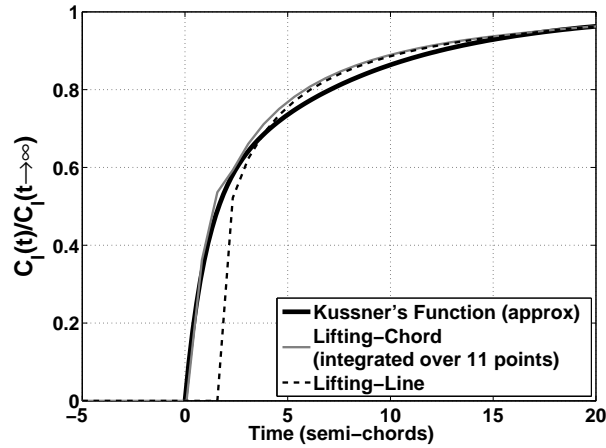


Figure 3.4: Analytical and numerical solutions to Küssner's problem compared. (The leading edge of the aerofoil encounters the gust at time $t = 0$).

3.2.3 Interaction with an isolated vortex

To illustrate the behaviour of the two different blade models in capturing the BVI-induced aerodynamic response of the blade, Fig. 3.5 shows the predicted response of an aerofoil to an encounter with an isolated vortex. In the example shown in the figure, the vortex passes $0.25c$ below the quarter-chord line of the aerofoil while convecting downstream at a Mach number of 0.626. The core radius of the interacting vortex is 0.162 chords (i.e. $c/6.172$), thus yielding a BVI of comparable dimensions to the simulated vortex core size encountered in the context of the numerical simulations of the HART II system described in the later chapters of this dissertation. This is distinct from the physical core size of the interacting vortex as measured in the HART II experiment, which is generally much smaller when compared to the chord of the blade.

This case allows the ability of each of the blade models to reproduce the highly impulsive airloads that are characteristic of blade vortex interactions to be examined in a more realistic context than that presented in the previous two sections of this Chapter. In the figure, the predictions of the lifting-line and lifting-chord models are compared to the predictions of a conventional CFD method (Ref. 82) which uses a pressure-velocity formulation of the Euler equations throughout the computational domain surrounding the aerofoil. This method is able to provide an accurate representation of the pressure

response of the aerofoil than the simpler lifting-line or lifting-chord models, and compares favourably to experimental data for an interaction of these dimensions (Ref. 83). The lifting-line model responds much later to the vortex-induced flow-field than does the lifting-chord model, and, in comparison, over-predicts significantly the maximum loading on the aerofoil that results from the interaction. Indeed, the loading on the aerofoil once the vortex has passed downstream of the aerofoil is far better predicted by the lifting-chord model than the lifting-line model, indicating a significantly better match between the circulation that is generated on the blade using this model and the vorticity that is shed into the wake downstream of the trailing edge of the aerofoil.

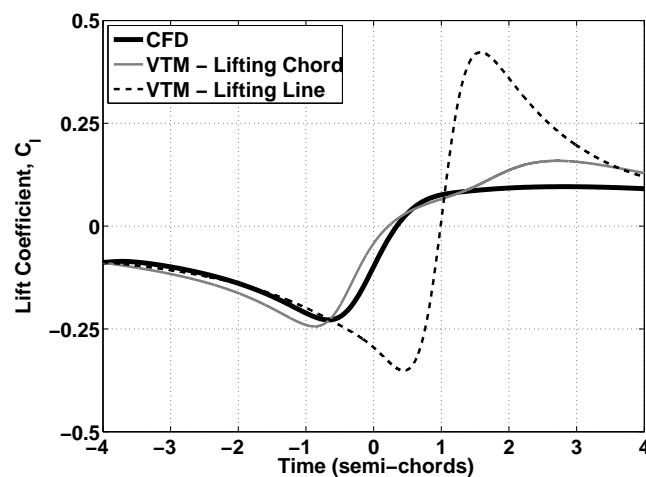


Figure 3.5: Predicted aerodynamic response of an aerofoil to interaction with an isolated vortex. (The vortex passes $0.25c$ below the quarter-chord of the aerofoil at time $t = 0$).

The relative sensitivity of the two blade models to the size of the interacting vortex is illustrated in Fig. 3.6, where the predicted response of an aerofoil to a direct interaction with a set of isolated vortices, each with the same circulation but with various core sizes, is shown. Both models predict an increase in the amplitude of the induced loading peak as the core size of the vortex is reduced, but, using the lifting-line approach, the relative increase in amplitude is more significant. A slight phase shift is also visible between the predictions of the two blade models. The consequence of these observations for the accuracy of the prediction, not only of the BVI-induced airloads on the rotor but also of the subsequent structure of the wake, are explored in the later Chapters of the dissertation.

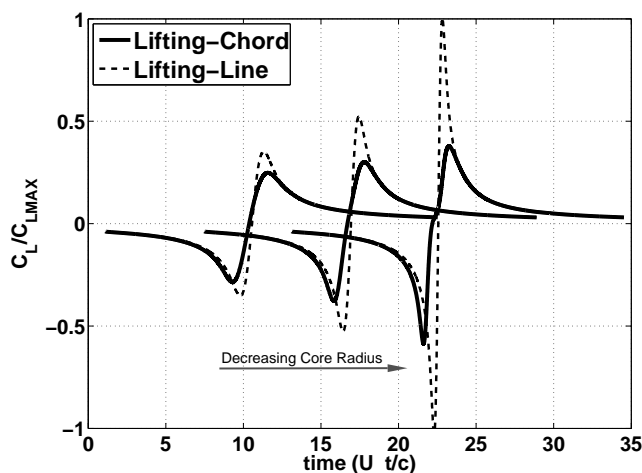


Figure 3.6: *Predicted aerodynamic response of an aerofoil to interaction with isolated vortices with varying core sizes but constant circulation, core size decreases from left to right. (The vortex passes below the quarter chord of the aerofoil at time $t = 0$).*

Each of the methods, although both in wide use, show fundamentally different behaviour in the presence of BVI-scale features in the wake. Indeed, Figs 3.5 and 3.6 suggest that the lifting-line approach, due to its single-point boundary condition, might misrepresent the vortex-induced airload on the blade, particularly when the interacting vortices have core sizes that are significantly smaller than the blade chord. In contrast, the lifting-chord model is much less sensitive to the detail contained within the velocity field, since it is instead forced by the (weighted) integral of the velocity along the entire chord of the blade. The expected consequence is that this model might produce more robust predictions of the blade airloads that are reliant rather upon the invariant, integral properties of the vortex such as its circulation.

3.3 Summary

The local aerodynamics of the rotor blades are modelled within the Vorticity Transport Model (VTM) using two different approaches. The first blade aerodynamic model is relatively simple and is based on an extension of the Weissinger-L formulation of lifting-line theory. In this model the strength of a bound vortex, attached to the quarter-chord of the blade, is determined by enforcing a zero through-flow boundary condition at one

discrete point, located at the three-quarter chord of the aerofoil. The second model is based on an extension of classical unsteady thin aerofoil theory and uses Peters's state-space formulation for the blade airloads. In this so-called 'lifting-chord' approach, the aerodynamic environment of the blade is represented via a series of integrals over the chord of the blade, thus yielding a higher-order approximation to the aerodynamic boundary condition on the blade than is given by lifting-line theory. The lifting-chord model has been shown to distinguish accurately between those effects on the blade airloads which are due to a sudden change in angle of attack and those which are due to a vertical gust. The lifting-chord approach also more accurately represents the unsteady lift response of an aerofoil to an encounter with an isolated, freely convecting vortex, in terms of both the phase and the amplitude of the induced loading peaks. The results presented here suggest that the quality of prediction of the higher harmonic components of the blade airloads might be strongly influenced by the fidelity of the model that is used to represent the aerodynamics of the blades. This contention will be examined in detail in the following Chapters of this dissertation.

Chapter 4

Airload prediction

In this Chapter, the airload as predicted by the Vorticity Transport Model (VTM) is compared to experimental data for the three flight cases of the HART II test – the Baseline (BL) case with conventional control inputs, and the two cases with higher harmonic control inputs applied to the rotor – the so-called Minimum Noise (MN) and Minimum Vibration (MV) cases. In addition, simulations at three different spatial and temporal resolutions are compared to expose the effect of grid resolution on the ability of each of the blade models described in Chapter 3 to predict the airloads on the rotor. In all cases, the rotor was trimmed to the experimental thrust coefficient and to zero aerodynamic pitch and zero roll moments about its hub. During the HART II test programme, the sectional airload, C_N , at 87% of the blade span was estimated by conditionally averaging the signal from a set of pressure transducers mounted at this section of the blade. Computational predictions are compared to the experimental sectional airload at this radial station to expose the ability of the method to capture accurately both the low-frequency and high-frequency components of the blade airload, as described in Sections 4.2.1 and 4.2.2, respectively. It is the high-frequency airload that is of particular interest in the drive to predict accurately the noise that is associated with BVI. The effect on the predicted airload when a representation of the experimental drive enclosure (or fuselage) of the HART II experimental system is included is investigated in Section 4.2.3.

In all the simulations which are described in this dissertation, the elastic deflections of

the rotor blades were prescribed to follow an interpolation of the experimentally measured data. The interpolation which was used is formulated in variable-separable form, as described in Section 2.6. In general, and where it has not been explicitly stated, the interpolation that was used incorporated six basis functions in the radial direction and nine basis functions in the azimuthal direction. The displacements of the blades that result from this interpolation are compared against the raw experimental data in Section 4.1. The sectional airload at 87% of the blade span that is predicted when using this variable-separable interpolation is also compared with a second data synthesis approach (Ref. 1) that is based on a modal analysis of the deformations in Section 4.1.

4.1 Verification of structural dynamics

The raw experimental data for the elastic blade torsion (θ_{el}), flap (Z_{el}) and lag (Y_{el}) deflections measured for the reference blade during the HART II BL flight case are compared in Fig. 4.1 to the interpolation in variable-separable form that is obtained using six radial coefficients and nine coefficients in the azimuthal direction, as described in Section 2.6. The difference between the interpolation and the experimental data set, as shown in part (c) of the figure, is within the stated error bounds on the measurements of $\pm 0.5^\circ$ for the elastic torsion and $\pm 0.5\text{mm}$ for the flap and lag deflections.

Figure 4.2 shows the blade deflection at the 87% radial station, i.e. at the station at which the blade airload was measured in the HART II experiment. This figure shows that the correlation between the experimentally measured motion of the rotor blade, and that prescribed in the numerical simulations using the interpolation in variable-separable form, is extremely good. The main discrepancy occurs in the torsional displacement at about 100° azimuth where the displacement of the blade is marginally over-predicted by the interpolation. This discrepancy between the experimental data and the interpolation is reduced further outboard at the blade tip (Fig. 4.3). As the vortices form at the tips of the blades, the deflection at the tip has the greatest influence on the position of the vortical structures in the wake, as the solution progresses.

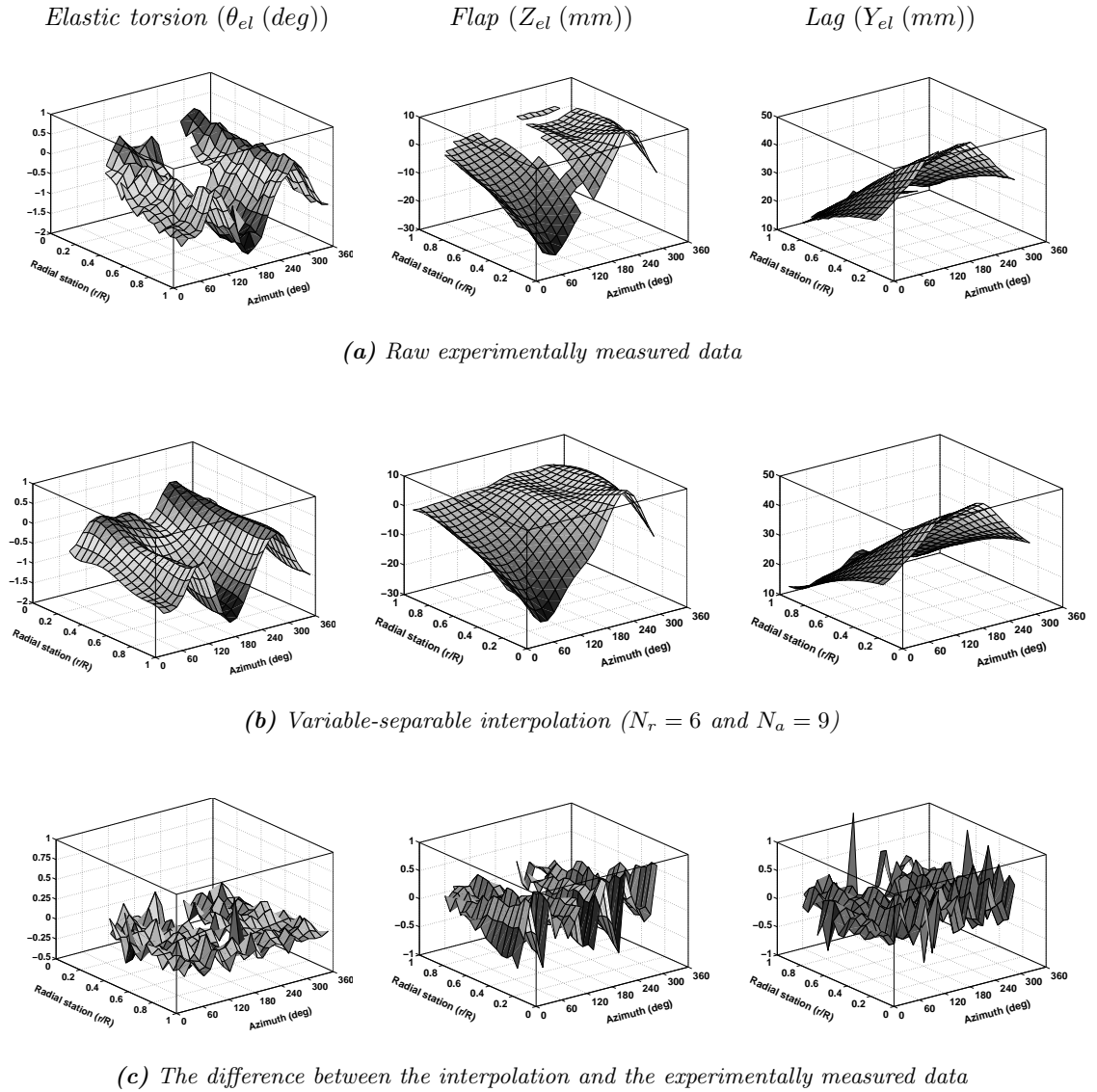


Figure 4.1: Comparison of the interpolated and experimentally measured deflections for the reference blade of the HART II model rotor over a single rotor revolution.

The sensitivity of the calculations to the number of interpolation functions used to capture the structural deflection of the blades was investigated by comparing the airloads that were predicted when using two different interpolations; one which used four azimuthal harmonics (i.e. nine interpolation coefficients in the azimuthal direction) and one which used six azimuthal harmonics (i.e. thirteen interpolation coefficients in the azimuthal direction). The number of coefficients in the radial direction was kept constant at six. Figure 4.4 compares the blade loading at the 87% radial station, for the HART II BL flight case, that was obtained using the two different interpolations. Very little change

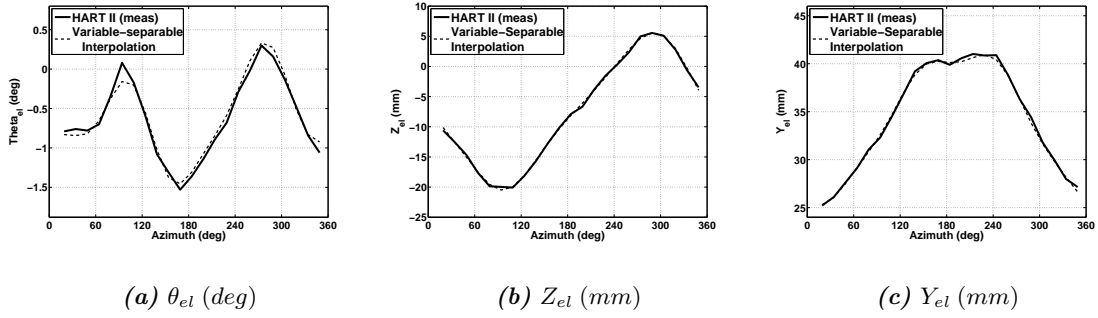


Figure 4.2: Comparison of the interpolated and experimentally measured deflection at 87% span for the reference blade of the HART II model rotor.

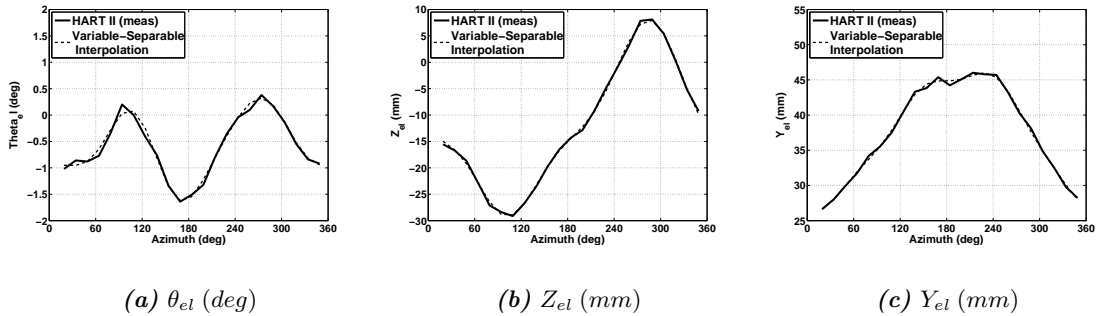
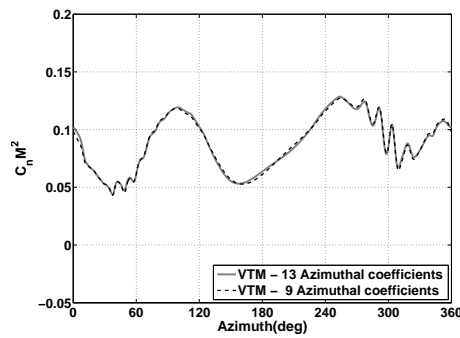


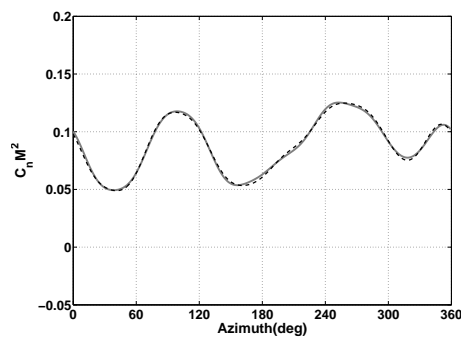
Figure 4.3: Comparison of the interpolated and experimentally measured deflection at the blade tip for the reference blade of the HART II model rotor.

in the predicted airloads is observed when the number of coefficients in the azimuthal direction is increased from nine to thirteen. The greatest effect of changing the number of azimuthal interpolation functions is confined to the higher harmonic component of the loading at the rear of the rotor disc where, in any case, a number of missing markers rendered the accuracy of the interpolation most in doubt (Fig. 4.5). Further investigation revealed that the noise in the modelled structural deformations of the blades, that the interpolation process was designed to eliminate, increased significantly, with an associated reduction in the quality of predictions, if the number of azimuthal harmonics included in the interpolation was increased beyond six.

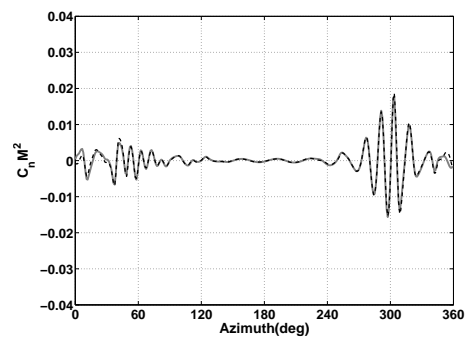
A prescription of the blade dynamics was also generated using the data synthesis method described by van der Wall in Ref. 1, where reconstruction of the blade dynamics is based on a best fit to the lowest pre-computed mode shapes for the structural deformation of the



(a) Full signal

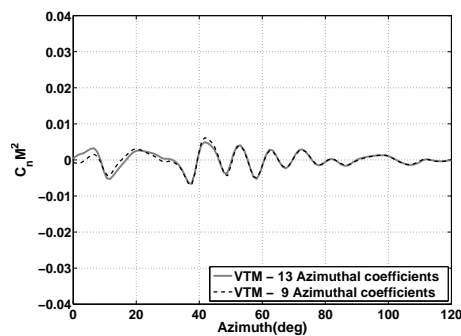


(b) Signal filtered to include only lower harmonic components (0-10th harmonic)

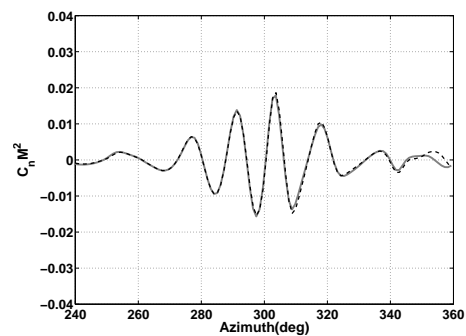


(c) Signal filtered to include only higher harmonic components (>10th harmonic)

Figure 4.4: Prediction of the blade loading ($C_N M^2$) at 87% span (BL case, with six coefficients in the radial direction and varying numbers of coefficients in the azimuthal direction).

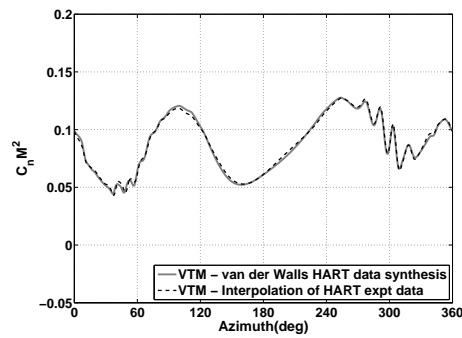


(a) Advancing side of the disc

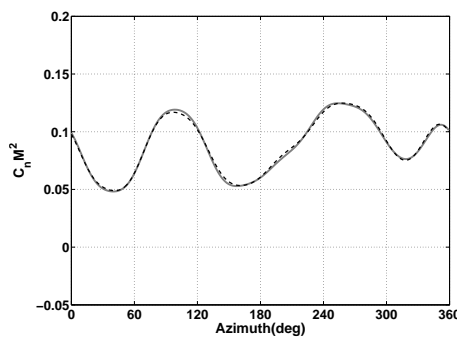


(b) Retreating side of the disc

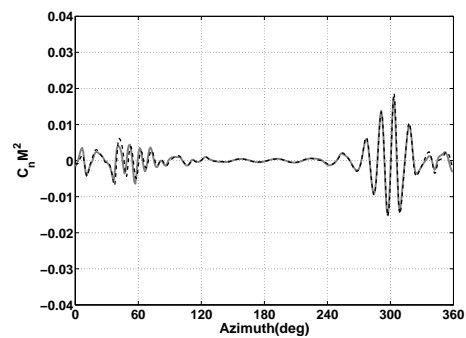
Figure 4.5: Prediction of the blade loading ($C_N M^2$) at 87% span (BL case, with six coefficients in the radial direction and varying numbers of coefficients in the azimuthal direction, signal filtered to include only higher harmonic components, greater than 10/rev).



(a) Full signal

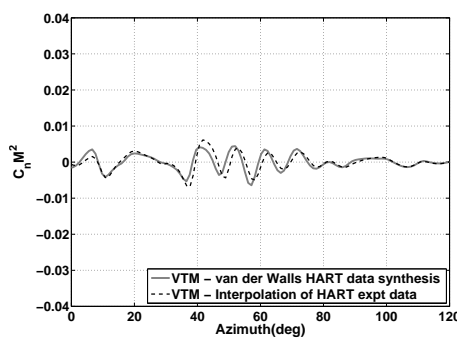


(b) Signal filtered to include only lower harmonic components (0-10th harmonic)

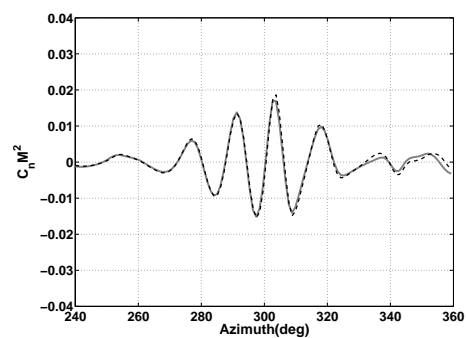


(c) Signal filtered to include only higher harmonic components (>10th harmonic)

Figure 4.6: Prediction of the blade loading ($C_N M^2$) at 87% span (BL case, comparison of predictions using van der Wall's synthesised blade deflections (Ref. 1) and variable-separable interpolation on the HART II experimental data).



(a) Advancing side



(b) Retreating side

Figure 4.7: Prediction of the blade loading ($C_N M^2$) at 87% span (BL case, comparison of predictions using van der Wall's synthesised blade deflections (Ref. 1) and variable-separable interpolation on the HART II experimental data, signal filtered to include only higher harmonic components, greater than 10/rev).

blades. Using this approach, the mode shapes for flap, lag and torsion are first obtained from a finite element method. These mode shapes are then represented in the radial direction using polynomials of up to 7th order. Fourier series for the azimuthal variation of the amplitudes of each of the modes are then determined by enforcing a least squares fit to the experimental data. The advantage of this approach is that the physical boundary conditions are explicitly applied. Figure 4.6 compares the airload at the 87% radial station of the HART II blade that is predicted by the VTM when using van der Wall's interpolation and when using the variable-separable interpolation described above. The predictions of the lower harmonic content of the loading signal (Fig. 4.6(b)) are virtually indistinguishable. The largest differences are found at the rear of the rotor disc ($\psi = 350^\circ$ to 10°) in the higher harmonic signal (Fig. 4.7), where a slight change in the phase of the BVI impulses on the advancing side of the rotor disc is the most noticeable difference between the two sets of results. The similarity between the predictions that are obtained using the two different methods lends support to the validity of the variable-separable interpolation that is used in all the simulations presented in the following Sections of this dissertation.

4.2 Predictions of the HART II blade airload

Figure 4.8 shows the predicted non-dimensionalised normal force coefficient ($C_N M^2$) for the HART II BL case, plotted as a series of contours over the rotor disc. The airload predicted by the VTM at each of the three different resolutions of the flow-field defined in Table 4.1, and using the lifting-line and lifting-chord models for the blades are compared. The blade vortex interactions are visible in the contour maps as thin ridges of relatively high loading towards the rear of the disc, in the first and fourth quadrants of the rotor. The interactions are strongest outboard towards the blade tips, particularly on the retreating side of the disc. Where the lifting-line approach is used, an increase in grid resolution results in a marked increase in the amplitude of the BVI peaks and the associated loading gradients become significantly steeper. In contrast, the lifting-chord approach shows much less sensitivity to the size of the computational cells. This difference in the relative

sensitivity of each of the blade models to changes in the resolution of the computational grid is discussed in more detail in Section 4.2.2.

Table 4.1: *Computational resolution*

	size of smallest cells		timesteps per rotor revolution	degrees per timestep
coarse	R/55.5	c/3.36	350	1.03°
medium	R/83.3	c/5.04	525	0.69°
fine	R/125.0	c/7.56	800	0.45°

Similar contours of the non-dimensionalised normal force coefficient for all three flight cases of the HART II test are shown in Fig. 4.9. In the BL case, the contours of highest loading occur in a relatively even band across the front of the disc. The loading in this band is higher in the MN case than in the BL case and is less even, with peaks in loading further outboard on the disc, towards the advancing and retreating sides. In the MV case the peaks in the overall loading are shifted further forward on the retreating side and further aft on the advancing side of the disc when compared to the MN case. The changes in the location on the rotor disc where the BVI events occur with the addition of HHC are also apparent in these plots and are discussed in more detail in the next Section of this Chapter.

The measured blade airload at the 87% radial station for the three HART II flight cases, expressed in terms of non-dimensionalised normal force coefficient ($C_N M^2$), are compared in Fig. 4.10 to the loading predicted by the VTM. In general, the calculated loading at this radial station compares well with the experimental data for all flight cases. The advancing side is perhaps the least well resolved, with the largest discrepancies between prediction and experiment on this side of the disc occurring in the low-frequency component of the airload. The predictions of the loading on the retreating side of the disc correlate well with the experimental data for all three flight cases. The figures show nevertheless that the lifting-line method is more sensitive than the lifting-chord approach to changes in the cell size that is used to represent the wake.

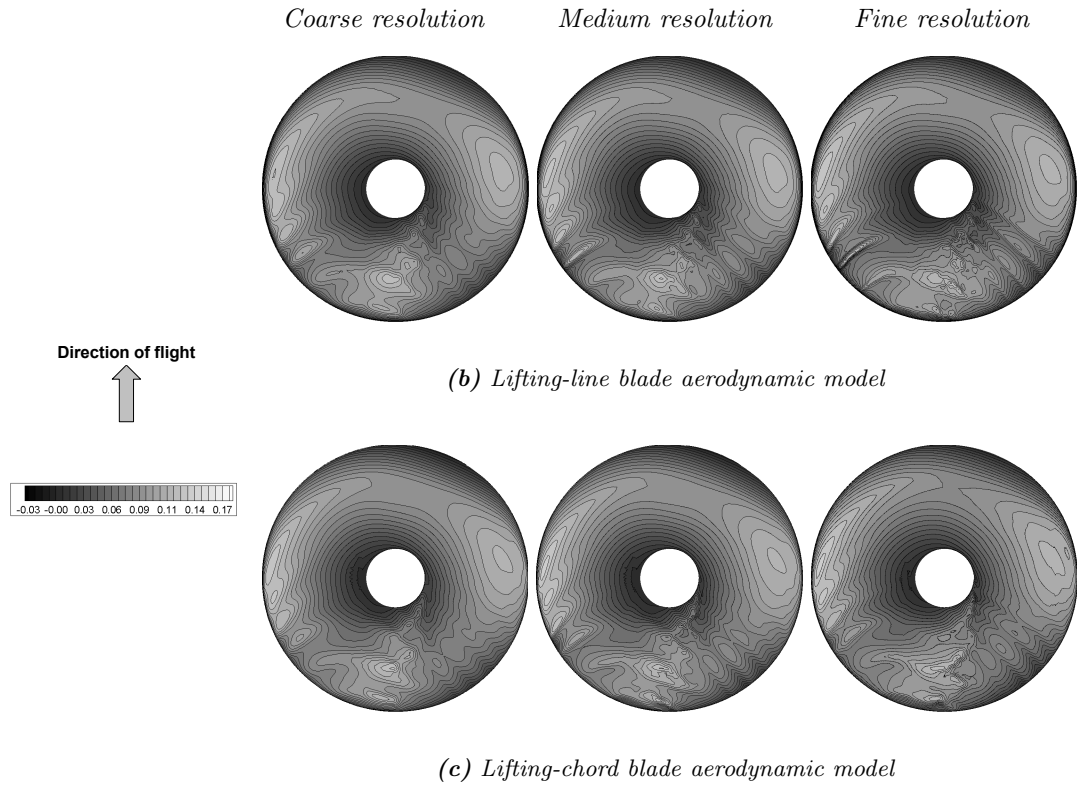


Figure 4.8: *Contours of non-dimensional lift ($C_N M^2$) as predicted by the VTM at various computational resolutions using the lifting-line and the lifting-chord representations of the blade aerodynamics, for the HART II BL case. (A representation of the drive enclosure has not been included in the calculations).*

4.2.1 Low-frequency component of airload

Figure 4.11 shows the non-dimensionalised normal force coefficient ($C_N M^2$) for all three flight cases, after filtering at ten per rotor revolution to separate out the low-frequency component of the signal. These figures illustrate clearly that in all three flight cases the major differences between the experimental data and the numerically predicted lift for the low-frequency component of the signal lie mainly to the advancing side of the disc between 0° and 120° azimuth. The discrepancies in this component of the airload are similar regardless of computational resolution and also irrespective of the model that is used to represent the aerodynamics of the blade. Several reasons for the observed discrepancies can be postulated. Incorrect prediction of the strength of the vorticity trailed from the roots of the blades might, for instance, adversely affect predictions of the flow, and hence the loading experienced by the blades as they pass near the rear of the disc. A parametric study has shown, however, that there is very little qualitative improvement in the blade

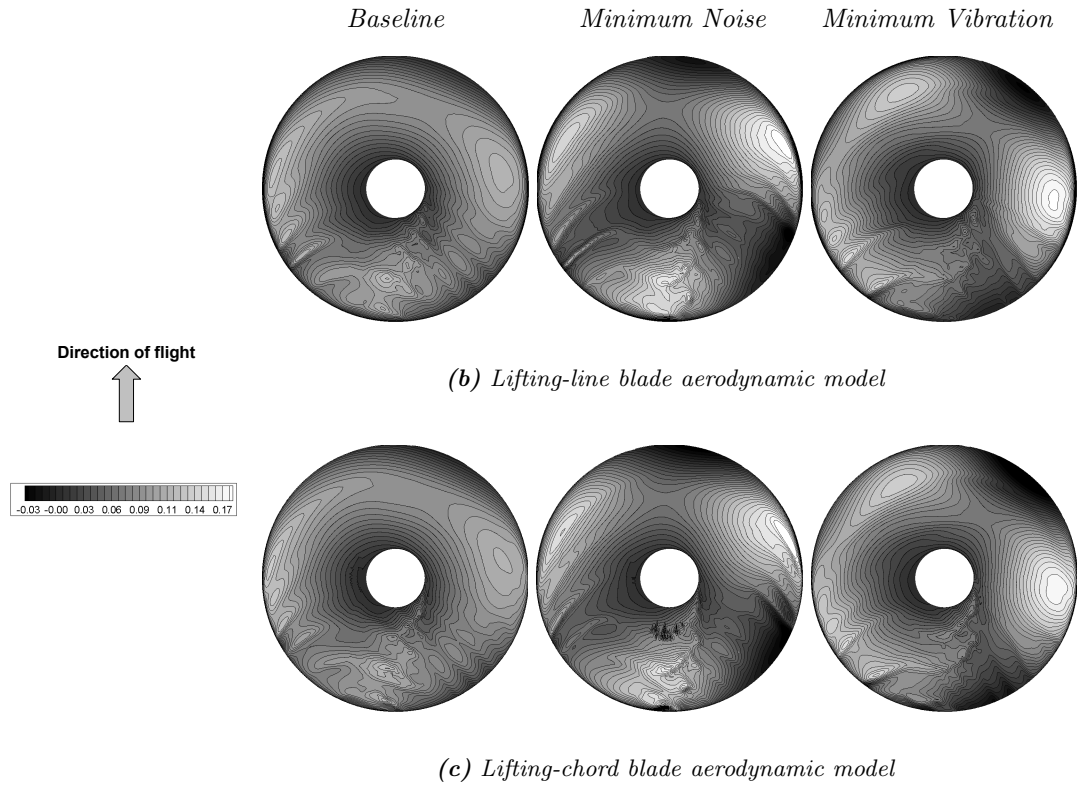


Figure 4.9: *Contours of non-dimensional lift ($C_N M^2$) as predicted by the VTM at the medium computational resolution using the lifting-line and the lifting-chord representations of the blade aerodynamics, for all three HART II flight cases. (A representation of the drive enclosure has not been included in the calculations).*

loading obtained by varying the boundary condition that is applied at the root of the blade and hence to the strength of the vortices emanating from there (Figs. 4.12 and 4.13).

An additional factor that should be considered is that the loading distribution on the advancing side of the HART II rotor under the experimental conditions is quite unusual in being almost uniformly spread along the length of the blade. This yields a sheet of trailed vorticity behind the blade that is relatively weak and thus takes some time to roll-up to form a coherent tip vortex. The vortical structure of the wake of the HART II rotor is predicted very accurately by the VTM, hence the contribution of any inaccuracy in prediction of this roll-up process to the observed errors in blade loading is, at most, very subtle (see Chapter 5 for further discussion of the wake structure and the roll-up process).

As it is this component of the loading that is primarily affected by control inputs and blade

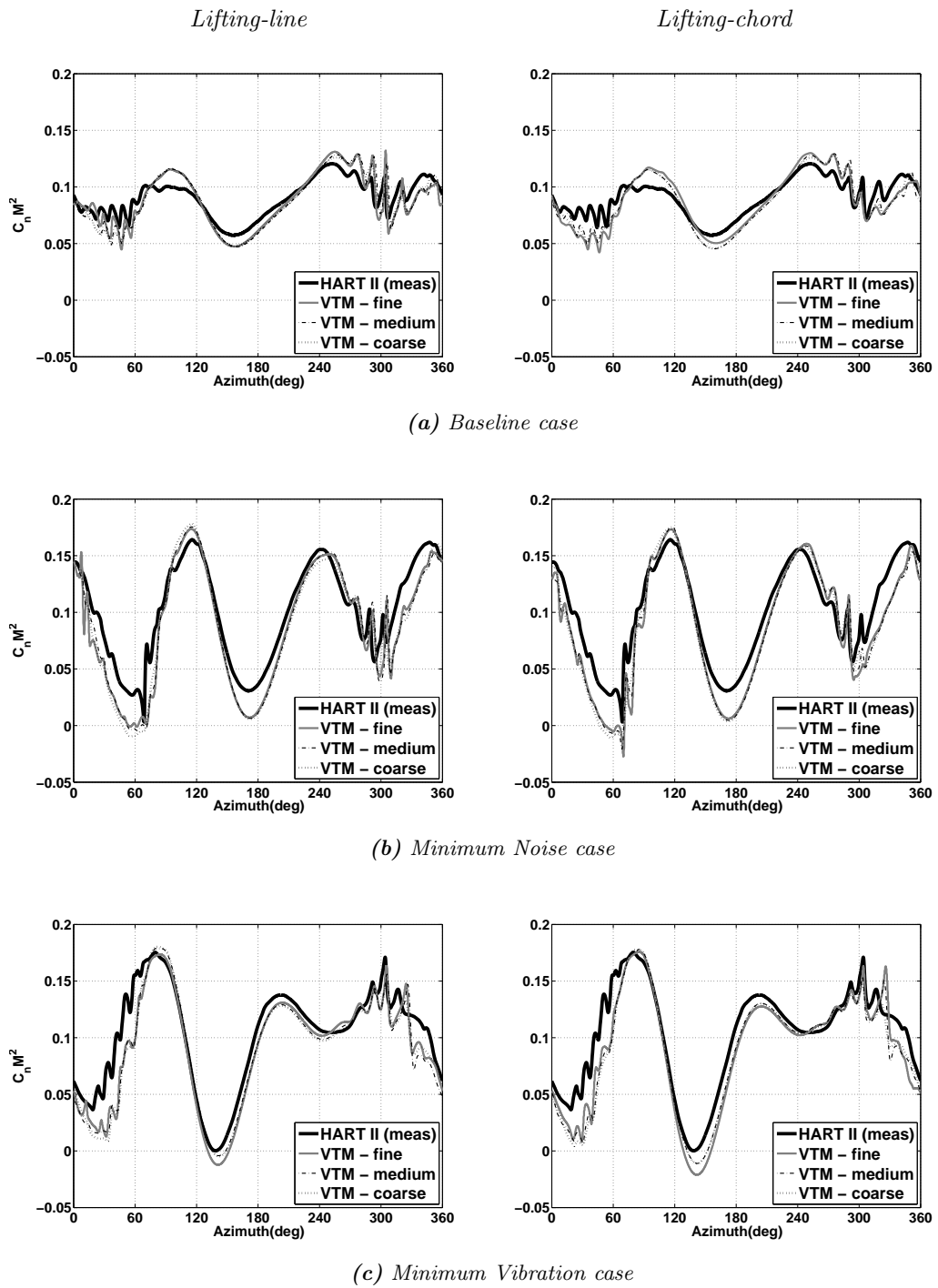


Figure 4.10: Comparison of blade loading ($C_N M^2$) at 87% span, as predicted using lifting-line and lifting-chord representations of the blade aerodynamics, against experimental data for all three HART II flight cases. (A representation of the drive enclosure has not been included in the calculations).

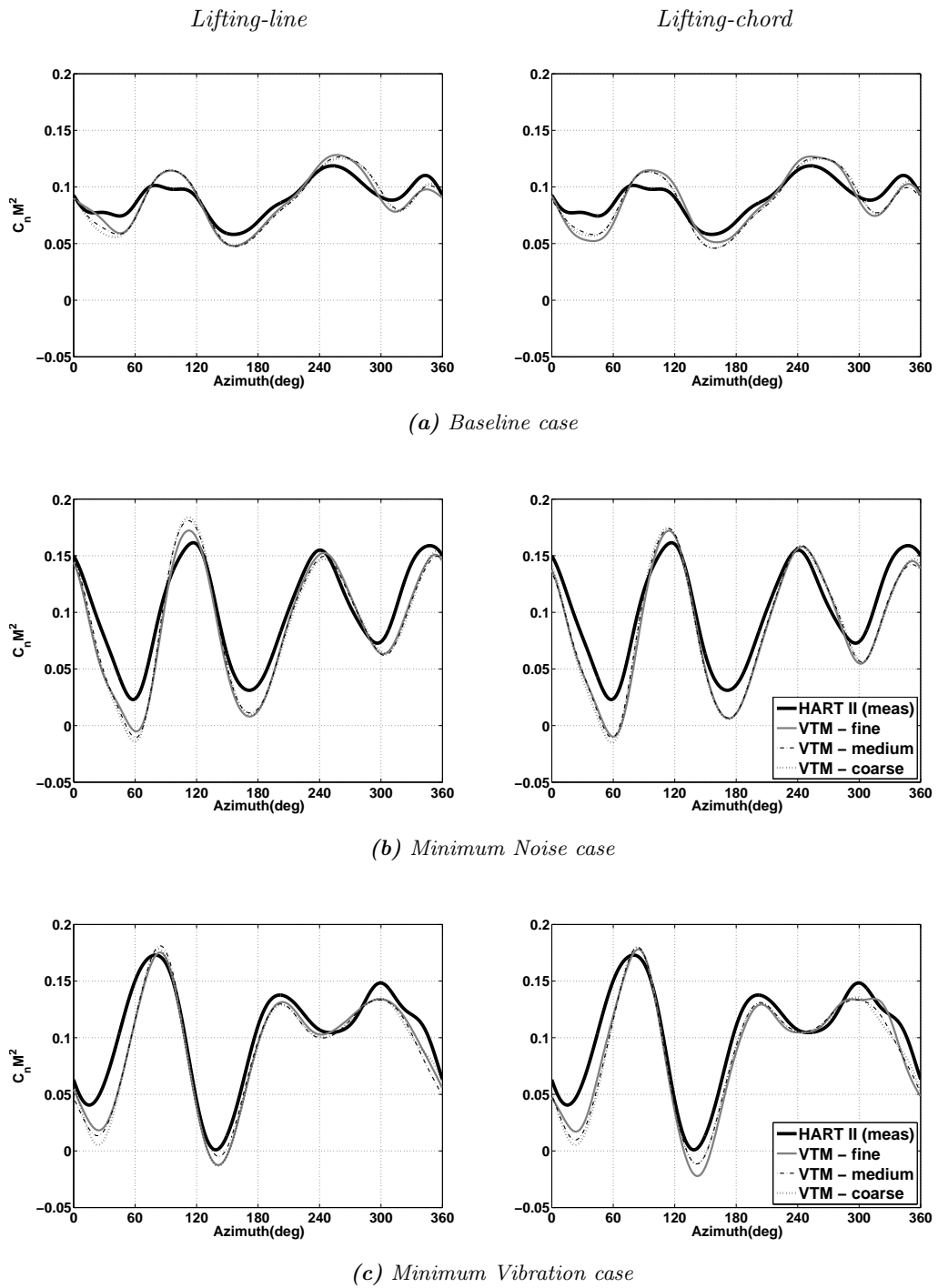
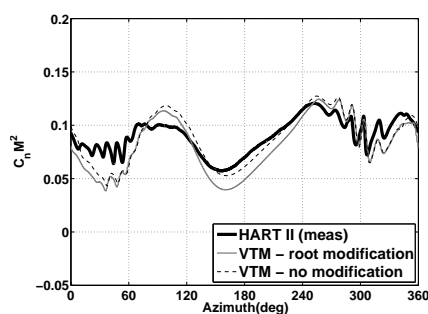
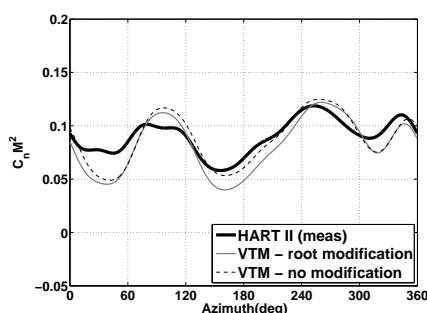


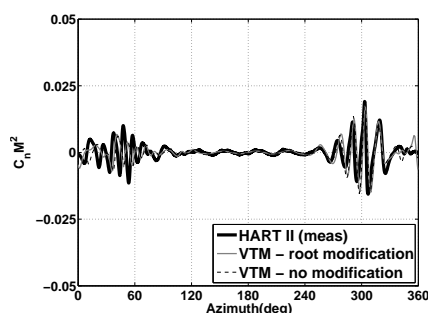
Figure 4.11: Comparison of blade loading ($C_N M^2$) at 87% span, as predicted using lifting-line and lifting-chord representations of the blade aerodynamics, against experimental data for all three HART II flight cases. (A representation of the drive enclosure has not been included in the calculations).



(a) Full signal



(b) Signal filtered to include only lower harmonic components (0-10th harmonic)



(c) Signal filtered to include only higher harmonic components (>10th harmonic)

Figure 4.12: Comparison of blade loading ($C_N M^2$) at 87% span, as predicted using lifting-line representation of the blade aerodynamics, with and without a representation of the blade area between the hub and the root cut-out. (A representation of the drive enclosure has not been included in the calculations).

structural deformation, it is most likely that the observed discrepancies in the prediction of low-frequency component of the blade loading are due to errors in the interpolation that was used to prescribe the blade dynamics within the simulation. Indeed, it is suggestive that the most significant discrepancies between the experimental data for the torsional deformation of the blades and the interpolation used in the simulation coincide rather closely with those regions of the advancing side of the rotor where the loading on the blade is least accurately predicted. The missing experimental data for the structural deformation of the blades around 0° and 180° azimuth may have had a particularly strong effect on the quality of the structural model on those regions of the advancing side of the rotor that are most strongly influenced by BVI. This explanation is supported by the calculations of Boyd (Ref. 37) and Lim and Strawn (Ref. 38), where a coupled CSD/CFD

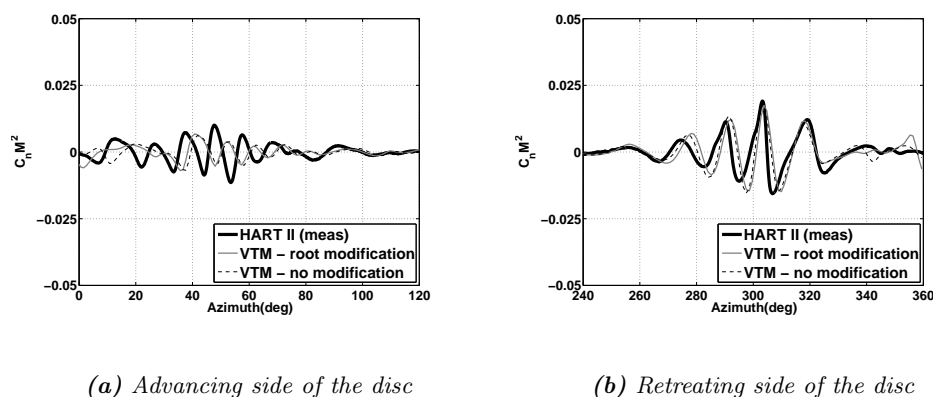


Figure 4.13: Comparison of blade loading ($C_N M^2$) at 87% span, as predicted using lifting-line representation of the blade aerodynamics, with and without a representation of the blade area between the hub and the root cut-out. The signal has been filtered to include only higher harmonic components, greater than 10/rev. (A representation of the drive enclosure has not been included in the calculations).

approach was used to substitute a numerical analysis of the structural dynamics of the rotor blades for the prescribed structural deflections used here. Their simulations yield particularly good correlations with experimental data for the low-frequency component of the blade airload.

4.2.2 High-frequency component of airload

The high-frequency component of the blade airload is almost exclusively due to the localised interactions between the rotor blades and the vortices within the rotor wake. In Fig. 4.14, the contours of the predicted non-dimensionalised normal force coefficient ($C_N M^2$) have been filtered to include only the high-frequency components of the signal, i.e. those greater than ten per rotor revolution, to expose in greater detail the distribution of these BVI events across the rotor disc.

This figure illustrates the effect of HHC inputs on the position and strength of the BVIs. In the BL case, in which no higher harmonic control is applied, the BVI loading peaks are located outboard on the rotor disc and towards its rear, i.e. in quadrants one and four. The interactions on the retreating side of the disc are stronger as the interacting vortices are orientated more nearly parallel to the blade than on the advancing side (see Chapter 5). In comparison to the BL case, the BVI events in the MN case, particularly

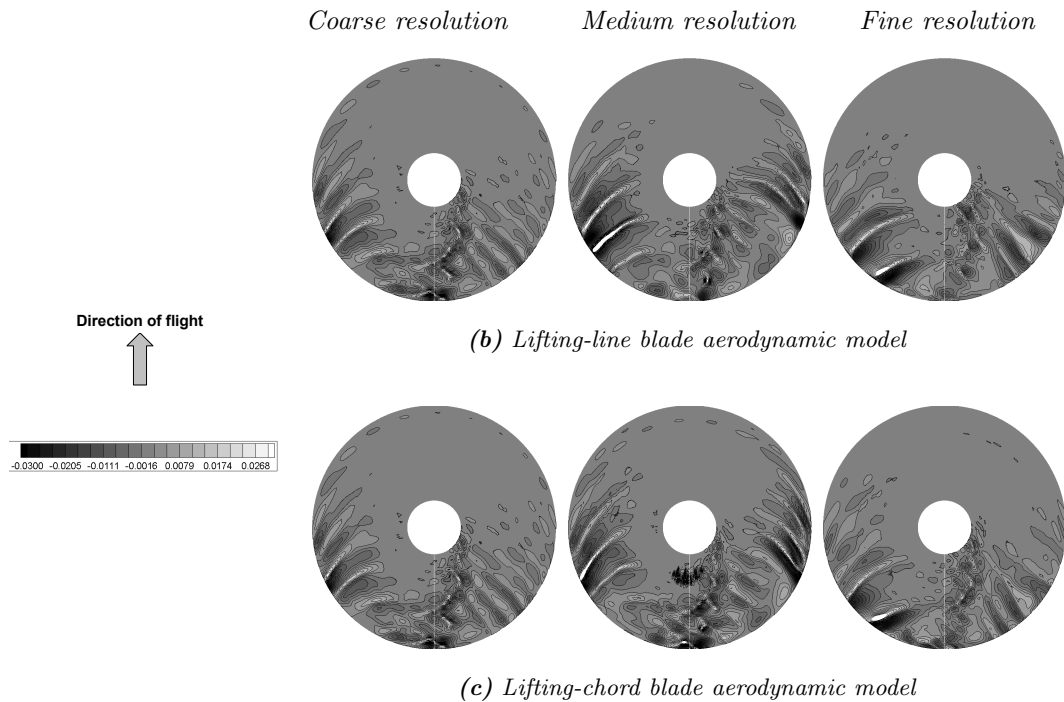


Figure 4.14: *Contours of non-dimensional lift ($C_N M^2$) as predicted by the VTM at the medium computational resolution using the lifting-line and the lifting-chord representations of the blade aerodynamics. The signal has been filtered to include only the higher harmonic components, greater than 10/rev. (A representation of the drive enclosure has not been included in the calculations).*

within the first quadrant on the advancing side of the rotor, are located significantly more inboard. Since the Mach number of the blade increases towards the tip, those interactions which occur inboard take place at lower Mach numbers. Moreover, the tip vortices pass close to the disc further forward than in the BL case (again see Chapter 5), and thus the area of the disc over which the BVI events occur extends further forward. On the retreating side, again the BVIs occur further forward in the MN case than in the BL case and, as a result, the interacting vortices are no longer orientated parallel to the blade. Both the reduction in Mach number where the interactions take place and the change in orientation of the interaction reduce the amount of noise that is radiated towards the ground, as will be shown in Chapter 6.

In the MV case, the azimuthal locations of the BVI events remain similar to those of the BL case on both the advancing and retreating sides of the rotor but the associated loading peaks are shifted more outboard towards the blade tips. The higher Mach numbers asso-

ciated with these interactions produce an increase in the noise radiation from both sides of the disc (see Chapter 6). The trends observed in the VTM calculations are comparable to those obtained by plotting the experimentally measured pressure along the leading edge of the blade for the three HART II flight cases (Refs. 31,32). The computations also reveal the presence of relatively strong interactions with the root-vortex system that is produced by the blades. These interactions are not apparent in the experimental data, however, and may be an artifact of the omission of any representation of the rotor hub assembly from the calculations.

Figures 4.15-4.17 show the non-dimensionalised normal force coefficient ($C_N M^2$) for the 87% radial station, at which pressure measurements were gathered during the HART II test, after it has been filtered to contain only the high-frequency component (i.e. that induced by the interactions between the blades and the vortices in the wake) of the loading. In these figures, the BVI-induced loading fields on the retreating and advancing sides of the rotor have been produced with expanded azimuthal scale to aid their interpretation.

For each of the flight cases, the numerical representation of the BVI events on the retreating side of the rotor is generally satisfactory, apart from a rather gross misrepresentation of the amplitude and position of the furthest-aft BVI in the MV case. In addition, the predicted amplitude of this loading peak is very sensitive to the cell size used in the simulation. Indeed, the differences in the grid-sensitivity of the two blade aerodynamic models in their prediction of the BVI-induced loading are most obvious on this side of the disc.

As the grid resolution is increased, the amplitudes of the peaks in the BVI-induced loading on the blade that are predicted by the lifting-line model increase markedly, resulting in a gross over-prediction in amplitude of the BVI-loading peaks at the finest computational resolution. As alluded to in Section 3.2.3, the deficiencies in prediction of the BVI-induced airloads when the lifting-line model is used are due to the misrepresentation of the aerodynamic response of the blade when subjected to the very localised perturbations in its aerodynamic environment that are characteristic of helicopter blade vortex interactions. This characteristic can be explained further in terms of the relative sensitivity of each of the blade aerodynamic models to the details of the velocity profile that is induced at the

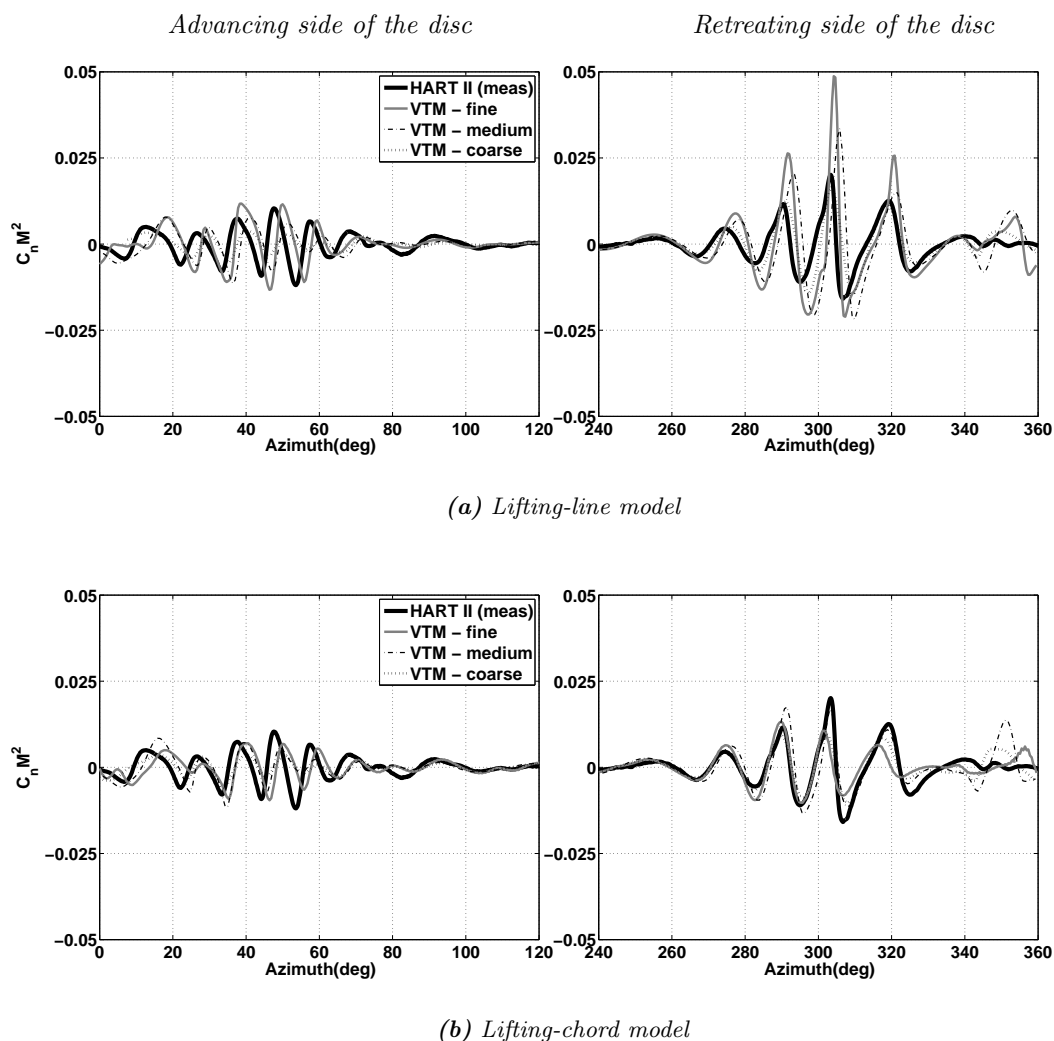


Figure 4.15: Comparison of blade loading ($C_N M^2$) at 87% span, as predicted using lifting-line and lifting-chord representations of the blade aerodynamics, against experimental data for the HART II BL case. The signal has been filtered to include only higher harmonic components, greater than 10/rev. (A representation of the drive enclosure has not been included in the calculations).

blade by the interacting vortex. As the grid is refined within the VTM, the vorticity that is associated with any particular vortex is confined to fewer cells. This results in a velocity profile for the vortex that becomes more spiky as the size of the computational cells that are used to resolve the flow are reduced. With its single-point boundary condition (see Section 3.1.1), the lifting-line model is overly sensitive to the maxima and minima within the velocity field that is encountered by the blade. In contrast, the lifting-chord model, forced as it is by the (weighted) integral of the velocity along the entire chord of the blade, is much less responsive to the detail contained within the velocity field and is instead

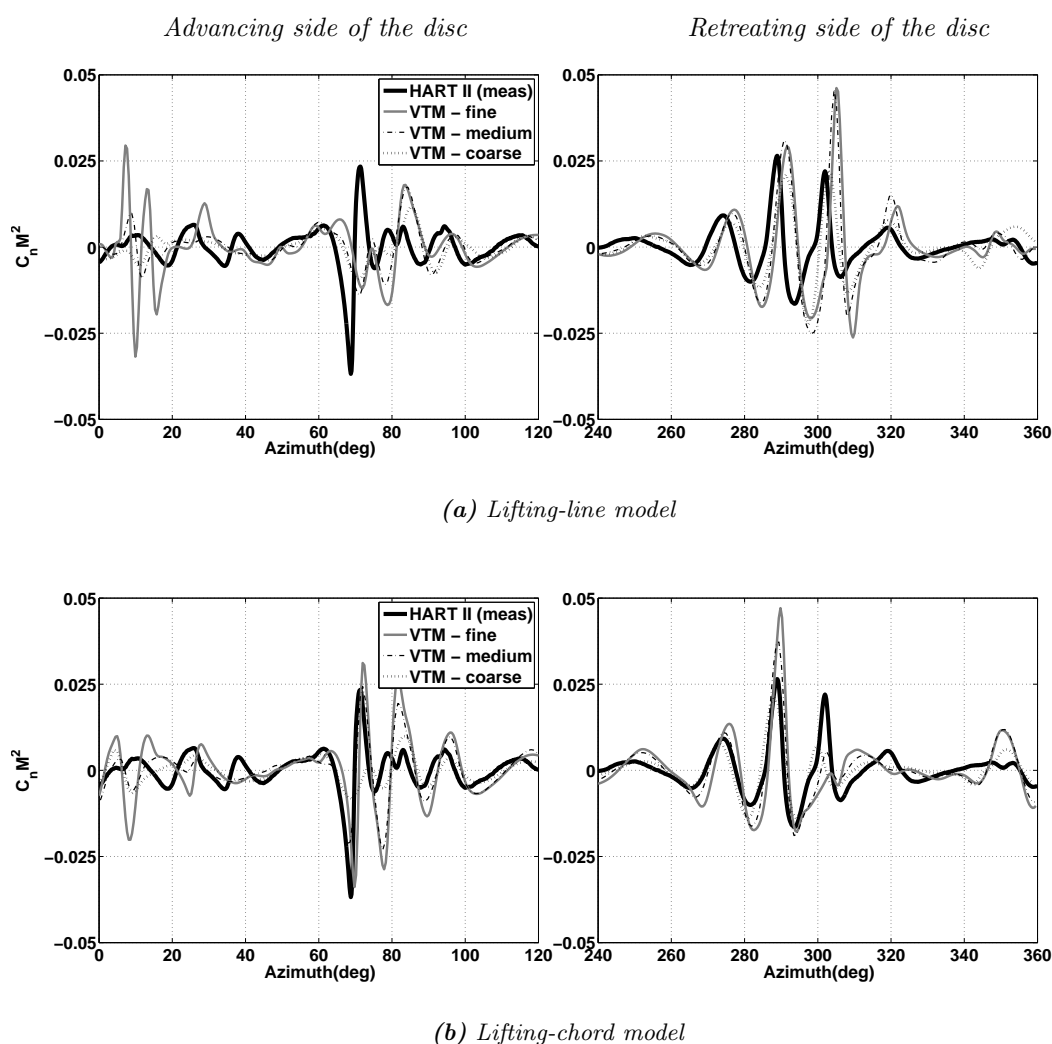


Figure 4.16: Comparison of blade loading ($C_N M^2$) at 87% span, as predicted using lifting-line and lifting-chord representations of the blade aerodynamics, against experimental data for the HART II MN case. The signal has been filtered to include only higher harmonic components, greater than 10/rev. (A representation of the drive enclosure has not been included in the calculations).

more heavily influenced by the invariant, integral properties of the flow-field such as its circulation or net vorticity.

In general, on the retreating side of the disc, a marked improvement in the accuracy of the predicted high-frequency airloads of the HART II rotor is obtained when the lifting-chord model for the blade aerodynamics is used instead of the lifting-line type approach. The advancing side of the disc presents a somewhat more confusing picture, however. For all three flight cases, all the BVIs on this side of the rotor are captured by the numerics, but there are errors in the phasing and amplitude of the BVI-induced loading peaks in

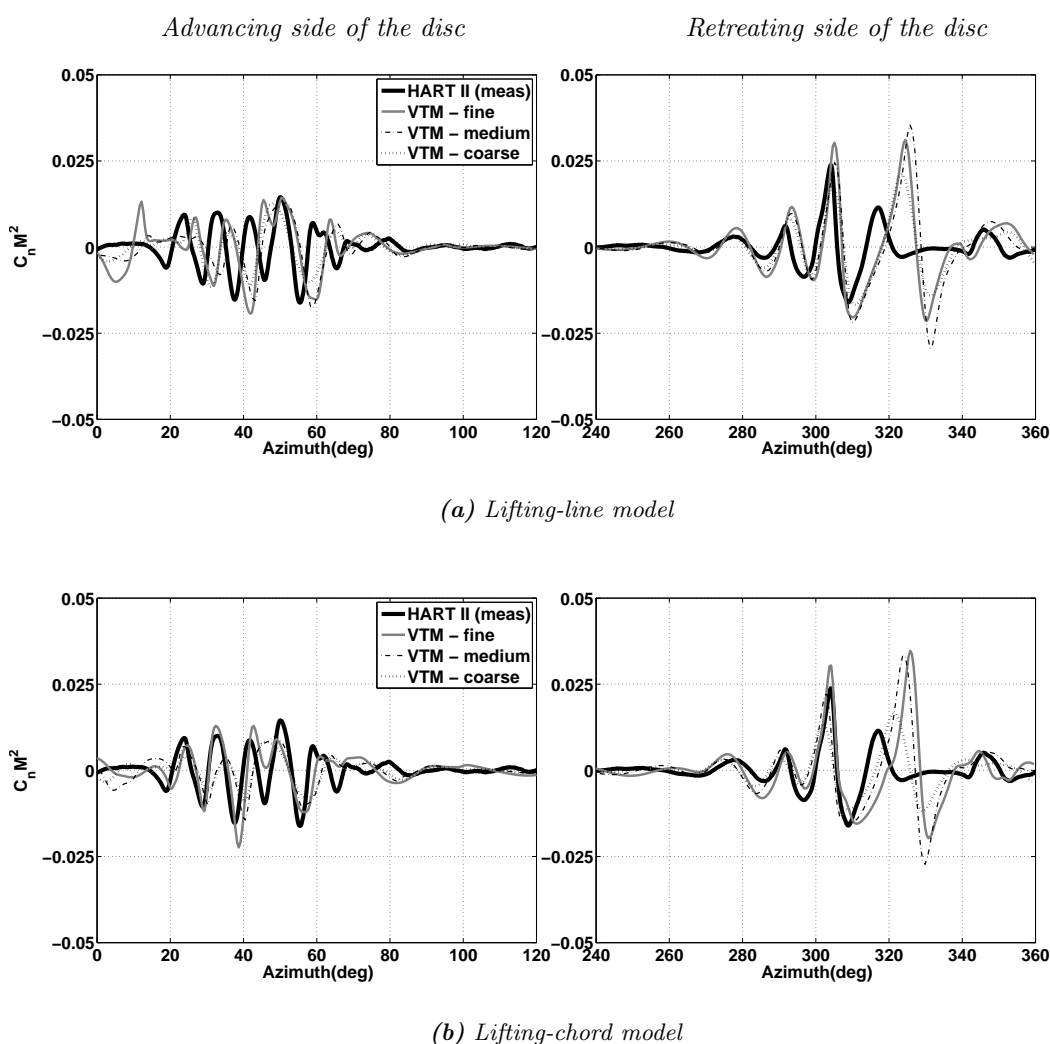


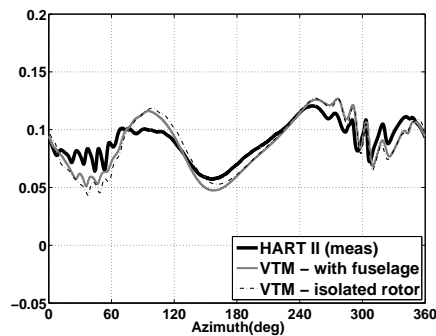
Figure 4.17: Comparison of blade loading ($C_N M^2$) at 87% span, as predicted using lifting-line and lifting-chord representations of the blade aerodynamics, against experimental data for the HART II MV case. The signal has been filtered to include only higher harmonic components, greater than 10/rev. (A representation of the drive enclosure has not been included in the calculations).

almost all cases. The MN and MV cases (Figs. 4.16 and 4.17, respectively) show somewhat greater discrepancy between the predictions and the experimental data than the BL case.

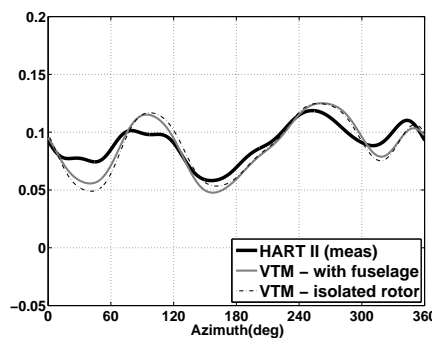
In the BL case there is generally good agreement between measurement and prediction, but the strongest BVI event on the advancing side of the disc is slightly misrepresented in phase by the numerical method. In the measured signal the loading peak with the largest amplitude occurs at approximately 50° azimuth. In contrast, the numerical calculations using coarse or medium grid resolutions predict the BVI event that occurs at an azimuth of 40° to be marginally stronger than the BVI at 50° . The predicted loading intensity is thus

shifted towards the rear of the disc compared to experiment. At the finest computational resolution, the difference in magnitude between each of these two BVI impulses is minimal, however. It is believed that this sensitivity in the relative strength of these BVIs to the computational resolution has a strong influence on the predicted position of the acoustic maximum on the advancing side of the disc, as will be discussed in Chapter 6.

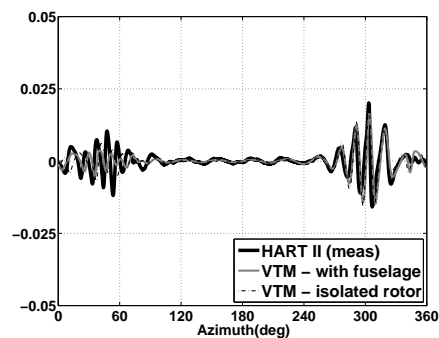
In the MN case, the most intense BVI impulse, at an azimuth of 70° on the advancing side, is under-predicted in amplitude when the lifting-line model is used, regardless of the resolution of the flow-field. In contrast, as the grid resolution is increased the lifting-chord model very accurately captures this particular loading peak. This is discussed further in Section 5.1.1.



(a) Full signal



(b) Signal filtered to include only lower harmonic components (0-10th harmonic)



(c) Signal filtered to include only higher harmonic components (>10th harmonic)

Figure 4.18: Comparison of blade loading ($C_N M^2$) at 87% span, as predicted using the lifting-line representation of the blade aerodynamics, against experimental data for all three HART II flight cases, with and without a representation of the drive enclosure (fuselage) included in the calculations.

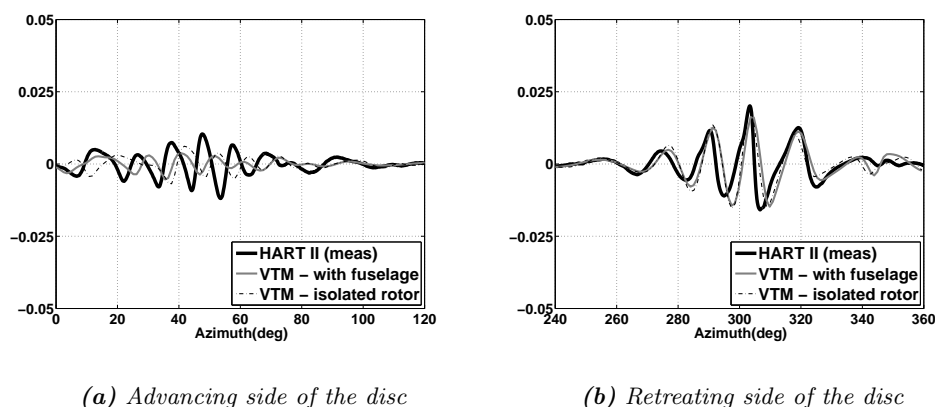


Figure 4.19: Comparison of blade loading ($C_N M^2$) at 87% span, as predicted using the lifting-line representation of the blade aerodynamics, against experimental data for all three HART II flight cases, with and without a representation of the drive enclosure (fuselage) included in the calculations. The signal has been filtered to include only higher harmonic components, greater than 10/rev.

4.2.3 Effect of including a representation of the drive enclosure

The effect on the blade loading of including a representation of the rotor drive enclosure within the computations was investigated for the HART II BL case. The results of simulations with and without the drive enclosure present are compared in Figs. 4.18 and 4.19. In all cases the presence of the drive enclosure has minimal effect on the lower harmonic component of the loading, however. Including a representation of the drive enclosure does, in some cases, reduce to a small extent the phase shift between the experimental data and the computational results for the BVI-induced loading on the advancing side of the rotor disc. The predicted blade loading does thus show a measurable sensitivity to rather subtle changes in the structure of the wake. The vortex positions are shifted by the presence of the fuselage although the changes are not enough to have a major affect the blade loading.

4.3 Summary

The airload predicted by the VTM for all three HART II flight cases compares very favourably with the experimentally measured airloads at the 87% radial station. On the retreating side of the rotor, all BVI events discernible in the experimental data are

reproduced by the numerics, usually with the correct phase. Generally, on the advancing side of the rotor, the numerical resolution of the BVI-induced loads is less accurate both in amplitude and phase, yet all BVIs seen in the experimental data are still captured. For the MN and MV cases, both blade models have been shown to capture accurately the shifts in position of the BVI events on the rotor that result from the application of HHC. The regions where the prediction of the low-frequency component of the airload (principally influenced by control inputs and blade dynamics) is less accurately, coincide with the regions of the rotor in which deficiencies in the prediction of the BVI-induced airload are also encountered. This suggests that a small error in the prescription of the blade dynamics is a contributing factor to the observed discrepancies between numerics and experiment.

Calculations at three computational resolutions were used to expose the effect of grid resolution on the quality of predictions. Where the lifting-line model was used to represent the aerodynamics of the blades, the predicted high-frequency, BVI-induced component of the loading is found to be extremely sensitive to the cell size that was used in the computations. The predicted amplitude of the BVI-induced features in the loading on the blades increases significantly as the cell size that is used to resolve the wake is reduced. A marked improvement in the accuracy of the predicted high-frequency airloads of the HART II rotor is obtained when a lifting-chord model for the blade aerodynamics is used instead of the lifting-line type approach. Errors in the amplitude and phase of the BVI-loading peaks are reduced and the quality of the prediction is affected to a lesser extent by the computational resolution. In particular, the over-prediction of the amplitude of the BVI events, which occurs on the retreating side of the disc as the resolution of the computation is increased when using the lifting-line model, is avoided.

The predicted blade loading shows a sensitivity to the subtle changes in the structure of the wake, caused either by the inclusion of a fuselage in the computation or by the small changes in the vorticity distribution that is sourced in the flow behind the blade, when different blade aerodynamic models are used.

The insensitivity of the lifting-chord model to the resolution of the computation can be

explained in terms of its reduced sensitivity to the localised, small-scale features of the flow-field and the dependence of its predictions rather on the integral, invariant properties of the flow-field. In the context of helicopter BVI, the primary advantage of this approach would thus appear to be the possibility that it offers of true numerical convergence of predictions as the resolution of the computational grid is increased. This will be investigated further, however, at the time of writing the computational facilities available were not yet adequate to test this hypothesis further.

Chapter 5

Wake geometry

The results presented in Chapter 4 have shown that the Vorticity Transport Model is able to predict accurately the high-frequency fluctuations in loading that are induced by BVIs on the rotor disc. This Chapter, through a qualitative and quantitative analysis of the geometry of the wake, aims to confirm that this is due to the ability of the method to represent accurately the wake that is produced by the rotating blades. Accurate prediction of the amplitude and phasing of the loading perturbations on the rotor that are induced by the blade-vortex interactions is critically dependent upon the correct simulation of the geometry and strength of the vortical structures within the rotor wake. As the aerodynamic environment in which a rotor operates is extremely complex, the modelling of the evolution of the vortices within the wake, in terms particularly of their correct position and strength over time, is somewhat challenging.

The principal discrepancies in airload prediction described in Chapter 4 were confined almost exclusively to the rear of the advancing side of the rotor. If errors in reproducing the deflections of the blades could be discounted, these were thought to be due to minor inaccuracies in modelling the development of the rotor wake, particularly the roll-up of the vortex sheet immediately behind the blades to form the tip vortices on the advancing side of the rotor disc. In this Chapter, the possible origins of these deficiencies are examined by comparing the vortex geometry and vortex core characteristics predicted by the VTM to those recorded during the HART II rotor test.

A three-component Particle Image Velocimetry (3C-PIV) technique (Ref. 84) was used in the HART II test programme to give instantaneous measurements of the velocity field contained within a series of highly-resolved observation areas, near to the rotor. These observation areas were located along five longitudinal slices through the flow between $Y/R = 0.4$ and $Y/R = 0.97$ as indicated in Fig. 5.1. The size of each observation area and the spatial resolution of the flow within it could be varied by using two differing systems, each with different lenses. Global flow analysis over a wide area was carried out using a lower spatial resolution and more detailed, smaller areas surrounding the vortex cores were investigated at a higher resolution. The main advantage of the 3C-PIV method that was used in the HART II test was that it allowed rapid, accurate measurements of the flow-field especially when compared with the Laser Doppler Velocimetry (LDV) method used in the earlier HART I test. The 3C-PIV measurements that were gathered have been post-processed to estimate the core size, position and circulation of the blade tip vortices as the wake ages and is convected downstream of the rotor. The positions of the vortex centres were estimated from the simple average of approximately 100 PIV images of size 0.45m by 0.38m ($0.225R$ by $0.19R$) as described in Ref. 85. This data can be used efficiently to investigate the ability of the VTM to resolve accurately the details of the wake. In particular, the trajectories of the individual tip vortices as they are convected back and through the rotor disc, are compared the computed wake structure against experimental estimates of the vortex core positions derived from the detailed PIV measurements of the flow-field.

5.1 Wake visualisation

The geometry of the VTM-predicted wake of the HART II system at the medium computational resolution as described in Table 4.1, is visualised in Fig. 5.2, for each of the three flight cases. A surface is plotted in the flow on which the vorticity has constant magnitude. The rotor drive enclosure has contours showing the instantaneous pressure on its surface. This figure illustrates well the characteristic behaviour of the VTM, regardless of the model used for the aerodynamics of the rotor blade, in retaining the spatial com-

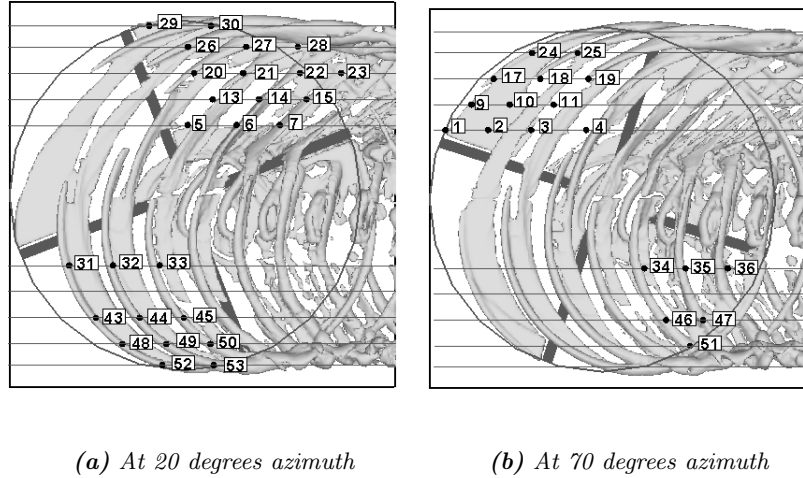


Figure 5.1: Locations of PIV measurement planes superimposed on the wake structure predicted by the VTM for the HART II BL case.

pactness of the vortical structures that are present in the flow even after numerous rotor revolutions have elapsed. Indeed, it is this property of the model that makes the VTM particularly well-suited to predicting loading perturbations on the scale of blade-vortex interactions, as already shown in Section 4.2.2. The modifications to the trajectories of the tip vortices, that result from the application of HHC, are clearly visible when comparing the resultant wake structure of the MN and MV cases with the BL case. In all three cases, the relatively strong root-vortex structure, as well as the broad vortex sheet that is generated behind the blades as they traverse the advancing side of the rotor, can be seen clearly. The image also reveals some detail of how this outboard sheet eventually rolls up to form a concentrated tip vortex at some distance behind the blades, particularly on the advancing side of the rotor. In the BL and MV flight cases, the BVI events on the retreating side of the disc are caused by near-parallel interactions between the rotor blade and the tip vortex (see Section 4.2.2). The modification to the tip vortex trajectories that is introduced by the HHC in the minimum noise case causes these vortices to re-orientate so that they interact more obliquely with the rotating blades, than in the BL case. This may be one of the causes of the reduction in noise that is found in this flight case (see Section 6.1 where this is discussed in more detail).

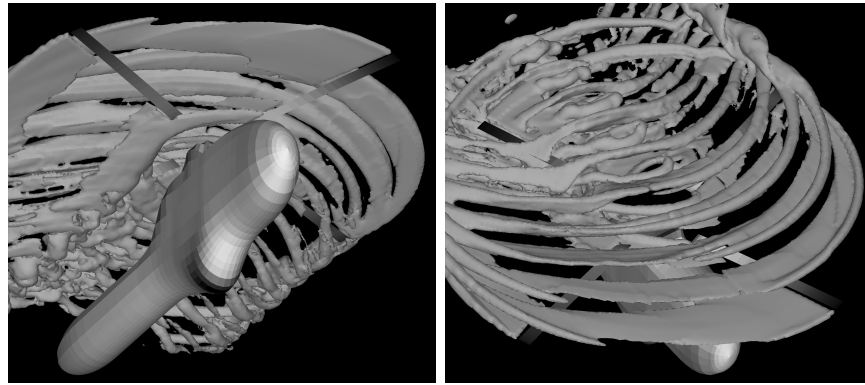
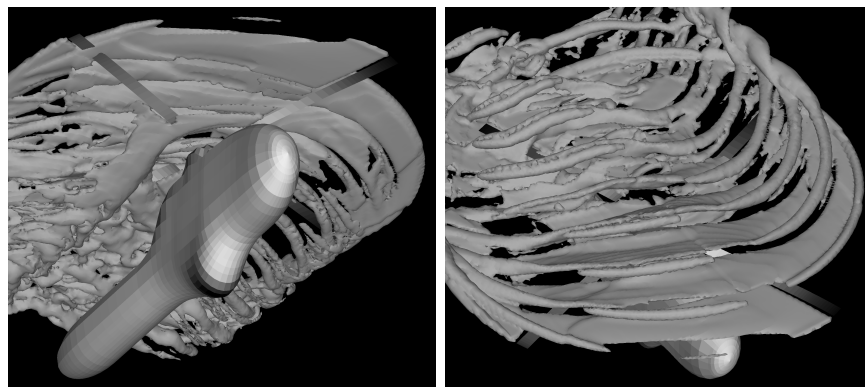
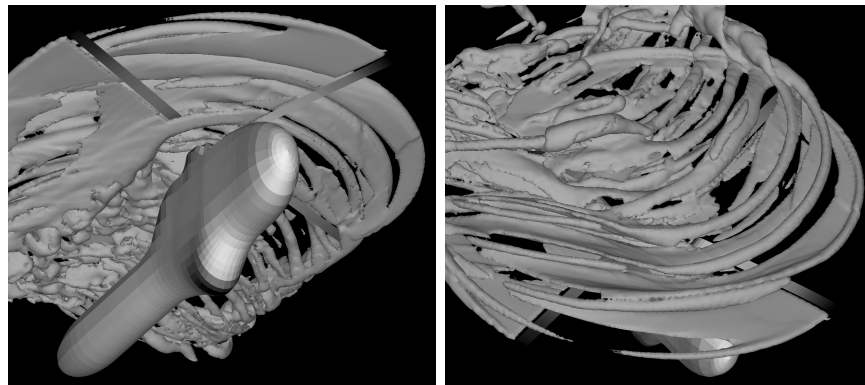
(a) *Baseline*(b) *Minimum Noise*(c) *Minimum Vibration*

Figure 5.2: *Visualisation of the VTM-predicted wake geometry from simulations of the HART II rotor at the medium computational resolution (a representation of the drive enclosure has been included in the calculations).*

5.1.1 Wake sensitivity to blade aerodynamic model

Figure 5.3 compares the wake structure that is predicted by the VTM at the medium resolution for the MN case when the lifting-chord representation of the aerodynamics of

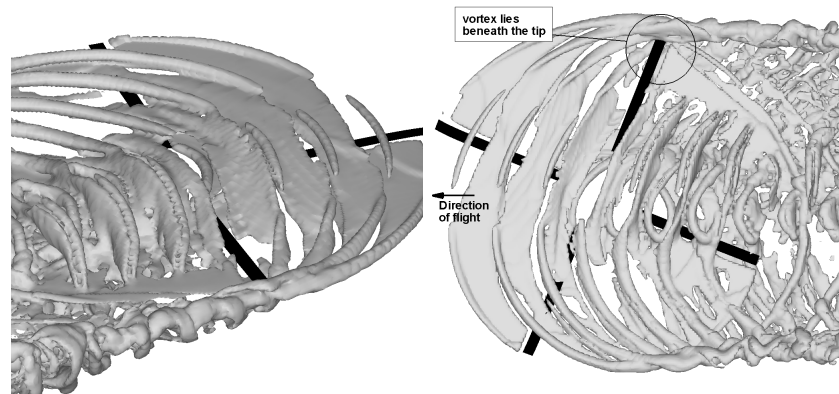
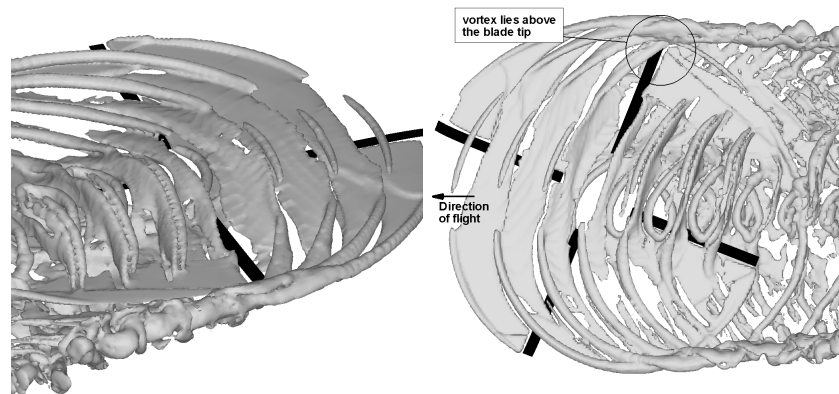
(a) *Lifting-line model*(b) *Lifting-chord model*

Figure 5.3: Geometry of the rotor wake, with the reference blade at 70° azimuth, as predicted using lifting-line and lifting-chord representations of the blade aerodynamics, for the HART II MN flight case. (A representation of the drive enclosure has not been included in the calculations).

the blade is used to that predicted when the lifting-line model is used. This figure shows the sensitivity of the predicted wake structure to the model that is used to represent the blade aerodynamics. In the calculation in which the lifting-line model has been used, the vortex that is responsible for the most prominent BVI in the MN case passes beneath the blade whereas when the lifting-chord model is used the vortex passes above the blade. The VTM predicted airloads are sensitive to the very subtle changes in the vorticity distribution which is sourced into the flow by the blades when different blade aerodynamic models are used, and in this case, given the shallow angle between the vortex and the blade, it can easily be conceived how a small change in the predicted position of the vortex could have

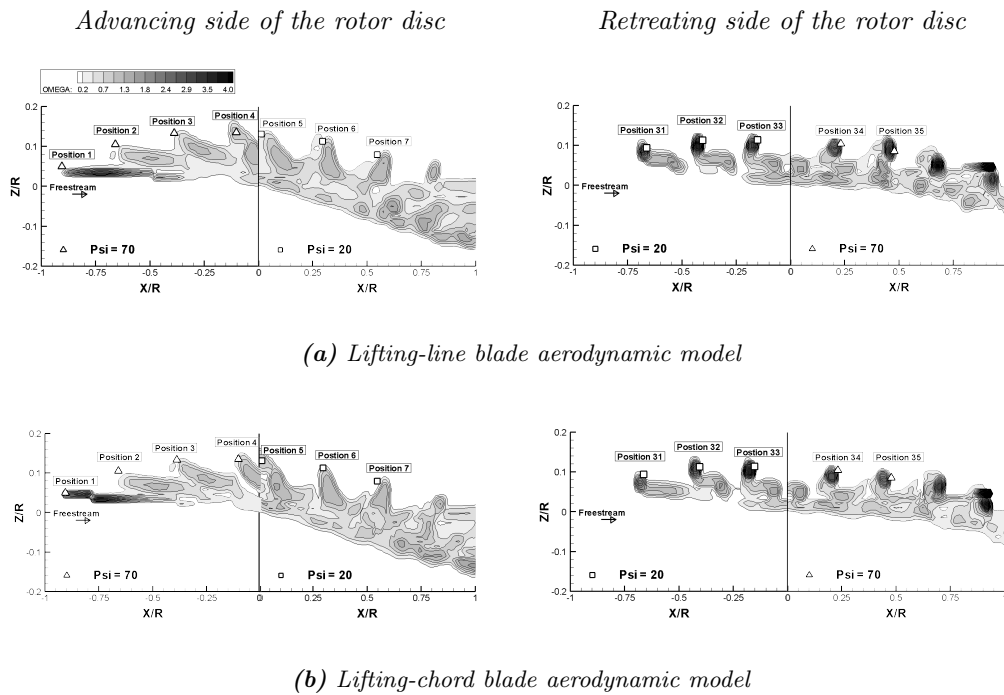


Figure 5.4: Computed wake structure (contours of vorticity magnitude) and vortex core positions (symbols) estimated from the experimental data compared on a longitudinal slice through the wake at 40% of the rotor radius. (HART II BL flight case).

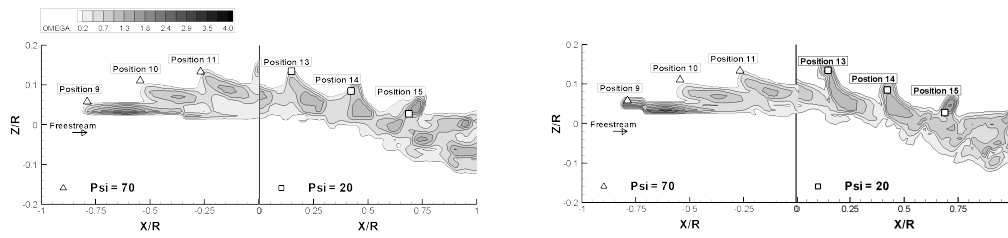
a large effect on the predictions of the associated BVI airload.

5.2 Trajectory of tip vortices

To illustrate quantitatively the ability of the model to capture the geometry of the rotor wake, Figs. 5.4 to 5.8 compare contour plots of vorticity magnitude, as predicted using each of the two models for the aerodynamics of the blades, against experimental estimates of the positions of the vortex cores on each of longitudinal slices where measurements were gathered. In each of these figures, experimental measurements of the positions of the vortex cores are plotted as symbols, and are labelled with a number corresponding to the location of the PIV measurement plane.

To prevent the rotor blades from obscuring the images, measurements of the flow structure in the first and third quadrants of the rotor were performed with the rotor at an azimuth of 20° , while similar measurements of the flow in the second and fourth quadrants were

Advancing side of the rotor disc

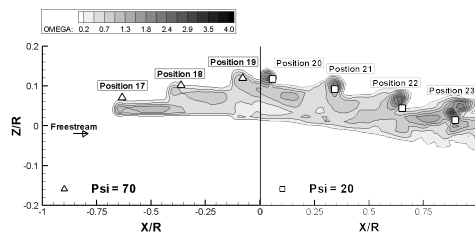


(a) Lifting-line blade aerodynamic model

(b) Lifting-chord blade aerodynamic model

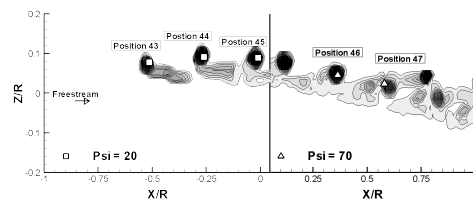
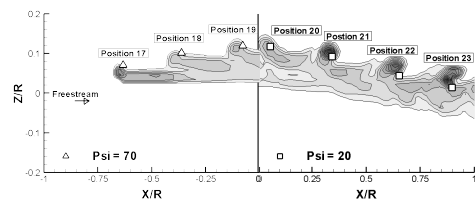
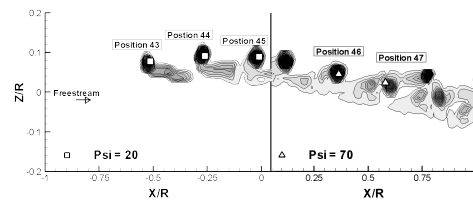
Figure 5.5: Computed wake structure (contours of vorticity magnitude) and vortex core positions (symbols) estimated from the experimental data compared on a longitudinal slice through the wake at 55% of the rotor radius. (HART II BL flight case).

Advancing side of the rotor disc



(a) Lifting-line blade aerodynamic model

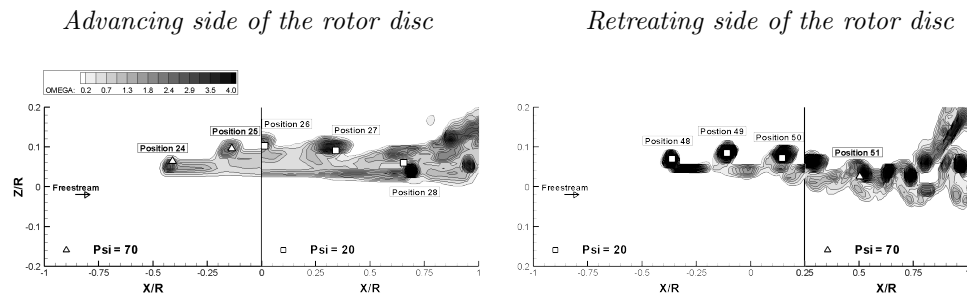
Retreating side of the rotor disc



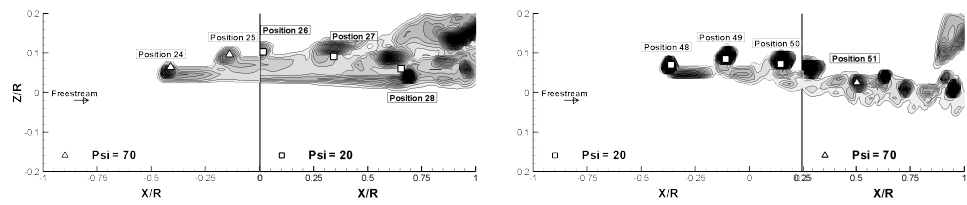
(b) Lifting-chord blade aerodynamic model

Figure 5.6: Computed wake structure (contours of vorticity magnitude) and vortex core positions (symbols) estimated from the experimental data compared on a longitudinal slice through the wake at 70% of the rotor radius. (HART II BL flight case).

made with the rotor at an azimuth of 70° . This difference accounts for the misalignment of the contours between the forward and aft sections of the rotor disc that is visible in the figures. Time lags in the measurement equipment yield an error of 3.5° in the measured blade azimuth position, but this has also been accounted for in the presentation of the data. In the hub co-ordinate system, Z is positive in the upwards direction and X is positive aft. The rotor hub is located at the origin of the coordinate system.

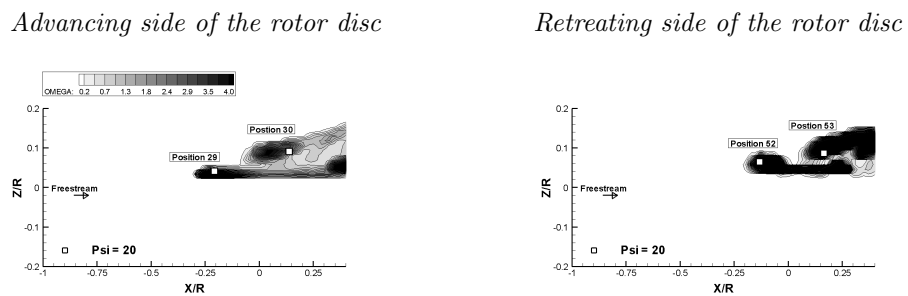


(a) Lifting-line blade aerodynamic model



(b) Lifting-chord blade aerodynamic model

Figure 5.7: Computed wake structure (contours of vorticity magnitude) and vortex core positions (symbols) estimated from the experimental data compared on a longitudinal slice through the wake at 85% of the rotor radius. (HART II BL flight case).



(a) Lifting-line blade aerodynamic model



(b) Lifting-chord blade aerodynamic model

Figure 5.8: Computed wake structure (contours of vorticity magnitude) and vortex core positions (symbols) estimated from the experimental data compared on a longitudinal slice through the wake at 97% of the rotor radius. (HART II BL flight case).

5.2.1 Influence of blade aerodynamic model

Figures 5.4 to 5.8 illustrate the ability of the VTM to capture accurately the geometry of the rotor wake, irrespective of the method by which the blade loading is calculated and hence by which the vorticity source into the flow-field is calculated. The locations of the maxima in the computed vorticity distribution in the wake show, in general, very good correlation with the experimentally measured vortex positions. This is true for the slices close to the rotor hub and for those which lie closer to the tips of the blades.

On the forward half of the rotor disc, the prediction of the vortex positions is better on the retreating side than on the advancing side of the rotor, which is consistent with the observed accuracy of the blade airload predictions. Such a trend is less obvious towards the rear of the rotor disc. Indeed, the positions of the vorticity maxima, as predicted by the VTM using both lifting-chord and lifting-line blade aerodynamic models, are all well within one chord length ($c/R = 0.0605$) of the experimentally measured positions of the vortex cores.

The most obvious differences between the two different models for the loading on the blades is how they represent the structural features of the tip vortex when the vortex is relatively young, for example when resolved on the observation planes at Position 1 in Fig. 5.4 and Position 17 in Fig. 5.6. In both cases, the lifting-chord model predicts more accurately the position of the young tip vortex by capturing to some extent the slight curvature to the inboard sheet of vorticity as it rolls up just downstream of the advancing blade. With the grid resolutions that are presently achievable, these features are at the limit of what are possible to resolve.

It was postulated in Chapter 4 that problems in resolving both the low-frequency and the BVI-induced loading on the advancing side of the rotor could be due to misrepresentation of the root vortex system that is generated by the rotor (perhaps as a result of the omission of any representation of the blade attachments or rotor hub in the simulations) and hence its effect in distorting the more outboard sections of the wake. This interpretation seems unlikely, however, in the light of the data presented in Fig. 5.4 for the wake structure

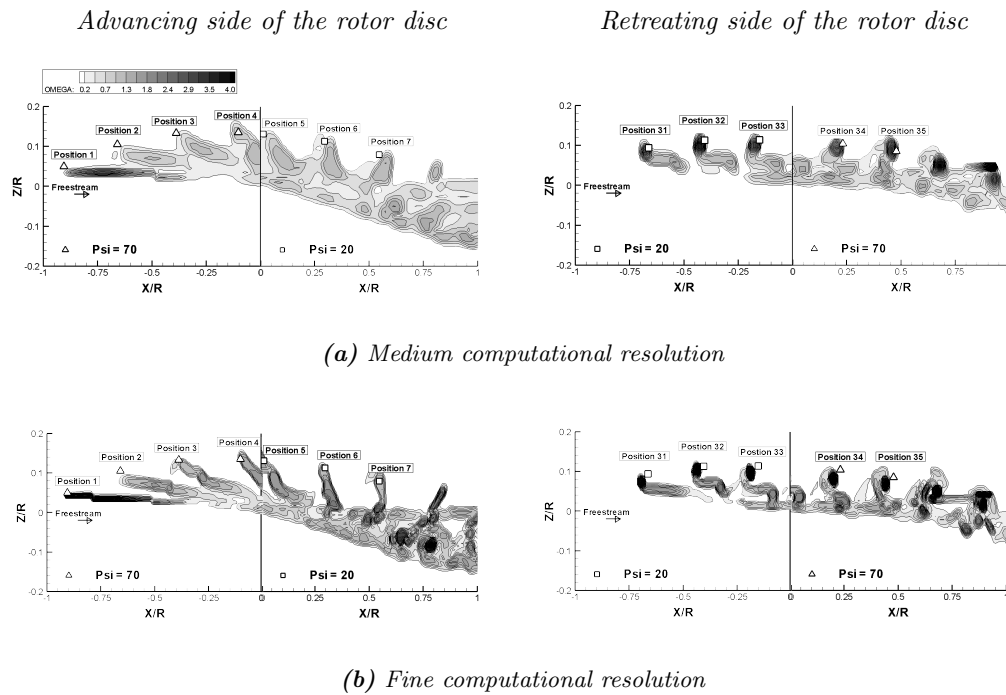


Figure 5.9: Computed structure of wake vorticity (contours) and measured vortex core positions (symbols) compared on longitudinal slices through the wake at 40% of the rotor radius, at both the medium and fine computational resolutions. (HART II BL flight case).

at 40% of the rotor span which shows very good agreement to experimental data, at a position relatively close to the root cut-out.

5.2.2 Effect of grid resolution

A comparison of the results for medium and fine resolutions (as defined in Table 4.1) of the computational domain in Fig. 5.9 and Fig. 5.10 shows that an increase in the spatial resolution of the flow-field results in a markedly improved definition of the various vortical structures within the wake, but does not alter significantly the predicted positions of the vortex cores within the flow. The exception is on the advancing side of the rotor, particularly at $Y/R = 0.4$, where a refinement of the computational mesh reduces the error in the prediction of the positions of the vortex cores from about one third of the blade chord to within the resolution of the plotted data. On the other hand, cross referencing the predictions of blade loading in Chapter 4 with the data presented here does suggest a consistency between the small improvement in vortex position that results from an increase in the resolution of the wake and a slight improvement in the phasing of the BVI-induced

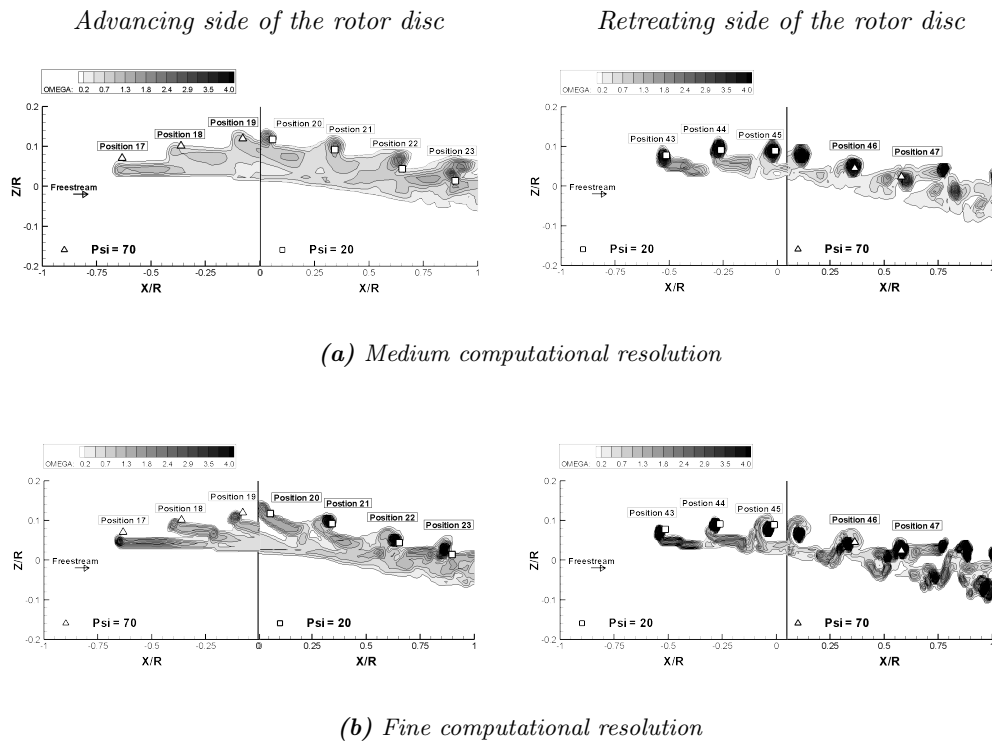
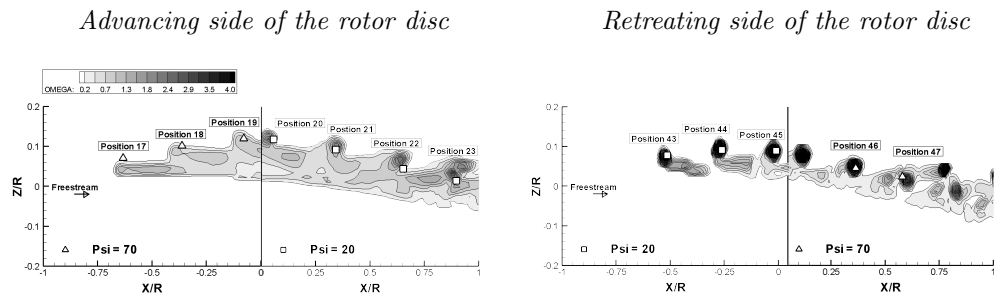


Figure 5.10: Computed structure of wake vorticity (contours) and measured vortex core positions (symbols) compared on longitudinal slices through the wake at 70% of the rotor radius, at both the medium and fine computational resolutions. (HART II BL flight case).

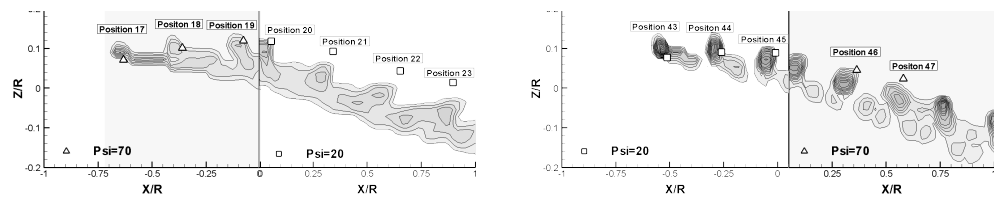
loading on the advancing side of the rotor disc. The concentration of the vorticity that is associated with each tip vortex into more tightly compacted structures as the resolution of the flow domain is increased, lends some insight into the causes of the over-predictions in amplitude of the BVI-induced loading peaks, particularly when the lifting-line model for the blade aerodynamics is used.

5.2.3 Effect of including a representation of the drive enclosure

Figure 5.11 shows the vortex positions at 70% along the blade for the HART II BL flight case when an isolated rotor is modelled and those where a representation of the drive housing has been included in the computation. Representing the drive housing in the computations results in an upward deflection of the predicted wake geometry compared to that when the fuselage is ignored, and improves considerably the match between the experimentally measured and predicted vortex positions.

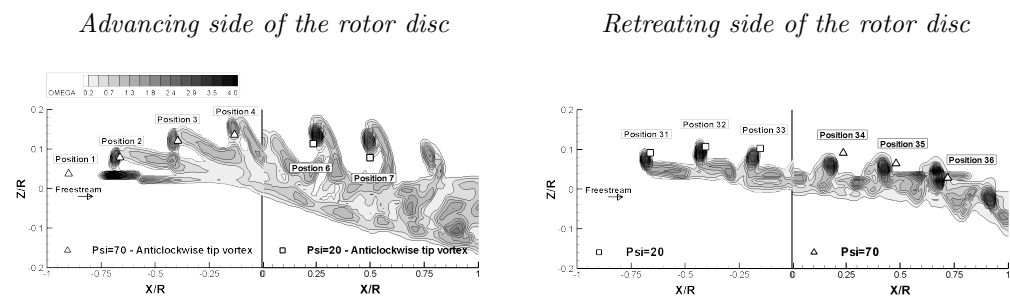


(a) With a representation of the drive housing

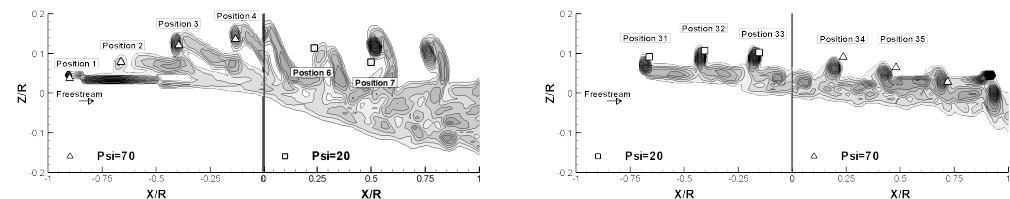


(b) Isolated rotor

Figure 5.11: Computed structure of wake vorticity (contours) and measured vortex core positions (symbols) compared on longitudinal slices through the wake at 70% of the rotor radius, with and without a representation of the drive enclosure. (HART II BL flight case).



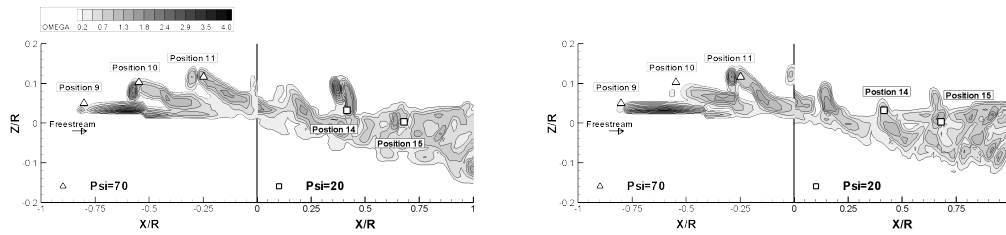
(a) Lifting-line blade aerodynamic model



(b) Lifting-chord blade aerodynamic model

Figure 5.12: Computed wake structure (contours of vorticity magnitude) and vortex core positions (symbols) estimated from the experimental data compared on a longitudinal slice through the wake at 40% of the rotor radius. (HART II MN flight case).

Advancing side of the rotor disc

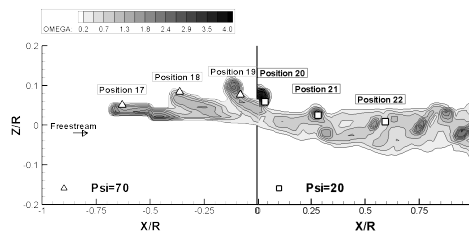


(a) Lifting-line blade aerodynamic model

(b) Lifting-chord blade aerodynamic model

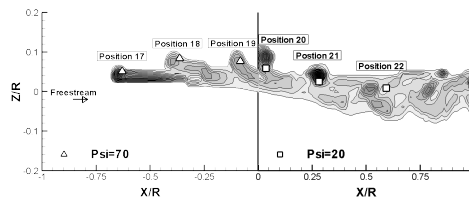
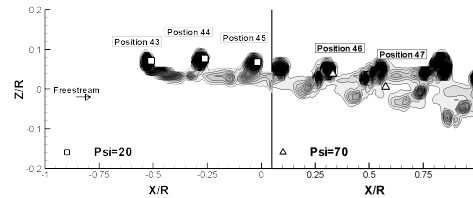
Figure 5.13: Computed wake structure (contours of vorticity magnitude) and vortex core positions (symbols) estimated from the experimental data compared on a longitudinal slice through the wake at 55% of the rotor radius. (HART II MN flight case).

Advancing side of the rotor disc



(a) Lifting-line blade aerodynamic model

Retreating side of the rotor disc



(b) Lifting-chord blade aerodynamic model

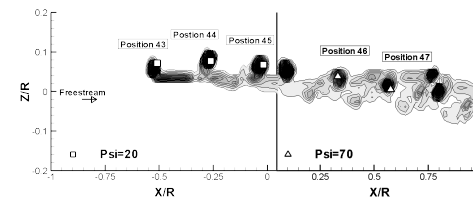
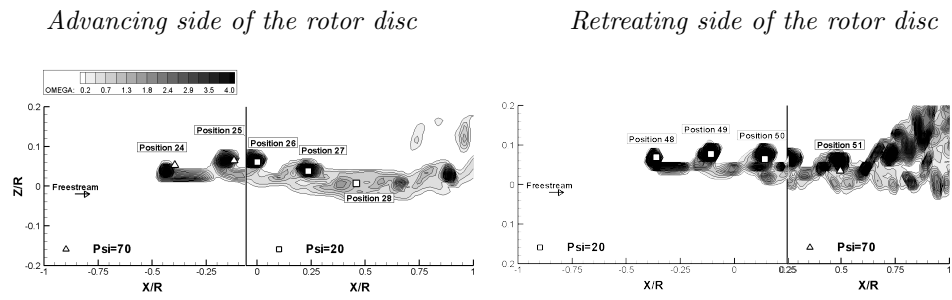


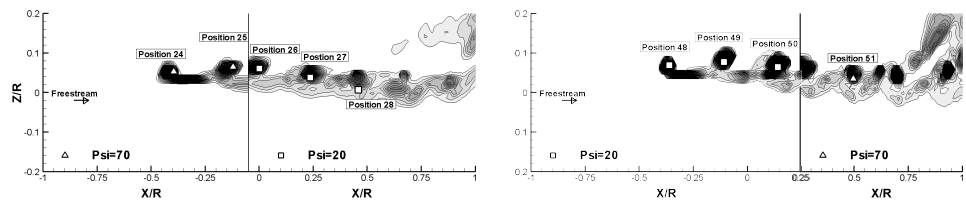
Figure 5.14: Computed wake structure (contours of vorticity magnitude) and vortex core positions (symbols) estimated from the experimental data compared on a longitudinal slice through the wake at 70% of the rotor radius. (HART II MN flight case).

5.2.4 Minimum noise and minimum vibration cases

Figs. 5.12 to 5.16 show contour plots of vorticity magnitude, as predicted using each of the two models for the aerodynamics of the blades, against experimental estimates of the positions of the vortex cores on each of the longitudinal slices where measurements were gathered for the minimum noise case. The computation included a representation of the drive housing and, as in the BL case, the locations of predicted maximum vorticity in the

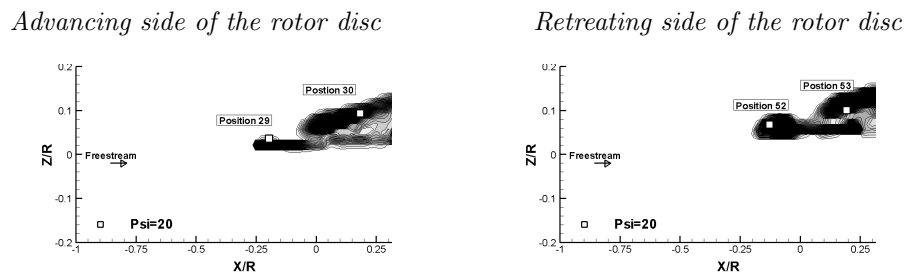


(a) Lifting-line blade aerodynamic model

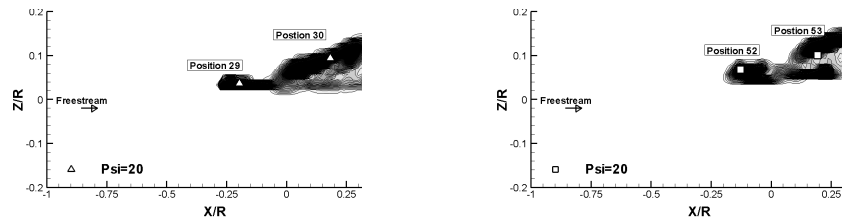


(b) Lifting-chord blade aerodynamic model

Figure 5.15: Computed wake structure (contours of vorticity magnitude) and vortex core positions (symbols) estimated from the experimental data compared on a longitudinal slice through the wake at 85% of the rotor radius. (HART II MN flight case).



(a) Lifting-line blade aerodynamic model



(b) Lifting-chord blade aerodynamic model

Figure 5.16: Computed wake structure (contours of vorticity magnitude) and vortex core positions (symbols) estimated from the experimental data compared on a longitudinal slice through the wake at 97% of the rotor radius. (HART II MN flight case).

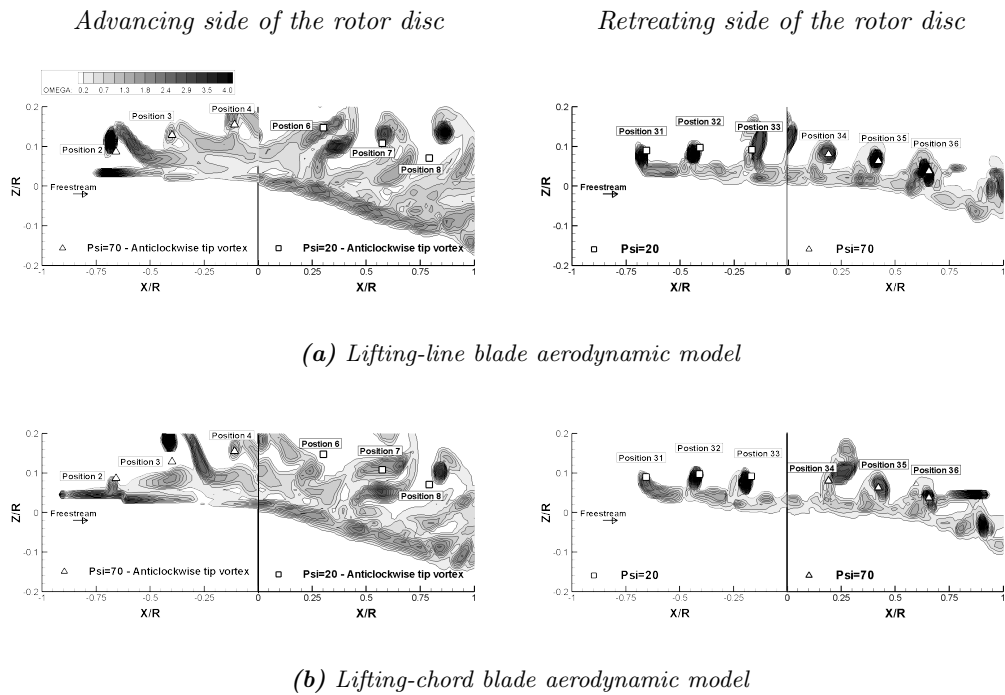


Figure 5.17: Computed wake structure (contours of vorticity magnitude) and vortex core positions (symbols) estimated from the experimental data compared on a longitudinal slice through the wake at 40% of the rotor radius. (HART II MV flight case).

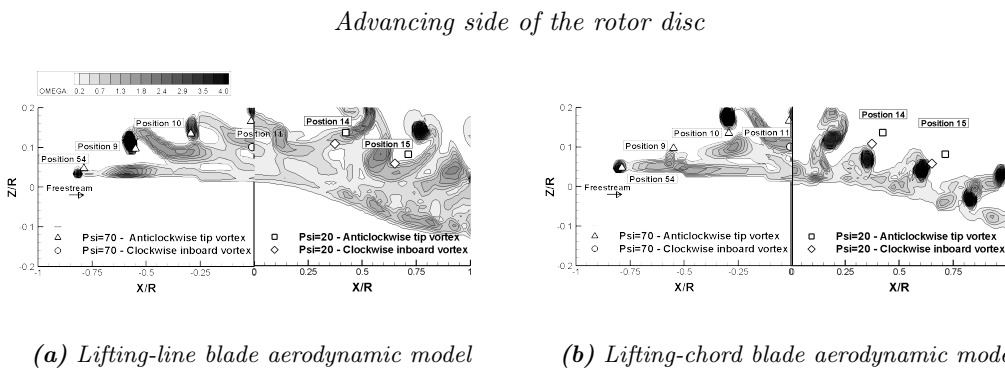
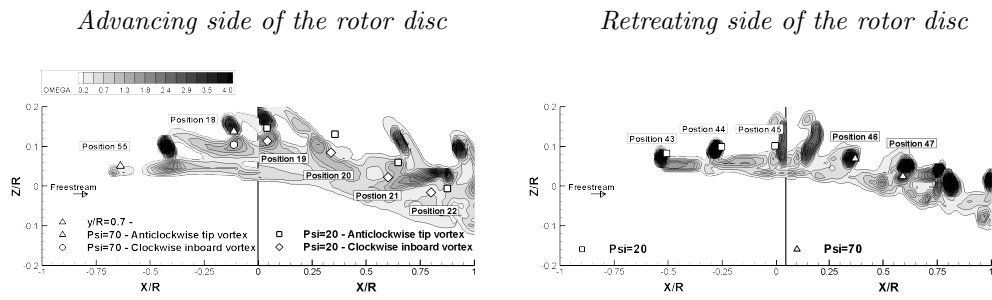


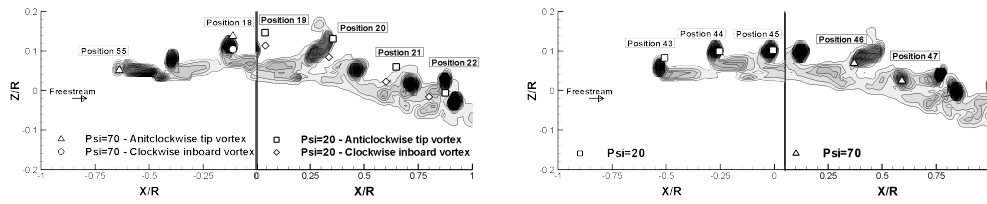
Figure 5.18: Computed wake structure (contours of vorticity magnitude) and vortex core positions (symbols) estimated from the experimental data compared on a longitudinal slice through the wake at 55% of the rotor radius. (HART II MV flight case).

flow match very accurately the experimentally measured positions of the vortex cores. On the retreating side of the rotor, the vortices at position 47 and further downstream are perhaps deflected a little too strongly by the presence of the drive housing, resulting in vortex cores that lie slightly higher than the positions of the cores that were estimated from the experimental data.

The wake structure of the minimum vibration case, depicted in Figs. 5.17 to 5.21, is

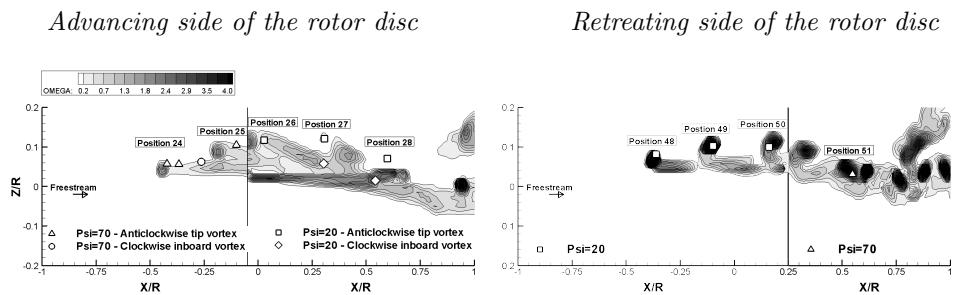


(a) Lifting-line blade aerodynamic model

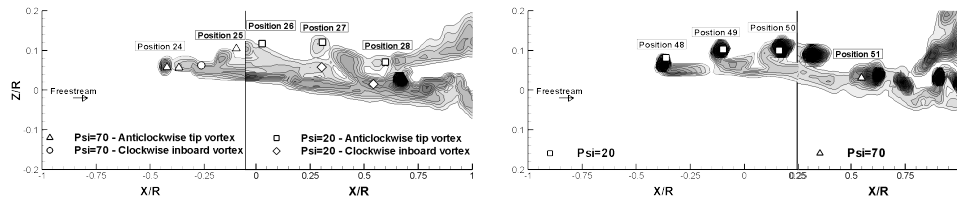


(b) Lifting-chord blade aerodynamic model

Figure 5.19: Computed wake structure (contours of vorticity magnitude) and vortex core positions (symbols) estimated from the experimental data compared on a longitudinal slice through the wake at 70% of the rotor radius. (HART II MV flight case).



(a) Lifting-line blade aerodynamic model

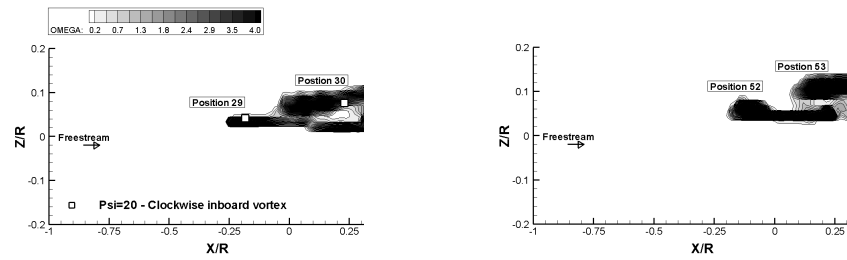


(b) Lifting-chord blade aerodynamic model

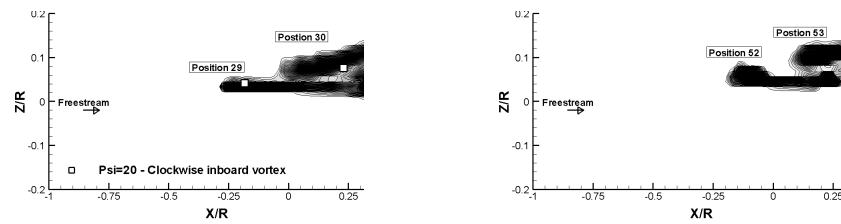
Figure 5.20: Computed wake structure (contours of vorticity magnitude) and vortex core positions (symbols) estimated from the experimental data compared on a longitudinal slice through the wake at 85% of the rotor radius. (HART II MV flight case).

Advancing side of the rotor disc

Retreating side of the rotor disc



(a) *Lifting-line blade aerodynamic model*



(b) *Lifting-chord blade aerodynamic model*

Figure 5.21: *Computed wake structure (contours of vorticity magnitude) and vortex core positions (symbols) estimated from the experimental data compared on a longitudinal slice through the wake at 97% of the rotor radius. (HART II MV flight case).*

especially interesting. The experimental data shows the existence of a twinned tip-vortex structure on the advancing side of the rotor disc. The existence of this structure was attributed to the reversed loading at the tip of the advancing blade under the conditions of this particular test. This is supported by the computational predictions, which show the vorticity distribution on the slice to consist of a sequence of paired vortices, one rotating clockwise and the other anti-clockwise. The positions of both the clockwise and anti-clockwise vortices are in good agreement with the experimental data until position 21 – further aft the anti-clockwise tip vortices lie slightly higher than is observed experimentally. In contrast, the vortex positions at equivalent locations on the retreating side of the rotor are extremely well predicted by the computational method.

A rather revealing consistency is thus observed between the regions of the rotor where the major discrepancies in the predicted BVI-induced airload are encountered and where the prediction of the wake structure is at its least satisfactory. The results presented here serve to emphasise the extremely demanding requirements on the accuracy of the model

of the rotor wake and the structural dynamics of the blades if truly accurate prediction of the BVI-induced airloads on the rotor is to result.

5.3 Roll-up of the tip vortex

Resolving the positions of the vortices in the wake, even to the accuracy of a fraction of a chord-length as demonstrated in the previous section, might thus not be sufficient for accurate prediction of the BVI-induced loading on the rotor. It is well known that finer-scale convective and diffusive processes within the wake influence the distribution of the vorticity on the length-scale of the vortex core (see, for instance, Ref. 86) and are likely, if incorrectly represented, to result in significant errors in the prediction of BVI. For concentrated vortical structures, accurate resolution of the fine-scale structure is especially important where the miss-distance between the vortex and the blade is very small, but, on the other hand, detailed structural effects become less important with increasing miss-distance because of the properties of the Biot-Savart relationship between the velocity and the vorticity. Indeed, given the descending flight condition that was modelled during the tests (and as can be inferred from the vortex trajectories shown in Figs. 5.4 to 5.8), very few of the BVI events on the HART II rotor are due to close interactions between the vortices and the blades. Where extended vortex structures are involved, however, it is possible that predictions of BVI-induced loading may be adversely affected by poor resolution of the fine-scale distribution of the vorticity in the wake even where miss-distances are significantly larger. Indeed, a possible cause of the discrepancy in resolution of the BVI-induced airloads on the advancing side of the rotor, suggested in Chapter 4, was a possible under-resolution of the process whereby the tip vortex of the blades on the advancing side of the rotor is formed, and hence a slight mis-distribution of the vorticity within the trailing vortex structure behind the blades.

The formation of the blade-tip vortices of the HART II rotor is known to be an extremely complex process. The flight condition of the baseline HART II case, combined with the twist distribution on the blades, results in a very flat loading profile along the span of the blade as it traverses the advancing side of the rotor. The vorticity that is deposited into

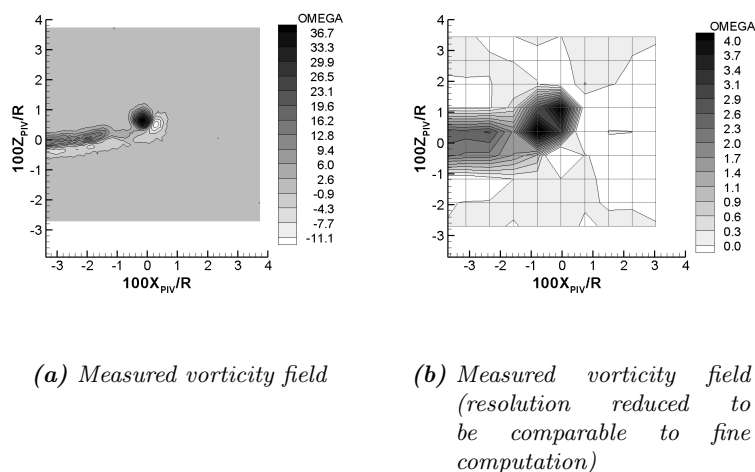
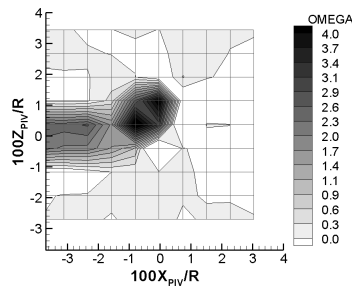


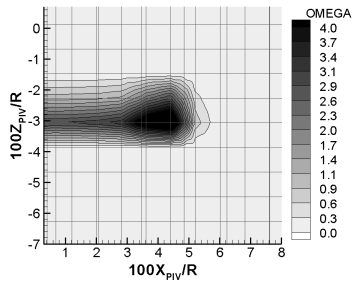
Figure 5.22: *Experimental vorticity distribution at the resolution of the PIV experimental data compared to experimental data where the resolution has been reduced to be comparable to that of the fine computation. (Position 17a, i.e. vortex age 5.3°).*

the flow immediately behind the trailing edge of the blade thus forms a broad sheet, with relatively weak but uniform strength across its width, rather than a concentrated vortex (See Fig. 5.2). This sheet of vorticity then takes some time to roll up, forming a compact tip vortex only after about one quarter of a revolution of the rotor has elapsed. During the HART II experiment, a sequence of PIV measurements at time intervals corresponding to 5° of rotor azimuth was captured on a single observation plane (plane 17 in Fig. 5.1) behind the advancing blade to follow the evolution of the vortex sheet from its creation to its eventual roll-up to form a compact vortical structure. A number of similar measurements were taken on observation planes further downstream to allow the structure of the tip vortex to be investigated well after the initial roll-up process had run to completion (see Fig. 5.1).

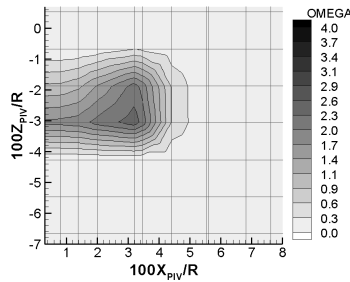
This data can be exploited very effectively to address the question of how well the very fine-scale processes that occur within the wake of the rotor are represented within the VTM. The evolution of the VTM-predicted vorticity distribution on several observation planes was thus compared against this experimental data in order to assess the ability of the VTM to capture both quantitatively and qualitatively the roll-up of the vortex sheet behind the blades on the advancing side of the HART II rotor. The vorticity component normal to



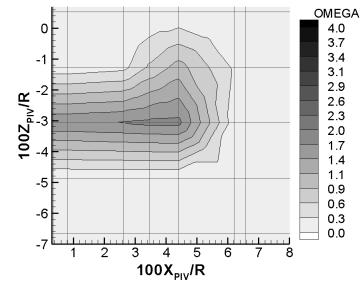
(a) Measured vorticity field
(resolution reduced to be
comparable to fine com-
putation)



(b) Lifting-line model:
fine resolution



(c) Lifting-line model:
medium resolution



(d) Lifting-line model:
coarse resolution

Figure 5.23: Comparison of vorticity field on the advancing side of the rotor, at a wake age of 5.3° (BL case, position 17a), using lifting-line representation of the blade aerodynamics and at various computational resolutions.

the measurement plane was extracted from the numerical data by suitable interrogation of the three-dimensional vorticity field surrounding the rotor, and was estimated from the experimental PIV data by numerical differentiation of the measured velocity field.

Figure 5.22 shows a sample comparison between the experimental vorticity distribution at the full resolution of the PIV measurements, and when re-sampled at the resolution of the finest grid used in the simulations. In the plots that follow the VTM-predicted vorticity distributions are compared to the experimental data that has been re-sampled in this way. The grid-lines on the plots of predicted vorticity distribution coincide with

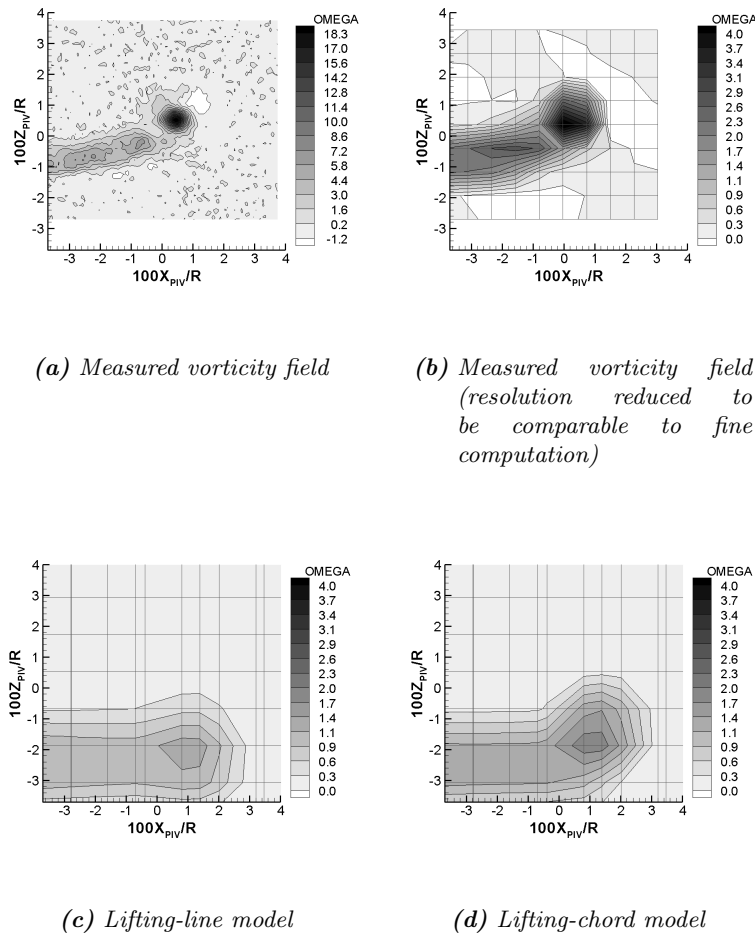
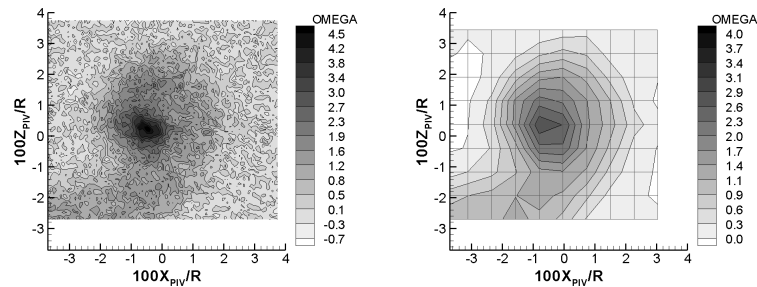


Figure 5.24: Comparison of vorticity field on the advancing side of the rotor, at a wake age of 25.3° (BL case, position 17), using lifting-line and lifting chord representations of the blade aerodynamics and at the medium computational resolution.

the boundaries of the computational cells¹. Figure 5.23 compares the predicted and measured structures of the vorticity distribution at a very early age — just 5.3° after the blade has passed through the observation plane. Note that some shifting of the numerical observation plane relative to the experimental one has been necessary to capture fully the vorticity concentration associated with the core of the tip vortex. The anomalies in the predicted tip vortex trajectory that make this shift necessary will be discussed in more detail. The experimental measurements show the beginnings of a concentrated tip vortex just outboard of a well-defined inboard wake sheet. Qualitatively, the structure of the

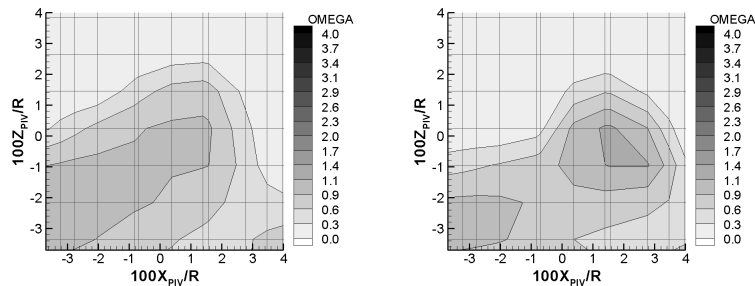
¹The unevenness of the lines is a consequence of the PIV observation planes cutting obliquely across the underlying VTM cell structure.

measured vorticity distribution is very well captured by the VTM, particularly as the resolution of the calculation is increased.



(a) Measured vorticity field

(b) Measured vorticity field
(resolution reduced to be comparable to fine computation)



(c) Lifting-line model

(d) Lifting-chord model

Figure 5.25: Comparison of vorticity field on the advancing side of the rotor, at a wake age of 205.3° (BL case, position 19), using lifting-line and lifting chord representations of the blade aerodynamics and at the medium computational resolution.

Figure 5.24 presents a similar comparison of the vorticity distribution behind the blade at a somewhat later age (25.3°) during the roll-up process. Interestingly though, the slight curvature of the inboard sheet of vorticity, that at this position is well captured by the lifting-chord aerodynamic model, is missed entirely by the VTM when the lifting-line model is used to generate the source of vorticity from the blade into the flow. Moreover, the lifting-chord model more accurately reproduces the experimentally measured position of the vortex core on this observation plane than does the lifting-line model. As similar grid discretisation has been used for each blade model, it can be argued that the fine-scale

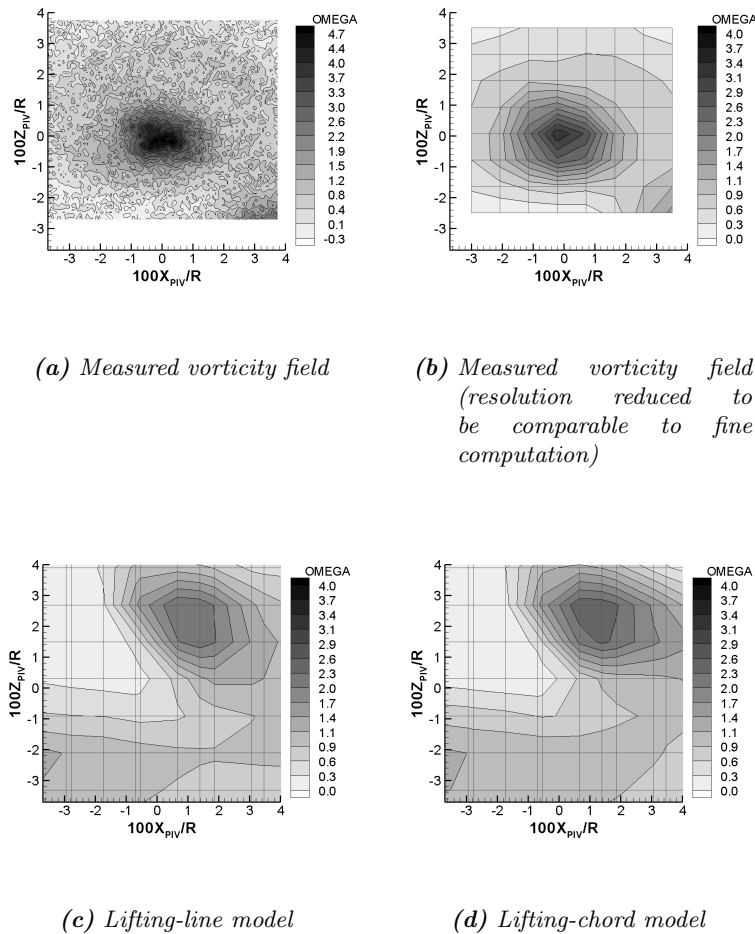


Figure 5.26: Comparison of vorticity field on the advancing side of the rotor, at a wake age of 425.3° (BL case, position 22), using lifting-line and lifting chord representations of the blade aerodynamics and at the medium computational resolution.

features of the wake produced by the VTM are relatively sensitive to small differences in the distribution of vorticity as it is sourced from the blades into the flow-field.

Figures 5.25 and 5.26 present the wake structure at a significantly later age than in Fig. 5.24 (at 205.3° and 425.3° wake age, i.e. on PIV planes 19 and 22) once the vortex sheet behind the rotor blade has almost entirely concentrated into a coherent tip vortex (no shifting of the observation plane is necessary in these cases to capture fully the vortex core). These figures show again the very good qualitative agreement between predictions and the measured shape and size of the tip vortex and inboard sheet as this structure evolves to form a coherent, isolated vortex. The arc-like vortical features within the vorticity

distribution on the observation plane at position 19 are more accurately captured by the lifting-chord model than by the lifting-line approach. As is to be expected though, the choice of model for the aerodynamics of the rotor blades has little or no effect on the positions of the vortex cores further downstream, or indeed on the detailed structure of the flow once the vortices have aged considerably. This is illustrated in Fig. 5.26 where qualitatively, there is little difference in the flow fields that are produced by the two different blade models far downstream of the generating blade.

The calculations suggest that quite a significant blade-to-blade variability exists in the structure of the tip vortex. Figure 5.27 shows the numerical predictions of the vortical structure 5.3° behind each of the four blades of the HART II rotor. This variability is entirely due to the slightly different structural dynamics of each of the blades, but confirmation of the numerical predictions, in particular of the curiously weak structure that is created behind ‘blade 2’, awaits release of more of the HART II data into the public domain. In contrast, a comparison of parts (b) and (e) of this figure reveals very little variability from revolution to revolution in the predicted structure of the wake, illustrating the convergence of the calculations onto a robust and repeatable trim state.

Several somewhat more objective measures of the development of the tip vortex can be extracted from the data to allow more rigorous assessment of the capabilities of the numerical method. The change in circulation of the tip vortex with age can be estimated (subject to certain caveats regarding the strength of the associated vortex sheet) by integrating the vorticity distribution over the area of each observation plane. Figure 5.28 shows that the numerical approach is able to track the measured circulation of the tip vortex extremely well, even to relatively large wake ages. Figure 5.29 shows furthermore that the predicted circulation of the tip vortex is relatively insensitive to grid resolution. The ability to capture the overall strength of the vortex and to convect the vorticity without significant dissipation in a manner that is relatively independent of the discretisation of the computational domain is one of the prime strengths of the vorticity-conserving approach that is implemented within the VTM.

The change in core size of the tip vortex with age can be estimated from the vorticity dis-

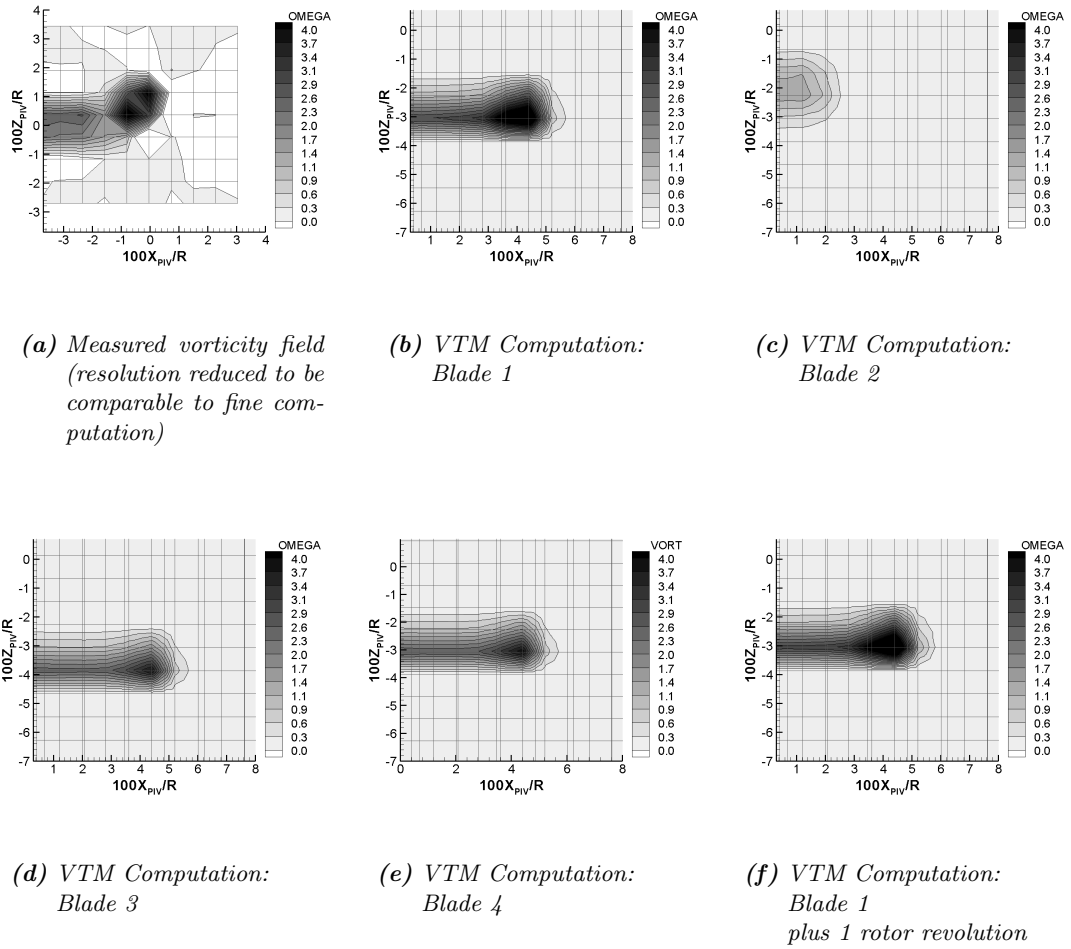


Figure 5.27: Comparison of vorticity field on the advancing side of the rotor, at a wake age of 5.3° (BL case, position 17a) behind each blade of the HART II rotor, showing the blade-to-blade variability of the wake structure, using a lifting-line representation of the blade aerodynamics and at the fine computational resolution.

tributions after assuming a specific profile for the vorticity distribution within the vortex. An Oseen vortex profile (in other words a normal distribution of vorticity within the tip vortex) generally provides a good fit to the vortical structures that are predicted by the VTM, particularly where they are somewhat under-resolved by the computational grid. Assuming the Oseen profile to be appropriate, the core radius r_c of the vortices can be estimated, in terms of the circulation Γ and the peak value of vorticity ω_{max} , in the vortex as $r_c/R = \sqrt{0.400 |\Gamma/\omega_{max} R^2|}$. The variation in core radius with age that is obtained by analysis of the experimental data is compared in Fig. 5.30 to similar estimates obtained from simulations using the VTM. The rate of growth of the vortex during the initial stages

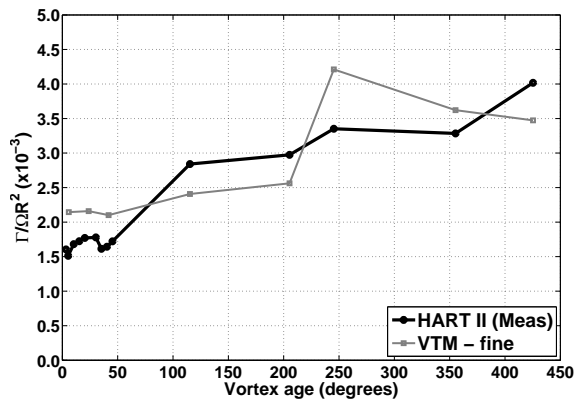


Figure 5.28: Variation of tip vortex circulation with wake age (Advancing side of the rotor disc, baseline HART II case).

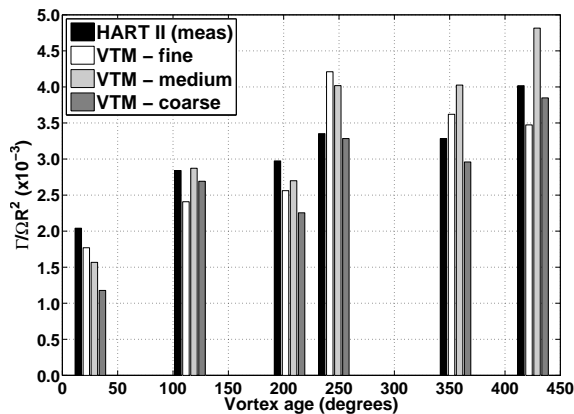


Figure 5.29: Variation of the tip vortex circulation with wake age for various computational resolutions (Advancing side of the rotor disc, baseline HART II case).

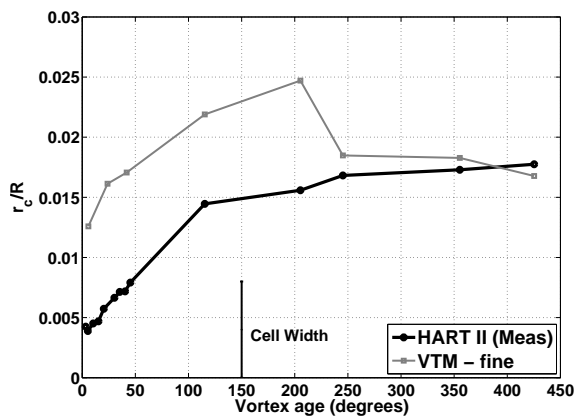
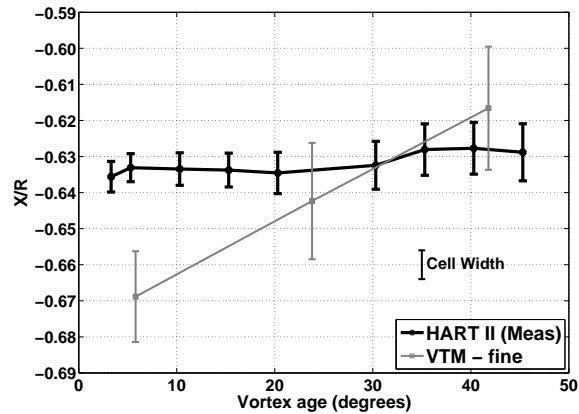
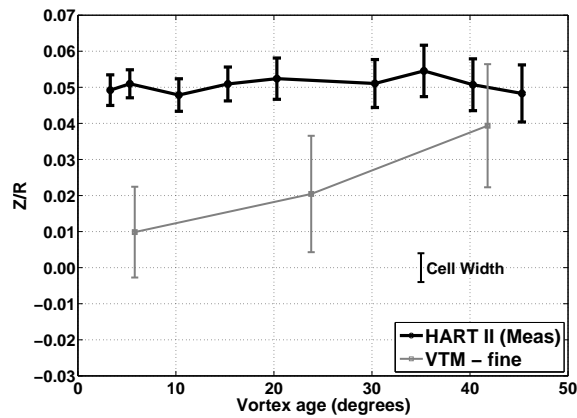


Figure 5.30: Variation of the vortex core radius with wake age (Advancing side of the rotor disc, baseline HART II case).

of the roll-up process is predicted exceptionally well by the VTM, implying that the entrainment of the inboard sheet into the developing tip vortex is accurately represented by



(a) Longitudinal position of the vortex with respect to the rotor centre



(b) Vertical position of the vortex with respect to the rotor centre

Figure 5.31: Position of the vortex core as a function of wake age on the advancing side of the rotor disc. Bars attached to data represent the size of the vortex core. (Baseline HART II case, position 17).

the method. Even at the finest computational resolution attempted here, however, the radius of the vortex at very early age is about double the measured value, and hence the calculation must be considered to be under-resolved. The rather sudden contraction of the radius of the vortex at a wake age of about 200° is a fairly well-understood characteristic of the WAF method, and is caused by the interaction of the flux limiters with the underlying computational grid to form a stable (soliton-like) solution to the vortex structure that spans a particular integer number of cells. The number of cells is dependent on the exact type of limiter that is used in the calculation. Not much should thus be read into the

very close agreement between the measured and predicted core sizes post this contraction since it most likely is a fortuitous coincidence between the measured profile and the cell size used in the computation.

Finally, the position of the centre of the developing tip vortex as a function of wake age can be estimated by determining the location of the point of maximum vorticity on each of the PIV observation planes. This is plotted in Fig. 5.31 where it is seen that the computed trajectory of the vortex follows fairly closely the trajectory that is measured experimentally. An initial offset in the vortex position of about half a blade chord appears to be a result of the finite discretisation of the surface of the blade into panels, and a small resultant positional inaccuracy in the interpolation of the vorticity into the computational domain. No doubt this inaccuracy is a contributor to the small discrepancies in the vortex positions that manifest further downstream in the wake, as shown in Figs. 5.4 to 5.7. The bars attached to the data represent the estimated size of the vortex core and, given the relatively coarse discretisation of the vortex location that is imposed by the relatively coarse resolution of the grid compared to the diameter of the vortex, the close agreement in the predicted and measured trajectories of the wake at the very early wake ages shown in the figure is encouraging nevertheless.

5.4 Summary

PIV images of the wake structure were compared against numerical predictions of the detailed geometry of the rotor wake using three different computational resolutions of the flow. VTM predictions of the geometry of the wake are shown to match very closely to the experimental data, no matter which method is used to represent the aerodynamics of the rotor blades. The predicted positions of the vortex cores on several longitudinal slices through the flow, both close to the rotor hub and further outboard along the blade span agree with the measured data to within a fraction of the blade chord. Qualitative analysis of the evolution of the tip vortex on the advancing side of the rotor shows the formation of a coherent tip vortex from the extended sheet of vorticity immediately behind the blade to be captured rather well. The slight curvature of the sheet of vorticity behind the trailing

edge of the blade is captured more accurately by the lifting-chord approach than by the lifting-line approach. The positions of the youngest vortex cores on the forward half of the advancing side of the disc are thus also more accurately determined by this method. As is to be expected, the aerodynamic model has much less effect on the predicted vortex positions as the wake increases in age. Detailed analysis of the circulation that is induced by the tip vortices shows that the vorticity conserving properties of the VTM result in the integrity of the vortical structures in the wake being preserved to well downstream of the rotor. This property of the method has been demonstrated to be independent of the resolution of the computation.

In the light of these results it is unlikely that inaccuracies in the prediction of the roll-up of the tip vortex or indeed the strong root-vortex system are responsible for the inaccuracies in the airload prediction found to the rear of the advancing side of the disc. Inaccuracies in predicting the high-frequency loading on the rotor are also unlikely to be caused by any deficiency in the representation of the wake, although viscous effects may need to be considered in future, in order to decouple the vortex core size from the cell size. The inaccuracies in the amplitude of the BVI-induced loading are thus more likely due to the inherent deficiencies of the lifting-line approach used to model the blade aerodynamics.

Chapter 6

Acoustic prediction

The accuracy of the airload predictions, particularly of the loads that are induced by blade vortex interactions, influences directly the accuracy to which the acoustic signature of the rotor can be predicted. In the HART II experiment, noise measurements were performed with an array of 13 microphones mounted transversally to the axis of the tunnel on a ground plane that was located 2.215m ($1.1R$) below the rotor hub. A map of the sound intensity on the ground plane was generated by moving this microphone array along the axis of the tunnel. This data can be used effectively to determine the influence of the airload predictions on the position and amplitude of the predicted sound pressure maxima on both the advancing and retreating sides of the rotor disc. The positions of each of the acoustic maxima and also any regions of decay determine the overall directivity of the noise produced. The directivity of the noise can be assessed qualitatively by comparing the predicted maps of measured sound intensity on the ground to that measured during the HART II experiment.

In this Chapter the ability of each blade aerodynamic model to predict accurately the blade airloads, to the level required to accurately predict the acoustic signature of the rotor, is examined. To this end, in Section 6.1, the experimentally-measured sound pressure levels (SPL) are compared to numerical predictions which are calculated from the airloads predicted by the VTM using a Farassat-1A formulation of the Ffowcs Williams-Hawkings Equations (See Section 2.8). Simulations of all three flight cases of the HART II test

programme were carried out at three different spatial and temporal resolutions to expose the effect of the resolution of the flow features in the wake on the acoustic predictions. To relate the noise that is radiated by the rotor to the individual BVI events at its source, the time history of the acoustic pressure is used to determine the positions on the rotor disc, of the major sources of the noise, that is measured at the SPL maximum on each side of the rotor. The radiated noise can thus be traced back to the individual BVI events that are the major contributors to the noise at these observer locations.

6.1 Sound Pressure Levels

Figures 6.1, 6.3 and 6.5 compare the measured sound pressure levels, on a ground plane located at 1.1R below the rotor hub, to those computed from the airloads which were predicted by the VTM. The acoustic field that is radiated by the rotor is computed using a post-processor for the blade aerodynamic loads that implements the Farassat-1A formulation (Ref. 19) of the Ffowcs Williams-Hawkings (FW-H) equation (Ref. 16), as described in Section 2.8. In all cases the data has been filtered to include only the frequencies between six and forty times the blade passage frequency. This is generally accepted to be the range that is dominated by BVI noise. Figures 6.2, 6.4 and 6.6 show the computed sound pressure levels, on a ground plane located at 1.1R below the rotor hub, from which the measured sound pressure levels have been subtracted to reveal the spatial distribution of the error between the measurements and the VTM predictions.

The acoustic calculation does not account for the scattering and absorption of acoustic energy by solid bodies within the flow. Whilst scattering and absorption does not affect the principal sources of sound in the flow-field they do influence the distribution of noise once it reaches the ground plane. This deficiency is visible in Fig. 6.1 for the BL case, for example, where scattering and absorption by the drive enclosure (fuselage) most likely is responsible for the thin region of reduced noise that is present in the experimental data (Fig. 6.1(a)) in the centre and to the rear of the rotor disc but which is not captured by the numerical method (Fig. 6.1(b-d)).

For all three of the HART II flight cases, the distribution of acoustic pressure on the ground plane is characterised by two acoustic maxima which occur: one on the advancing side and one on the retreating side of the disc. The sound pressure can also be seen to decay rapidly upstream of the rotor towards the retreating side of the disc. The experimental results show the maximum SPL on the ground plane to be lower in the MN case than in the BL case and the directivity to be shifted towards the front of the rotor. In contrast, the maximum SPL in the MV case is higher but the directivity pattern is similar to that

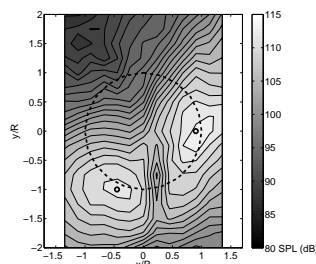
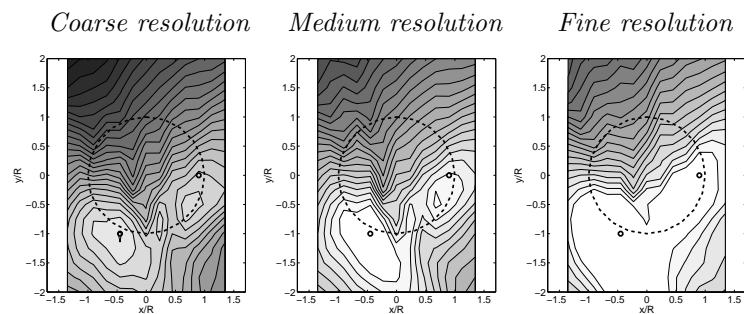
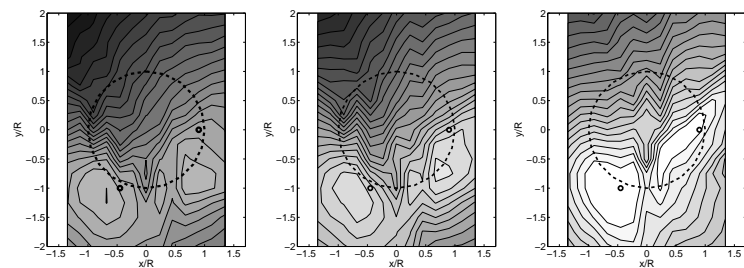
(a) *HART II measured*(b) *Lifting-line blade aerodynamic model*(c) *Lifting-chord blade aerodynamic model*

Figure 6.1: Predicted and measured SPL noise contours for the HART BL flight case. (The rotor position is marked by a dashed circle and small circles mark the positions of the microphones located at the SPL maxima in the measured data).

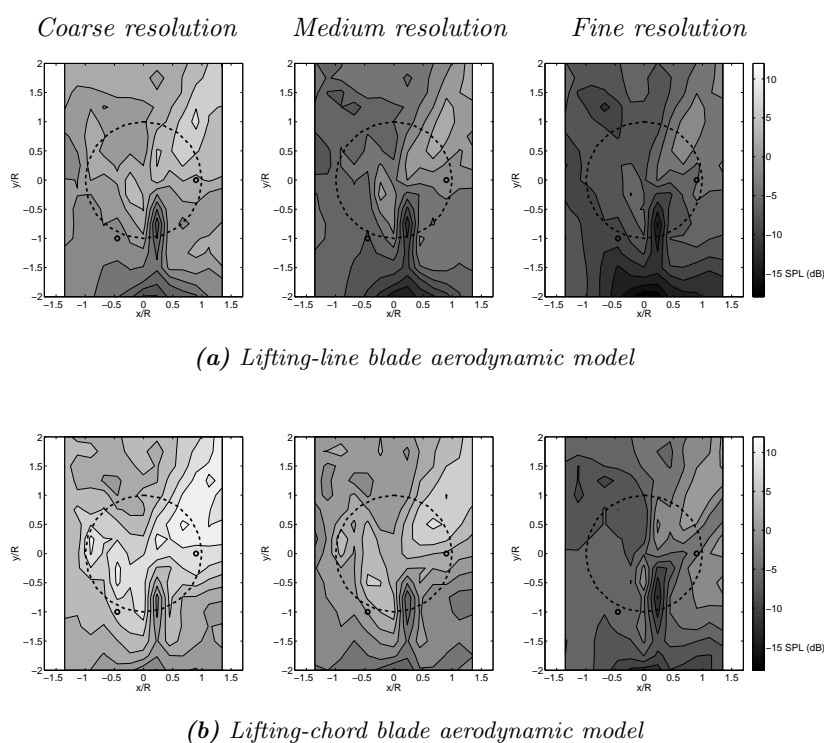


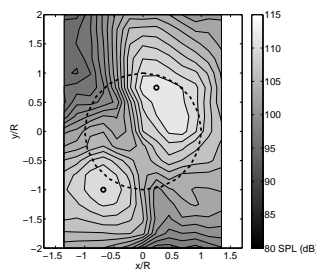
Figure 6.2: *Difference between the predicted and measured SPL noise contours for the HART BL flight case. (The rotor position is marked by a dashed circle and small circles mark the positions of the microphones located at the SPL maxima in the measured data).*

in the BL case.

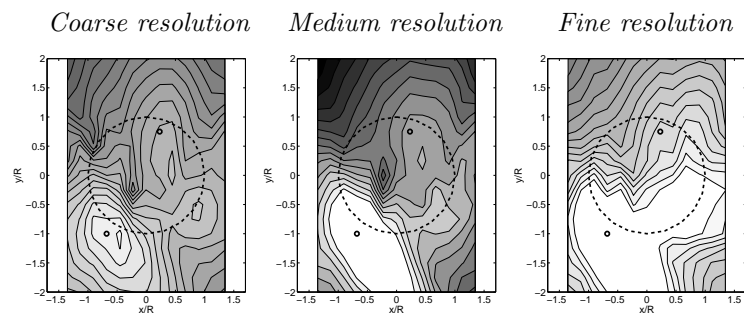
In general, as is the case with the airload predictions, the SPL predicted by the VTM shows a better correlation with the measured data on the retreating side of the disc than on the advancing side. The upstream decay in the noise level on the retreating side of the rotor disc, which is present in both the BL and MV cases, is well resolved irrespective of the aerodynamic model or the computational resolution that is used. The directivity of the sound is therefore captured well by the numerical method. The change in directivity found in the MN case compared to the BL case is also captured reasonably well by the numerics. The two SPL maxima, present in all the test cases, are also captured in the numerical predictions, albeit with some errors in their position and peak SPL value. The SPL maximum on the retreating side of the disc is generally more accurately captured, both in terms of its position and its amplitude, than the maximum that is present on the advancing side of the disc.

Where the lifting-line approach is used to model the aerodynamics of the blades, the over-

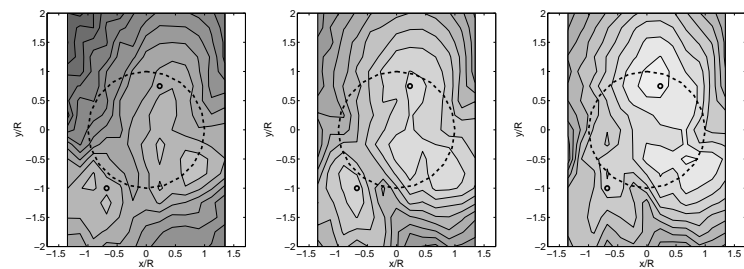
prediction in the amplitude of the BVI loading peaks with increase in the grid resolution translates into an over-prediction of the acoustic pressure levels on the ground plane beneath the rotor. Indeed, the peak value of the SPL at the maxima on both sides of the rotor increases significantly as the computational resolution is increased. The lifting-chord approach shows much less sensitivity to the computational resolution of the wake, with the result that the predicted peak value of the SPL, particularly at the maximum on the



(a) HART II measured



(b) Lifting-line blade aerodynamic model



(c) Lifting-chord blade aerodynamic model

Figure 6.3: Predicted and measured SPL noise contours for the HART MN flight case. (The rotor position is marked by a dashed circle and small circles mark the positions of the microphones located at the SPL maxima in the measured data).

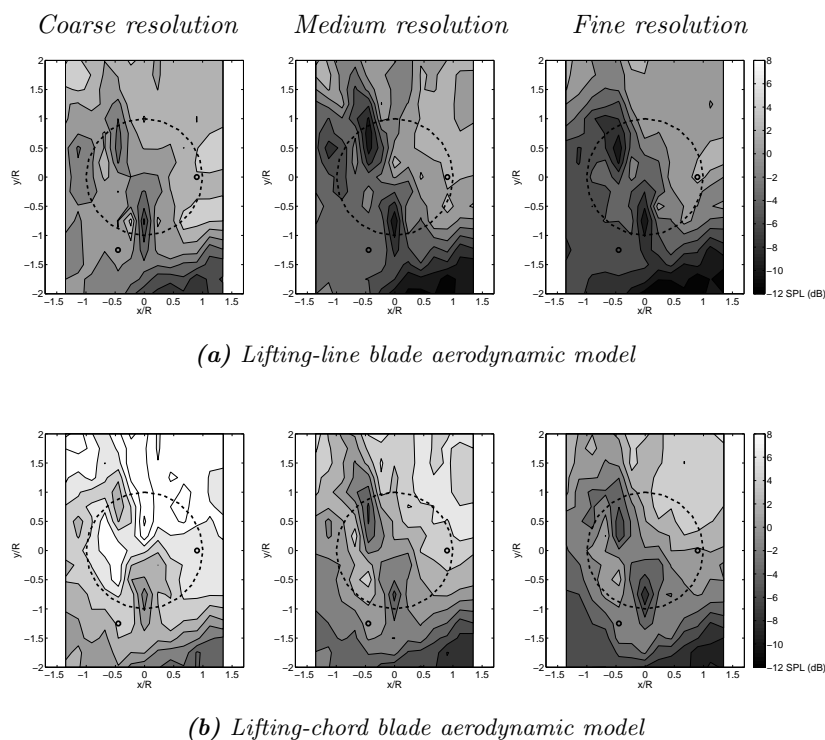


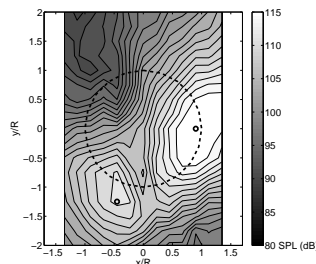
Figure 6.4: Difference between the predicted and measured SPL noise contours for the HART MN flight case. (The rotor position is marked by a dashed circle and small circles mark the positions of the microphones located at the SPL maxima in the measured data).

retreating side of the disc, compares well with the measured value. The method does still however over-predict the maximum noise levels when the finest computational resolution is used, although to a much lesser extent than when the lifting-line approach is adopted.

The error, shown in Figs. 6.2, 6.4 and 6.6, between the computed sound pressure level and that measured during the experiment is significantly reduced when the lifting-chord method is used to represent the aerodynamics of the rotor blades. Moreover, an increase in the computational resolution decreases the error in the acoustic predictions if the lifting-chord model is used, whereas the overall error increases significantly with the resolution if the lifting-line model is used.

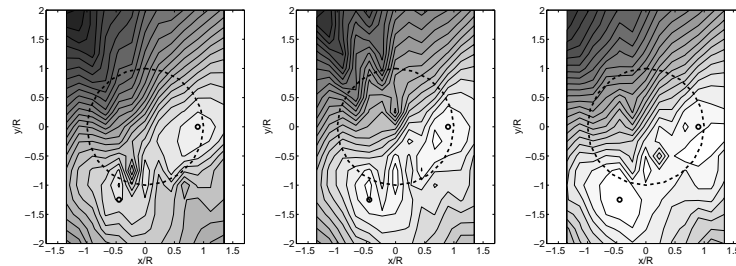
The reason for this behaviour is relatively straightforward. As the resolution of the computation is increased, the convection algorithm used within the VTM acts to resolve the vortex core over a smaller and smaller area, with the result that the vortical structures become more and more concentrated. A smaller vortex core radius for a given vortex strength implies higher peak velocities in the vortex. These produce more impulsive changes in the

loading and thus higher noise intensity when the vortex passes close to the blade (as shown in Fig. 6.1). The VTM is known to preserve very accurately the circulation in the flow-field (Ref. 50 and see Section 5.3) but as the vorticity distribution is concentrated onto a smaller and smaller area as the size of the cells is decreased, it results in an increasingly impulsive acoustic pressure when the vortex interacts with the blade. While the

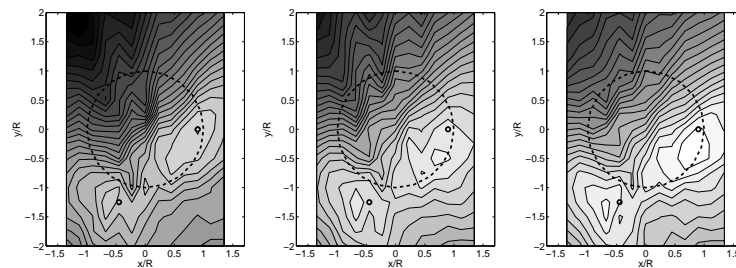


(a) HART II measured

Coarse resolution Medium resolution Fine resolution



(b) Lifting-line blade aerodynamic model



(c) Lifting-chord blade aerodynamic model

Figure 6.5: Predicted and measured SPL noise contours for the HART MV flight case. (The rotor position is marked by a dashed circle and small circles mark the positions of the microphones located at the SPL maxima in the measured data).

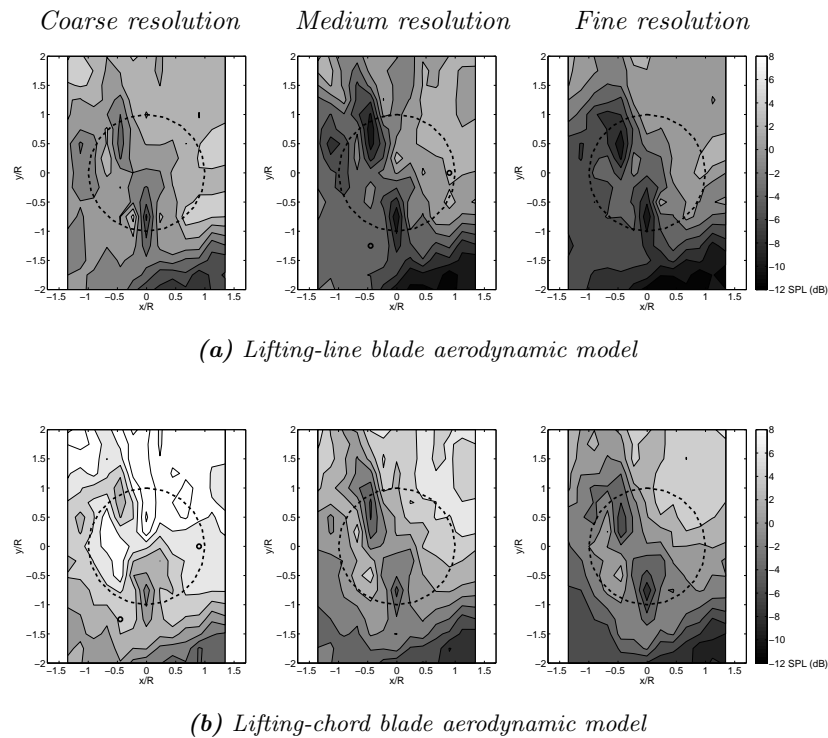


Figure 6.6: *Difference between the predicted and measured SPL noise contours for the HART MV flight case. (The rotor position is marked by a dashed circle and small circles mark the positions of the microphones located at the SPL maxima in the measured data).*

blade airload is less sensitive to maxima and minima in the velocity profile when using the lifting-chord approach, the acoustic post-processing method, depending as it does on the loading gradients rather than directly on the amplitude of the BVI-loading peaks, appears not to be so benign.

The calculations at both coarse and medium resolution predict the location of the SPL maximum on the advancing side of the rotor for all three HART II flight cases, except perhaps the MV case, to be further to the rear of the rotor disc than the position of the experimentally measured maximum. This discrepancy is marginally more apparent when the lifting-chord model is used than when the lifting-line model is used, even though the airloads are generally better predicted using the lifting-chord approach.

Several explanations for this anomaly are possible. The shift in the predicted phase of the higher harmonic components of the blade airload (Figs. 4.15 and 4.17 parts (a) and (c)) relative to the experimental data for the advancing side of the rotor will have some effect

on the location at which the maximum sound pressure level on the ground plane will occur. This error in phase is present when either the lifting-line or lifting-chord models are used, however, and therefore this observation does not explain the difference exhibited between the acoustic predictions that are obtained using the two blade aerodynamic models. The error in the relative strength of the two peaks at an azimuth of between 40° and 50° mentioned previously may also have some effect on the position of the predicted SPL maximum. This is discussed in more detail in the next Section.

6.2 Acoustic sources

The relationship between the noise produced at the acoustic maxima and the source of the noise in the individual BVI events on the rotor is examined in this Section. Parts (a) of Figs. 6.7–6.12 compare the predicted and measured time histories of acoustic pressure at the positions of the two microphones located at the points of measured maximum noise level on the advancing and retreating sides of the rotor for the BL case (Microphones M11 and M4 respectively). The positions of these microphones are represented by the small circles on the acoustic SPL plot in parts (b) of the same figures. The time histories are produced with expanded timescale corresponding to a single blade passage. The predicted distribution of acoustic source density due to loading on the disc is also plotted (in parts (b) of the figures) from the perspective of an observer located at the relevant microphone. The source density is evaluated from the loading noise term in the Ffowcs Williams-Hawkings equations and is plotted in ‘source time’ – in other words the sources are located at their position on the disc when the sound at the particular observer time was generated. In parts (b) of Figs. 6.7–6.12, the white lines indicate the locus of sources at the time of several of the stronger acoustic features in the numerical predictions of the noise produced by the rotor. These loci can be used to identify the positions of the BVI events that are responsible for the corresponding acoustic feature – as is done in parts (c) of the figures. Similar figures are produced for both the minimum noise (Figs. 6.14–6.19) and minimum vibration cases (Figs. 6.20–6.25).

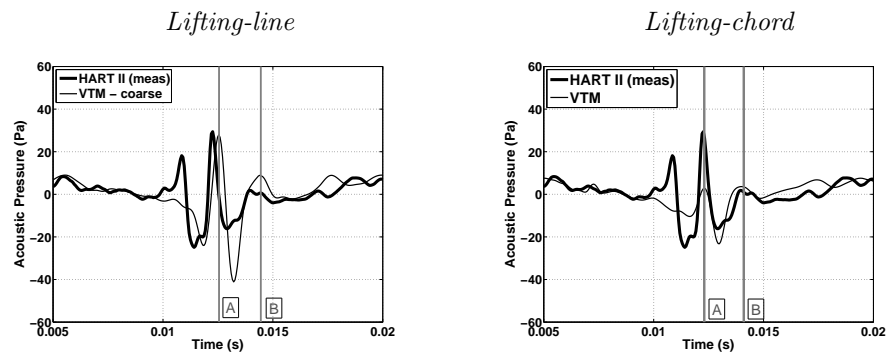
6.2.1 Baseline HART II flight case

In general, for the BL case, the computations reproduce the BVI acoustic signature at the microphone on the retreating side of the rotor with the correct phase but the amplitude of several of the acoustic peaks is very sensitive to the grid resolution and to the aerodynamic model that is used to represent the blade airloads. The lifting-chord model more accurately captures the phase of the signal and the accuracy of the prediction is influenced to a lesser extent by reducing the cell size than when the lifting-line model is used. The measured acoustic signature at this microphone contains a group of three peaks which occur at observer times of 0.01s, 0.013s and 0.014s respectively. The corresponding numerically-predicted acoustic features are marked as ‘A’ and ‘B’ in Figs. 6.7–6.9 parts (a) and (b). The most intense feature – marked ‘A’ in Figs. 6.7–6.9 – is the result of the strong parallel BVI which occurs at a blade azimuth of about 300° . It is interesting to note that the lifting-chord model predicts this intense BVI to occur about 10° earlier than when the lifting-line model is used (Figs. 6.7–6.9 parts (c)). This shift may account for the consistent azimuthal discrepancy in the location of the SPL maximum on this side of the disc that is predicted by the two approaches. The reason for the rather obviously missing peak in the numerically-generated signal at an observer time of 0.01s remains obscure, but the appearance (or not) of certain features in the acoustic signature is known to be crucially dependent, on occasion, on the relative amplitude and phasing of several consecutive BVI events. The reason for this discrepancy may thus be difficult to localise.

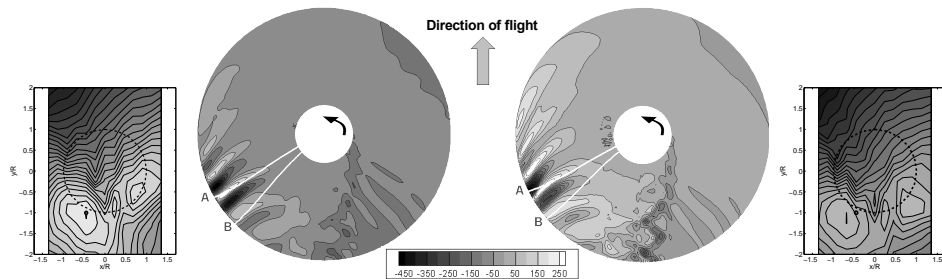
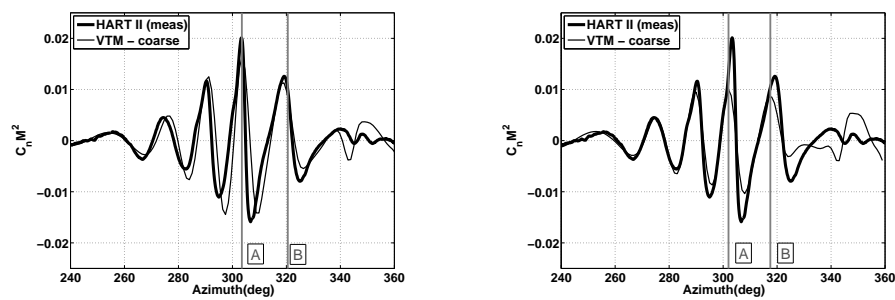
The measured time history of acoustic pressure at the microphone located on the advancing side of the rotor disc is characterised by two strong acoustic pulses per blade passage (see parts (a) and (b) of Figs. 6.10–6.12), the stronger of which occurs at an observer time of approximately 0.016s. The computations reproduce reasonably well the BVI noise signature at this location, but there is a consistent error in phase between the numerical and measured data. The amplitude of the predicted acoustic peaks is also very sensitive to the resolution of the flow-field, no matter which blade model is used.

The principal peak in the predicted acoustic signature at the maximum on the advancing side of the rotor is associated with a BVI event on this side of the disc, which occurs when

the reference blade is located at approximately 40° azimuth (marked ‘A’ in Figs. 6.10–6.12). Figure 6.13 shows the geometry of the wake at this instant and reveals the root vortices which are extruded from blades 1, 2 and 3, as well as a relatively old tip vortex from blade 4 to be interacting strongly with the reference blade. As mentioned earlier, (see Section 4.2.1) there is some question as to the accuracy of the representation of the root vortex system. Given the absence of any model of the rotor hub assembly in the simulations, any error in the prediction of the strength of the vorticity trailed from the roots of the blade would adversely affect the predictions of the flow and hence the predictions of acoustic pressure that is generated by the blades as they pass near the rear of the disc. An overly strong root vortex structure could quite feasibly distort the trajectories of the tip vortices that are responsible for the BVIs as they pass upward and through the zones of maximum BVI activity on the rotor disc, or indeed combine with the vorticity in the interacting vortex, resulting in an over-prediction of the intensity of the interaction. Data presented in Section 4.2.1 suggests that this effect will be relatively mild, however. In all cases, the predominant peak in the acoustic signal at the maximum on the advancing side of the rotor occurs later in the simulations than in the experimental data, suggesting indeed that at least a small misplacement of the vortex might be responsible for the discrepancies in the numerical representation of this acoustic feature.

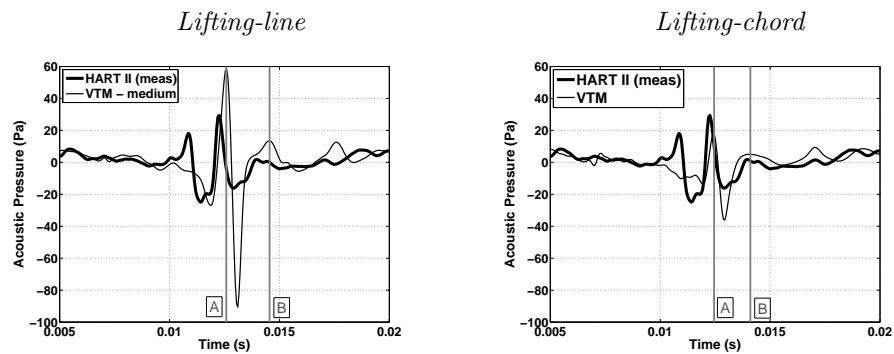


(a) Time history of acoustic pressure for a single blade passage

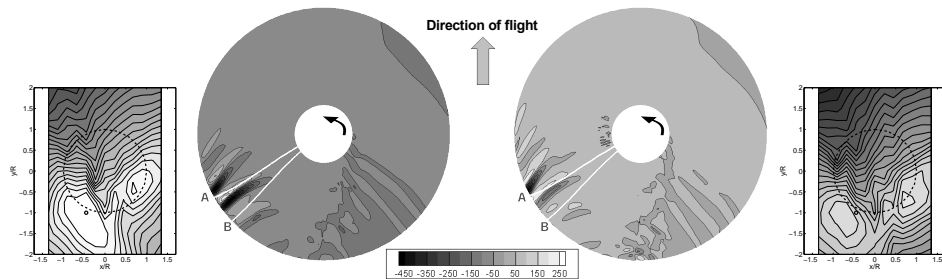
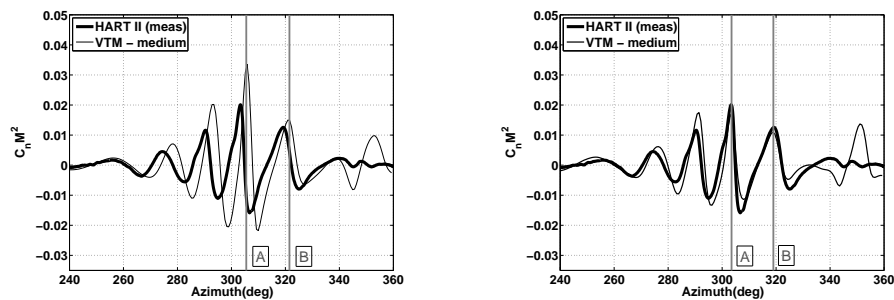
(b) Predicted acoustic source density (loading noise, Pa/m^3)

(c) BVI-induced airloads

Figure 6.7: Time history of acoustic pressure for one blade passage and the corresponding BVI-induced airloads and source density distribution on the rotor for an observer (marked by small circle) located at the experimentally-measured SPL maximum on the re-treating side of the rotor (HART II BL case). Numerical results are for the **coarse** computational resolution.

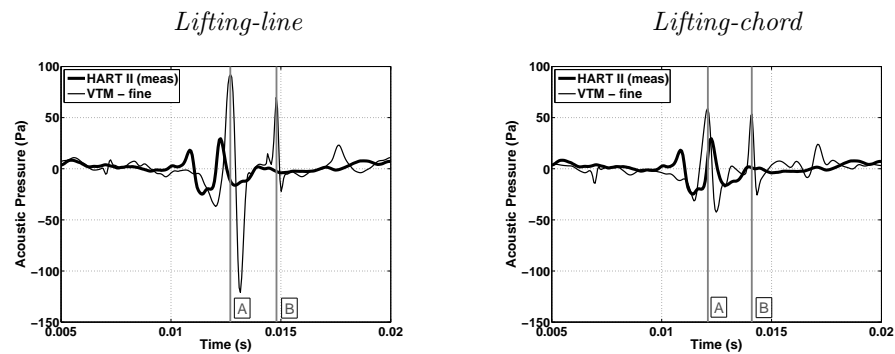


(a) Time history of acoustic pressure for a single blade passage

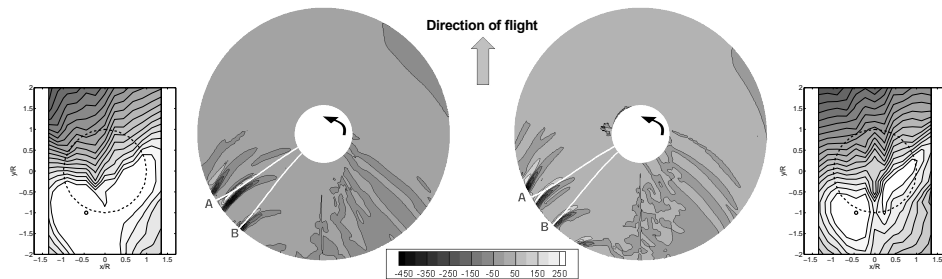
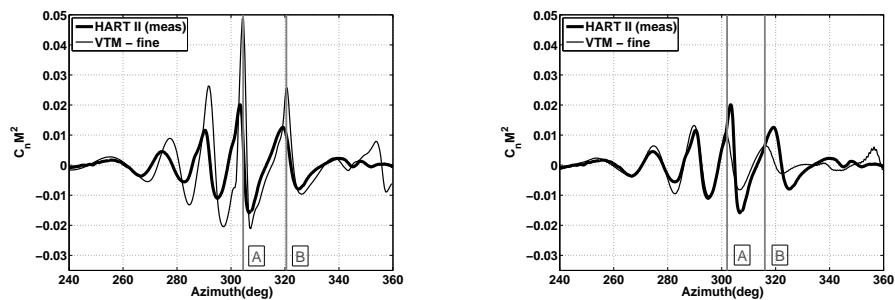
(b) Predicted acoustic source density (loading noise, Pa/m^3)

(c) BVI-induced airloads

Figure 6.8: Time history of acoustic pressure for one blade passage and the corresponding BVI-induced airloads and source density distribution on the rotor for an observer (marked by small circle) located at the experimentally-measured SPL maximum on the retreating side of the rotor (HART II BL case). Numerical results are for the **medium** computational resolution.

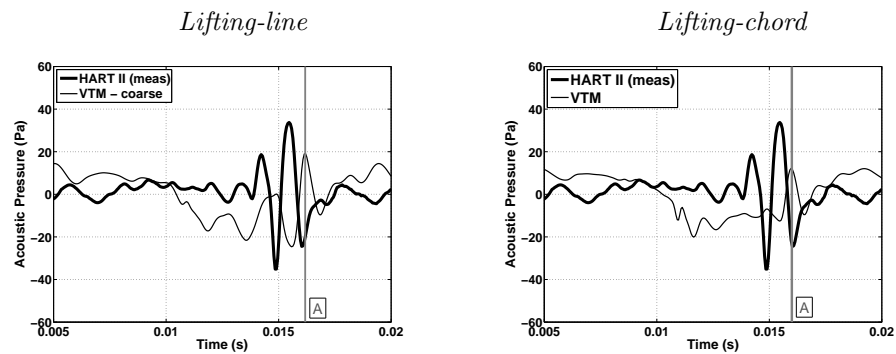


(a) Time history of acoustic pressure for a single blade passage

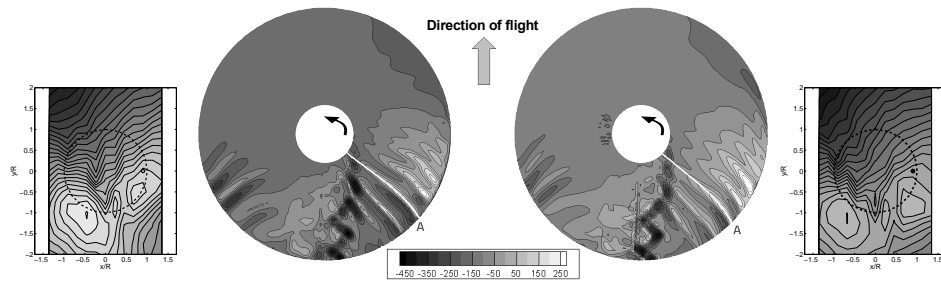
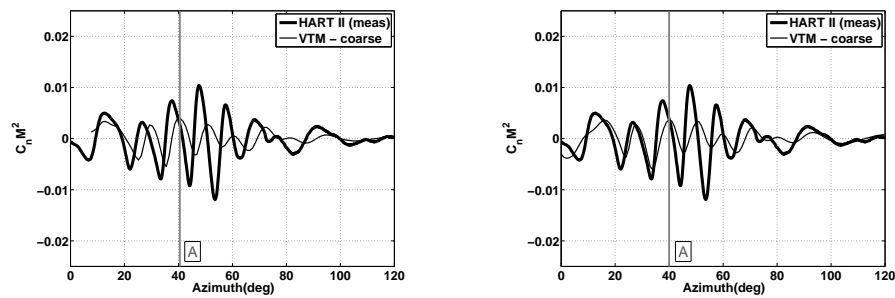
(b) Predicted acoustic source density (loading noise, Pa/m^3)

(c) BVI-induced airloads

Figure 6.9: Time history of acoustic pressure for one blade passage and the corresponding BVI-induced airloads and source density distribution on the rotor for an observer (marked by small circle) located at the experimentally-measured SPL maximum on the re-treating side of the rotor (HART II BL case). Numerical results are for the **fine** computational resolution.

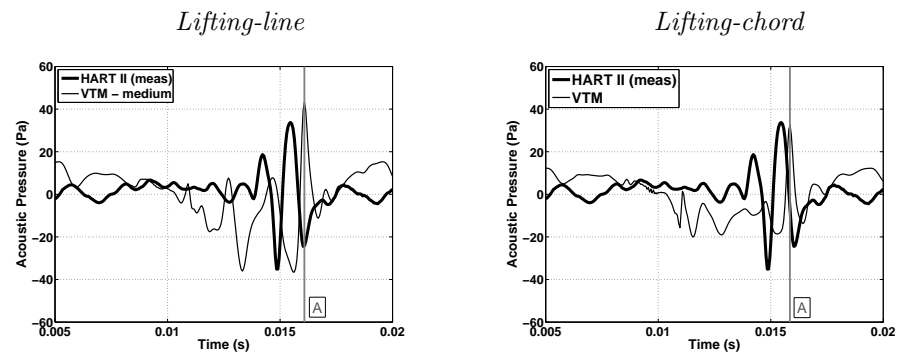


(a) Time history of acoustic pressure for a single blade passage

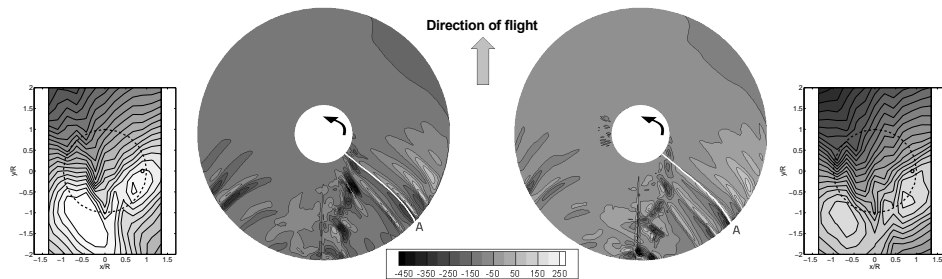
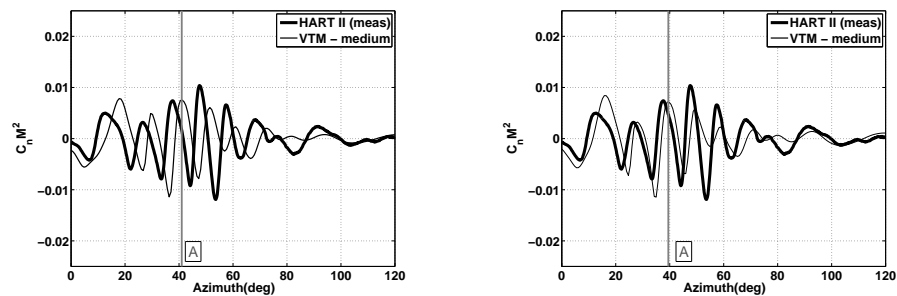
(b) Predicted acoustic source density (loading noise, Pa/m^3)

(c) BVI-induced airloads

Figure 6.10: Time history of acoustic pressure for one blade passage and the corresponding BVI-induced airloads and source density distribution on the rotor for an observer (marked by small circle) located at the experimentally-measured SPL maximum on the advancing side of the rotor (HART II BL case). Numerical results are for the **coarse** computational resolution.

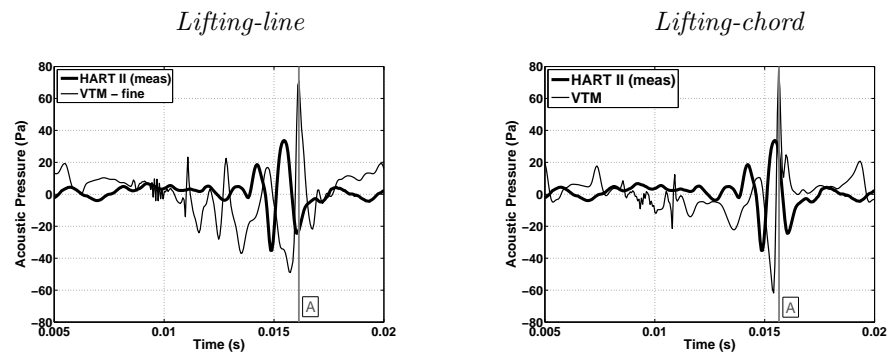


(a) Time history of acoustic pressure for a single blade passage

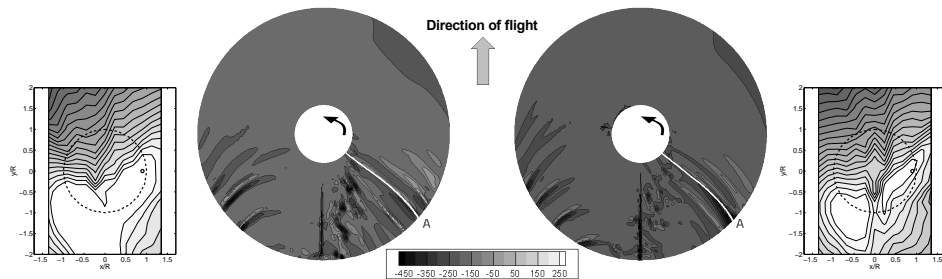
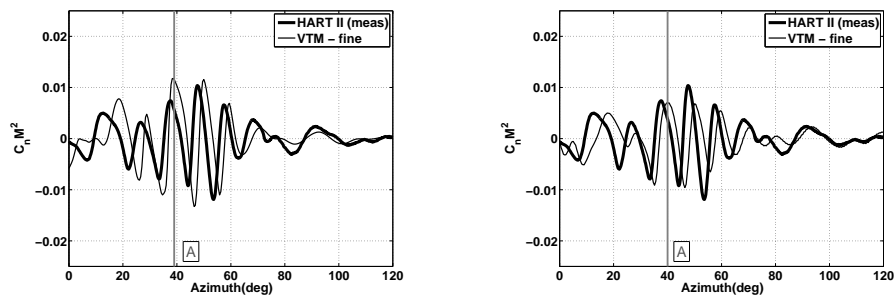
(b) Predicted acoustic source density (loading noise, Pa/m^3)

(c) BVI-induced airloads

Figure 6.11: Time history of acoustic pressure for one blade passage and the corresponding BVI-induced airloads and source density distribution on the rotor for an observer (marked by small circle) located at the experimentally-measured SPL maximum on the advancing side of the rotor (HART II BL case). Numerical results are for the **medium** computational resolution.



(a) Time history of acoustic pressure for a single blade passage

(b) Predicted acoustic source density (loading noise, Pa/m^3)

(c) BVI-induced airloads

Figure 6.12: Time history of acoustic pressure for one blade passage and the corresponding BVI-induced airloads and source density distribution on the rotor for an observer (marked by small circle) located at the experimentally-measured SPL maximum on the advancing side of the rotor (HART II BL case). Numerical results are for the **fine** computational resolution.

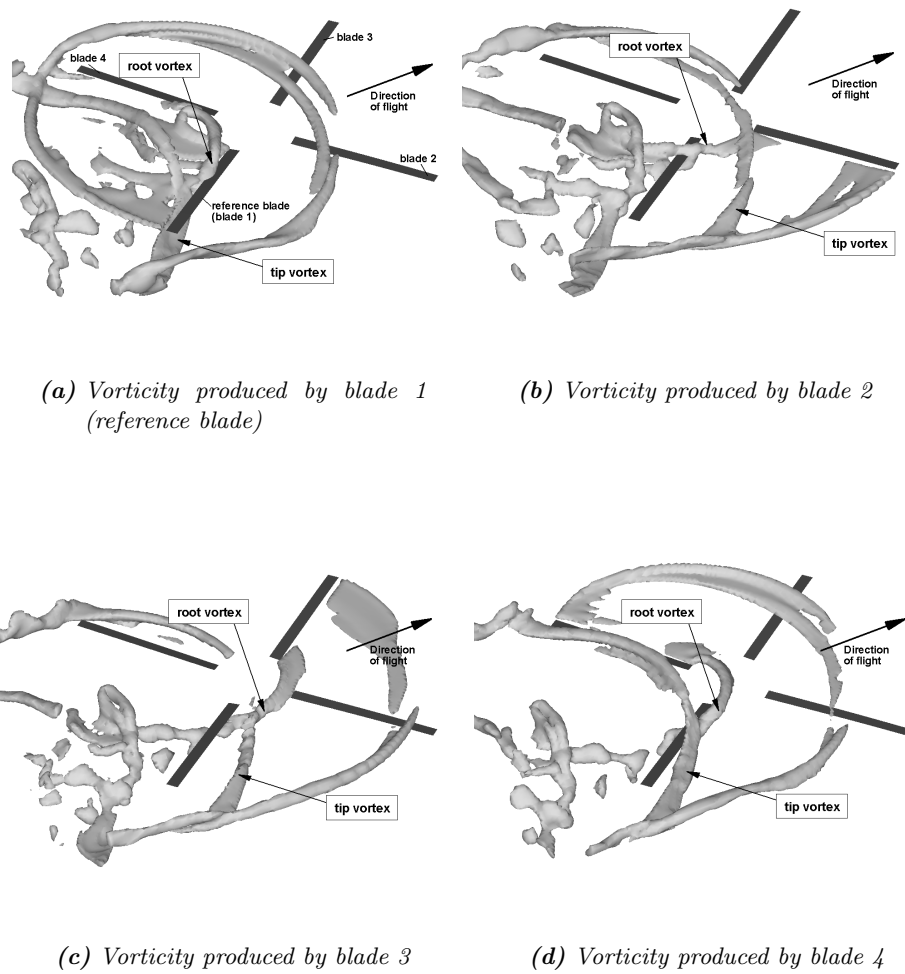


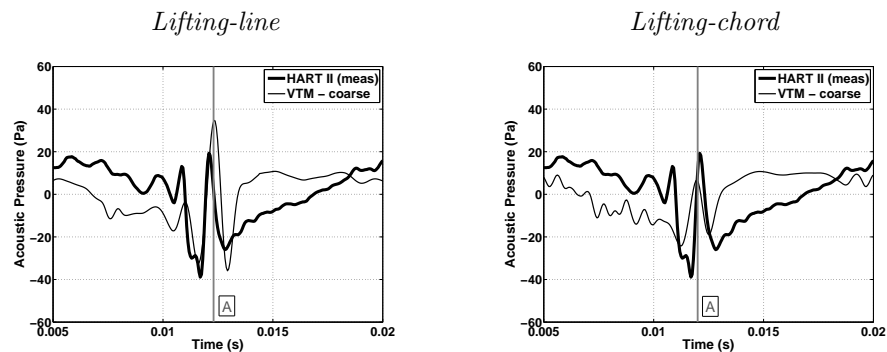
Figure 6.13: Geometry of the root and tip vortices as generated by each blade, when the reference blade lies at an azimuth of 40° .

6.2.2 Minimum noise HART II flight case

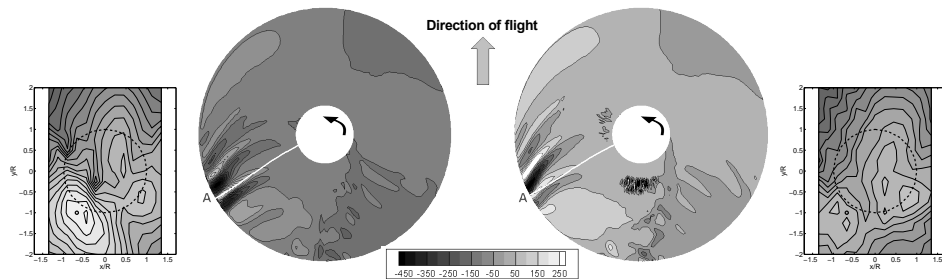
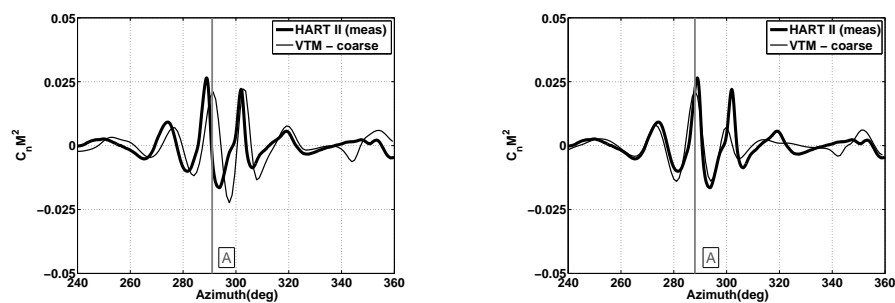
Figs. 6.14–6.19 show similar data to Figs. 6.7–6.12 but for the HART II MN flight case. Predicted and measured time histories of acoustic pressure at the positions of the two microphones located at the points of measured maximum noise level on the advancing and retreating sides of the rotor (Microphones M8 and M4 respectively), are shown in parts (a) of the figures. As in the BL case, for the MN case, the BVI acoustic signature at the microphone on the retreating side of the rotor is much better predicted by the computations than that on the advancing side of the disc. The dominant acoustic peak on the retreating side occurs at an observer time of 0.012s (marked as ‘A’ in Figs. 6.14–6.16) and is generally predicted with the correct phase and amplitude if the lifting-chord model is used to represent the aerodynamics of the rotor blades, regardless of the resolution of the computation. Where the lifting-line model is used, the amplitude of this acoustic peak is very sensitive to the grid resolution, and, as a result, the model consistently over-predicts the acoustic maximum on this side of the disc. Although the phase of the signal is generally well predicted by the lifting-line model, it is more accurately captured by lifting-chord model. This is most likely due to the differences between the two aerodynamic models in their predictions of the position of the most intense BVI on the retreating side of the rotor. Parts (c) of Figs. 6.14–6.16 show that, in the predictions of the lifting-chord model, and indeed, in the experimental data, the strongest BVI event occurs at 290° azimuth. The lifting-line model consistently over predicts the BVI-induced peak at 305° azimuth, and thus this BVI becomes the dominant peak in the airload predictions where this model has been used in the calculations. Although the earlier BVI event at 290° azimuth is not the main contributor to the noise produced at the acoustic maximum on the retreating side of the rotor, it is likely that the relative strength of the two BVI events which occur between 280° and 310° do affect the phasing of the corresponding acoustic features that are produced on this side of the rotor disc.

On the advancing side of the rotor disc, the discrepancies between the measured time history of acoustic pressure and the signal that is predicted by the VTM are much larger. The experimental signal is characterised by a strong negative peak at an observer time of

approximately 0.007s (marked 'A' in parts (a) and (b) of Figs. 6.10–6.12). Although this feature is clearly reproduced in the predicted signal there are errors in both phasing and amplitude at all computational resolutions and using both blade aerodynamic models. It is therefore not surprising that it is the acoustic maximum on this side of the rotor disc in this flight case that is the least well predicted of all the cases that have been simulated in this dissertation. Indeed, this observation is also consistent with those made regarding the predictions of the high-frequency blade airloads for the MN case, which show the largest errors in phase and amplitude for this flight case irrespective of the computational resolution or the blade model that has been used. Increasing the computational resolution increases somewhat the accuracy of the predictions of the BVI features in the acoustic pressure where the lifting-chord model has been used to represent the aerodynamics of the rotor blades within the computation. As a result, the SPL maximum on the advancing side shows the most favourable correlation with the measured data when predicted using the the lifting-chord model at the fine computational resolution.

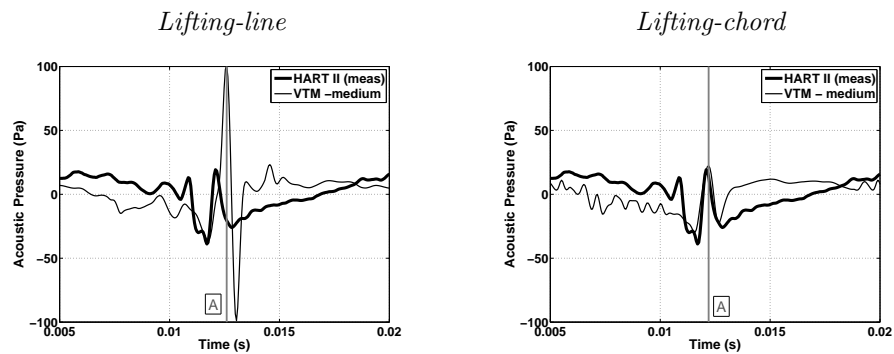


(a) Time history of acoustic pressure for a single blade passage

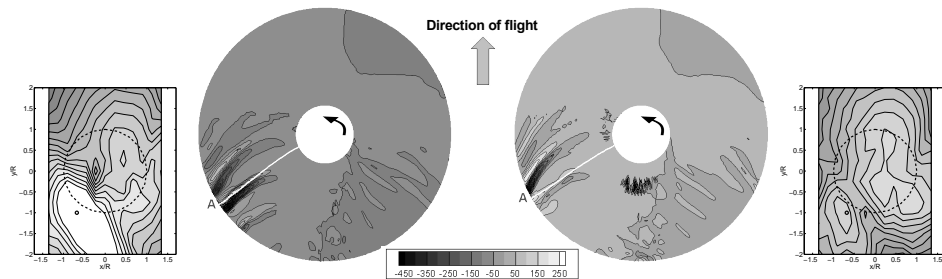
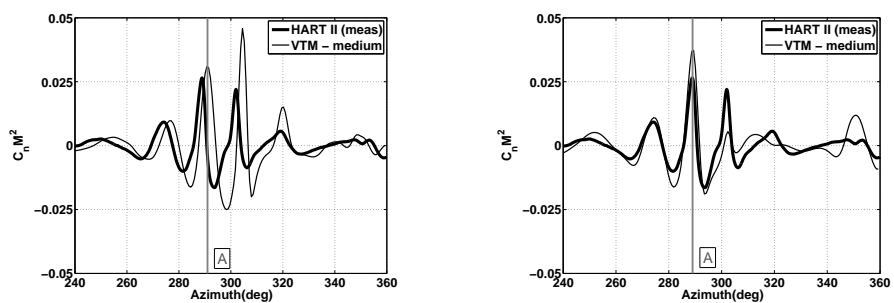
(b) Predicted acoustic source density (loading noise, Pa/m^3)

(c) BVI-induced airloads

Figure 6.14: Time history of acoustic pressure for one blade passage and the corresponding BVI-induced airloads and source density distribution on the rotor for an observer (marked by small circle) located at the experimentally-measured SPL maximum on the retreating side of the rotor (HART II MN case). Numerical results are for the **coarse** computational resolution.

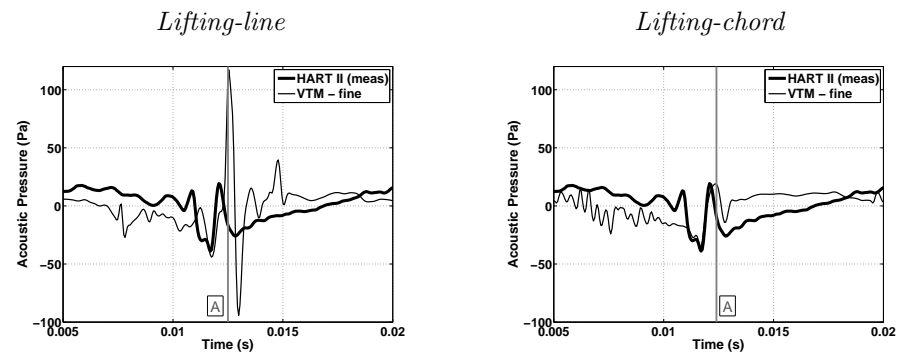


(a) Time history of acoustic pressure for a single blade passage

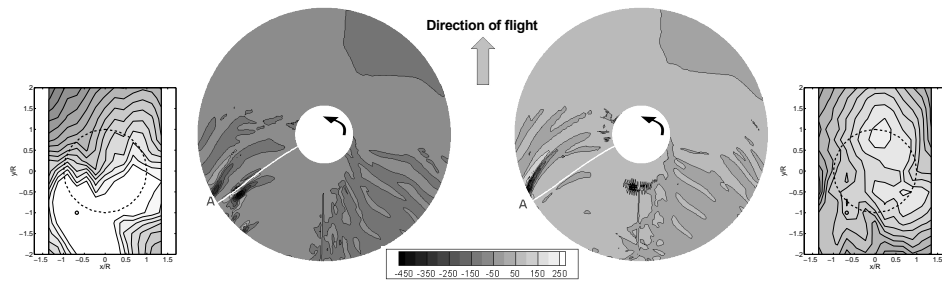
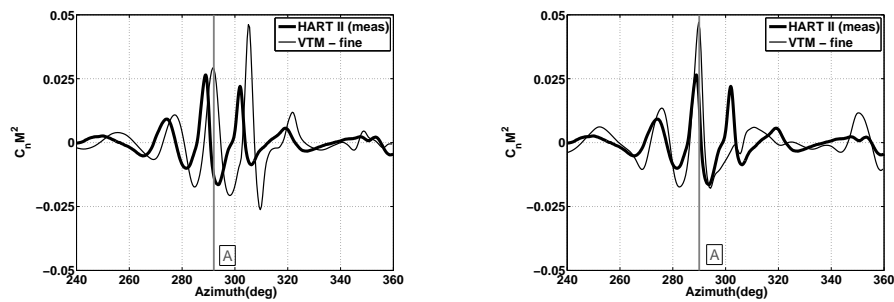
(b) Predicted acoustic source density (loading noise, Pa/m^3)

(c) BVI-induced airloads

Figure 6.15: Time history of acoustic pressure for one blade passage and the corresponding BVI-induced airloads and source density distribution on the rotor for an observer (marked by small circle) located at the experimentally-measured SPL maximum on the retreating side of the rotor (HART II MN case). Numerical results are for the **medium** computational resolution.

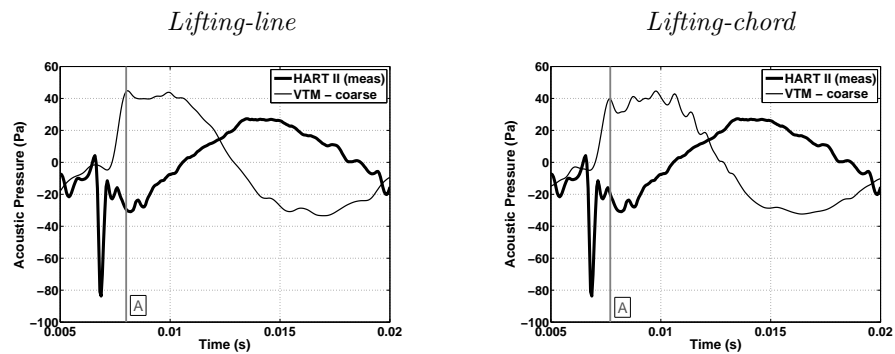


(a) Time history of acoustic pressure for a single blade passage

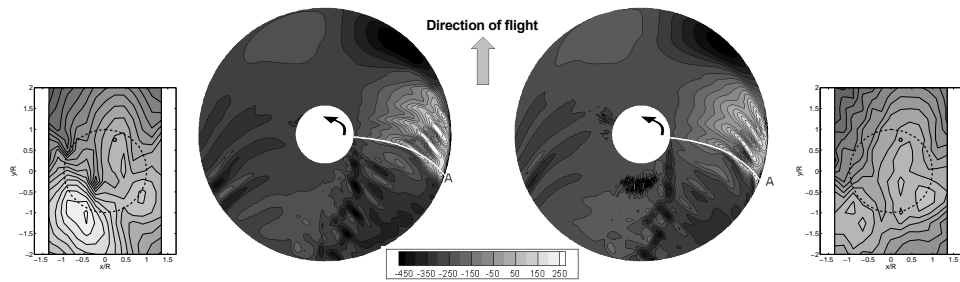
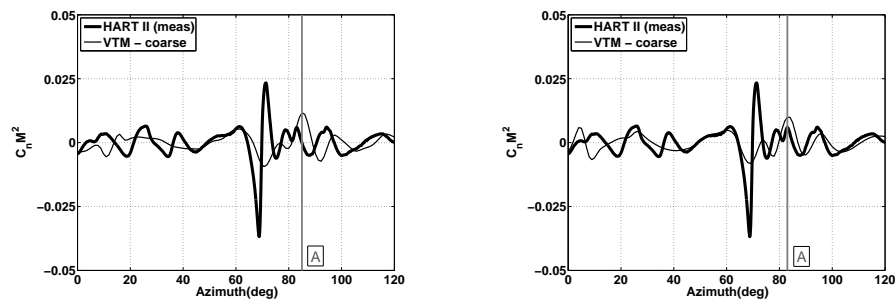
(b) Predicted acoustic source density (loading noise, Pa/m^3)

(c) BVI-induced airloads

Figure 6.16: Time history of acoustic pressure for one blade passage and the corresponding BVI-induced airloads and source density distribution on the rotor for an observer (marked by small circle) located at the experimentally-measured SPL maximum on the retreating side of the rotor (HART II MN case). Numerical results are for the **fine** computational resolution.

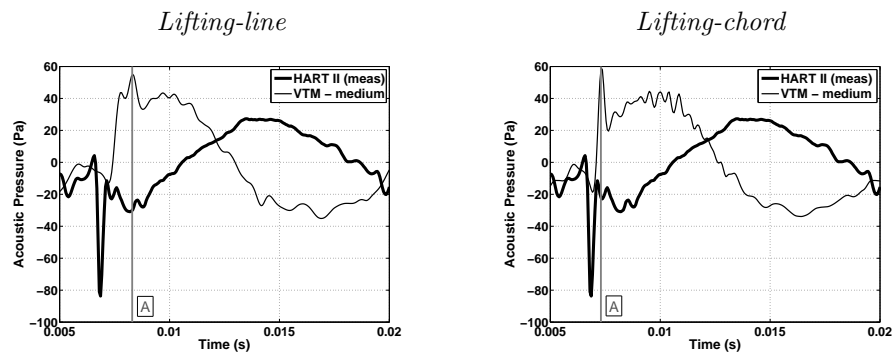


(a) Time history of acoustic pressure for a single blade passage

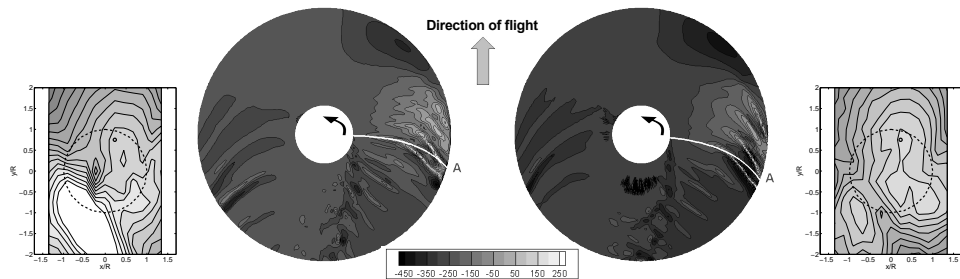
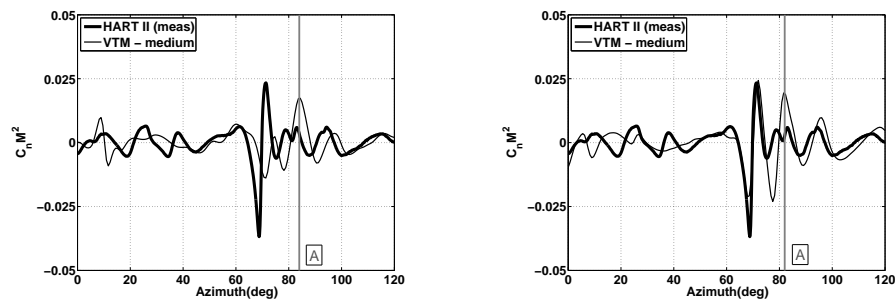
(b) Predicted acoustic source density (loading noise, Pa/m^3)

(c) BVI-induced airloads

Figure 6.17: Time history of acoustic pressure for one blade passage and the corresponding BVI-induced airloads and source density distribution on the rotor for an observer (marked by small circle) located at the experimentally-measured SPL maximum on the advancing side of the rotor (HART II MN case). Numerical results are for the **coarse** computational resolution.

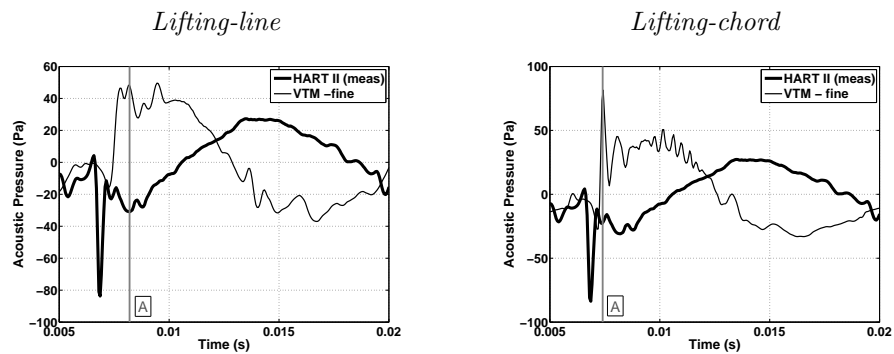


(a) Time history of acoustic pressure for a single blade passage

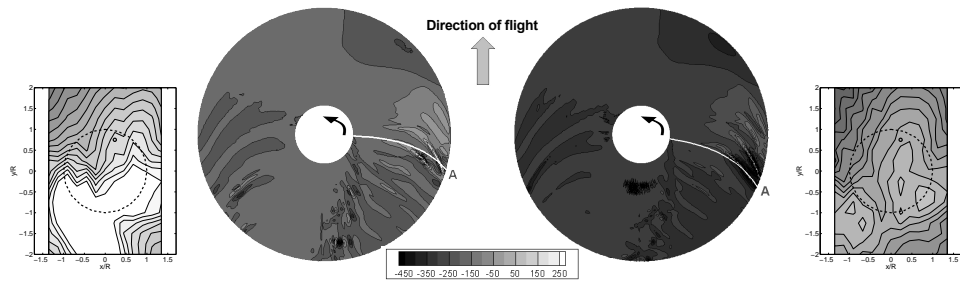
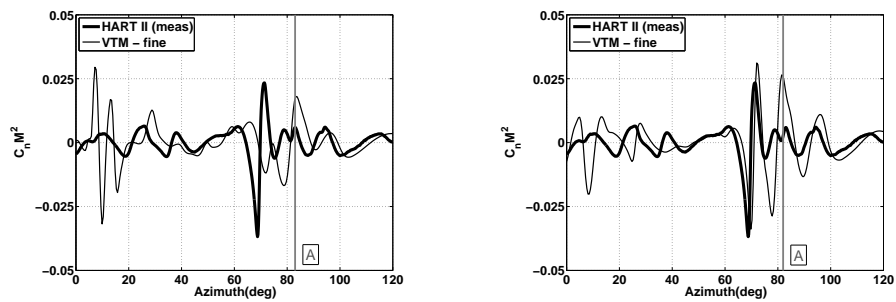
(b) Predicted acoustic source density (loading noise, Pa/m^3)

(c) BVI-induced airloads

Figure 6.18: Time history of acoustic pressure for one blade passage and the corresponding BVI-induced airloads and source density distribution on the rotor for an observer (marked by small circle) located at the experimentally-measured SPL maximum on the advancing side of the rotor (HART II MN case). Numerical results are for the **medium** computational resolution.



(a) Time history of acoustic pressure for a single blade passage

(b) Predicted acoustic source density (loading noise, Pa/m^3)

(c) BVI-induced airloads

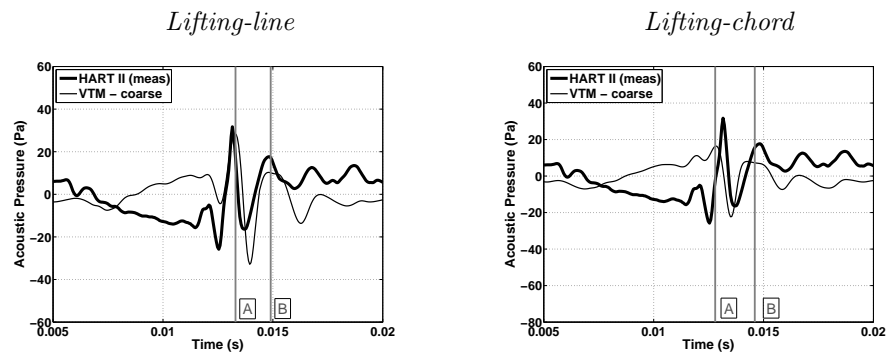
Figure 6.19: Time history of acoustic pressure for one blade passage and the corresponding BVI-induced airloads and source density distribution on the rotor for an observer (marked by small circle) located at the experimentally-measured SPL maximum on the advancing side of the rotor (HART II MN case). Numerical results are for the **fine** computational resolution.

6.2.3 Minimum vibration HART II flight case

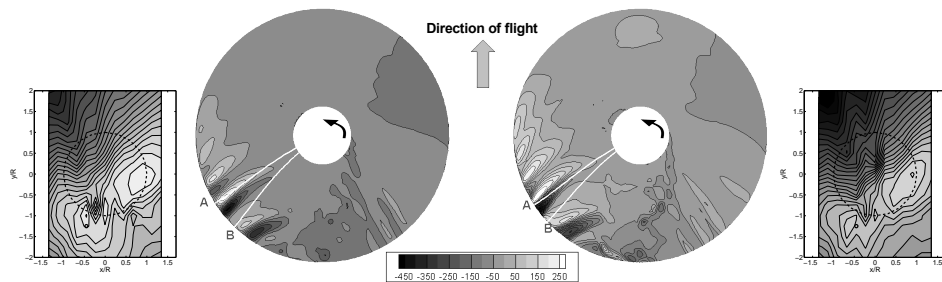
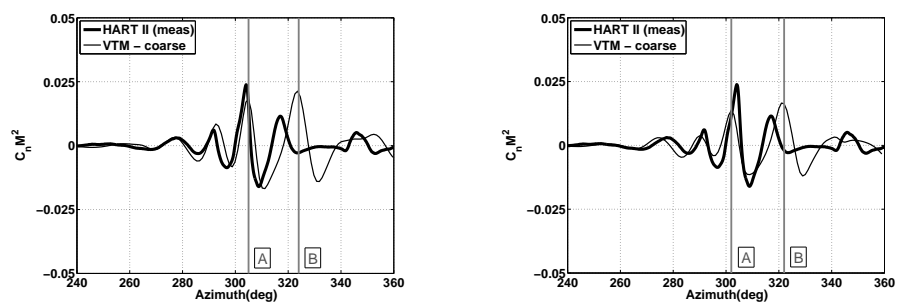
Figs. 6.20–6.25 compare the predicted and measured time histories of acoustic pressure at the positions of the two microphones located at the points of measured maximum noise level on the advancing and retreating sides of the rotor for the MV case (Microphones M10 and M5 respectively). On the retreating side of the disc, the time history of acoustic pressure is very similar to that of the BL flight case, which is not surprising, given that the geometry of the wake and, in particular, the position and intensity of the BVI events on this side of the rotor, are very similar in both cases. The two principal peaks in the MN case occur at observer times of approximately 0.013s and 0.015s and are marked as ‘A’ and ‘B’ in Figs. 6.20–6.22 parts (a). The plots of acoustic density (parts (b) in Figs. 6.20–6.22) show two very strong BVI events in the fourth quadrant of the rotor disc. The interaction which produces the most impulsive acoustic feature occurs at a blade azimuth of about 310° and, in a similar way to that in the BL case, is most likely due to a near-parallel BVI. Again, the predicted acoustic pressure shows a marked improvement in comparison to experimental data when the lifting-chord model has been used to represent the aerodynamic of the blades. This is because this model more accurately the phase and the amplitude of the acoustic features that are present compared to the lifting-line model.

The time history of the acoustic pressure on the advancing side of the disc is much more complicated. The measured signal is dominated by three strong peaks at observer times of 0.014s, 0.015s and 0.016s, respectively. Although similar peaks are apparent in the numerically-predicted signal there are large discrepancies in the phase and amplitude of these acoustic features. The observed features correspond to fairly similar BVI-induced loading peaks at blade azimuths of 23° , 35° and 45° , as shown in parts (c) of Figs. 6.23–6.25, each having much the same amplitude and pulse width. Correspondingly, the measured acoustic signal also contains three principal acoustic peaks, each of similar pulse width and amplitude. In the predicted BVI-induced airloads, a consistent phase shift relative to the measured data results in an error in the predicted phase of the acoustic pressure signal, and, ultimately, in a slight error in the prediction of the SPL maximum on this side of the rotor disc. In addition to the BVI events that are observed in the plots of

acoustic source density, the ridge that is visible in the contours in the second quadrant of the rotor disc is worthy of note. This is most likely due to the reversed loading at the tip of the advancing blade under the conditions of this particular test, which causes the formation of a twin vortex structure on this side of the rotor (see Section 5.2.4). This feature, although interesting is not thought to contribute significantly to the acoustic radiation from the rotor, however.

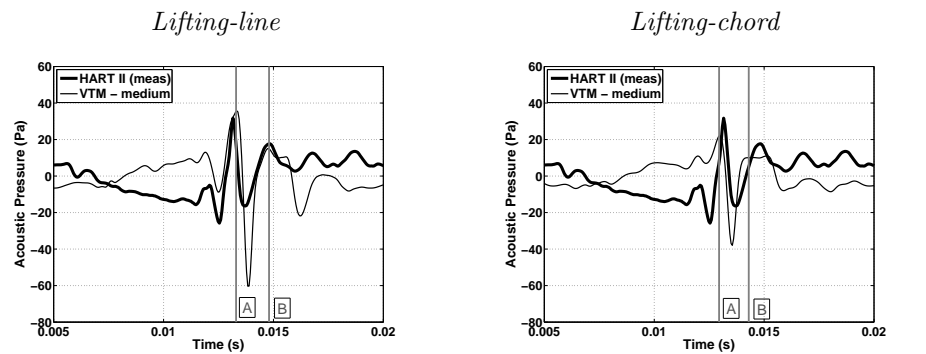


(a) Time history of acoustic pressure for a single blade passage

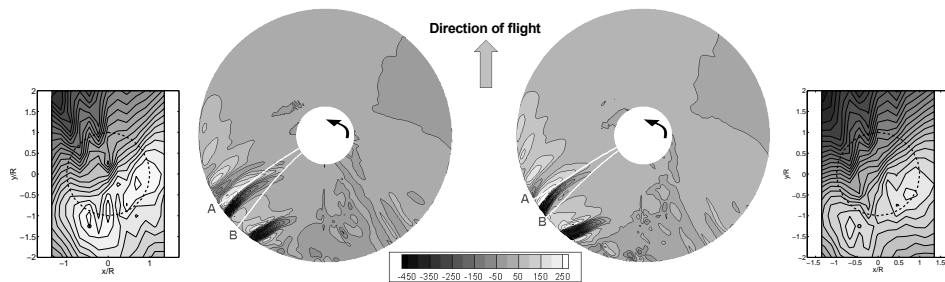
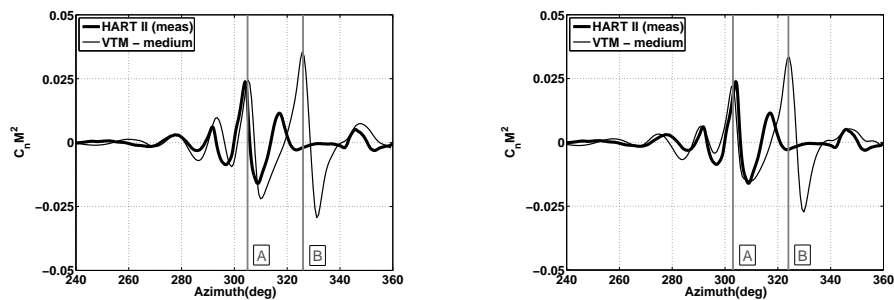
(b) Predicted acoustic source density (loading noise, Pa/m^3)

(c) BVI-induced airloads

Figure 6.20: Time history of acoustic pressure for one blade passage and the corresponding BVI-induced airloads and source density distribution on the rotor for an observer (marked by small circle) located at the experimentally-measured SPL maximum on the retreating side of the rotor (HART II MV case). Numerical results are for the **coarse** computational resolution.

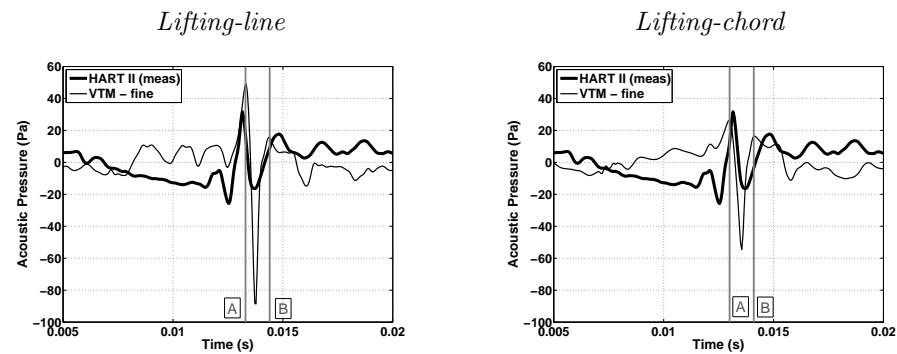


(a) Time history of acoustic pressure for a single blade passage

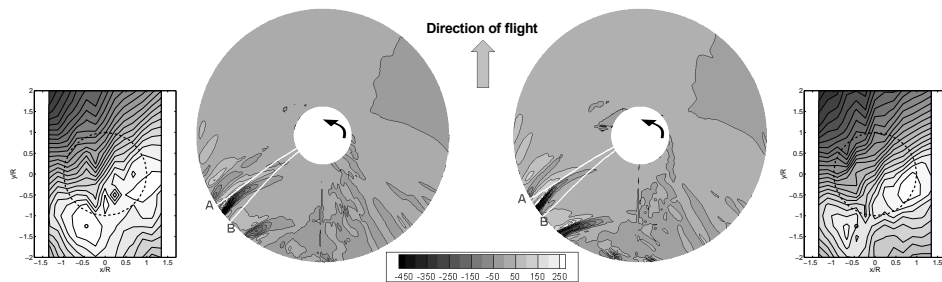
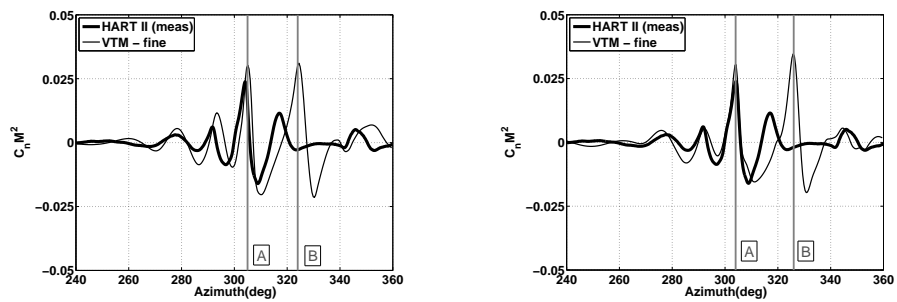
(b) Predicted acoustic source density (loading noise, Pa/m^3)

(c) BVI-induced airloads

Figure 6.21: Time history of acoustic pressure for one blade passage and the corresponding BVI-induced airloads and source density distribution on the rotor for an observer (marked by small circle) located at the experimentally-measured SPL maximum on the retreating side of the rotor (HART II MV case). Numerical results are for the **medium** computational resolution.

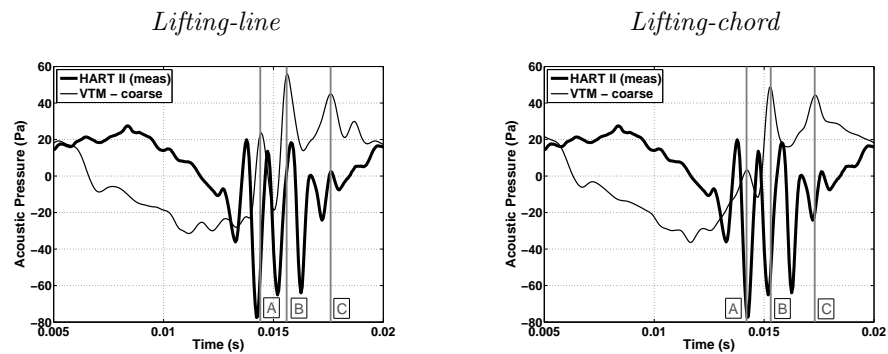


(a) Time history of acoustic pressure for a single blade passage

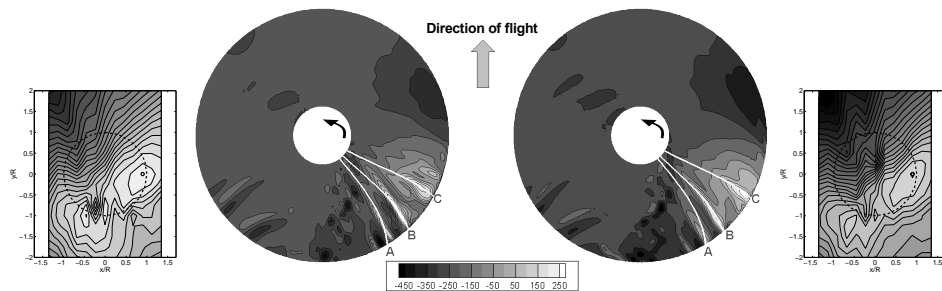
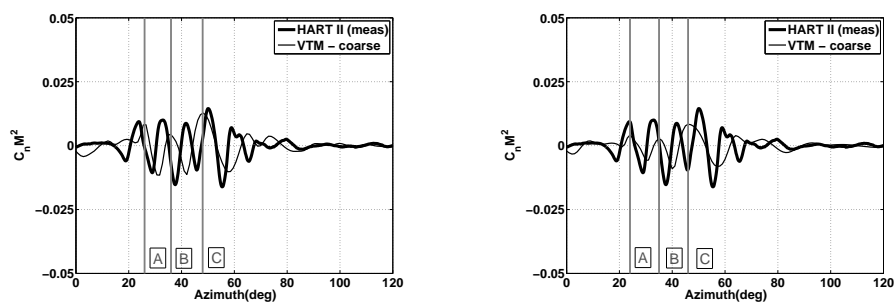
(b) Predicted acoustic source density (loading noise, Pa/m^3)

(c) BVI-induced airloads

Figure 6.22: Time history of acoustic pressure for one blade passage and the corresponding BVI-induced airloads and source density distribution on the rotor for an observer (marked by small circle) located at the experimentally-measured SPL maximum on the retreating side of the rotor (HART II MV case). Numerical results are for the **fine** computational resolution.

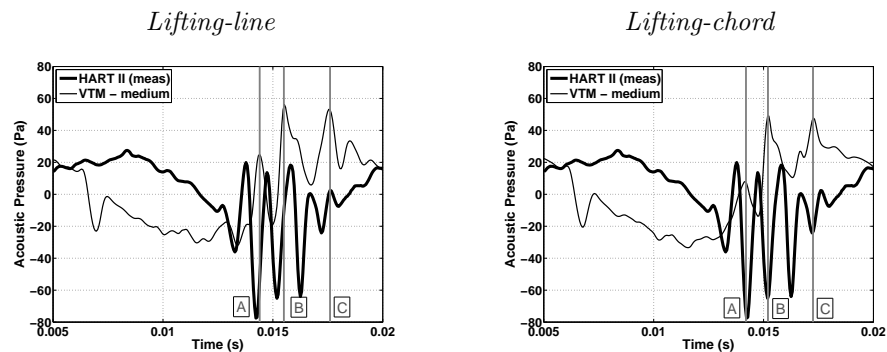


(a) Time history of acoustic pressure for a single blade passage

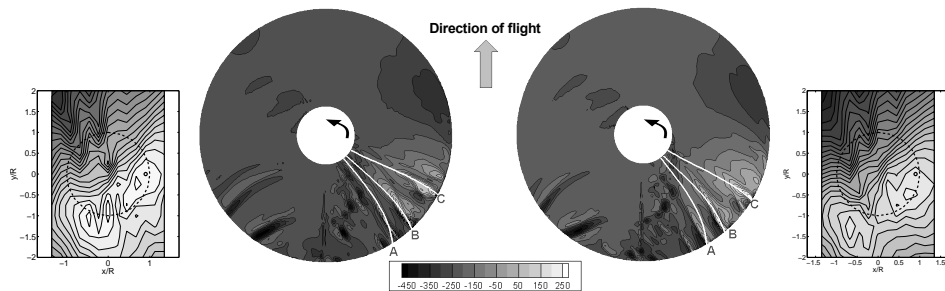
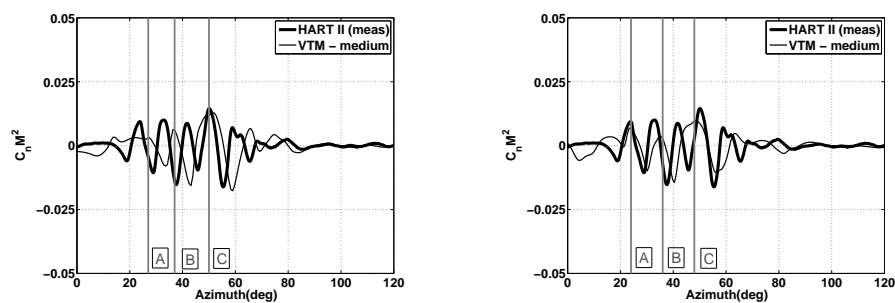
(b) Predicted acoustic source density (loading noise, Pa/m^3)

(c) BVI-induced airloads

Figure 6.23: Time history of acoustic pressure for one blade passage and the corresponding BVI-induced airloads and source density distribution on the rotor for an observer (marked by small circle) located at the experimentally-measured SPL maximum on the advancing side of the rotor (HART II MV case). Numerical results are for the **coarse** computational resolution.

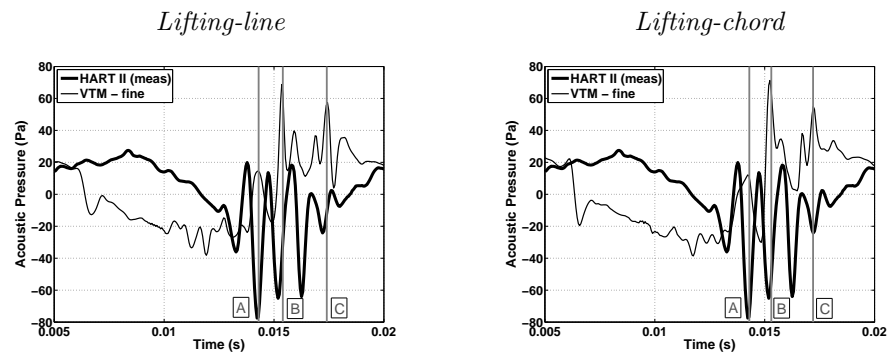


(a) Time history of acoustic pressure for a single blade passage

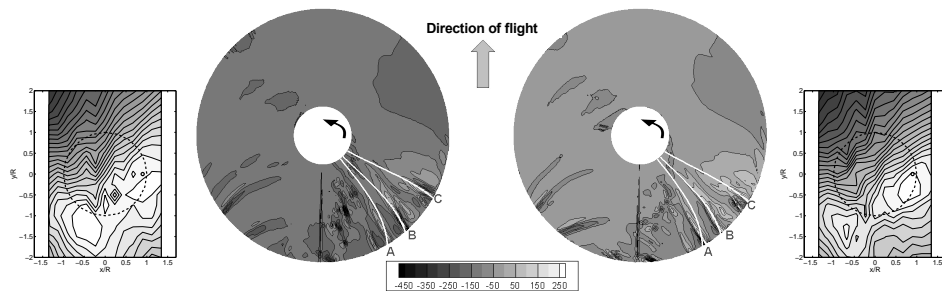
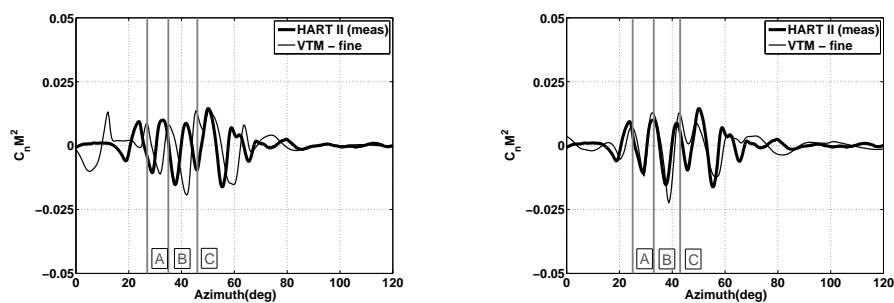
(b) Predicted acoustic source density (loading noise, Pa/m^3)

(c) BVI-induced airloads

Figure 6.24: Time history of acoustic pressure for one blade passage and the corresponding BVI-induced airloads and source density distribution on the rotor for an observer (marked by small circle) located at the experimentally-measured SPL maximum on the advancing side of the rotor (HART II MV case). Numerical results are for the **medium** computational resolution.



(a) Time history of acoustic pressure for a single blade passage

(b) Predicted acoustic source density (loading noise, Pa/m^3)

(c) BVI-induced airloads

Figure 6.25: Time history of acoustic pressure for one blade passage and the corresponding BVI-induced airloads and source density distribution on the rotor for an observer (marked by small circle) located at the experimentally-measured SPL maximum on the advancing side of the rotor (HART II MV case). Numerical results are for the **fine** computational resolution.

6.3 Summary

The experimentally-measured sound pressure levels (SPL) are compared to numerical predictions which are calculated from the airloads predicted by the VTM using a Farassat-1A formulation of the Ffowcs Williams-Hawkings Equations. The directivity of the radiated noise pattern is generally captured well by the numerics, as is the location and magnitude of the maxima in the sound pressure level on the ground plane below the rotor, at least on the retreating side of the disc. The upstream decay of the radiated signal is also well-captured, particularly in the BL flight case. Yet again the larger deficiencies in prediction are encountered on the advancing side of the rotor, where magnitude and phase errors in the predicted BVI-induced component of the blade loading translate into more significant errors in the position and magnitude of the maximum in the sound pressure field on this side of the rotor compared to that on the retreating side.

The time history of the acoustic pressure at the SPL maximum on each side of the disc is used to determine the time of several of the stronger acoustic features in the numerical predictions. Loci of sources at the observer times when the stronger acoustic features occur, are plotted on the predicted distribution of acoustic source density, and are used to determine the positions on the rotor disc of the major acoustic sources. The principal features in the acoustic pressure signal can then be tracked back to the individual BVI loading peaks in the airload predictions.

Three computational resolutions were used to expose the effect of grid resolution on the quality of predictions. Where the lifting-line model was used to represent the aerodynamics of the blades, the resulting time history of the acoustic pressure that is predicted is found to be extremely sensitive to the cell size that is used in the computations. The predicted amplitude of the BVI-induced acoustic features increases significantly as the cell size that is used to resolve the wake is reduced. The over-prediction of the amplitude of the BVI-induced acoustic features which occurs as the resolution of the computation is reduced to some degree when using the lifting-chord model. While the blade airload is less sensitive to maxima and minima in the velocity profile when using the lifting-chord approach, the acoustic post-processing method, depends on the loading gradients rather than directly

on the amplitude of the BVI-loading peaks, and is therefore more sensitive. In almost all cases, however, increasing the resolution of the computational grid increases the accuracy of the acoustic predictions when the lifting-chord model is used, and thus the lifting-chord model at the highest resolution produces the best representation of the distribution of sound pressure on the ground plane below the rotor.

Chapter 7

Conclusions

Interactions between the blades of the helicopter rotor and vortical structures within the wake that they generate, known as blade-vortex interactions (BVIs), are a significant source of impulsive loading and noise. Reduction of noise has become a priority within the helicopter industry and, as such, there is a need to develop methods that can predict accurately the radiated noise for flight conditions where blade-vortex interactions are dominant. Particularly in the context of rotor design, such methods are required to produce high fidelity predictions of the rotor aero-acoustic noise but at a much reduced computational cost when compared to methods that are currently available. Since both the distance between the blade and the vortex and the strength of the interacting vortex have a strong effect on the magnitude of any BVI event, accurate prediction of BVI-induced airload relies critically upon the correct simulation of the blade deformation and of the position and strength of vortical structures within the rotor wake. Accurate modelling of the wake trailed from the helicopter rotor has thus become one of the primary challenges for the developers of Computational Fluid Dynamics (CFD) methods designed for rotorcraft applications. The complexity of the rotor wake, and the strong mutual dependence of the aerodynamics and structural dynamics, renders accurate prediction of the BVI-related blade airloads and acoustics a particularly challenging task.

The Vorticity Transport Model (VTM), developed by Brown, couples a model for the aerodynamics of the blade to an Eulerian representation of the dynamics of the vorticity in the

flow-field. The governing equations in vorticity-velocity form are solved on a structured Cartesian grid and Toro's Weighted Average Flux method is used to track the evolution of vorticity through the computational domain. Wave-amplifier functions are used within the Weighted Average Flux method to control effectively the compactness of the vortical structures in the flow-field while still conserving the total vorticity present in the computational domain. This property makes the VTM particularly suitable to representing the vortices that are present within the wake of a helicopter in flight. The grid structure used in the VTM is adaptive and is free to follow the evolution of the wake. This eliminates the requirement for explicit numerical boundary conditions at the edge of the computational domain and increases the computational efficiency of the method. The VTM offers significant flexibility in the way that the source of vorticity into the wake can be generated and thus the method by which local aerodynamics of the blades are modelled. This flexibility makes the VTM ideal for studying the effect of the blade aerodynamic model on the fidelity of the prediction of the high-frequency, BVI-induced loads on the rotor and hence on the accuracy with which the acoustic signature of the aircraft can be predicted.

Airload, wake and acoustic predictions using the VTM have been compared against wind tunnel data obtained during the HART II experimental programme, for a model rotor based on the characteristics of those of the Bo105 helicopter. The rotor was flown in a descending flight condition in which the loading on its blades contained significant high-frequency content due to the presence of blade vortex interactions. This data has been used to analyse the ability of two blade aerodynamic models to capture the detailed, high frequency, BVI-induced loading on the rotor and thus the acoustic signature of the aircraft.

The local aerodynamics of the rotor blades are modelled within the Vorticity Transport Model using two different approaches. The first model is an extension of the Weissinger-L lifting-line model, in which the strength of a bound vortex, placed at the quarter-chord of each blade panel, is determined by imposing a zero-through flow boundary condition at a single point located at the three-quarter chord of the panel. This predictions of airload and acoustics obtained using this approach are compared to those obtained using a second, 'lifting-chord' method that is based on Peters's formulation of classical unsteady thin

aerofoil theory. In this approach, the aerodynamic environment of the blade is represented via a series of weighted integrals over the chord of each blade panel, thus yielding a higher-order approximation to the aerodynamic boundary condition on the blade than is given by lifting-line theory. The version of the VTM that was used includes a prescription of the blade dynamics that is derived from the HART II experimental data, thus allowing any effects on the quality of the simulation that are due to structural deformations of the rotor blades to be separated from those that are induced by the aerodynamics of the system.

Detailed analysis of the circulation that is induced by the tip vortices shows the vorticity conserving properties of the VTM to result in the integrity of the vortical structures in the wake being preserved to well downstream of the rotor, essentially independently of the resolution of the calculation. The predicted positions of the vortex cores, on a series of several longitudinal slices through the flow, agree with measured data to within a fraction of the blade chord. Accurate prediction of the wake geometry translates into very accurate prediction of the higher-harmonic, BVI-induced component of the aerodynamic loading on the blades. Where the wake prediction is the most accurate, generally on the retreating side of the rotor, all BVI events discernible in the experimental data are reproduced by the numerics, usually with the correct phase and often with the correct amplitude. Where the prediction of the wake geometry is poorer, generally on the advancing side of the rotor, the numerical resolution of the BVI-induced loads is less accurate both in amplitude and phase, yet all BVIs seen in the experimental data are still captured.

Small discrepancies in the positions of the individual vortices do tend to build up though as the wake convects downstream of the rotor, principally on the advancing side of the disc where the roll-up of the wake sheet that is created behind the blade is known to be a rather complex process. Nevertheless, elements of this roll-up process are well-captured by the VTM, including the formation of a vortex-pair type structure from the tip of the advancing blade in the HART II minimum noise test case. Qualitative analysis of the evolution of the tip vortex on the advancing side of the rotor shows the formation of a coherent tip vortex from the extended sheet of vorticity immediately behind the blade to be captured rather well when compared to PIV images of the wake structure.

In general, the predicted airload compares very favourably with the experimentally measured airloads at the 87% radial station, for all three HART II flight cases. The major differences between the experimental data and the numerically predicted airload lie mainly in the low-frequency component of the signal and to the advancing side of the rotor disc. The discrepancies in this component of the airload are similar regardless of computational resolution and also irrespective of the model that is used to represent the aerodynamics of the blade. As the low-frequency component of the blade airload is primarily affected by control inputs and blade structural deformation, it is most likely that the observed discrepancies in the prediction of the low-frequency component of the blade loading are due to errors in the interpolation that was used to prescribe the blade dynamics within the simulation.

Three computational resolutions were used to expose the effect of grid resolution on the quality of predictions. Where the lifting-line model was used to represent the aerodynamics of the blades, the high-frequency, BVI-induced component of the loading is extremely sensitive to the resolution of the computational grid. Although the phase and impulse width is only marginally influenced, the predicted amplitude of the BVI-induced spikes in the loading on the blades increases significantly as the cell size that is used to resolve the wake is reduced. This is because the lifting-line model fundamentally misrepresents the aerodynamic response of the blade particularly when subjected to the very localised perturbations in its aerodynamic environment as in the case of high-frequency blade vortex interactions. As the resolution of the computation is further increased it is likely that the amplitudes of the BVI-loading peaks will be further over-predicted. This suggests a major failing in the lifting-line approach in that its predictions will remain grid dependent for interactions with vortices that have core sizes significantly smaller than the chord. As a result there is minimal possibility of achieving a numerically converged solution using this approach.

In contrast, errors in the amplitude and phase of the BVI-loading peaks are reduced, and the quality of the prediction is affected to a lesser extent by the computational resolution, when a lifting-chord model for the blade aerodynamics is used instead of the lifting-line

type approach. In particular, on the retreating side of the disc, the over-prediction of the amplitude of the BVI events which occurs as the resolution of the computation is increased when using a lifting-line model is avoided. The insensitivity of the lifting-chord model to the resolution of the computation can be explained in terms of its reduced sensitivity to the localised, small-scale features of the flow field and the dependence of its predictions rather on the integral, invariant properties of the flow field. In the context of helicopter BVI, the primary advantage of this approach would appear to be thus the possibility that it offers of true numerical convergence of predictions as the resolution of the computational grid is increased. This should be investigated further, however, as at the time of writing the computational facilities that were available were not yet adequate to test this hypothesis.

Even though the geometry of the wake is well predicted by the VTM, it needs to be borne in mind that the BVI-induced airloads are also influenced by the internal distribution of the vorticity within the wake structure. As a result, the modelling of viscous effects may need to be considered in future in order to decouple the vortex core size from the cell size. The size of the computational cells poses a fundamental lower bound on the size of the vortex that can be resolved. Thus, the calculations at even the highest resolution described here over-predict, by a factor of at least two, the size of the tip vortex during its initial formation. Calculations at higher resolution than those attempted here will soon be feasible, and it is quite likely, given the action of the flux limiters within the convective algorithm of the VTM, that future increases in resolution will result in further localisation of the vortices. In the absence of any process, such as viscous diffusion, that might counter their effect, the grid dependent, soliton-like properties of the wake structure that are induced by the flux limiters (some hint of which was seen in the predictions of vortex core radius) may result in vortex localisation to the point where the structures that are produced are unphysically small. This will need to be addressed in future by adopting a model for the dissipative mechanisms within the wake. It is important though that such a model does not interfere with those beneficial characteristics of the approach that allow it to preserve the integrity of the structure in the wake for the very long times needed to resolve blade-vortex and similar interactions within the helicopter system.

The acoustic field that is radiated by the rotor is computed using a post-processor for the blade aerodynamic loads that implements the Farassat-1A formulation of the Ffowcs Williams-Hawking equations. The thickness noise is modelled independently by attaching a source-sink pair to each blade panel. Noise due to quadrupole terms is neglected in the present work. The absorption and scattering due to the presence of any other bodies in the flow-field is also not modelled. The experimentally-measured directivity of the radiated noise pattern is generally well captured by the numerics, as is the location and magnitude of the maxima in the sound pressure level on the ground plane below the rotor, at least on the retreating side of the disc. The upstream decay of the radiated signal is also well-captured, particularly in the BL flight case. Yet again the larger deficiencies in prediction are encountered on the advancing side of the rotor, where magnitude and phase errors in the predicted BVI-induced component of the blade loading translate into more significant errors in the position and magnitude of the maximum in the sound pressure field on this side of the rotor than on the retreating side.

The time history of acoustic pressure is found to be extremely sensitive to the cell size that is used in the computations, particularly when the lifting-line model was used to represent the aerodynamics of the blades. The predicted amplitude of the BVI-induced acoustic features increases significantly as the cell size that is used to resolve the wake is reduced. The acoustic predictions rely on the loading gradients rather than directly on the amplitude of the BVI-loading peaks and thus are much more sensitive to changes in the resolution of the flow-field, even when the lifting-chord approach is used. In future, for any improvement in the fidelity of the acoustic prediction to be achieved, a high-order representation of the unsteady aerodynamic response of the rotor blades will be required. With the present advancement in computational resources, the most likely candidate in this respect will be the hybrid primitive-variable VTM approach, in which conventional CFD is used to provide a solution for the flow-field in the immediate vicinity of the rotor blades and the VTM is used to track the evolution of vorticity in the wake. In order for such an approach to be viable, the outstanding problems of modelling of transition and separation which currently plague conventional CFD applications need to be adequately resolved, however.

References

- [1] van der Wall, B. G., “Mode identification and data synthesis of HART II blade deflection data,” IB 111-2007/28, <ftp://HART-II@ftp.dlr.de>, 2007.
- [2] Brooks, T. F. and Burley, C. L., “Blade Wake Interaction Noise for a Main Rotor,” *Journal of the American Helicopter Society*, Vol. 49, No. 1, 2004, pp. 11–27.
- [3] Schmitz, F. and Yu, Y., “Helicopter impulsive noise: Theoretical and experimental status,” *Journal of Sound and Vibration*, Vol. 109, No. 3, 1986, pp. 361–422.
- [4] Lawson, M. V., “Progress towards quieter civil helicopters,” *Aeronautical Journal*, Vol. 96, July 1992, pp. 209–223.
- [5] Yu, Y., “Rotor blade vortex interaction noise,” *Progress in Aerospace Sciences*, Vol. 36, Feb. 2000, pp. 97–115.
- [6] Yu, Y., “Rotor blade-vortex interaction noise- Generating mechanisms and its control concepts,” *Proceedings of the AHS Specialists Meeting on Aeromechanics Technology and Product Design*, Bridgeport, CT, USA, 1995.
- [7] Brentner, K. S. and Farassat, F., “Modeling aerodynamically generated sound of helicopter rotors,” *Progress in Aerospace Sciences*, Vol. 39, No. 2-3, 2003, pp. 83–120.
- [8] Brentner, K. S. and Farassat, F., “Helicopter Noise Prediction: The Current Status and Future Direction,” *Journal of Sound and Vibration*, Vol. 170, No. 1, 1994, pp. 79–96.

- [9] Leverton, J. W. and Taylor, F. W., "Helicopter blade slap," *Journal of Sound Vibration*, Vol. 4, Nov. 1966.
- [10] Gutin, L., "On the sound of a rotating airscrew," *translated as NACA TM 1192*, 1948.
- [11] Wright, S., "Sound radiation from a lifting rotor generated by asymmetric disk loading," *Journal of Sound and Vibration*, Vol. 9, No. 2, 1969, pp. 223–226, IN7–IN8, 227–240.
- [12] S. Widnall, "Helicopter Noise due to Blade-Vortex Interaction," *The Journal of the Acoustical Society of America*, Vol. 50, No. 1B, 1971, pp. 354–365.
- [13] Lowson, M. V., *Proceedings of the Royal Society of London, Series A, Mathematical and Physical Sciences*, Vol. 286, August 1965, pp. 559–572.
- [14] Lowson, M. V. and Ollerhead, J. B., "A theoretical study of helicopter rotor noise," *Journal of Sound Vibration*, Vol. 9, March 1969, pp. 197–222.
- [15] Lighthill, M. J., "On Sound Generated Aerodynamically. I. General Theory," *Proceedings of the Royal Society of London. Series A. Mathematical and Physical Sciences*, Vol. 211, No. 1107, 1952, pp. 564–587.
- [16] Ffowcs Williams, J. E. and Hawkings, D. L., "Sound Generation by Turbulence and Surfaces in Arbitrary Motion," *Philosophical Transactions of the Royal Society of London. Series A, Mathematical and Physical Sciences*, Vol. 264, No. 1151, 1969, pp. 321–342.
- [17] Hawkings, D. L. and Lowson, M. V., "Theory of open supersonic rotor noise," *Journal of Sound and Vibration*, Vol. 36, No. 1, 1974, pp. 1–20.
- [18] Farassat, F., "Theory of Noise Generation From Moving Bodies With an Application to Helicopter Rotors," *NASA TR R-451*, 1975.
- [19] Farassat, F. and Succi, G. P., "The prediction of helicopter rotor discrete frequency noise," *Vertica*, Vol. 7, No. 4, 1983, pp. 309–320.

- [20] Farassat, F. and Succi, G. P., “A review of propeller discrete frequency noise prediction technology with emphasis on two current methods for time domain calculations,” *Journal of Sound and Vibration*, Vol. 71, No. 3, 1980, pp. 399–419.
- [21] Schmitz, F. H. and Boxwell, D. A., “In-Flight Far-Field Measurement of Helicopter Impulsive Noise,” *Journal of the American Helicopter Society*, Vol. 21, No. 4, 1976, pp. 2–16.
- [22] Boxwell, D. A. and Schmitz, F. H., “Full-scale measurements of blade-vortex interaction noise,” *Journal of the American Helicopter Society*, Vol. 27, Oct. 1982, pp. 11–27.
- [23] Schmitz, F. H., Boxwell, D. A., Léwy, S., and Dahan, C., “Model- to Full-Scale Comparisons of Helicopter Blade-Vortex Interaction Noise,” *Journal of the American Helicopter Society*, Vol. 29, No. 2, 1984, pp. 16–25.
- [24] Martin, R. M., “NASA/AHS rotorcraft noise reduction program - NASA Langley Acoustics Division contributions,” *Vertiflite*, Vol. 35, June 1989, pp. 48–52.
- [25] Martin, R. M. and Splettstoesser, W. R., “Acoustic results of the blade-vortex interaction acoustic test of a 40 percent model rotor in the DNW,” *Proceeding of AHS National Specialists’ Meeting on Aerodynamics and Aeroacoustics*, Arlington, TX, USA, 1987.
- [26] Visintainer, J. A., Burley, C. L., Marcolini, M. A., and Liu, S. R., “Acoustic predictions using measured pressures from a model rotor in the DNW,” *Proceedings of the American Helicopter Society 47th Annual forum*, Vol. 2, Phoenix, AZ, USA, May 1991, pp. 791–806.
- [27] Liu, S. R. and Marcolini, M. A., “The acoustic results of a United Technologies scale model helicopter rotor tested at DNW,” *Proceedings of the American Helicopter Society 46th Annual forum*, Vol. 1, Washington, DC, USA, May 1990, pp. 347–366.
- [28] Burley, C. L. and Martin, R. M., “Tip-path-plane angle effects on rotor blade-vortex interaction noise levels and directivity,” *Proceedings of the American Helicopter Society 44th Annual forum*, Washington, DC, USA, 1988, pp. 757–771.

- [29] Spletstoesser, W. R., Niesl, G., Cenedese, F., Nitti, F., and Papanikas, D. G., “Experimental results of the European HELINOISE aeroacoustic rotor test,” *Journal of the American Helicopter Society*, Vol. 40, April 1995, pp. 3–14.
- [30] Klöppel, V., Kroll, N., Costes, M., Morino, L., Simons, I., W., S., and Lawson, M., “The BRITE/EURAM Programme “HELISHAPE” – A Successful Step to better Helicopter Aerodynamic and Aeroacoustic Description.” *DLR Electronic Library* [<http://elib.dlr.de/perl/oai2>], Germany, 1997.
- [31] van der Wall, B. G., Junker, B., Burley, C., Brooks, T., Yu, Y., Tung, C., Raffel, M., Richard, H., Wagner, W., Mercker, E., Pengel, K., Holthusen, H., Beaumier, P., and Delrieux, Y., “The HART II test in the LLF of the DNW - a Major Step towards Rotor Wake Understanding,” *Proceedings of the 28th European Rotorcraft Forum*, Bristol, England, 2002.
- [32] van der Wall, B. G., Burley, C., Yu, Y., Richard, H., Pengel, K., and Beaumier, P., “The HART II test—Measurement of helicopter rotor wakes,” *Aerospace Science and Technology*, Vol. 8, No. 4, 2004, pp. 273–284.
- [33] Lim, J., Tung, C., Yu, Y., Burley, C., Brooks, T., Boyd, D., van der Wall, B. G., Schneider, O., Richard, H., Raffel, M., Beaumier, P., Delrieux, Y., Pengel, K., and Mercker, E., “HART II: Prediction of Blade-Vortex Interaction Loading,” *Proceedings of the 29th European Rotorcraft Forum*, Friedrichshafen, Germany, 2003.
- [34] Yu, Y., Tung, C., van der Wall, B. G., Pausder, H., Burley, C., Brooks, T., Beaumier, P., Delrieux, Y., Mercker, E., and Pengel, K., “The HART-II Test: Rotor Wakes and Aeroacoustics with Higher-Harmonic Pitch Control (HHC) Inputs – The Joint German/French/Dutch/US Project,” *Proceedings of the American Helicopter Society 58th Annual Forum*, Montreal, Canada, 2002.
- [35] Gallman, J. M., Tung, C., Schultz, K.-J., Spletstoesser, W., Buchholz, H., Spiegel, P., Burley, C. L., Brooks, T. F., and Boyd, D. D., “Effect of Wake Structure on Blade-Vortex Interaction Phenomena: Acoustic Prediction and Validation,” *Proceedings of the 1st Joint CEAS/AIAA Aeroacoustic Conference*, Munich, Germany, 1995.

- [36] Datta, A., Nixon, M., and Chopra, I., “Review of Rotor Loads Prediction with the Emergence of Rotorcraft CFD,” *Journal of the American Helicopter Society*, Vol. 52, No. 4, 2007, pp. 287–317.
- [37] Boyd, D. D., “HART II Acoustic Predictions using a Coupled CFD/CSD Method,” *Proceedings of the American Helicopter Society 65th Annual Forum*, Grapevine, TX, USA, 2009.
- [38] Lim, J. W. and Strawn, R. C., “Prediction of HART II Rotor BVI Loading and Wake System Using CFD/CSD Loose Coupling,” *Proceedings of the 45th AIAA Aerospace Sciences Meeting and Exhibit*, Paper AIAA-2007-1281, Reno, NV, USA.
- [39] Yu, D. O., Jung, M. S., Kwon, O. J., and Yu, Y. H., “Predicting Blade Loading and Wake Structure of the HART II Rotor using Adaptive Unstructured Meshes,” *Proceedings of the AHS 2nd International Forum on Rotorcraft Multidisciplinary Technology*, Seoul, Korea, 2009.
- [40] Lim, J. and Dimanlig, A. C. B., “An Investigation of the Fuselage Effect for HART II Using a CFD/CSD Coupled Analysis,” *Proceedings of the AHS 2nd International Forum on Rotorcraft Multidisciplinary Technology*, Seoul, Korea, 2009.
- [41] Bailly, J., Delrieux, Y., and Beaumier, P., “HART II: Experimental Analysis and Validation of ONERA Methodology for the Prediction of Blade-Vortex Interaction,” *Proceedings of the 30th European Rotorcraft Forum*, Marseille, France, 2004.
- [42] Lim, J. and van der Wall, B. G., “Investigation of the effect of a multiple trailer wake model for descending flights,” *Proceedings of the American Helicopter Society 61st Annual Forum*, 2005, pp. 1063–1081.
- [43] Ojima, A. and Kamemoto, K., “Numerical Investigation of Rotor Wake in Forward Flight by using a Vortex Method,” *Proceedings of the AHS 2nd International Forum on Rotorcraft Multidisciplinary Technology*, Seoul, Korea, 2009.
- [44] van der Wall, B. G. and Yin, J., “Cruise-Speed BVI Noise Computation by Comprehensive Code and Validation with HART I Data,” *Proceedings of the AHS 2nd International Forum on Rotorcraft Multidisciplinary Technology*, Seoul, Korea, 2009.

- [45] van der Wall, B. G. and Yin, J., "Simulation of Active Rotor Control by Comprehensive Rotor Code with Prescribed Wake using HART II Data," *Proceedings of the American Helicopter Society 65th Annual Forum*, Grapevine, TX, USA, May 2009.
- [46] Beddoes, T. S., "A wake model for high resolution airloads," *Proceedings of International Conference on Rotorcraft Basic Research*, Research Triangle Park, NC, USA, 1985, pp. 19–21.
- [47] Brown, R. E., "Rotor Wake Modeling for Flight Dynamic Simulation of Helicopters," *AIAA Journal*, Vol. 38, No. 1, 2000, pp. 57–63.
- [48] Brown, R. E. and Line, A., "Efficient High-Resolution Wake Modelling using the Vorticity Transport Model," *AIAA Journal*, Vol. 43, No. 7, 2005, pp. 1434–1443.
- [49] Kelly, M. E., Duraisamy, K., and Brown, R. E., "Predicting Blade Vortex Interaction, Airloads and Acoustics using the Vorticity Transport Model," *Proceedings of the AHS 9th Specialists' Meeting on Aeromechanics*, San Francisco, CA, USA, 2008.
- [50] Kelly, M. E. and Brown, R. E., "Predicting the wake structure of the HART II rotor using the Vorticity Transport Model," *Proceedings of the 34th European Rotorcraft Forum*, Liverpool, UK, 2008.
- [51] Kelly, M. E. and Brown, R. E., "The effect of blade aerodynamic modelling on the prediction of high-frequency rotor airloads," *Proceedings of the American Helicopter Society 65th Annual Forum*, Grapevine, TX, USA, 2009.
- [52] Kelly, M. E. and Brown, R. E., "The Effect of Blade Aerodynamic Modelling on the Prediction of the Blade Airloads and the Acoustic Signature of the HART II Rotor," *Proceedings of the 35th European Rotorcraft Forum*, Hamburg, Germany, 2009.
- [53] Whitehouse, G., Boschitsch, A., Quackenbush, T., Wachspress, D., and Brown, R. E., "Novel Eulerian Vorticity Transport Wake Module for Rotorcraft Flow Analysis," *Proceedings of the American Helicopter Society 63rd Annual Forum*, Virginia Beach, VA, USA, 2007.

- [54] Kim, H. W. and Brown, R. E., “Modelling the Aerodynamics of Coaxial Helicopters - from an Isolated Rotor to a Complete Aircraft,” *Proceedings of the 1st EU-Korea Conference on Science and Technology*, Heidelberg, Germany, August 2008.
- [55] Kim, H. W. and Brown, R. E., “Impact of Trim Strategy and Rotor Stiffness on Coaxial Rotor Performance,” *Proceedings of the 1st AHS/KSASS International Forum on Rotorcraft Multidisciplinary Technology*, Seoul, Korea, 2007.
- [56] Kim, H. W., Kenyon, A. R., Duraisamy, K., and Brown, R. E., “Interactional Aerodynamics and Acoustics of a Hingeless Coaxial Helicopter with an Auxiliary Propeller in Forward Flight,” *Aeronautical Journal*, Vol. 113, No. 1140, 2009.
- [57] Whitehouse, G. R. and Brown, R. E., “Modelling a Helicopter Rotor’s Response to Encounters with Aircraft Wakes,” *Proceedings of the 28th European Rotorcraft Forum*, Bristol, England, UK, September 2002.
- [58] Kenyon, A. R. and Brown, R. E., “Wake Dynamics and Rotor–Fuselage Aerodynamic Interactions ,” *Journal of the American Helicopter Society*, Vol. 54, No. 1, 2009.
- [59] Fletcher, T. M. and Brown, R. E., “Main rotor - tail rotor interaction and its implications for helicopter directional control,” *Journal of the American Helicopter Society*, Vol. 53, No. 2, 2008, pp. 125–138.
- [60] Whitehouse, G. R. and Brown, R. E., “Helicopter Rotor Response to Wake Encounters in Ground Effect,” *Proceedings of the American Helicopter Society 59th Annual Forum*, Phoenix, AZ, USA, May 2003.
- [61] Phillips, C. and Brown, R. E., “Eulerian Simulation of the Fluid Dynamics of Helicopter Brownout,” *Journal of Aircraft*, Vol. 46, No. 4, 2009.
- [62] Phillips, C. and Brown, R. E., “The Effect of Helicopter Configuration on the Fluid Dynamics of Brownout,” *Proceedings of the 34th European Rotorcraft Forum*, Liverpool, England, UK, September 2008.
- [63] Ahlin, G. A. and Brown, R. E., “Wake Structure and Kinematics in the Vortex Ring State,” *Journal of the American Helicopter Society*, Vol. 54, No. 3, 2009.

- [64] Toro, E. F., “A Weighted Average Flux Method for Hyperbolic Conservation Laws,” *Proceedings of the Royal Society of London, Series A: Mathematical and Physical Sciences*, Vol. 423, 1989, pp. 401–418.
- [65] Brown, R. E., “Numerical Solution of the Two-Dimensional Navier-Stokes Equations Using Viscous-Convective Operator Splitting,” *M.Sc. Thesis, College of Aeronautics, Cranfield Inst. of Technology*, 1990.
- [66] Strang, G., “On the Construction and Comparison of Finite Difference Schemes,” *Journal of Numerical Analysis*, Vol. 5, 1968, pp. 995–1011.
- [67] Greengard, L. and Rokhlin, V., “A fast algorithm for particle simulations,” *J. Comput. Phys.*, Vol. 73, No. 2, 1987, pp. 325–348.
- [68] Schneider, O., “Analysis of SPR measurements from HART II,” *Aerospace Science and Technology*, Vol. 9, No. 5, 2005, pp. 409–420.
- [69] Schneider, O., van der Wall, B. G., and Pengel, K., “HART II Blade Motion Measured by Stereo Pattern Recognition (SPR),” *Proceedings of the American Helicopter Society 59th Annual Forum*, Phoenix, AZ, USA, 2003.
- [70] Pengel, K., Müller, R., and van der Wall, B. G., “Stereo Pattern Recognition – the technique for reliable rotor blade deformation and twist measurement,” *Proceedings of the AHS International Specialists’ Meeting on Advanced Rotorcraft Technology and Life Saving Activities*, Utsunomiya, Japan, 2002.
- [71] Lim, J., Nygaard, T., Strawn, R., and Potsdam, M., “BVI airloads prediction using CFD/CSD loose coupling,” *Proceedings of the AHS Specialists’ Meeting on Vertical Lift Design Conference*, San Francisco, CA, USA, 2006.
- [72] Leishman, J., *Principles of Helicopter Aerodynamics (Cambridge Aerospace Series)*, Cambridge University Press, 2nd ed., April 2006.
- [73] Leishman, J. G. and Beddoes, T. S., “A Semi-Empirical Model for Dynamic Stall,” *Journal of the American Helicopter Society*, Vol. 34, No. 3, 1989, pp. 3–17.

- [74] Prandtl, L., “Applications of Modern Hydrodynamics to Aeronautics,” *NACA Report 116*, 1921.
- [75] Weissinger, J., “The lift distribution of swept-back wings,” *NACA-TM-1120*, 1947.
- [76] Jones, R. T., *Wing Theory*, Princeton, NJ: Princeton Univ. Press, 1990.
- [77] van Holten, T., “Some notes on unsteady lifting-line theory,” *Journal of Fluid Mechanics*, Vol. 77, 1976, pp. 561–579.
- [78] Peters, D., Hsieh, M.-C., and Torrero, A., “A state-space airloads theory for flexible airfoils,” *Journal of the American Helicopter Society*, Vol. 52, No. 4, 2007, pp. 318–328.
- [79] Wagner, H., “Über die Entstehung des dynamischen Auftriebes von Tragflügeln,” *Zeitschrift für Angewandte Mathematik und Mechanik*, Vol. 5, No. 1, 1925, pp. 17–35.
- [80] Jones, R. T., “The unsteady lift of a wing of finite aspect ratio,” *NACA Report 681*, 1939, pp. 31–38.
- [81] Küssner, H. G., “Zusammenfassender Bericht über den instationären Auftrieb von Flügeln,” *Luftfahrt-Forschung*, Vol. 13, No. 12, 1936, pp. 410–424.
- [82] Duraisamy, K. and Brown, R. E., “Aerodynamic Response of a Hovering Rotor to Ramp Changes in Pitch Input,” *Proceedings of the American Helicopter Society 64th Annual Forum*, Montreal, Canada, 2008.
- [83] Thom, A. and Duraisamy, K., “High Resolution Computation of the Aerodynamics and Acoustics of Blade Vortex Interaction,” *Proceedings of the American Helicopter Society 65th Annual Forum*, Grapevine, TX, USA, May 2009.
- [84] van der Wall, B. G. and Richard, H., “Analysis Methodology for 3C PIV Data,” *Proceedings of the 31st European Rotorcraft Forum*, Florence, Italy, 2005.
- [85] van der Wall, B. G. and Richard, H., “Analysis Methodology for 3C PIV Data of Rotary Wing Vortices,” *Experiments in Fluids*, Vol. 40, No. 4, 2006, pp. 798–812.

-
- [86] Ramasamy, M., Johnson, B., and Leishman, G., “Tip Vortex Measurements Using Dual Plane Digital Particle Image Velocimetry,” *Proceedings of the American Helicopter Society 64th Annual Forum*, Montreal, Canada, 2008.

Appendix A

Interpolation coefficients for blade deformations

A.1 Elastic torsion motion (θ_{el}) coefficients

a_{ij}	$j = 1$	$j = 2$	$j = 3$	$j = 4$	$j = 5$	$j = 6$	$j = 7$	$j = 8$	$j = 9$
$i = 1$	-0.73	-2.64	2.21	0.96	3.35	0.13	0.82	0.27	1.43
$i = 2$	8.99	24.90	-24.17	-10.45	-37.80	-1.89	-5.55	-5.70	-15.66
$i = 3$	-34.10	-89.11	88.06	41.23	145.02	10.43	10.58	26.36	62.17
$i = 4$	53.50	148.18	-144.24	-73.70	-261.14	-24.05	-2.57	-51.51	-113.89
$i = 5$	-40.94	-117.63	111.63	60.89	220.94	24.29	-9.48	47.13	98.47
$i = 6$	12.69	36.11	-33.37	-19.02	-71.09	-8.94	6.40	-16.43	-32.50

Table A.1: Interpolation coefficients to recreate the elastic torsion motion of Blade 1. (HART II BL case, degrees, R in metres).

a_{ij}	$j = 1$	$j = 2$	$j = 3$	$j = 4$	$j = 5$	$j = 6$	$j = 7$	$j = 8$	$j = 9$
$i = 1$	-6.74	-0.23	-2.29	-2.39	-8.01	0.98	-1.59	-2.44	-5.02
$i = 2$	55.71	2.95	14.32	22.36	54.63	-10.54	10.38	19.21	36.60
$i = 3$	-167.25	-12.08	-29.61	-75.72	-140.81	42.16	-21.35	-58.40	-98.45
$i = 4$	226.52	18.57	20.72	121.51	164.58	-78.46	11.87	84.20	121.49
$i = 5$	-146.92	-11.45	4.14	-93.37	-86.16	67.99	8.48	-56.90	-67.44
$i = 6$	37.49	2.07	-7.23	27.50	15.20	-22.19	-7.81	14.34	12.72

Table A.2: Interpolation coefficients to recreate the elastic torsion motion of Blade 2. (HART II BL case, degrees, R in metres).

a_{ij}	$j = 1$	$j = 2$	$j = 3$	$j = 4$	$j = 5$	$j = 6$	$j = 7$	$j = 8$	$j = 9$
$i = 1$	-2.92	1.95	2.04	-0.76	1.87	0.59	-0.94	-0.94	0.23
$i = 2$	24.42	-18.21	-17.82	5.54	-27.97	-5.08	11.42	5.47	-6.56
$i = 3$	-79.61	63.82	56.20	-12.34	123.56	19.04	-48.77	-10.39	34.68
$i = 4$	110.14	-108.57	-80.45	10.47	-244.15	-34.90	93.89	5.88	-72.97
$i = 5$	-71.67	88.63	54.00	-2.11	221.07	30.20	-83.20	3.43	68.53
$i = 6$	18.50	-27.89	-13.76	-0.89	-74.89	-9.82	27.73	-3.33	-23.98

Table A.3: Interpolation coefficients to recreate the elastic torsion motion of Blade 3. (HART II BL case, degrees, R in metres).

a_{ij}	$j = 1$	$j = 2$	$j = 3$	$j = 4$	$j = 5$	$j = 6$	$j = 7$	$j = 8$	$j = 9$
$i = 1$	-2.47	0.52	-0.77	-2.14	-0.84	1.80	3.27	-0.68	-2.94
$i = 2$	24.95	-5.22	6.51	19.65	1.08	-17.87	-32.56	3.55	24.77
$i = 3$	-82.97	19.39	-22.74	-68.33	7.05	65.44	118.19	-3.64	-78.92
$i = 4$	116.34	-36.13	41.11	113.78	-25.23	-112.63	-201.54	-7.58	120.05
$i = 5$	-76.24	31.60	-35.24	-92.29	26.81	92.05	163.73	17.47	-87.51
$i = 6$	19.40	-10.42	11.38	29.24	-9.40	-28.85	-51.05	-9.07	24.58

Table A.4: Interpolation coefficients to recreate the elastic torsion motion of Blade 4 (HART II BL case, degrees, R in metres).

A.2 Elastic flap motion (Z_{el}) coefficients

a_{ij}	$j = 1$	$j = 2$	$j = 3$	$j = 4$	$j = 5$	$j = 6$	$j = 7$	$j = 8$	$j = 9$
$i = 1$	-3.18	2.41	-3.55	-3.07	-7.92	2.07	-0.89	-3.00	-2.31
$i = 2$	34.62	-33.54	35.65	30.41	56.76	-18.58	8.45	24.55	13.78
$i = 3$	-150.81	106.42	-137.32	-120.92	-144.56	56.81	-25.63	-76.98	-23.86
$i = 4$	284.47	-202.20	241.98	204.12	224.51	-111.88	47.14	113.38	12.13
$i = 5$	-263.24	159.02	-192.09	-159.20	-199.29	116.72	-47.49	-79.28	1.66
$i = 6$	85.94	-47.70	58.68	47.95	69.05	-43.13	16.41	21.41	-1.66

Table A.5: Interpolation coefficients to recreate the elastic flap motion of Blade 1. (HART II BL case, mm, R in metres).

a_{ij}	$j = 1$	$j = 2$	$j = 3$	$j = 4$	$j = 5$	$j = 6$	$j = 7$	$j = 8$	$j = 9$
$i = 1$	2.18	0.81	-6.87	-2.13	-3.33	1.26	-5.42	-3.84	-0.48
$i = 2$	-10.91	-16.19	56.99	21.52	10.08	-11.77	46.57	34.05	-5.03
$i = 3$	-12.23	44.59	-183.00	-79.21	29.31	35.12	-152.43	-114.53	49.92
$i = 4$	34.76	-90.71	296.14	130.92	-89.97	-61.57	255.66	189.62	-121.86
$i = 5$	-60.37	61.80	-223.31	-98.94	71.57	57.98	-215.06	-152.81	114.95
$i = 6$	24.75	-14.83	65.31	28.80	-20.21	-18.42	68.83	48.42	-37.41

Table A.6: Interpolation coefficients to recreate the elastic flap motion of Blade 2. (HART II BL case, mm, R in metres).

a_{ij}	$j = 1$	$j = 2$	$j = 3$	$j = 4$	$j = 5$	$j = 6$	$j = 7$	$j = 8$	$j = 9$
$i = 1$	10.21	2.18	-9.85	-1.60	9.43	-2.24	-8.04	-1.93	7.45
$i = 2$	-88.73	-31.31	102.98	16.07	-110.13	25.43	86.87	14.92	-81.66
$i = 3$	274.74	100.31	-389.68	-54.72	466.19	-109.33	-339.12	-43.23	330.11
$i = 4$	-476.39	-199.57	722.46	90.28	-849.39	198.66	620.02	66.01	-608.77
$i = 5$	381.51	162.92	-612.85	-68.23	704.62	-164.29	-533.81	-49.14	519.26
$i = 6$	-122.98	-50.49	197.18	20.11	-223.05	54.02	172.20	14.50	-166.69

Table A.7: Interpolation coefficients to recreate the elastic flap motion of Blade 3. (HART II BL case, mm, R in metres).

a_{ij}	$j = 1$	$j = 2$	$j = 3$	$j = 4$	$j = 5$	$j = 6$	$j = 7$	$j = 8$	$j = 9$
$i = 1$	2.42	-0.34	-0.83	-3.40	-2.80	1.55	-0.13	-2.63	-0.59
$i = 2$	-14.23	-5.89	9.74	34.55	14.22	-14.79	3.13	22.61	-0.24
$i = 3$	10.01	6.25	-43.76	-133.13	-0.54	42.15	-19.44	-74.52	17.63
$i = 4$	9.56	-25.54	90.29	227.63	-5.75	-77.37	49.12	117.93	-45.96
$i = 5$	-40.18	6.70	-69.03	-180.86	-18.48	77.79	-54.53	-89.92	39.28
$i = 6$	16.38	3.56	19.41	55.45	13.40	-27.07	19.97	26.91	-10.68

Table A.8: Interpolation coefficients to recreate the elastic flap motion of Blade 4. (HART II BL case, mm, R in metres).

A.3 Elastic lag motion (Y_{el}) coefficients

a_{ij}	$j = 1$	$j = 2$	$j = 3$	$j = 4$	$j = 5$	$j = 6$	$j = 7$	$j = 8$	$j = 9$
$i = 1$	14.44	-0.04	-5.27	0.63	10.52	-2.07	-5.09	1.17	2.04
$i = 2$	-53.83	1.08	29.60	-9.58	-63.46	20.35	43.47	-9.73	0.85
$i = 3$	291.23	-6.24	-91.45	34.74	136.58	-73.07	-139.34	29.03	-48.14
$i = 4$	-436.55	-0.15	101.76	-57.44	-125.88	119.96	220.14	-42.08	133.87
$i = 5$	307.91	5.38	-54.44	44.23	38.97	-90.56	-168.99	27.84	-139.37
$i = 6$	-85.75	-2.93	10.67	-12.59	2.10	25.70	49.90	-6.75	50.41

Table A.9: Interpolation coefficients to recreate the elastic lag motion of Blade 1. (HART II BL case, mm, R in metres).

a_{ij}	$j = 1$	$j = 2$	$j = 3$	$j = 4$	$j = 5$	$j = 6$	$j = 7$	$j = 8$	$j = 9$
$i = 1$	9.25	-3.65	4.18	-0.24	2.54	-2.63	2.99	0.22	-2.13
$i = 2$	-8.32	36.64	-50.04	2.86	-3.00	23.63	-30.54	-7.44	33.95
$i = 3$	140.85	-138.99	174.27	1.93	-53.98	-78.00	119.01	22.77	-160.84
$i = 4$	-204.01	234.05	-327.82	-10.00	172.90	119.62	-214.08	-26.95	326.36
$i = 5$	138.49	-192.99	281.49	7.65	-183.62	-85.70	181.73	8.78	-299.98
$i = 6$	-38.36	62.13	-91.36	-1.10	65.47	23.39	-59.14	1.78	102.11

Table A.10: Interpolation coefficients to recreate the elastic lag motion of Blade 2. (HART II BL case, mm, R in metres).

a_{ij}	$j = 1$	$j = 2$	$j = 3$	$j = 4$	$j = 5$	$j = 6$	$j = 7$	$j = 8$	$j = 9$
$i = 1$	12.33	-2.80	3.46	0.42	11.09	-1.88	5.54	-0.12	1.92
$i = 2$	-49.79	28.39	-61.18	-4.75	-59.23	19.25	-65.55	4.31	2.76
$i = 3$	300.46	-111.47	259.41	9.37	112.02	-72.34	278.82	-29.62	-62.90
$i = 4$	-453.48	186.25	-539.15	-2.22	-63.77	127.95	-535.05	71.13	175.14
$i = 5$	310.53	-151.34	499.70	-9.48	-27.34	-106.37	475.48	-74.58	-185.21
$i = 6$	-80.76	47.83	-172.07	6.64	26.88	33.83	-159.47	28.26	67.96

Table A.11: Interpolation coefficients to recreate the elastic lag motion of Blade 3. (HART II BL case, mm, R in metres).

a_{ij}	$j = 1$	$j = 2$	$j = 3$	$j = 4$	$j = 5$	$j = 6$	$j = 7$	$j = 8$	$j = 9$
$i = 1$	21.98	-1.41	-6.98	6.29	27.07	-2.84	-4.95	2.24	10.03
$i = 2$	-131.73	16.68	44.27	-70.85	-217.85	29.11	32.11	-3.56	-71.96
$i = 3$	571.68	-64.99	-118.64	257.58	683.80	-106.85	-80.31	-32.36	207.90
$i = 4$	-910.11	103.78	114.07	-449.41	-1056.93	180.08	91.15	119.92	-296.43
$i = 5$	679.56	-80.44	-41.51	377.00	806.12	-142.18	-43.47	-145.22	208.64
$i = 6$	-196.00	24.19	0.36	-121.84	-242.50	43.18	4.92	59.18	-58.65

Table A.12: Interpolation coefficients to recreate the elastic lag motion of Blade 4. (HART II BL case, mm, R in metres).